



The  
University  
Of  
Sheffield.

Department  
Of  
Mechanical  
Engineering.

## **Characterisation and Modelling of Normal and Compound Impact Wear in Common Engineering Alloys**

A thesis submitted to the University of Sheffield  
for the degree of Doctor of Philosophy in the Faculty of Engineering

Author: Mohanad Qasim Zalzalah  
Date: June 2021  
Supervisors: **Dr. Tom Slatter**  
**Prof. Roger Lewis**

## Abstract

Impact wear is one of the types of wear that have been least researched previously and therefore data on the causes is still quite scarce. It occurs in many engineering and industrial components, posing severe wear problems and limiting service life, but has not been studied as frequently as other wear mechanisms (e.g., abrasion, adhesion, erosive). Impact wear also occurs widely in industrial machinery such as valves, bearings and cams used in energy, metallurgy, petroleum industry and electric power applications, and tools used in mining for rock drilling. Knowing what and how different impact wear parameters affect the wear intensity would be helpful to gaining better understanding of their effects on the impact wear and eventually longer optimal life of the equipment.

The work presented in this thesis aimed to investigate the previously undetermined contribution of the ‘zero wear’ volume for five metallic alloys under repetitive normal impact with point contact geometry. These materials are: austenitic stainless steel AISI 304; medium carbon steel (EN8); ductile cast iron (EN-GJS-600-3); aluminium alloy (AlSi9Cu3) and phosphor bronze (PB102).

The mechanical performance and wear resistance of these materials were assessed using an impact hammering wear rig, while the wear scar features were examined using microscopy techniques and 3D profilometry of the surfaces through use of an Alicona SL in addition to both Vickers hardness and microhardness tests. The analysis of the wear scars suggests that zero wear volume (volume loss due to compression and specimen surface moving in space to a different location but remains in the contact zone) is the main contributor to the total volume ‘loss’ for all materials, and, for specific materials, plastic flow volume and bulk hardness could be a significant parameter in characterising zero wear volume and scar depth.

The research also focused on the crucial role of impact angle for three metal alloys: two types of austenitic stainless steel (AISI 304 and AISI 316) and medium carbon steel (EN8). Wear resistance and mechanical performance were evaluated using the same techniques as utilised for zero wear volume and metallurgical characterisation was achieved through surface and subsurface examination for plastic deformation, grain size, crack initiation and propagation on both the surface and subsurface, and eventually cracks types (intergranular or transgranular). The results suggest that the impact wear damage mechanism changed depending on the impact angle and it has a significant effect on the wear loss of tested materials and the depth of plastic region and deformed grains.

Microhardness profiles for the wear scar were plotted for all ductile materials during this work for both surface and subsurface under different impact angles using an automated hardness tester (Struers Durascan). The results suggest that the hardening value and depth are inversely proportional to impact angle and reduced significantly from normal impact  $90^\circ$  to compound impact  $60^\circ$  and  $45^\circ$ .

Finally, the research developed a new predictive model extracted from the experimental work on both AISI types, 304 and 316, and the EN8 medium carbon steel that was compared with other published papers, taking into consideration the role of impact angle during impact throughout the calculation of both the normal and tangential components of impact force.

## **Acknowledgment**

First and foremost, I would like to thank God, the almighty, for the knowledge gained and the learning experiences, for granting me the strength, stamina, and knowledge, so that I have been finally able to accomplish the thesis.

I would like to express my sincere gratitude to my research supervisors Dr. Tom Slatter and Prof. Roger Lewis, for their continuous support of my Ph.D. study and related projects, for their patience guidance, enthusiastic encouragement, motivation, immense knowledge and invaluable advices. Their guidance helped me in all the time of research and writing of this thesis. I could not have imagined having better supervisors for my Ph.D. study

I would also like to thank the University of Sheffield – Department of Mechanical Engineering for providing the appropriate research environment and providing me with lectures and seminars that helped me during my research. Thanks to all my friends for the lovely time we spent it together in Sheffield, you were always supportive and kind.

To my family, particularly my parents, Mr. and Mrs. Zalalah, my sister and my brother for their endless spiritually support and love during not only my Ph.D. but through my whole life. Without their understanding and encouragement in the past few years, it would be impossible for me to complete my study. Thanks to my princesses Rawan, Rose, and Role for being with me in this long journey

Above all I would like to thank my wife Saja for your love, continuous support, unlimited encouragement and sacrifice of your time and your job to give me this opportunity to pursue my Ph.D. But most of all, thank you for being my soulmate. I owe you everything.

Finally, despite my passion for Tribology, the work reported in this thesis would not have been possible without the incorporeal and financial support of ministry of Oil in Iraq and LUKOIL company, for which I am grateful.

## **List of Publications from This Work**

- [1] M. Zalzal, R. Lewis, and T. Slatter, "A new predictive model for normal and compound impact wear," *Wear*, p. 203954, 2021.
- [2] Lewis R, Zalzal M & Slatter T " Impact Wear Failures", in ASM Handbook. Editors of book: Miller B, Shipley R, Parrington R, Dennies D . 3rd, 11A Failure Analysis and Prevention. ASM International, Cleveland, OH, USA 01 Mar 2021.
- [3] M. Zalzal, R. Lewis, and T. Slatter, "Defining the role of “zero wear volume” in percussive impact," *Wear*, p. 203535, 2020.
- [4] M. Watson, P. Christoforou, P. Herrera, D. Preece, J. Carrell, M. Harmon, et al., "An analysis of the quality of experimental design and reliability of results in tribology research," *Wear*, vol. 426, pp. 1712-1718, 2019.

## **Poster Presentation**

- [1] " Understanding and Modelling Impact Wear " at TriboUK Conference, Sheffield, 12 to 13 April 2018.
- [2] " Investigation on the effect of Zero Wear on Impact Wear " at The Institution of Mechanical Engineers, London, 6 December 2018.

# Contents

<b>Abstract</b> .....	<b>ii</b>
<b>Acknowledgment</b> .....	<b>iii</b>
<b>List of Publications from This Work</b> .....	<b>iv</b>
<b>Poster Presentation</b> .....	<b>iv</b>
<b>List of Figures</b> .....	<b>x</b>
<b>List of Tables</b> .....	<b>xix</b>
<b>Abbreviations</b> .....	<b>xx</b>
<b>Nomenclature</b> .....	<b>xxi</b>
<b>Greek and Latin Letters</b> .....	<b>xxiv</b>
<b>Chapter 1</b> .....	<b>1</b>
1.1 Introduction .....	1
1.2 Aim and Objectives of this Research.....	3
1.3 The Key Novelty of this Work is in Regard to the Following Knowledge Gaps: .....	3
1.4 Thesis Structure .....	4
<b>Chapter 2 Literature Review</b> .....	<b>6</b>
2.1 Introduction.....	6
2.2 General Impact Wear Mechanism.....	6
2.2.1 Material Removal Mechanism.....	6
2.2.2 Impact Wear of Metals .....	7
2.3 Experimental Impact Wear Testing.....	16
2.3.1 Impact Wear Rigs .....	16
2.3.2 Wear Measurements .....	19
2.4 Impact Wear Modelling and Simulation .....	20
2.4.1 Zero Wear Model.....	20
2.4.2 Extant Impact Wear Models.....	22
2.4.3 Impact Wear Numerical Simulation.....	28
2.5 Impact Wear Parameters .....	28
2.5.1 Role of Impact Angle, High Temperature and Impact Conditions .....	28
2.5.2 Role of Bulk Hardness and Surface Hardening.....	31
2.5.3 Change of Surface Roughness during Impact .....	33

2.6 Research Literature Grading .....	34
2.6.1 Methodology.....	34
2.6.2 Results .....	35
2.7 Literature Review Summary & Conclusions.....	37
<b>Chapter 3 Impact Wear Methodology.....</b>	<b>38</b>
3.1 Test Equipment and Specimens .....	38
3.1.1 Impact Test Rig .....	38
3.1.2 Materials Consideration and Test Specimens .....	41
3.1.3 Rig Procedure .....	42
3.2 Theoretical Characterisation of Impact Wear Test Apparatus .....	42
3.3 Experimental Characterisation of Impact Wear Test Apparatus .....	45
3.3.1 High Speed Analysis.....	45
3.3.2 Impact Force Analysis.....	47
3.4 Bulk Hardness .....	49
3.5 Hertzian Contact Stresses .....	51
3.5.1 Surface Stress Calculation .....	52
3.5.2 Subsurface Stress Calculation .....	53
3.5.3 Stresses Analysis Results .....	54
3.6 Zero Wear Methodology .....	56
3.7 Sample Preparation.....	57
3.7.1 Sectioning .....	57
3.7.2 Hot Mounting .....	58
3.7.3 Grinding and Polishing.....	58
3.7.4 Etching .....	59
3.8 Wear Observation.....	62
3.8.1 Optical Microscopy .....	62
3.8.2 Scanning Electron Microscopy (SEM).....	62
3.8.3 Surface Profile Measurements.....	63
3.9 Surface Roughness .....	65
3.10 Testing Procedure.....	66
3.11 Methodology Summary.....	68

<b>Chapter 4 The Role of Zero Wear Volume in Percussive Impact .....</b>	<b>69</b>
4.1 Introduction .....	69
4.2 Test Results .....	69
4.2.1 Wear Volume.....	69
4.2.2 Total Volume Loss .....	70
4.2.3 Role of Bulk Hardness During Normal Impact.....	72
4.3 Wear Scar Morphology .....	74
4.4 Wear Scar Analysis.....	77
4.5 Microhardness Results .....	79
4.6 Discussion.....	81
4.7 Zero Wear Summary .....	83
<b>Chapter 5 Investigation on Impact Wear and Damage Mechanism of Austenitic Stainless Steel 304.....</b>	<b>84</b>
5.1 Introduction.....	84
5.2 Impact Test Results .....	84
5.2.1 Wear Volume.....	84
5.2.2 Total Volume Loss .....	85
5.2.3 Impact Wear Scar Measurements .....	90
5.3 Wear Scar Analysis .....	93
5.3.1 Surface Examination.....	93
5.3.2 Subsurface Examination.....	104
5.3.3 Microhardness Results.....	117
5.3.4 Crack Orientation .....	121
5.4 Wear Debris .....	122
5.5 Discussion .....	129
5.5.1 Wear Volume and Wear Measurements .....	129
5.5.2 Wear Scar Analysis .....	130
5.6 Austenitic Stainless Steel 304 Summary.....	135
<b>Chapter 6 Role of Impact Angle on Surface and Subsurface Deformation of Alloy Steels .....</b>	<b>136</b>
6.1 Introduction .....	136
6.2 Impact Test Results .....	136

6.2.1 Wear Volume.....	136
6.2.2 Total Volume Loss .....	137
6.2.3 Impact Wear Scar Measurements.....	141
6.3 Wear Scar Analysis .....	143
6.3.1 Surface Examination.....	143
6.3.2 Subsurface Examination.....	149
6.3.3 Electro Etching of AISI 316.....	160
6.3.4 Chemical Etching of EN8 .....	167
6.3.5 Microhardness Results .....	172
6.3.6 Crack Orientation .....	175
6.4 Discussion.....	179
6.4.1 Wear Volume and Wear Measurements.....	179
6.4.2 Wear Scar Analysis.....	179
6.5 AISI 316 and EN8 Summary.....	184
<b>Chapter 7 New Proposed Impact Wear Model.....</b>	<b>185</b>
7.1 Introduction.....	185
7.2 Limitation of Extant Wear Models.....	185
7.3 Development of the New Model .....	185
7.3.1 Derivation of Model Parameters.....	187
7.4 Validation of the New Proposed Model .....	189
7.4.1 Austenitic Stainless Steel (AISI 304) .....	189
7.4.2 Austenitic Stainless Steel (AISI 316).....	190
7.4.3 Medium Carbon Steel (EN8).....	191
7.5 Discussion .....	192
7.6 Impact Wear Model Summary .....	195
<b>Chapter 8 Conclusions and Future Work.....</b>	<b>196</b>
8.1 Introduction .....	196
8.2 Summary .....	196
8.3 Conclusions .....	196
8.3.1 The Nature of Impact Wear Mechanisms.....	196
8.3.2 Suggestions on Measurement Methods.....	197
8.4 Novelty of Work .....	197

8.5 Reflection and Future Work .....	197
8.5.1 Impact Wear Rig.....	197
8.5.2 Zero Wear Volume and Tested Alloys.....	198
8.5.3 Role of High Temperature during Repetitive Normal and Compound Impacts.....	198
8.5.4 Austenitic Stainless Steels.....	198
8.5.5 Statistical Analysis .....	199
8.5.6 Impact Wear Model.....	199
<b>References.....</b>	<b>200</b>
<b>Appendix A .....</b>	<b>206</b>
Map Grading Criteria .....	206
<b>Appendix B .....</b>	<b>209</b>
MATLAB Coding for Tested Materials .....	209
Surface stresses calculation .....	209
Subsurface stresses calculations .....	210

## List of Figures

Figure 1.1 Different impact wear modes where specimen under (a) normal impact, and compound impact resulting in interfacial sliding due to; striker-specimen relative motion (b), (c) non-normal impingement angle. ....	1
Figure 1.2 Flow chart of thesis work.....	4
Figure 2.1 Impact Wear Mechanisms.....	7
Figure 2.2 Surface morphology of high carbon steel where, (a) show the delamination after 100,000 cycles and (b) represent the wear debris (plate shape) after 250,000 cycles extracted from [13] .....	7
Figure 2.3 SEM image for surface and subsurface deformation of both rail material (a, b) and weld joint material (c, d) showing the delamination on surface (a, c) and crack propagate parallel to surface (b, d) after 10,000 cycles with normal impact force of 200 N extracted from [15] .....	9
Figure 2.4 SEM image for surface damage of rail material (a) and rail weld joint (b) after 50,000 cycles and impact force of 400 N extracted from [15] .....	9
Figure 2.5 Shear stress in rolling, sliding and impact contacts extracted from [16] .....	10
Figure 2.6 Failure modes induced by white layer which (a) and (b) are the delamination mode and (c) is the spalling mode extracted from [17] .....	10
Figure 2.7 SEM image of medium carbon steel with impact angle 45° showing (a) surface and subsurface cracks and (b) the flake wear debris with obvious sliding mark extracted from [17] .....	11
Figure 2.8 SEM image of steel showing delamination layer extracted from [23].....	12
Figure 2.9 Schematic diagram of subsurface zones .....	13
Figure 2.10 SEM morphology of aluminium specimen where (a) and (b) shows the surface damage while (c) and (d) revealed the subsurface damage extracted from [25] .....	15
Figure 2.11 SEM image of copper alloy specimen showing the worn surface after 250,000 cycles extracted from [27].....	16
Figure 2.12 Ballistic impact wear rig extracted from [17] .....	17
Figure 2.13 Ballistic impact wear rig extracted from [20] .....	17
Figure 2.14 Hammering impact wear rig using cam and spring extracted from [28] .....	18
Figure 2.15 Hammering impact wear rig using electromagnetic fields extracted from [29].....	18
Figure 2.16 Schematic diagram of impact abrasive wear testing equipment extracted from [5] .....	19
Figure 2.17 Diagram represent spherical cap method extracted from [40] .....	20
Figure 2.18 Zero and measurable impact wear extracted from [41] .....	21
Figure 2.19 Schematic diagram of different impact angles.....	29
Figure 2.20 SEM image of medium carbon steel wear scar showing (a) the spherical wear debris and adhesive wear while delamination and surface cracks are shown in (b) extracted from [39] .....	30
Figure 2.21 Profiles measured along the horizontal and vertical diameters of wear scar extracted from [29] .....	34

Figure 2.22 Knowledge map of impact wear .....	36
Figure 3.1 Schematic diagram of impact rig .....	38
Figure 3.2 Controller box, thermocouple and heater cartridges connected to the designed block for use in high temperature measurements.....	40
Figure 3.3 The designed correlation between cam lift, cam velocity and cam acceleration relative to cam angle at 10Hz extracted from [40].....	42
Figure 3.4 Correlation between the velocity of the cam and striker vs the cam angle .....	44
Figure 3.5 Correlation between the theoretical velocity of impact and rig frequency .....	45
Figure 3.6 High speed camera motion.....	46
Figure 3.7 Impact force data for a single nominal impact in an apparatus operating for 1s .....	47
Figure 3.8 Impact force data for 0.1s showing four rebounds recorded for rig operating at 10Hz .....	48
Figure 3.9 Impact force values at different frequencies .....	49
Figure 3.10 Impact force for 1 sec at 3 Hz.....	49
Figure 3.11 Microhardness indentations of AISI 316 specimen as a matrix of 36 points below the impacted region (about 5 mm from the centre of the wear scar).....	51
Figure 3.12 Surface and subsurface stresses for AISI 304 under normal impact.....	54
Figure 3.13 Schematic illustrating the total volume loss during impact .....	57
Figure 3.14 Sectioning process .....	58
Figure 3.15 ASTM E112 for grain size of AISI 304 before impact.....	60
Figure 3.16 ASTM E112 for grain size of AISI 316 before impact.....	61
Figure 3.17 Microstructure of EN8 showing both unimpacted phases, pearlite (P) and ferrite ( $\alpha$ ) .....	62
Figure 3.18 Volume measurements of typical impact wear scar of AISI 304 with impact angle $60^\circ$ after 72,000 cycles by 3D non-contact profilometer shows (a) the impact wear scar and the reference plane while (b) the distortion outside the wear scar edges and (c) the volume of the wear scar .....	64
Figure 4.1 Wear volume of different materials after 36,000 cycles .....	69
Figure 4.2 Mean total volume loss for materials after 36,000 cycles.....	70
Figure 4.3 Plastic deformation and apparent contact area of AISI 304 under normal impact after (a) 9,000 cycle and (b) 16,800 cycle.....	71
Figure 4.4 Example surface deviation of AISI 304 under normal impact after 36,000 cycles.....	71
Figure 4.5 Correlation between bulk hardness and mass loss for different materials after 36,000 cycles .....	72
Figure 4.6 Total volume loss of materials after 36,000 cycles.....	73
Figure 4.7 Zero wear volume loss of materials after 36,000 cycles.....	73
Figure 4.8 Total volume loss on a worn EN8 specimen after 36,000 cycles .....	74
Figure 4.9 Correlation between hardness and impact wear scar diameter after 36,000 cycles .....	75

Figure 4.10 Typical wear scar profile after 36,000 cycles for each material tested. ....	75
Figure 4.11 Typical wear scars for (a) ductile cast iron, (b) EN8, (c) AISI 304, (d) phosphor bronze and (e) aluminium alloy after 36,000 cycles .....	76
Figure 4.12 Typical impact wear scar for tested materials after 36,000 cycles for (a) ductile cast iron, (b) EN8, (c) AISI 304, (d) phosphor bronze and (e) aluminium alloy .....	77
Figure 4.13 Damage mechanism in the centre of the impact scar for tested materials after 36,000 cycles for (a) ductile cast iron, (b) EN8, (c) AISI 304, (d) phosphor bronze and (e) aluminium alloy .....	78
Figure 4.14 Plastic flow formation on the edges and micro-cracks after 36,000 cycles for (a) ductile cast iron, (b) aluminium alloy and (c) EN8 .....	78
Figure 4.15 Microhardness measurements under normal impact for (a) aluminium alloy, (b) phosphor bronze, (c) AISI 304, (d) ductile cast iron and (e) EN8 after 36,000 cycles .....	79
Figure 4.16 Microhardness indentation of EN8 below the bottom edge of wear scar after 36,000 cycles .....	80
Figure 5.1 Mean wear volume for AISI 304 as a function of impact conditions .....	85
Figure 5.2 Total volume loss as measured on a worn surface (reference plane (turquoise), 'above surface' (green, yellow and orange) = plastic flow volume and 'below surface' (red) = total volume loss) at impact angle 60° after 72,000 cycles.....	85
Figure 5.3 Mean total volume loss for AISI 304 Vs impact angles and number of impact cycles .....	86
Figure 5.4 Mean total volume loss, and of each component of the volume loss, for AISI 304 after 72,000 cycles with different impact angles .....	87
Figure 5.5 Mean total volume loss, and of each component of the volume loss, for AISI 304 with compound impacts 45° and different impact cycles.....	88
Figure 5.6 Total volume loss for AISI 304 calculated by spherical cap estimation Vs impact angles and number of impact cycles.....	89
Figure 5.7 Typical diametric and depth of the wear scar with different cycles for AISI 304 under (a) normal impact, (b) compound impact 60° and, (c) compound impact 45° .....	91
Figure 5.8 3D Image of typical depth and pile up profile of impact scars for material with different impact conditions: (a) under normal impact 90°, (b) with impact angle 60°, (c) with impact angle 45° .....	92
Figure 5.9 Typical 2D image of AISI 304 shows the centre and the edges of wear scar .....	93
Figure 5.10 SEM micrograph of worn surface for material after 54,000 cycles under normal impacts reveals the centre of impact wear scar.....	94
Figure 5.11 Crushed region between the hardened surface and new substrate in the centre of impact wear scar for material after 54,000 cycles .....	95
Figure 5.12 SEM micrograph of worn surface for material after 72,000 cycles under normal impacts reveals (a) the centre of impact wear scar and (b) higher magnification of (a) showing the crushed region highlighted in red .....	95
Figure 5.13 Extensively fragmented layer for material after 72,000 cycles.....	96

Figure 5.14 Wear damage mechanism for the centre of wear scar for material after 36,000 cycles under compound impact 60° where (a) and (b) show the abrasive wear and the crushed region, (c) and (d) show the ploughing process due to abrasive wear .....	97
Figure 5.15 SEM micrograph of worn surface for material after 36,000 cycles under compound impact 60° reveals the bottom edge of the wear scar .....	98
Figure 5.16 SEM micrograph reveals the worn centre regions of wear scar after 54,000 cycles under compound impact 60° .....	98
Figure 5.17 SEM micrograph reveals the accumulated plastic flow near the bottom edge of wear scar after 54,000 cycles under compound impact 60° .....	99
Figure 5.18 Multiple layers of delamination near the bottom of the wear scar for material after 72,000 cycles under compound impact 60° with different magnifications .....	100
Figure 5.19 SEM micrographs of worn surface for material after 36,000 cycles under compound impact 45° revealing the different wear damage mechanisms for the centre of wear scar where (a) and (b) shows the crushed particles while (c) and (d) reveals the abrasive wear and grooves .....	101
Figure 5.20 SEM micrograph of worn surface for material after 36,000 cycles under compound impact 45° revealing the bottom edge of the wear scar .....	102
Figure 5.21 SEM micrograph of worn surface for material after 54,000 cycles under compound impact 45° revealing different wear damage mechanisms for the centre of wear scar .....	103
Figure 5.22 SEM micrograph of worn surface for material after 54,000 cycles under compound impact 45° revealing the bottom of wear scar .....	103
Figure 5.23 showing wear damage mechanism for the centre of wear scar of for material after 72,000 cycles under compound impact 45° where (a) shows pitting and two body abrasive wear, (b), (c) and (d) shows an obvious multiple cracks, crushed particles and abrasive wear with grooves .....	104
Figure 5.24 SEM image for material after 72,000 cycles under normal impact showing delamination and pitting .....	105
Figure 5.25 SEM image of subsurface damage for material after 72,000 cycles under compound impact 60° .....	106
Figure 5.26 SEM image of subsurface damage for material after 72,000 cycles under compound impact 60° showing the crushed region in the centre of the wear scar .....	107
Figure 5.27 SEM image of large delamination layer due to subsurface crack for material after 72,000 cycles under compound impact 60° with crushed particles .....	107
Figure 5.28 SEM image showing multiple layers delamination for material after 72,000 cycles under compound impact 60° near the bottom edge .....	108
Figure 5.29 SEM image of plastic flow on the bottom edge of the wear scar for material after 72,000 cycles under compound impact 60° .....	108
Figure 5.30 Optical microscope image showing the wear damage mechanism for material after 72,000 cycles under compound impact 45° .....	109
Figure 5.31 SEM image of pile up materials extruded outside the wear scar for material after 72,000 under compound impact 45° .....	109

Figure 5.32 Optical microscope images with perpendicular sectioning to the impact direction for the centre of wear scar of three specimens showing the wear damage at: (a) normal impact 90°, (b) compound impact 60°, (c) and (d) compound impact 45° after 72,000 cycles .....	110
Figure 5.33 Cross sectional optical microscope image for AISI 304 after 72,000 cycles under normal impact showing centre region of wear scar .....	111
Figure 5.34 Electro etching for material under normal impact for the centre of the wear scar: (a) after 72,000 cycles showing the deformed and undeformed grains, (b) showing the red dotted region in (a) .....	111
Figure 5.35 Optical microscope image of electro etching for material under compound impact 60° showing the centre of the wear scar after 72,000 cycles showing the impact wear zones .....	112
Figure 5.36 SEM images revealing wear damage mechanisms affecting the worn surface layer (zone 3) for material under compound impact 60° where (a) shows the crushed region, (b) reveals the parallel cracks while (c) shows cracks normal to the surface and (d) shows the large parallel crack that separate the worn layer.....	113
Figure 5.37 SEM image of pile up materials on the bottom edge after 72,000 cycles under compound impact 60° as revealed by electro etching .....	114
Figure 5.38 Cross sectional optical microscope image for material after 72,000 cycles under compound impact 45° for (a) centre of wear scar and (b) the bottom edge .....	114
Figure 5.39 Optical microscope image of electro etching for material under compound impact 45° for the centre of wear scar after 72,000 cycles showing the impact wear zones.....	115
Figure 5.40 SEM image reveals the wear damage mechanisms occurring in the worn surface layer for material after 72,000 cycles under compound impact 45° .....	116
Figure 5.41 SEM image after electro etching for material reveals the deformed grains on the bottom edge and the extrusion of pile up materials outside the wear scar of specimen after 72,000 cycles under compound impact 45° .....	117
Figure 5.42 Microhardness profile of original and impacted austenitic stainless steel samples at impact force of 3476 N with different impact conditions where (a) is normal impact 90°, (b) is compound impact 60° and (c) is compound impact 45° .....	118
Figure 5.43 Optical microscope image for the microhardness indentation inside the deformed grains of austenitic stainless steel 304 for compound impact 45° after 54,000.....	120
Figure 5.44 SEM image of transgranular crack propagation inside the grains for material under normal impact after 54,000 cycles.....	121
Figure 5.45 SEM images showing transgranular (within the grains) and intergranular (inside the grain boundaries) crack propagation for material under (a) normal impact 90° after 54,000 cycles and (b) compound impact 45° after 36,000 cycles .....	122
Figure 5.46 SEM image of wear debris for material after 72,000 cycles under normal impact where (a) and (b) show the centre of the wear scar, (c) the bottom edge of the wear scar, (d) outside of the wear scar .....	123
Figure 5.47 OM of wear debris below impact wear scar for material after 72,000 cycles under impact angle 60°.....	123

Figure 5.48 SEM image of wear debris from worn surface after 72,000 cycles under impact angle 60° .....	124
Figure 5.49 OM of wear debris below impact wear scar for material after 72,000 cycles under impact angle 45° .....	124
Figure 5.50 Collected wear debris from worn surface for material under compound impact 45° after 72,000 cycles .....	125
Figure 5.51 Differences in shapes and sizes of wear debris from worn surface for material under compound impact 45° after 72,000 cycles .....	126
Figure 5.52 Flake wear debris from worn surface for material under compound impact 45° after 72,000 cycles .....	126
Figure 5.53 Sliding wear marks on large flake wear debris of worn surface for material under compound impact 45° after 72,000 cycles .....	127
Figure 5.54 SEM image of a chunk of wear debris from worn surface for material after 72,000 cycles under compound impact 45° .....	128
Figure 5.55 SEM image shows the adhered wear particles transferred from the specimen surface to the striker surface with impact angle 60° .....	131
Figure 6.1 Mean wear volume for materials vs different impact angles after 54,000 cycles .....	137
Figure 6.2 Total volume loss as measured on a worn AISI 316 surface (reference plane shown in turquoise), 'above surface' (green, yellow and orange region) is plastic flow volume and 'below surface' (red region) is total volume loss, at impact angle 60° after 54,000 cycles .....	138
Figure 6.3 Mean total volume loss for both materials vs impact angles at 54,000 cycles .....	138
Figure 6.4 Mean total volume loss and volume loss for each component for AISI 316 after 54,000 cycles with different impact angles .....	139
Figure 6.5 Mean total volume loss of AISI 304 and EN8 as calculated by spherical cap method Vs impact angles at 54,000 cycles .....	140
Figure 6.6 Typical diameter and depth of the wear scars for AISI 316 and EN8 after 54,000 cycles under (a) normal impact, (b) compound impact 60°, and (c) compound impact 45° .....	142
Figure 6.7 SEM image of the worn surface of AISI 316 showing the wear damage mechanism in the centre of the scar after 54,000 cycles under: (a) normal impact 90°, (b) impact angle 60° and (c) impact angle 45° .....	144
Figure 6.8 Multiple layers of delamination near the bottom edge of the wear scar for AISI 316 after 54,000 cycles under compound impact 60° with different magnifications .....	145
Figure 6.9 SEM image for the bottom of the wear scar for AISI 316 after 54,000 cycles showing the accumulation of plastic flow materials on or outside the bottom edge under: (a) normal impact 90°, (b) impact angle 60°, and (c) impact angle 45° .....	146
Figure 6.10 SEM images of the worn surface for EN8 showing the wear damage mechanism in the centre of the scar after 54,000 cycles under: (a) normal impact 90° showing the delamination and pitting, (b) impact angle 60° showing the abrasive wear, crushed particles and micro crack, and (c) impact angle 45° showing the abrasive wear, crushed particles and adhered wear debris .....	147

Figure 6.11 Multiple layers of delamination of the wear scar for EN8 after 54,000 cycles near the bottom edge under: (a) impact angle 60° and (b) impact angle 45° .....	148
Figure 6.12 SEM image for the bottom of the wear scar for EN8 after 54,000 cycles showing the accumulation of plastic flow materials on or outside the bottom edge under: (a) normal impact 90°, (b) impact angle 60°, and (c) impact angle 45° .....	149
Figure 6.13 SEM image for AISI 316 after 54,000 cycles under normal impact.....	150
Figure 6.14 SEM image of subsurface damage for AISI 316 after 54,000 cycles under compound impact 60° .....	151
Figure 6.15 SEM image of plastic flow on the bottom edge of the wear scar for AISI 316 after 54,000 cycles under compound impact 60° and multiple layers of delamination near the bottom edge .....	151
Figure 6.16 SEM image showing large subsurface cracks inside the worn surface for AISI 316 after 54,000 cycles under compound impact 45° .....	152
Figure 6.17 SEM image of large delamination layer due to surface and subsurface cracks in AISI 316 after 54,000 cycles under compound impact 45°, with crushed particles to the right side of the image .....	153
Figure 6.18 SEM image of pile up materials extruded outside the impact scar of AISI 316 after 54,000 cycles under compound impact 45° .....	154
Figure 6.19 SEM image for EN8 after 54,000 cycles under normal impact showing multiple layers of delamination .....	155
Figure 6.20 Accumulated plastic flow materials on both the top and bottom edge of the impact scar for EN8 after 54,000 cycles under normal impact .....	155
Figure 6.21 SEM image of subsurface damage for EN8 after 54,000 cycles under compound impact 60° .....	156
Figure 6.22 Multiple layers of delamination for EN8 near the bottom edge of the impact scar after 54,000cycles under compound impact 60° .....	157
Figure 6.23 SEM image of pile up materials on the bottom edge of the impact wear scar for EN8 after 54,000 cycles under compound impact 60° .....	157
Figure 6.24 SEM image showing the wear damage mechanisms for EN8 after 54,000 cycles under compound impact 45°: (a) shows three pits, (b) shows obvious crushed particles, and (c) reveals the delamination layer .....	158
Figure 6.25 SEM image of pile up materials extruded outside the impact scar in EN8 after 54,000 cycles under compound impact 45° .....	159
Figure 6.26 Optical images with perpendicular sectioning to the impact direction for the centre of the impact scar for EN8 showing the wear damage under: (a) normal impact 90°, (b) compound impact 60°, and (c) and (d) compound impact 45° after 54,000 cycles.....	160
Figure 6.27 Optical microscope image for AISI 316 after 54,000 cycles under normal impact.....	161
Figure 6.28 Optical microscope image of electro etching for AISI 316 under normal impact for the centre of the wear scar after 54,000 cycles showing the deformed and undeformed grains .....	161

Figure 6.29 Higher magnification of optical microscope image of electro etching for AISI 316 under normal impact for the centre region of the wear scar after 54,000 cycles showing the deformed and undeformed grains.....	162
Figure 6.30 Optical microscope image for AISI 316 after 54,000 cycles under compound impact 60° where (a) is the centre of the wear scar and (b) is the bottom edge .....	162
Figure 6.31 Optical microscope image of electro etching for AISI 316 steel under compound impact 60° for the centre of the wear scar after 54,000 cycles showing the deformed zones .....	163
Figure 6.32 Higher magnification for the centre region of the impact wear scar for AISI 316 after 54,000 cycles with impact angle 60° showing the highly deformed grains beneath the worn surface (zone 3) .....	164
Figure 6.33 OM image of pile up materials for AISI 316 on the bottom edge after 54,000 cycles under compound impact 60° as revealed by electro etching .....	164
Figure 6.34 Optical microscope image for AISI 316 after 54,000 cycles under compound impact 45° where (a) is the centre region, (b) is a region of interest for investigation and (c) is the bottom edge	165
Figure 6.35 Optical microscope image of electro etching for AISI 316 under compound impact 45° for the centre of the wear scar after 54,000 cycles showing the deformed zones .....	165
Figure 6.36 Higher magnification for the centre region of impact wear scar of AISI 316 after 54,000 cycles with impact angle 45° showing the highly deformed grains beneath the worn surface .....	166
Figure 6.37 Optical microscope images revealing wear damage mechanisms that have occurred in the worn surface layer for AISI 316 after 54,000 cycles with impact angle 45° .....	166
Figure 6.38 Optical microscope image of pile up materials for AISI 316 on the bottom edge after 54,000 cycles under compound impact 45° .....	167
Figure 6.39 Optical microscope image for EN8 after 54,000 cycles under normal impact 90° where (a) is the centre region, (b) is the top edge, and (c) is the bottom edge .....	167
Figure 6.40 Optical microscope image of chemical etching for EN8 under normal impact for the centre of the wear scar after 54,000 cycles .....	168
Figure 6.41 Optical microscope images of top (a) and bottom (b) edges for EN8 after 54,000 cycles under normal impact.....	168
Figure 6.42 Optical microscope image for EN8 after 54,000 cycles under compound impact 60° where (a) is the centre region, and (b) is the bottom edge .....	169
Figure 6.43 Optical microscope image of chemical etching for EN8 with impact angle 60° for the centre of the wear scar after 54,000 cycles showing the deformed zones.....	169
Figure 6.44 Optical microscope image of pile up materials on the bottom edge for EN8 after 54,000 cycles under compound impact 60° as revealed by chemical etching.....	170
Figure 6.45 Optical microscope image for EN8 after 54,000 cycles under compound impact 45° where (a) is the centre region of the wear scar and (b) is the bottom edge .....	170
Figure 6.46 Optical microscope image of chemical etching for EN8 with impact angle 45° for the centre of the wear scar after 54,000 cycles showing the deformed zones.....	171

Figure 6.47 Optical microscope image of extruded materials near the bottom edge for EN8 after 54,000 cycles under compound impact 45° as revealed by chemical etching.....	171
Figure 6.48 Microhardness profile of original and impacted regions of tested specimens for AISI 316 at impact force of 3476 N where (a) normal impact, (b) impact angle 60°, and (c) impact angle 45° ...	172
Figure 6.49 Microhardness profile of original and impacted regions of tested specimens for EN8 at impact force of 3476 N where (a) normal impact, (b) impact angle 60°, and (c) impact angle 45° ...	173
Figure 6.50 Optical microscope image for the microhardness indentation inside the deformed grains of AISI 316 for (a) compound impact 60° and (b) compound impact 45° after 54,000 cycles .....	175
Figure 6.51 Optical microscope image showing both transgranular and intergranular cracks propagation inside and within the grains for AISI 316 after 54,000 cycles under: (a) normal impact 90° and (b) compound impact angle 60° .....	176
Figure 6.52 Optical microscope image showing both transgranular and intergranular cracks propagation inside and within the grains for EN8 after 54,000 cycles under normal impact angle 90° .....	177
Figure 6.53 Optical microscope image showing both transgranular and intergranular cracks propagation inside and within the grains for EN8 after 54,000 cycles under: (a) and (b) compound impact 60°, and (c) impact angle 45° .....	178
Figure 6.54 SEM image shows the adhered wear particles transferred from the AISI 316 worn surface to the striker surface with impact angle 60° .....	180
Figure 7.1 Line fitting from the experimental data of (a) AISI 304, (b) AISI 316 and (c) EN8 under normal impact after 54,000 cycles .....	188
Figure 7.2 Experimental data of Rigaud & Le Bot [29] compared with the Zalzal-Lewis-Slater model data. ....	189
Figure 7.3 Experimental data of Yilmaz & Sadeler [28] under normal impact compared with Zalzal-Lewis-Slater model data.....	190
Figure 7.4 Comparison between the experimental data of Jiang et al. [15] for steel of rail material and rail weld joint material and data from Zalzal-Lewis-Slater model data. ....	191
Figure 7.5 Experimental data of 40Cr steel from Wang [39] compared with the Zalzal-Lewis-Slater model data. ....	192
Figure 7.6 Comparison between the model and the experimental results of AISI 304 under normal impacts and impact force 3476 N where; (a) wear volume measured by mass scale and (b) volume loss measured by 3D non-contact profilometer .....	193
Figure 7.7 Comparison between the model and the experimental results of AISI 304 under compound impacts where; (a) wear volume measured by mass scale and (b) volume loss measured by 3D non-contact profilometer .....	194

## List of Tables

Table 2.1 Impact wear coefficient values adapted from [45] .....	27
Table 3.1 Mechanical properties of tested materials and striker ball .....	41
Table 3.2 Chemical compositions of tested materials and striker ball .....	41
Table 3.3 Spring specifications used in impact hammering wear rig .....	42
Table 3.4 The mean displacement and velocity values per each impact cycle.....	46
Table 3.5 Hardness measurements of tested materials .....	50
Table 3.6 Microhardness measurements of tested materials .....	51
Table 3.7 Summary of stresses values for tested materials under normal impact.....	54
Table 3.8 Summary of stresses values for tested materials with impact angle 60° and normal impact force 3010 N.....	55
Table 3.9 Summary of stresses values for tested materials with impact angle 45° and normal impact force 2457 N.....	55
Table 3.10 Grinding and polishing processes.....	59
Table 3.11 Surface roughness measurements of tested materials by 3D non-contact profilometer Alicona .....	65
Table 3.12 Experimental tests for AISI 304 with different impact conditions.....	66
Table 5.1 Mean total volume loss of AISI 304 after 72,000 with standard deviation for each component .....	87
Table 5.2 Mean total volume loss of AISI 304 with standard deviation for each component with impact angle 45° and different number of cycles.....	88
Table 5.3 Comparison of total volume loss measured by two different methods with different number of cycles and angles .....	90
Table 5.4 Correlation between the impact force and surface hardening of AISI 304 .....	119
Table 5.5 Correlation between the impact force and surface hardening of AISI 304 at a distance of approximately 35µm below the impact surface in the centre of the wear scar .....	120
Table 6.1 Mean volume loss for AISI 316 after 54,000 cycles with standard deviation for each component .....	139
Table 6.2 Comparison of total volume loss as measured by two different methods for AISI 304 and EN8 with different impact angles and after 54,000 cycles .....	141
Table 6.3 Correlation between the impact force and surface hardening of the two materials.....	173
Table 6.4 Correlation between the impact force and surface hardening of AISI 316 at a distance of approximately 35µm below the impact surface in the centre of the wear scar .....	174
Table 7.1 Normal impact wear coefficient $K$ and exponent $n$ for tested materials .....	187
Table 7.2 Mean wear volume and total volume loss of AISI 304 under normal impact with different number of cycles .....	193

## Abbreviations

ASB	Adiabatic Shear Band
BSD	Back Scatter Detector
DOE	Design of Experiment
D. Z	Deformation Zone
EBSD	Electronic Back Scatter Diffraction
OM	Optical Microscope
SE	Secondary Electron
RT	Room Temperature
SEM	Scanning Electron Microscopy
SG	Steam Generator
STD	Standard Deviation
TEM	Transmission Electron Microscopy
W. L	Worn Layer
W. S	Worn Surface

# Nomenclature

All units used in this thesis are S.I units

$a$	Radius of elastic contact area [m]
$A$	The contact area after N cycles in Lewis model [m <sup>2</sup> ]
$A_i$	The initial elastic contact area in Lewis model [m <sup>2</sup> ]
ASTM	American Society for Testing and Materials
B	Level of factors used in DOE
$D_1$	The subsurface damage
$D_2$	The surface damage
$d_1$	The distance from the center of the arm to the pivot point [m]
$d_2$	The distance from the center of the striker holder to the pivot point [m]
$e$	Impact energy [J]
E	Young's Modulus of Elasticity [N·m <sup>-2</sup> ]
$E_1, E_2$	The Young's Modulus of the two contacted bodies in Hertz theory [N·m <sup>-2</sup> ]
$E_r$	Rebound energy [N·m <sup>-2</sup> ]
$E^*$	Reduced Modulus of Elasticity [N·m <sup>-2</sup> ]
$\Delta E$	The energy loss [J]
F	Applied load [N]
$F_n$	Normal component of impact force [N]
$F_r$	Friction force [N]
$F_t$	Tangential component of impact force [N]
G	Shear modulus or modulus of rigidity [N·m <sup>-2</sup> ]
h	Scar depth [m]
$h_l$	Impact scar depth [m]
$h_m$	Measurable wear depth [m]

$h_u$	Plastic flow height [m]
$h_z$	Zero wear depth [m]
$H_s$	Hardness of the softer material [ $\text{kg}\cdot\text{mm}^{-2}$ ]
$K$	Dimensional impact wear coefficient
$k$	Dimensionless sliding wear coefficient
$k_s$	The stiffness of non-conforming spherical contact
$K.E._s$	kinetic energy of the striker [J]
$L_c$	Distance between the arm pivot and the center of the cam base [m]
$L_s$	Distance between the arm pivot and the point where the striker act on the specimen [m]
$m_{ZLS}$	The sliding impact wear exponents in Zalzalal-Lewis-Slatter Model
$M_{\text{eff}}$	The effective mass [kg]
$M_1$	The mass of the silver steel arm [kg]
$M_2$	The mass of striker holder [kg]
$N$	Number of impact cycles
$N_0$	The number of cycles at which the zero limit is reached
$n_{\text{Fricke}}$	The impact wear exponent of Fricke Model
$n_{\text{Lewis}}$	The impact wear exponent of Lewis Model
$n_{\text{Wellinger}}$	The impact wear exponent of Wellinger Model
$n_{ZLS}$	The normal impact wear exponents in Zalzalal-Lewis-Slatter Model
$O$	Parameters used in DOE
$P$	Pearlite
$P(r)$	The surface pressure distribution
$P_m$	The average contact pressure measured by Hertzian theory [MPa]
$P_o$	Maximum contact pressure measured by Hertzian theory [MPa]

$\bar{P}$	Average load [N]
q	The exponent of contact area ratio in Lewis model
r	Impact wear scar radius [m]
R	The striker ball radius [m]
$R^*$	Relative radius of curvature [m]
$R_a$	Arithmetical mean deviation of the assessed profile
$R_q$	Root mean square
$\bar{t}$	Sliding or slipping time during compound impact [sec]
$t^*$	Impact or contact time [sec]
$\nu_1, \nu_2$	The Poisson's ratio of the two contacted bodies in Hertz theory
V	Impact velocity [m/s]
$v_c$	Cam velocity [m/s]
$v_s$	Striker velocity [m/s]
$V_i$	Impact velocity [m/s]
$V_{pf}$	Plastic flow volume [m <sup>3</sup> ]
$V_r$	Rebound velocity [m/s]
$V_t$	Total volume loss [m <sup>3</sup> ]
$V_w$	Wear volume [m <sup>3</sup> ]
$V_{zw}$	Zero wear volume [m <sup>3</sup> ]
W	Wear volume [m <sup>3</sup> ]
x	Sliding distance [m]

## Greek and Latin Letters

$\zeta$	Energy expended during sliding [J]
$\mu$	Friction coefficient
$\theta$	Impact angle
$\alpha, \beta, \gamma$	Constant impact wear parameters from Akhondizadeh Model
$\gamma$	material wear factor=1.1 for carbon steel and tool steel
$\partial$	The ratio of the surface damage $D_2$ to the subsurface damage $D_1$
$\alpha$	Ferrite
$\sigma_y$	Yield strength [MPa]
$\sigma_u$	Tensile strength [MPa]
$\sigma_r, \sigma_\theta, \sigma_z$	The stresses on surface and subsurface in polar coordinate [MPa]
$\sigma_1, \sigma_2, \sigma_3$	The principal stresses [MPa]
$\sigma_v$	Von Mises Stress [MPa]
$\tau_{max}$	The maximum subsurface shear stress [MPa]
$\tau_1$	Maximum Hertz shear stress = $0.31P_o$ [MPa]
$\tau_2$	Shear stress arising in relative tangential motion during impact = $\mu P_o$ [MPa]



# Chapter 1

## 1.1 Introduction

This chapter first provides a general view of the impact wear problem in industry and the most common types of metal alloys used in engineering applications that are thus relevant to the work presented in this thesis. The aim and objectives of this research are then identified, and finally, the thesis structure is presented as well as a brief explanation of each chapter.

Wear and failure prediction of components are of significant interest and challenge the design of materials and their application. Without sufficient knowledge of how materials fail, it is difficult to improve their performance; therefore, it is important to know how to prevent or slow down the wear rate. Wear can be defined as a process of interaction between surfaces which causes deformation and material loss to the contacted bodies. This process can be due to mechanical action (e.g. erosion, abrasion, adhesion, or impact) or chemical action (e.g. corrosion).

Impact wear, sometimes known as hammer(ing) wear, has been defined as the wear of a solid surface that is due to repetitive exposure to dynamic contact by another solid body(ies) that eventually could lead to mechanical degradation of an entire system [1].

The impact wear of solid bodies is categorised as either damage due to multiple impacts from a large number of smaller solid bodies impacting randomly on a much larger body (known as erosive wear); or repetitive impacts from a single solid body on another with contact in a well-defined location are more similar (known as percussive impact wear) [2].

Impact wear modes can be categorised into normal and compound impacts as illustrated in Figure 1.1. Both (b) and (c) involves compound impacts between the specimen and the striker (small arrow) resulting from relative motion or non- normal impact angle.

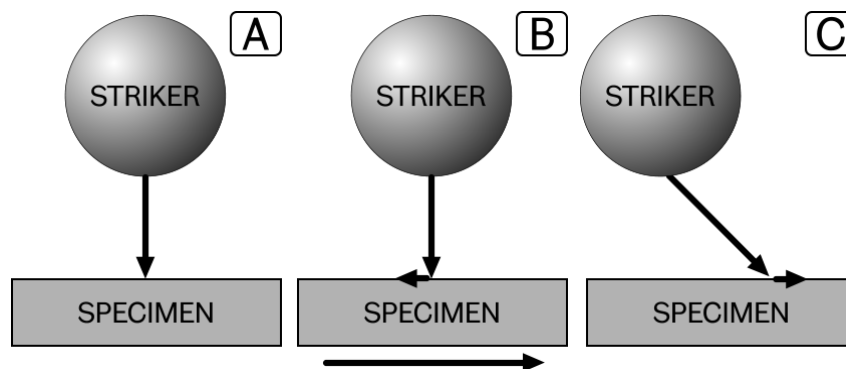


Figure 1.1 Different impact wear modes where specimen under (a) normal impact, and compound impact resulting in interfacial sliding due to; striker-specimen relative motion (b), (c) non-normal impingement angle.

Impact wear is one of the highest importance types in mining processing which demand wear resistant machines and components, because the forces and masses of interacting bodies are significant. Impact wear has been a problem since tools were first used in the late Neolithic period for manufacturing of stone axes [3]. Failures of tools used for drilling and machines used for mining coal and other media lead to unnecessary costs associated with regular replacement or refurbishment [4, 5].

Failures due to impact wear can be costly; for example, excessive wear of impacting poppet-type inlet and exhaust valves in internal combustion engines can lead to loss of cylinder pressure, increased emissions, reduced fuel economy, and ultimately engine failure [6-10]. In wind turbine gearboxes the

variable load from the wind causes components to hammer against each other [11] and drastically reduces the service life of these components. Severe wear of valves and valves seat inserts in automotive engines are frequently observed, impact wear is also being found in printer typefaces or in dental implants and heart valves where health is at stake. In industry, the rolling journal bearings suffering from impact wear is not rare.

The selected metal alloys (ferrous and nonferrous) used in this work represent a variety of materials that are widely used in engineering applications and that could fail due to repetitive impact wear during the life of a machine or a component. It is therefore important to broaden the knowledge about them and their resistance to wear caused by impacts.

Austenitic stainless steels alloys types (AISI 304 and AISI 316) are the most commonly used of this class of steel. They are easy to weld and have good mechanical properties with high work hardening ability due to the high ductility and excellent wear resistance provided by their high chromium and nickel contents. Both types of austenitic stainless steel are used at various temperatures in industrial and engineering applications such as; oil and gas, chemical storage, marine, piping, heat exchangers, food processors, nuclear reactors vessels, furnace parts, boilers used in fossil fuel electric power plants, and medical devices.

Medium carbon steel (e.g. EN8) is a readily machinable material that is widely used in industry for applications such as automotive parts, bolts, railway, gears and shafts due to its superior properties to mild steel and its reasonable cost.

Ductile cast iron (e.g. EN-GJS-600-3) consists of spherical graphite in a matrix of 70 % pearlite and 30 % ferrite and offers good machinability and excellent surface finish combined with high wear resistance, strength and fatigue. This material is used in many applications, such as forging dies, vehicle manufacturing, rotors, machine tool construction, shafts, gear cogs, crane pulleys, brake casing, bearings, running wheels, high pressure valves for gas and water, pumps and lift pulleys.

Aluminum cast alloy (e.g. AlSi9Cu3) has excellent cast ability, machinability and corrosion resistance, good strength and chemical resistance. While its copper content gives the alloy good high temperature strength and the combination of both Si and Cu ensures high mechanical strength. Typical applications for this alloy include complex machine and automotive engine parts such as cylinder heads, manufacturing of crankshafts and transmission housing, engine blocks and gear manufacturing.

A common grade of wrought phosphor bronze is PB102 and consists mainly of copper. Due to its high tin content (4.5-5.5) %, it offers high corrosion resistance that is close to that of aluminum alloys and high fatigue resistance. It also has high wear resistance, is easily joined by brazing and welding and has excellent cold forming properties. PB102 is utilised mostly in industrial applications including marine and chemical applications, automotive parts, electrical connectors, gears, bushes, pumps and valve trim, bearings, shafts, flanges, springs and washers.

They are a few impact wear models which have made a valuable contribution in the field of impact wear and these rely on generation of experimental data to produce accurate predictions of wear volume loss. However, these models depend on impact velocity or energy rather than the impact force, in addition to the wear damage mechanism type, could highly affect the amount of wear volume.

## 1.2 Aim and Objectives of this Research

The overall aim of this study was to improve the understanding at the fundamental level of failure due to wear of industrially relevant engineering materials under repetitive impact. The work encompasses practical experiments and supporting analysis to further characterise impact wear resistance of metallic alloys, based on the study of two types of austenitic stainless steel AISI types (304 and 316); a medium carbon steel (EN8); a ductile cast iron (EN-GJS-600-3); an aluminium alloy (AlSi9Cu3); and a phosphor bronze (PB102).

To achieve this aim, the following main objectives were identified:

1. Modify the existing Sheffield reciprocating hammer type impact wear rig to be able to:
  - Directly measure the impact force during repetitive normal impact by using a specific designed load cell (strain gauge type).
  - Heat test specimens for elevated temperature testing.
2. Perform experimental tests on selected metal alloys: austenitic stainless steel AISI 304; a medium carbon steel EN8; a ductile cast iron; an aluminium alloy; and a phosphor bronze, under normal impacts to define and measure zero wear volume.
3. Investigate the role of impact angle in the wear volume and damage mechanisms of three different metal alloys (AISI types (304 and 316) and EN8) and illustrate how the impact angle could affect the impact wear resistance of these materials.
4. Measure the expected increase in hardness due to the role of work hardening of ductile materials after N cycles using microhardness measurements for both normal and compound impacts.
5. Develop a new model to accurately predict the results of impact on a component under specific conditions, taking into account the role of different impact angles during impact.

## 1.3 The Key Novelty of this Work is in Regard to the Following Knowledge Gaps:

The key novelty and contributions from this study are shown below:

- Defining the role of zero wear volume in percussive impact which has been neglected in the previous papers and measuring this using a specific Equation for this purpose.
- Gaining better understanding of the wear damage to metallic materials exposed to different impact angles using an impact hammering wear rig (spring loaded type) throughout the surface and subsurface investigation.
- Using microhardness method to measure the expected increase in hardness for the centre of wear scar with different number of cycles and angles, such a trend has not been reported in any of the papers in the literature review.
- Developing a new predictive model that takes into account the role of shear force (tangential force) which has not been considered in any of the existing models.

## 1.4 Thesis Structure

The overall structure of this thesis is shown in Figure 1.2 below:

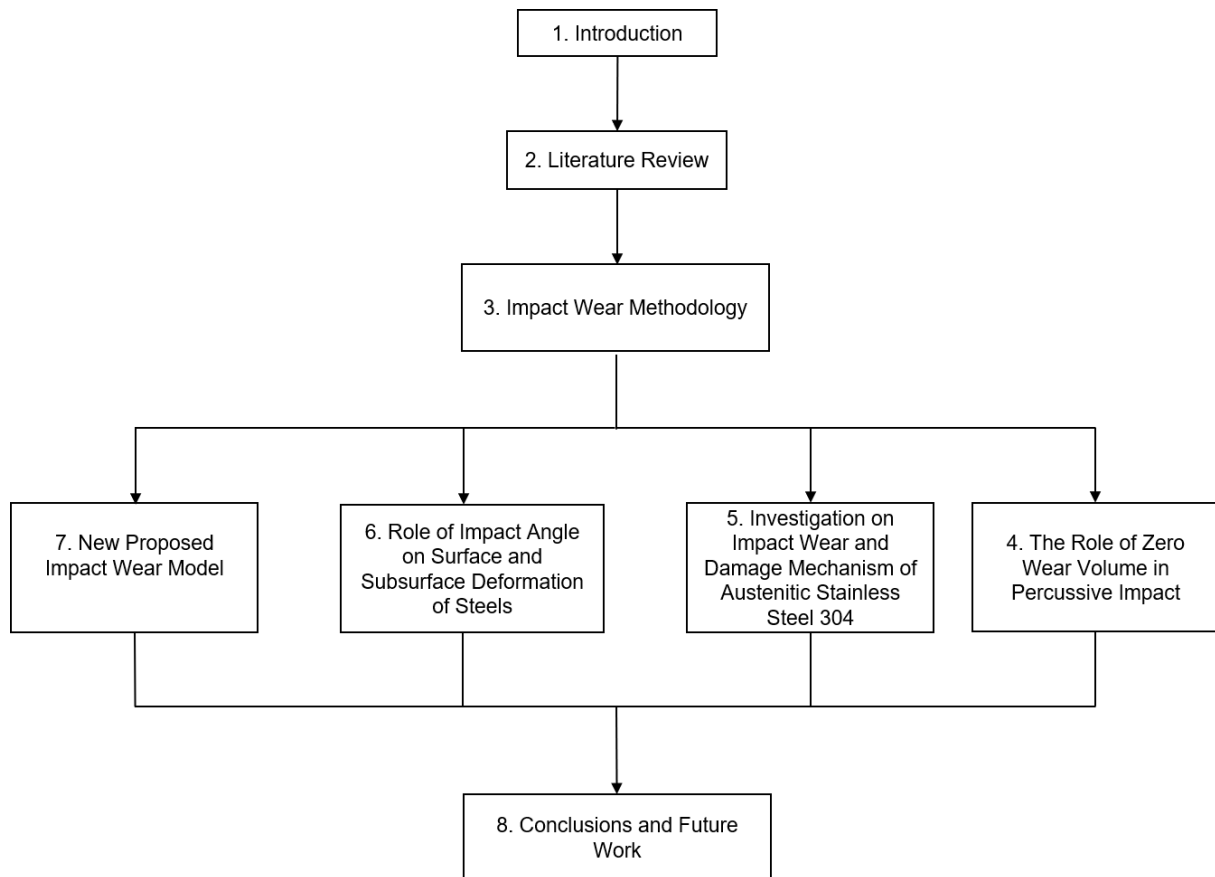


Figure 1.2 Flow chart of thesis work

This thesis is divided into eight chapters as shown below:

### Chapter One: Introduction

Presents an introduction to impact wear and sets out the aim and objectives of this work.

### Chapter Two: Literature Review

Presents a comprehensive review and discussion of previous works accomplished in the field of impact wear in order to investigate different aspects of impact wear and gain better understanding of the materials, conditions and parameters that have an effect on impact wear. In addition, the chapter evaluates the available impact wear models.

### Chapter Three: Impact Wear Methodology and Metallurgical Procedure

This chapter outlines the modification of an existing impact wear test rig hammering type used to damage different materials that are widely used in engineering and industry applications. Theoretical and experimental calculations for impact wear parameters are presented, with details of materials considerations and tested specimens, and both surface and subsurface Hertzian stress calculations for all tested materials. The zero wear methodology, sample preparation, surface and subsurface examination techniques used in the work, and Design of Experiment process are also presented here.

**Chapter Four: Defining the Role of Zero Wear Volume in Percussive Impact**

This chapter presents the results of zero wear volume on five different metallic materials widely used in engineering applications under repetitive normal impacts by using the impact wear rig, and presents the importance of zero wear.

**Chapter Five & Six: Investigation on Impact Wear and Damage Mechanism of Austenitic Stainless Steel Alloys Types (AISI304 and AISI316) and Medium Carbon Steel EN8**

This chapter presents the results of different impact conditions (number of cycles and impact angle) on the wear volume of AISI types (304 and 16) and EN8. Using the impact wear rig, the surface and subsurface damage were studied in detail during this work by applying different measurement techniques such as optical microscope (OM), scanning electron microscopy (SEM), micro hardness and 3D non-contact profilometer. Crack initiation and propagation, and their orientation, were also investigated.

**Chapter Seven: New Proposed Impact Wear Model**

This chapter presents a new model that takes into account the effect of the impact angle on wear volume of materials. The model is compared and validated with other published and peer reviewed work.

**Chapter Eight: Conclusions and Future Work**

The chapter presents the main conclusions extracted from the analysis and discussion, highlights the main key novelty, and suggests possible future work.

**References:** Citation of all papers used in this work

**Appendices:** The appendices present supporting information from the current study (map grading criteria and MATLAB code).

## Chapter 2 Literature Review

### 2.1 Introduction

This chapter presents a review of the literature relating to work completed in this study. It begins by identifying the potential areas of research through examination of similar work done within this area and analysis of the knowledge gaps that demand further investigation. In addition, to gain better understanding of the damage mechanisms behind impact wear and contribute to the field by establishing a new predictive model for a variety of materials and, where possible, to compare it with the previous findings.

### 2.2 General Impact Wear Mechanism

The mechanism of impact wear has been the important aspect in the study of tribology, from different categories of wear, impact wear is probably the least understood, yet it can cause significant damage to materials. Wear and damage of different ferrous and nonferrous materials under repetitive normal and compound impact could lead to degradation of the overall mechanical system durability. The wear damage is divided into two forms, plastic deformation and wear degradation. Impact wear can be associated with erosion when the size of impact object ranged to micron level (particles).

#### 2.2.1 Material Removal Mechanism

Different wear mechanisms are likely to exist during impact and, when examining impact wear scars, it is typical to find evidence of different mechanisms which could be the result of variation in contact conditions.

The body of literature suggests that during repeated impact, several mechanisms of materials removal from the surface could be involved [2]:

1. Oxidative (mild wear): tends to occur at low level of stress in both normal and compound impact contacts; oxide film will reduce the contact between bodies. EDX analysis for the contacted region is usually carried out to investigate the oxidation resistance of different materials [12].
2. Adhesive wear: occurs in both compound and normal impact contacts and is represented by material smearing and transfer from one body (one body wear) or from both contacted bodies (two body wear) and that results in formation of welded junctions at the asperity tips. The asperity tips are highly deformed regions, so cracks start to nucleate easily at these regions and then particles break away and the adhesive transfer is complete.
3. Abrasion: mainly found in compound impact, happens with one body or two body wear, and can be recognized by the formation of plough grooves.
4. Surface fatigue: is a more severe type of wear than the previous form and can be represented either by cracks parallel to the surface and delamination occurrence or cracks normal to the surface and spalling of surface materials.
5. Plastic deformation: when no material is removed from the surface (no mass loss) and either displacement of material occurs from the contact zone and ridges around the circumference of impact wear are formed, or the material remains in the contact zone and is compressed causing its surface to be at a different point, known as zero wear (as discussed in Chapter 4).

The impact wear mechanisms are summarised in Figure 2.1.

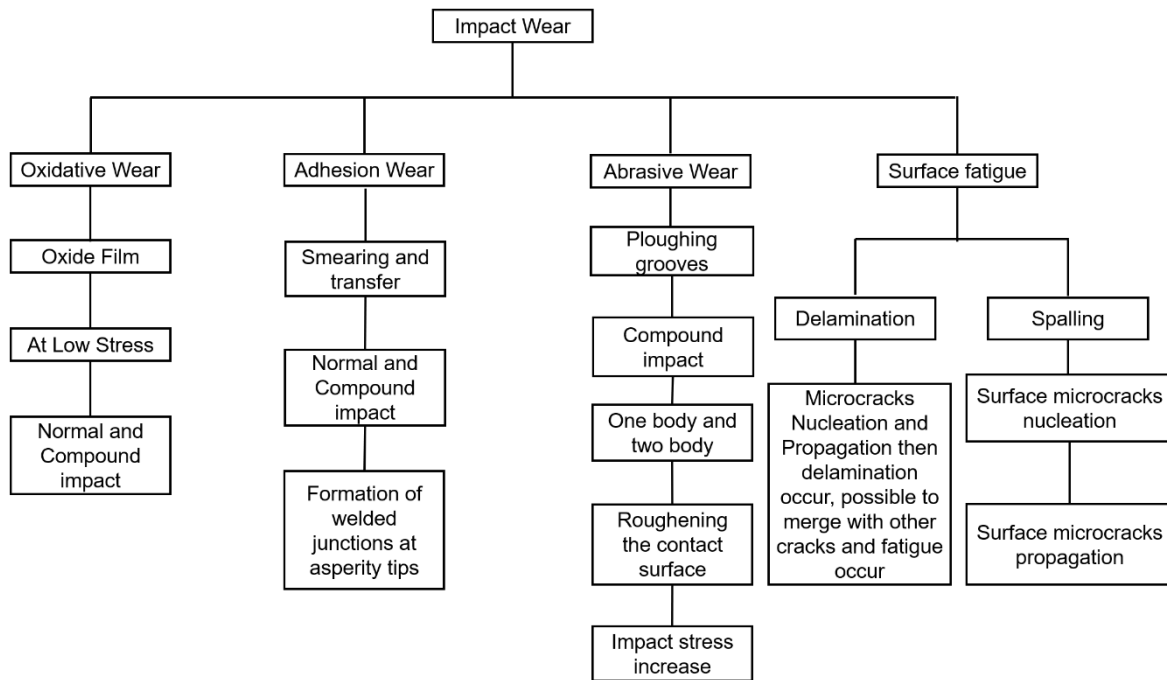


Figure 2.1 Impact Wear Mechanisms

## 2.2.2 Impact Wear of Metals

### 2.2.2.1 Impact Wear of Steel

A hammering impact wear rig was designed by Mahoney to study the effect of normal impact on high carbon steel (EN42) with surface roughness of  $1\ \mu\text{m}$  and using a ball bearing hammer with diameter 5 mm and made of high carbon alloy steel (EN31) [13].

The results showed that the mass loss of steel increases with increasing the number of impact cycles. SEM showed that extensive deformation in the impact wear scar is due to the highly deformed surface layer beginning to crack and eventually became detached from the surface as a delaminated layer and wear debris is plate shape and extensively fragmented as shown in Figure 2.2.

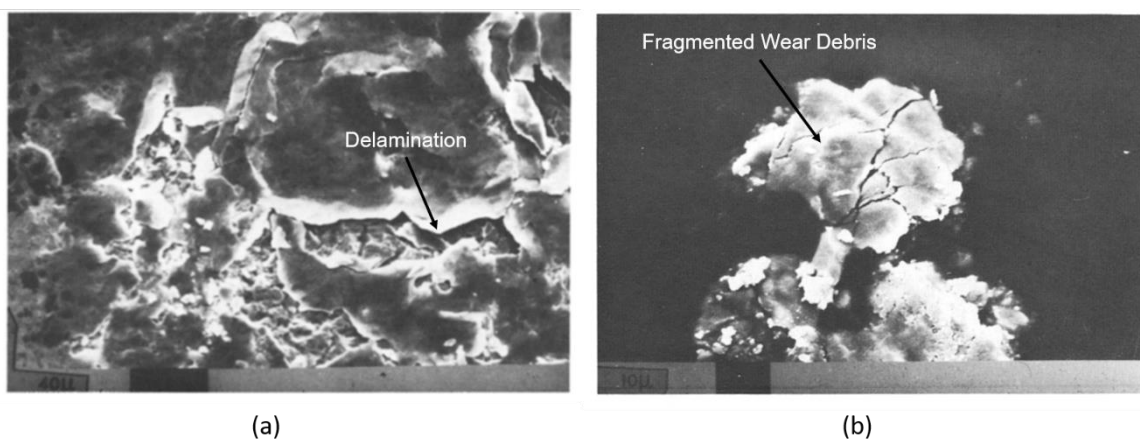


Figure 2.2 Surface morphology of high carbon steel where, (a) show the delamination after 100,000 cycles and (b) represent the wear debris (plate shape) after 250,000 cycles extracted from [13]

A hammering impact wear test rig was used to investigate the impact wear resistance of flat specimens of hardened carbon steel in normal and compound impact close to normal conditions (80°, 70°) [14], hardened carbon steel is used widely in agricultural equipment that undergoes repetitive impact wear.

Results revealed radial and circumferential cracks were produced outside and inside the contact area and flakes of material were removed from the surface near the center of depression at both normal and compound impact as delaminated layers.

Permanent deformation occurs from the first impact cycle, microhardness measurements for the centre region of the wear scar revealed an increase in hardness by 22.7 % compare with the bulk hardness of material measured from outside the contact region. These circumferential cracks outside the contact region in hardened steel were not found in the non-hardened steel (EN42) [14].

Rail weld joints are an important part of connecting rails and are widely used for ensuring the safety and stability of railway transport, the microstructure and mechanical properties of a rail weld joint are significantly different from those of rail material. This causes different wear damage for the rail weld joint and rail material [15].

By increasing the wheel speed, the impact force significantly increases between wheel and the rail weld joint and with the existence of these bulges or sags, it leads to serious damage of wheel and rail

An impact wear hammering rig was used to study the damage to both rail and weld joint materials under normal impact and dry conditions, the hardness of weld joint was 340 HV<sub>0.5</sub> higher than rail materials 313 HV<sub>0.5</sub>. The wear scar diameter and depth was measured using 3D non-contact profilometer while the wear volume was estimated by assuming that the scar has a spherical cap shape [15].

The results revealed that rail material has more wear volume loss than the weld joint which could be explained as deformation resistance to impact wear under same conditions, also a significant amount of pile up materials (plastic flow) on the edges of impact wear scar were found for both materials.

The wear volume of both the rail weld joint and rail material increases with increasing the number of impact cycles or impact force similar to the previous types of steel (EN42) and hardened steel, whereas the resistance to impact wear of the rail weld joint is better than that of the rail material. No evidence of circumferential cracks outside the contact region were found for both materials [15].

SEM examination under low impact force and number of cycles for both materials revealed adhesive wear and tiny delamination were the main wear damage and cracks initiated from surface and then propagated parallel to the surface for both materials as shown in Figure 2.3. By increasing the impact force and number of cycles both materials showed a transition to cracks formation, delamination and spalling and eventually fatigue wear as shown in Figure 2.4 [15].

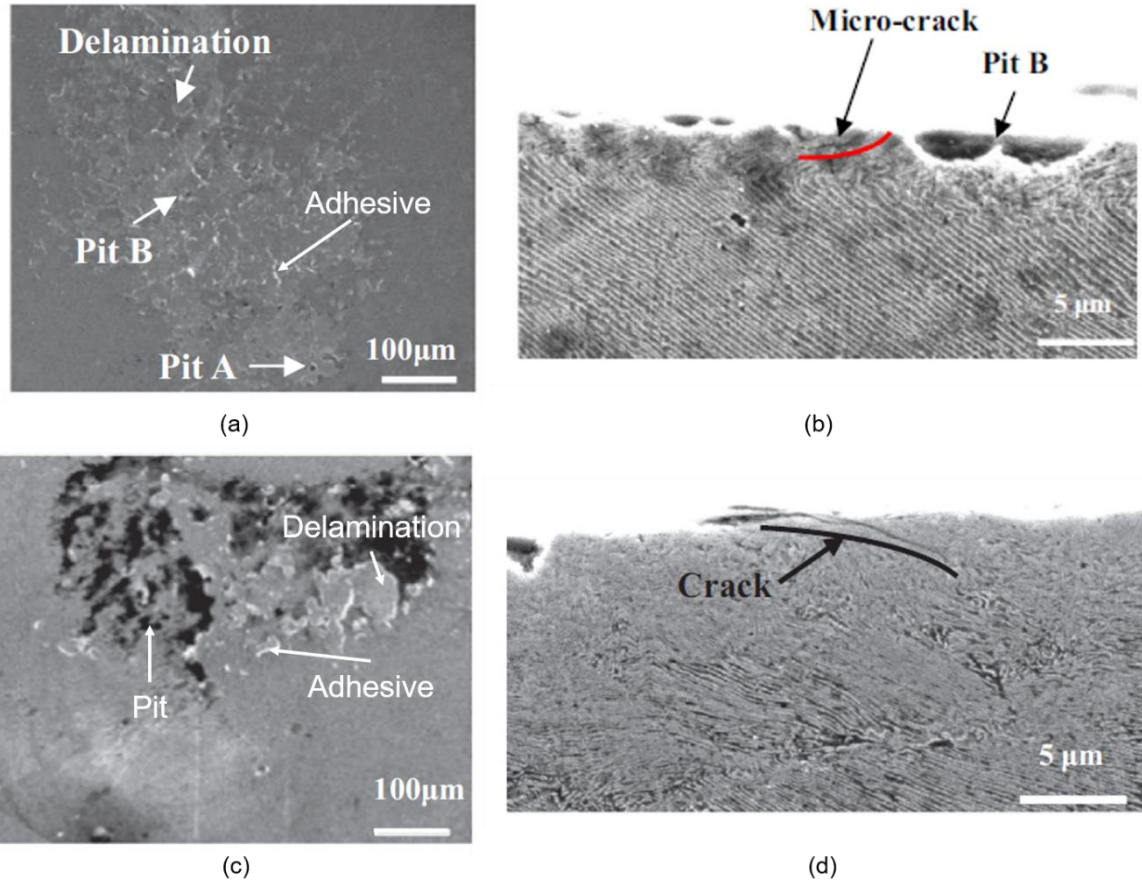


Figure 2.3 SEM image for surface and subsurface deformation of both rail material (a, b) and weld joint material (c, d) showing the delamination on surface (a, c) and crack propagate parallel to surface (b, d) after 10,000 cycles with normal impact force of 200 N extracted from [15]

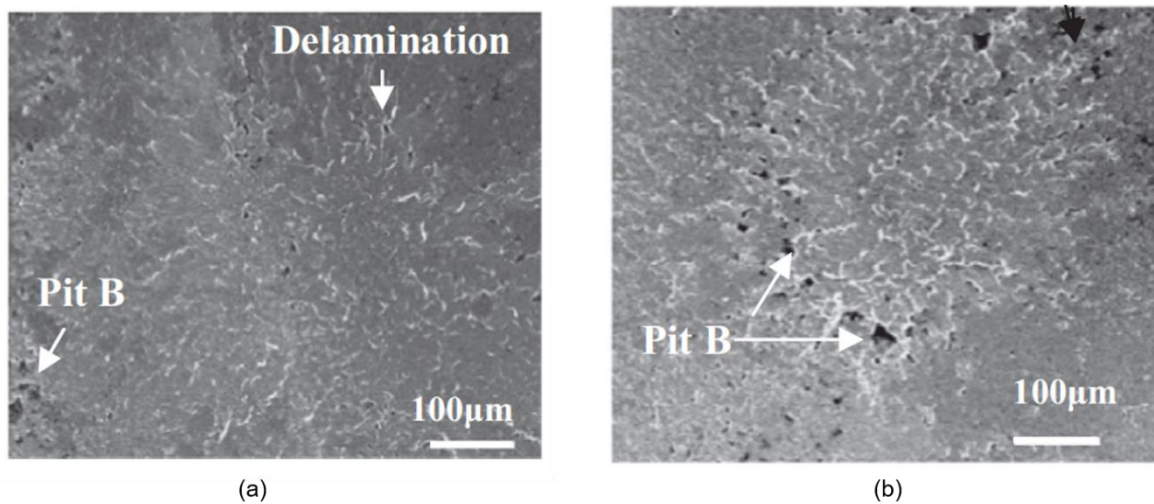


Figure 2.4 SEM image for surface damage of rail material (a) and rail weld joint (b) after 50,000 cycles and impact force of 400 N extracted from [15]

Impact often leads to surface fatigue which is localized fracturing of materials from a solid surface caused by action of repetitive compressive stressing of a surface. The compressive stresses are Hertzian in nature; in addition, the shear stress condition is different in impact from rolling and sliding as shown in Figure 2.5 [16].

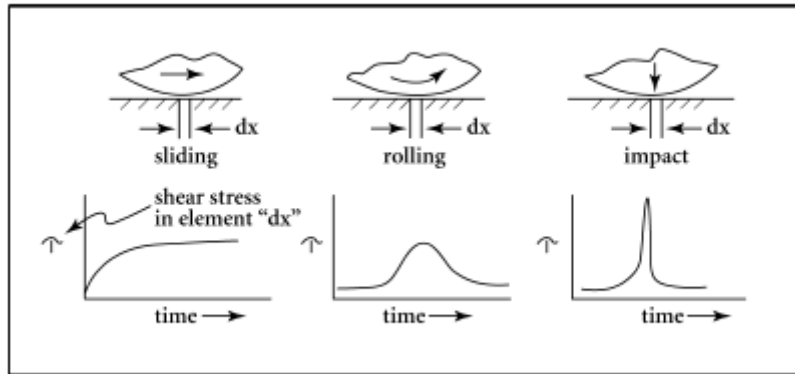


Figure 2.5 Shear stress in rolling, sliding and impact contacts extracted from [16]

Repetitive impact wear of medium carbon steel with bulk hardness of approximately 500 HV using impact wear test rig (ballistic type) under compound impact  $45^\circ$  revealed that the mass loss increases linearly with increasing the number of impact cycles similar to all previous types of steels and the fatigue failure is due to the formation of white layer [17].

Homogeneous white layer (WL) started to generate on the worn surface (WS) after only five impacts, initiation of microcracks inside the white layer occurred after further impacts, and eventually cracks started to propagate and cause failure [17].

Two mechanisms of failure modes have been identified within the white layer as shown in Figure 2.6.

1. Delamination due to microcracks that initiate on the white layer and then propagate parallel to the worn surface
2. Spalling due to microcracks propagate along the deformation zone (DZ)

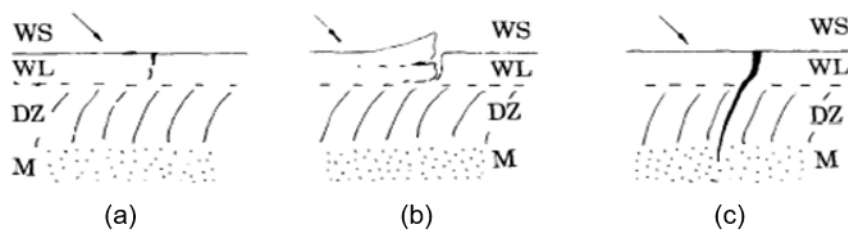


Figure 2.6 Failure modes induced by white layer which (a) and (b) are the delamination mode and (c) is the spalling mode extracted from [17]

Subsurface examination revealed that both surface and subsurface cracks were generated with impact angle  $45^\circ$  and the wear debris has a flake shape with obvious sliding marks as shown in Figure 2.7.

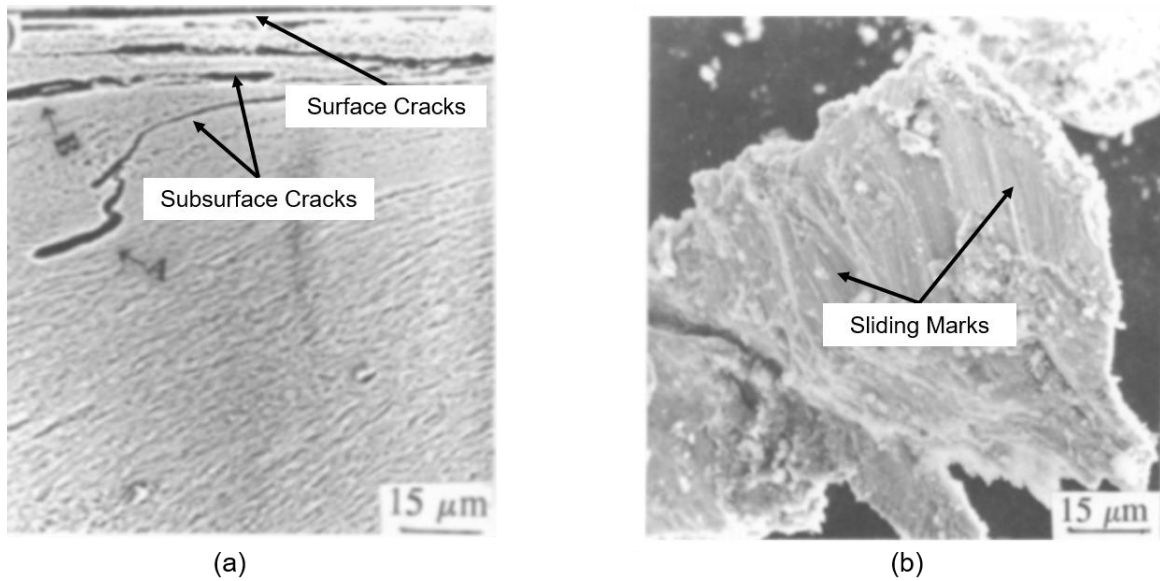


Figure 2.7 SEM image of medium carbon steel with impact angle  $45^\circ$  showing (a) surface and subsurface cracks and (b) the flake wear debris with obvious sliding mark extracted from [17]

The delamination results from the white layer deviate from the delamination theory presented by Suh. The traditional theory of delamination proposed by Suh suggested that the delamination occurs due to dislocation occurs at the surface and by increase the shear deformation on the surface, formation of microcracks and voids occurs at subsurface, by further repetitive impact these cracks will propagate parallel to the surface and delamination occurs [18].

While the results of Yang [17] indicate that the delamination is different wear mechanism from Suh, due to repetitive impact, a thin white layer is formed on the worn surface, then a thicker white layer is formed after further impacts. This layer is highly deformed one and an intensive work hardening layer with a significant increase in surface hardness up to 1000 HV, so the microcracks nucleate inside it easily and then propagate along the easiest path and delamination occurs.

The three factors that are responsible for the formation of white layer, either individually or in combination, are [19]:

1. Rapid heating and quenching
2. Mechanical deformation
3. Surface chemical reactions

Two main types of failure were found during compound impact of three auto-tempered martensitic steels and chromium carbide reinforced steel in both normal and compound impact using the high velocity particle impactor (HVPI) rig by Lindroos [20]:

1. Adiabatic shear band leading to formation of white layer
2. Subsurface shear fracture

Four grades of steel with a range of hardness (300-450) HV tested under different impact energies (0.98-19.6) J have been investigated under normal impact, the results of Rastegar [21] using 3D non-contact profilometer revealed the following:

For single impact: heavily plastic deformation for all four grades of steel and formation of thin layer of adiabatic shear band (ASB) about (20  $\mu\text{m}$ ), but no microcracks have been formed during single impact. Also, both the edges (plastic flow) and scar (below surface) volumes increase with increasing the impact energy. For multiple impact: volume loss increases with increasing the impact energy and steel grade with higher hardness showed lower volume loss while the steel grade with lower hardness showed higher volume loss.

Microhardness profile for the four grades of steel revealed higher hardness in the impacted zone compare with the bulk hardness which indicate the role of work hardening during impact.

Formation of white layer and extensive microcracks as a result of micro voids growth inside the ASB in addition to heavy plastic deformation region were observed for multiple impact and particles removed from material as flake wear debris [21].

Both single and multiple impacts showed that the subsurface deformation increase with increasing impact energy, impact energy plays a role in wear loss of materials, and increase in the impact energy would lead to an increase in the wear loss of materials, which agrees with results obtained by Lindroos and Fricke [20, 22].

The impact wear behaviour of three tempered steel subjected to various heat treatment process in order to generate different mechanical and wear properties has been investigated by Zhang using impact hammering wear rig under compound impact [23].

The results of Zhang revealed that the mass loss of the three types of tempered steel increases with increasing impact cycles as expected and the steel with best combination of hardness and toughness has the least mass loss, hardness has a significant effect on the wear properties [23].

Microstructural examination for both surface and subsurface using SEM and OM revealed that with increase the number of impact cycles, the dominant wear damage mechanisms of all three tempered steels has changed from slight plastic deformation to micro-cutting and adhesive wear in addition to micro fatigue. Fatigue occurs due to both cracks that initiated from surface or subsurface and then propagate and converge to form mostly fatigue delamination as shown in Figure 2.8.

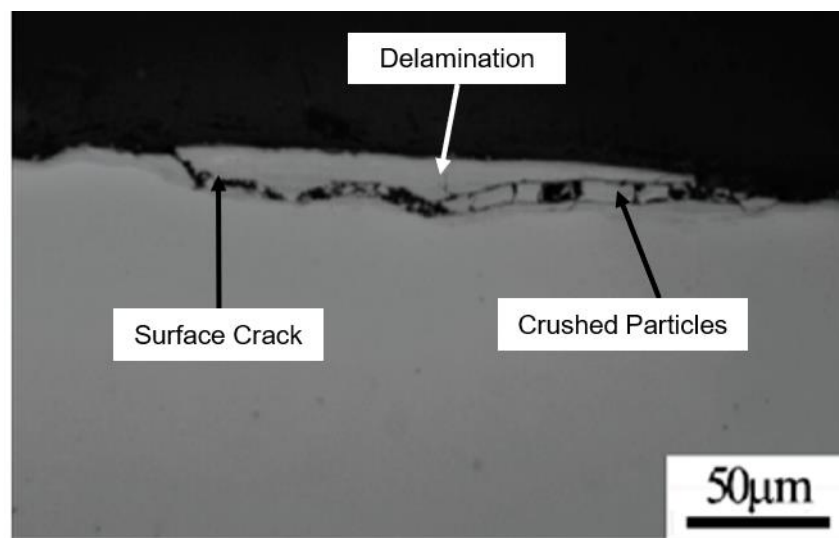


Figure 2.8 SEM image of steel showing delamination layer extracted from [23]

Figure 2.8 revealed that the delamination occurred due to cracks that initiated from surface and then propagated below the surface at a steep angle and then turned to the surface and delamination happened. Crushed particles were trapped between the delamination layer (same as the worn surface) and the deformed region [23].

Surface structure of two types of steels (austenitic stainless steel 566 HV<sub>0.1</sub> and austenitic Hadfield steel 741 HV<sub>0.1</sub>) have been investigated by Petrov using projectile test rig in normal impact conditions. The worn surface has been tested after 12,000 impact using TEM to get information about the internal structure that cannot be provided by SEM such as evidence of structure transformation from cold worked crystalline to nanocrystalline and finally to a fully amorphous surface layer [24].

The results of Petrov revealed formation of very thin amorphous layer (a few nanometres) above the work hardening layer in both steels. Also, it has been found that the major reason of the mass loss is likely to be fatigue under repeated impacts for both steels, but the wear resistance of austenitic stainless steel is higher than austenitic Hadfield steel. This could be due to the fact that the stainless steel fracture strength is twice than Hadfield steel [24].

The amorphous layer meaning lacking of crystalline structure and also known as metallic glass or glassy metal and it is produced through quick cooling and the layer is from few nanometers to some micrometers thickness and some research has been found it is useful for abrasion and adhesion wear resistance [24]. It may also important to mention that both materials have a lot of manganese Mn in their chemical composition (12-17) % and that could be a reason for the formation of this layer.

The impact wear damage mechanisms that occur to different types of steel is mainly surface fatigue due to both delamination and spalling with the existence of abrasive wear and adhesive wear during compound impact. The subsurface damage of steel or any other ductile material can be categorized into three zones as illustrated in Figure 2.9.

1. Zone 1 is the unaffected zone or the base material
2. Zone 2 is the plastically deformed region and falls between the unaffected zone and the surface zone
3. Zone 3 is the surface zone or the hardened layer zone which is severely plastically deformed

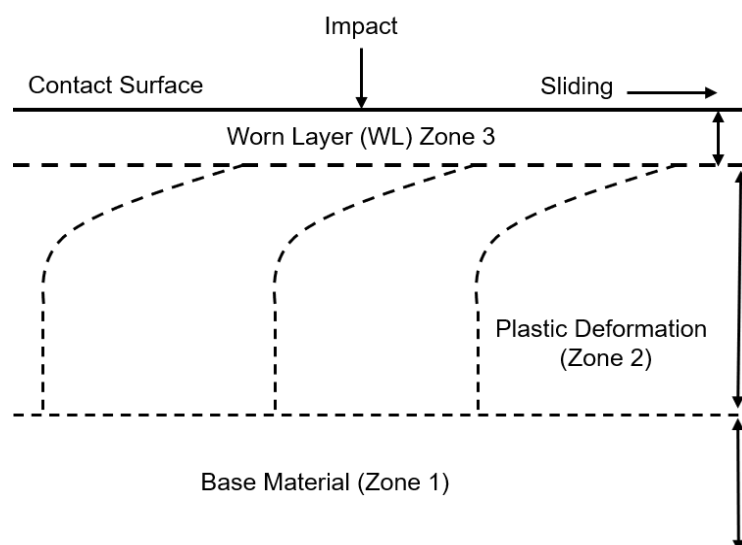


Figure 2.9 Schematic diagram of subsurface zones

The key trends to be considered in order to form a better understanding of the wear damage mechanism(s) due to impact can be outlined as follows:

1. It is obvious that the information on the impact wear of ferrous materials (mainly steel) focused on carbon steel and there is a lack of information and data about the impact wear damage for stainless steel and specifically the austenitic stainless steel such as AISI 304 and AISI 316. The current work investigated in details the surface and subsurface wear damage for those materials and identified the possible wear damage mechanisms that could occurs in both normal and compound impacts (see Chapter 5 and Chapter 6).
2. The available papers that identified the abrasive wear during compound impacts did not reveal if it occurs as two body abrasive wear or three body abrasive wear which could accelerate the wear volume loss. Therefore, the current work focused on providing better understanding to the abrasive damage for three different types of steel (AISI 304, AISI 316 and EN8) (see Chapter 5 and Chapter 6).
3. No papers are available that describe the nature of cracks during repetitive normal and compound impact (intergranular or transgranular) which has been investigated during this work for the three types of steels mentioned above (more details in Chapter 5 and Chapter 6).

#### **2.2.2.2 Impact Wear of Nonferrous Materials**

This section provides a review about the impact wear of nonferrous materials and it is not comprehensive (does not include other materials such as polymers or ceramic).

Aluminum, titanium and copper alloys are the only nonferrous materials available in the literature and investigated due to their wide use in engineering and industry applications. There is a little published information on the wear resistance of these materials.

The impact wear resistance of two aluminum alloys (2011-T3, 2124) was investigated by Rice [25] in both normal and compound impact using a reciprocating impact wear rig. The results with different number of cycles (10,000 to 250,000) in the elastic region revealed that the mass loss of aluminum alloys increases with increasing the number of impacts.

SEM examination of the surface showed that the wear mechanism seems to be plastic deformation, surface fatigue due to delamination and abrasive wear as represented by the formation of ploughing grooves. While SEM examination of the subsurface revealed voids and cracks were found inside zone 3 [25] (see Figure 2.10).

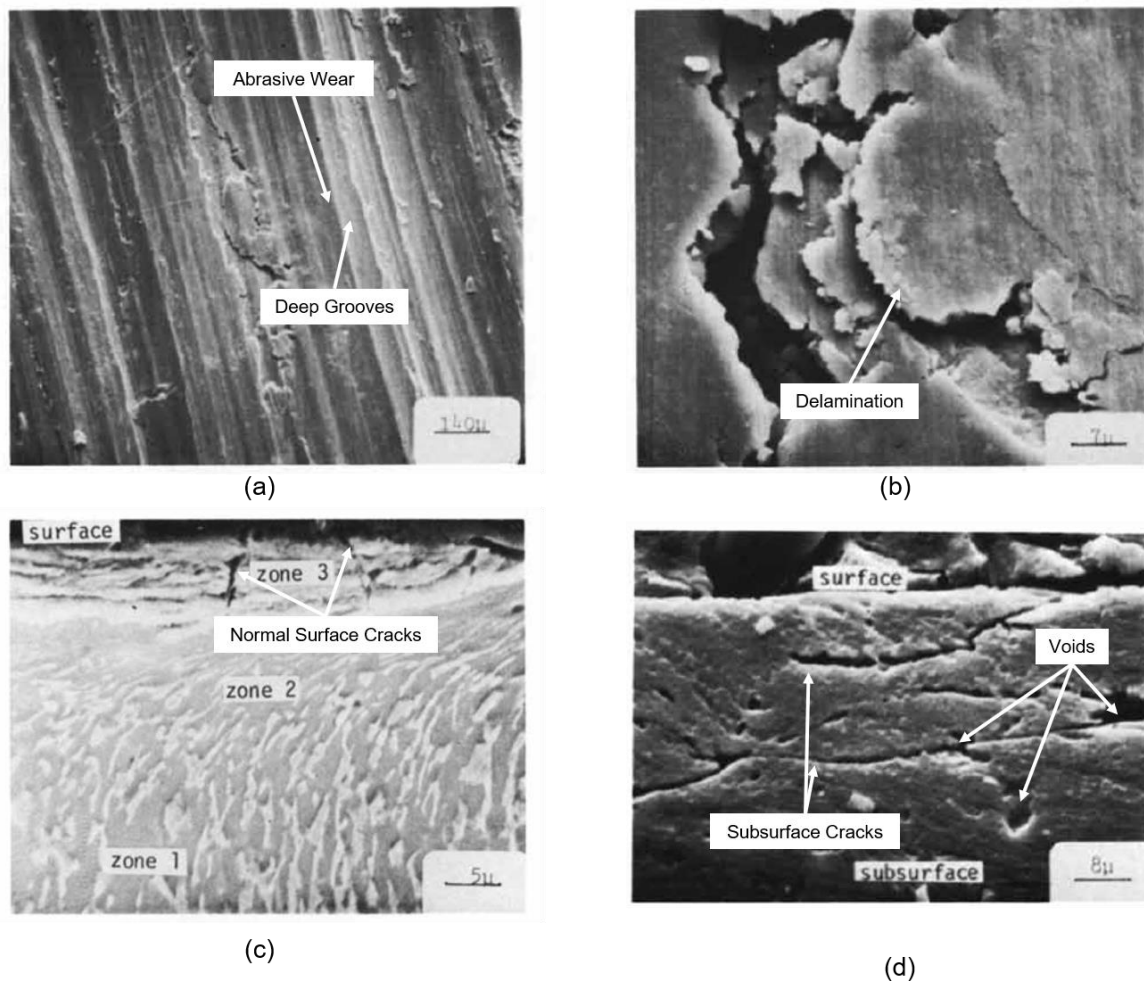


Figure 2.10 SEM morphology of aluminium specimen where (a) and (b) shows the surface damage while (c) and (d) revealed the subsurface damage extracted from [25]

Figure 2.10 shows that abrasive wear occurs during sliding impact with obvious grooves (a) and multiple layers of delamination (b), also subsurface examination revealed voids and cracks that initiated and propagated both normal and parallel to the surface. It can be seen that the subsurface region can be divided into three zones similar to that described in Figure 2.9 [25].

Titanium alloys have many good mechanical properties such as high strength capability and creep resistance and have consequently been used extensively in the field of gas turbine engines. The impact wear resistance of titanium alloys (IMI 685, RMI 5522S) was investigated by Rice [26] using the reciprocating impact wear rig in compound condition.

The results revealed that the mass loss of titanium alloys increases with increasing the number of impacts similar to aluminum alloys and steel alloys. The results of Rice [26] using SEM for surface revealed plastic deformation, surface fatigue due to delamination and finally abrasive wear as a result of ploughing grooves. While the subsurface examination by SEM showed no evidence of formation of cracks and voids in zone 3 as found in the aluminum Alloys [25]. The surface and subsurface damage is very similar to the aluminum specimen shown in Figure 2.10.

The impact wear resistance of copper alloy was investigated by Groeger [27] using the reciprocating impact wear rig in compound condition, and results indicated that the weight loss of copper alloy increases with increasing the number of impacts. SEM was performed for assessment of surface and subsurface damage.

For Surface: worn surface exhibits wear in the form of delamination and abrasive wear as a result of ploughing grooves as shown in Figure 2.11 and it did not show differences from that of aluminum and titanium alloys. For Subsurface: severe plastic deformation in zone 2 (plastic region) without voids or cracks formation.

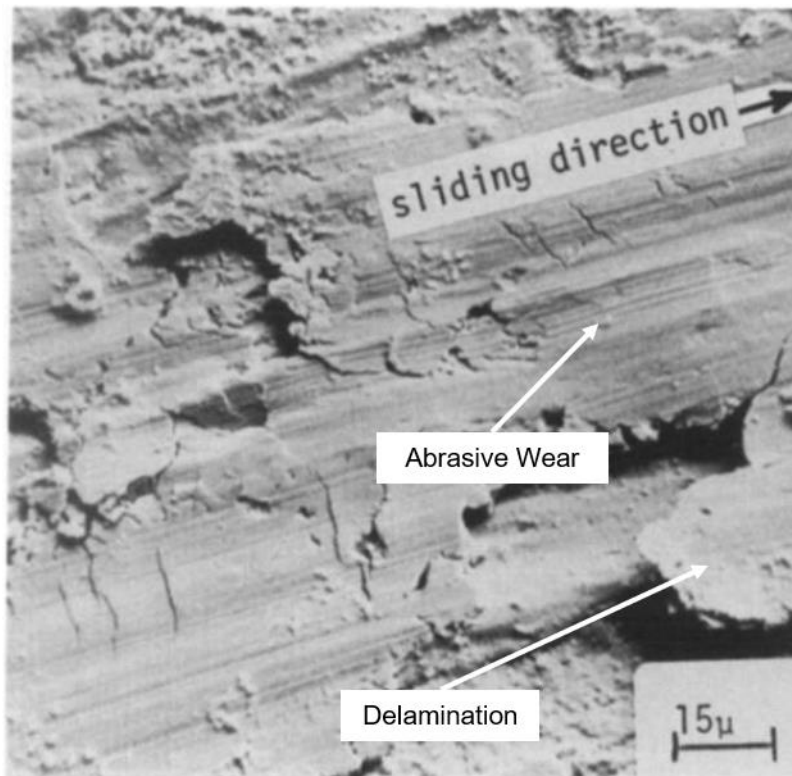


Figure 2.11 SEM image of copper alloy specimen showing the worn surface after 250,000 cycles extracted from [27]

The stress level represented by the impact force has a great effect on the amount of wear loss, with results indicating that increasing the stress level leads to increase in the wear losses of materials [25, 27].

The damage to surface and subsurface of nonferrous materials shows the same features described earlier for ferrous materials such as cracks initiation and propagation with the evidence of more clear cracks propagated normal to the surface from zone 3 to zone 2 (see Figure 2.10-c), but the abrasive wear is more obvious with nonferrous materials. Also, no wear debris was examined for any of nonferrous alloys.

## 2.3 Experimental Impact Wear Testing

### 2.3.1 Impact Wear Rigs

Two different types of test rigs have been designed and used widely in the field of impact wear for various materials.

### 2.3.1.1 Ballistic Impact Wear Rig

In ballistic impactor wear testers, repetitive impacts are achieved by firing projectiles at a counterface. To ensure the projectiles impact at the same point each time, guides are provided [2], some test rigs that use one projectile repeatedly impacting against a counterface are shown in Figure 2.12 and Figure 2.13 [17, 20].

Ballistic test rigs have two main disadvantages. The first is that, because of cleaning problems with the projectile guides, lubricated tests are difficult to carry out. The second is that it is sometimes difficult to retune the rigs to take different weight projectiles [2].

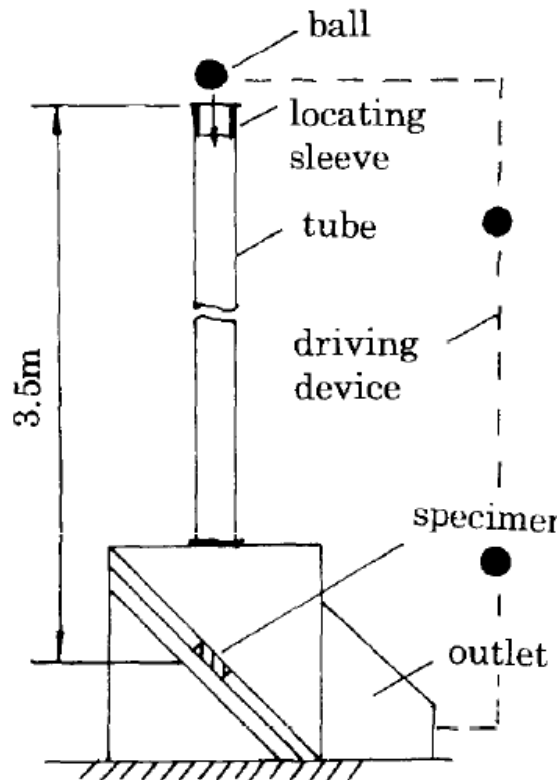


Figure 2.12 Ballistic impact wear rig extracted from [17]

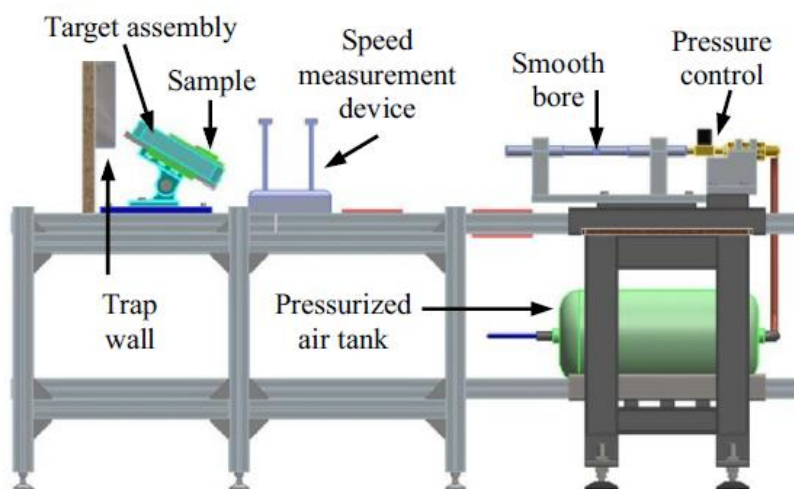


Figure 2.13 Ballistic impact wear rig extracted from [20]

### 2.3.1.2 Pivotal Impact Hammering Wear Rig

To date, the pivotal impact hammering wear rig designs have been widely used to identify material loss due to wear from repetitive impact, in both normal and compound impact.

In pivotal hammer impact wear test rigs, a hammer is made to impact a counterface. A stationary counterface is used for normal impact studies, while for compound studies, shear is imparted by altering the angle of the counterface before a test. Again, synchronization is required for rotating counterfaces to ensure impact occurs at the same point during each cycle.

A number of different designs of these pivotal hammer test rigs are used and various mechanisms are employed to move the hammer up and down including electromagnets and cams, typical examples are shown in Figure 2.14 and Figure 2.15 [28, 29]. Pivotal hammer test rigs overcome the contact lubrication and retuning problems encountered with ballistic rigs.

However, there are problems associated with the flexure arising in the hammers and the elastic vibrational modes of the hammers may complicate analysis.

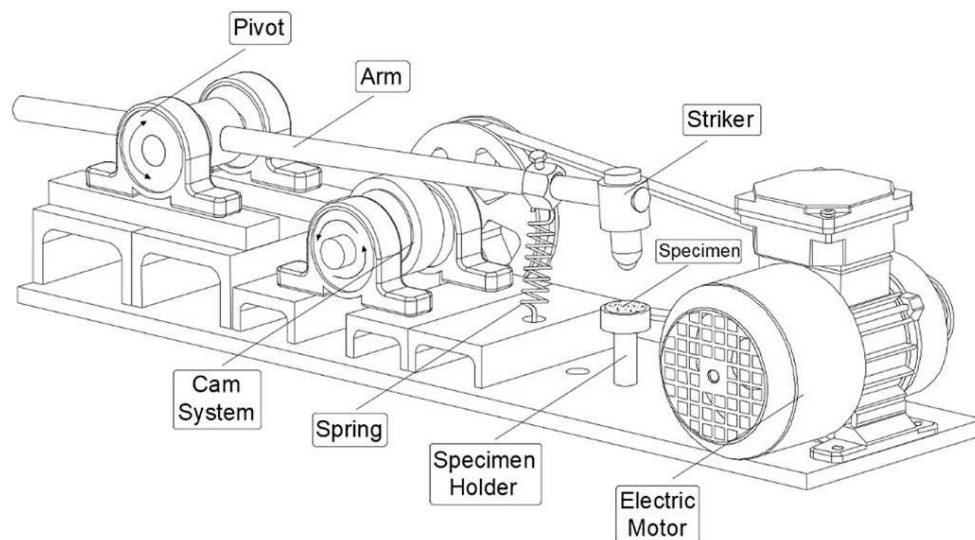


Figure 2.14 Hammering impact wear rig using cam and spring extracted from [28]

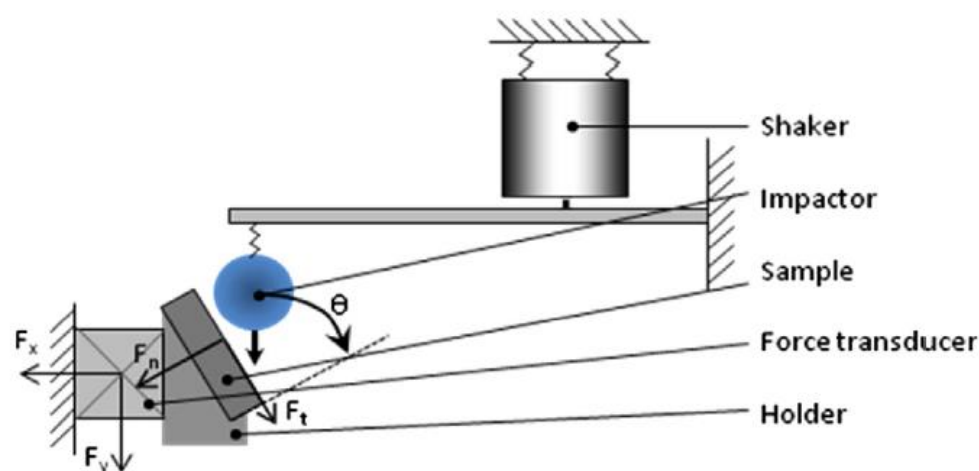


Figure 2.15 Hammering impact wear rig using electromagnetic fields extracted from [29]

Impact hammering wear rigs with abrasive particles are also used to investigate the impact abrasive wear of different materials. For steel this important in order to obtain a higher wear resistance for applications such as mining machines and grinding mills. Impact abrasive wear can be found in these applications and their combinations are the most important cost factors in the areas of mining and mineral processing as shown in Figure 2.16 [5].

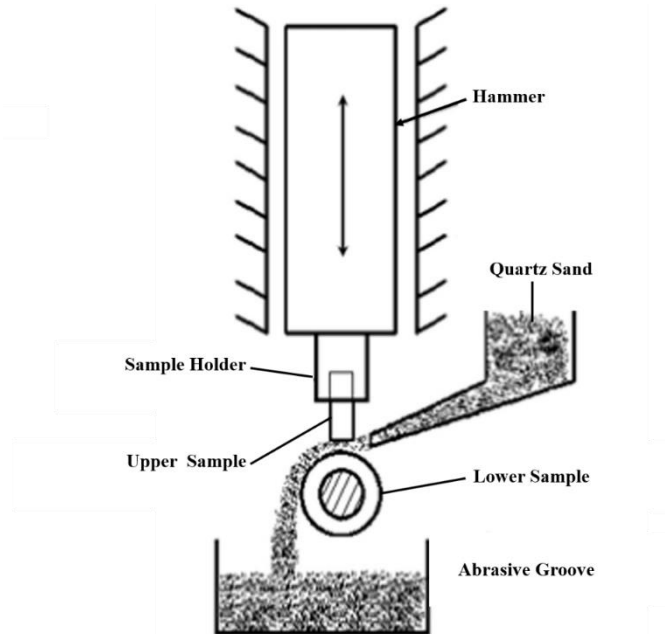


Figure 2.16 Schematic diagram of impact abrasive wear testing equipment extracted from [5]

## 2.3.2 Wear Measurements

The literature review revealed that two different methods were typically used to measure the wear volume loss of materials under repetitive impact; mass loss (by mass scale) and measurement (by profilometry) and calculation of volume loss. Based on the literature the mass scale is used more frequently than others, which used either spherical cap estimation or 3D non-contact profilometer to calculate the volume loss.

### 2.3.2.1 Mass Scale

The easiest and simplest way to determine the wear volume of materials under both normal and compound impact is by weighing the specimen before and after a number of impact cycles, using a scale with high accuracy, and calculating the mass loss.

Prior to testing, the striker and specimen are typically ultrasonically cleaned, dried and weighed to a precision of 0.1 mg. Mass loss can be found in the specimen only or in both the specimen and the striker.

Many studies reported in this literature review used mass losses to identify the wear losses of materials under repetitive impact [13, 14, 17, 22, 25-27, 30-36].

This method provides the most accurate measure of material removed, but does not indicate exactly where it is lost from. For this, profile measurements are needed.

### 2.3.2.2 Volume Loss

The volume of impact wear scar for point contact can be calculated by assuming that the scar has a spherical cap shape [7-9, 15, 29, 37] (based on 2D scar diameter and depth measurements) as shown in Figure 2.17 or could also be directly measured through 3D non-contact profilometer techniques [20, 21, 28, 38, 39].

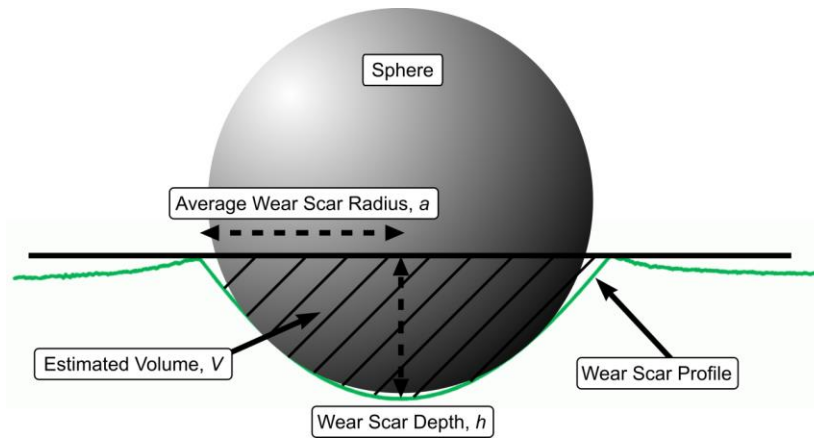


Figure 2.17 Diagram represent spherical cap method extracted from [40]

The first method of wear measurements can measure the mass loss of materials and this could be converted to wear volume throughout the density of material accurately. However, it cannot indicate the components of the wear scar geometry, which include depth and width or radius. Neither can it predict the plastic flow volume of the ridges often present on the outer circumference of the wear scar. Therefore, the second method seems to be more reliable in this situation (3D non-contact profilometer).

The latter can overcome those limitations but conversion of measurement data to the equivalent mass loss assumes uniform distribution of density. Extremes of surface geometry and reflectivity properties can also cause difficulties.

Error of mass scale may be raised from environmental factors such as unclean surface of scale due to dirt from other objects and any significant changes in laboratory temperature can lead to inaccurate results. Therefore, a 3D non-contact profilometer overcome these difficulties, but it needs to scan the surface in a proper way to create a reference plane and goes out of focus above and below the reference plane in a way that ensure both lower and upper volume are included in the scan.

## 2.4 Impact Wear Modelling and Simulation

### 2.4.1 Zero Wear Model

The only previous fundamental work of significance in this area is that of Engel which was conducted in the late 1970s. These studies initially defined, in terms of number of cycles, two stages that all materials undergo throughout repetitive impacts. The first stage is an induction period, where no material is lost, and the end of this stage is defined as the zero wear limit ( $N_0$ ), as shown in Figure 2.18. The second stage is the measurable wear region [41].

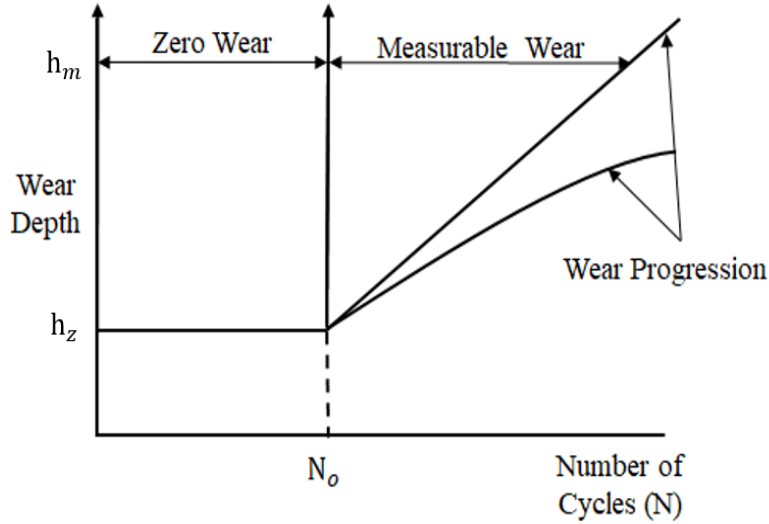


Figure 2.18 Zero and measurable impact wear extracted from [41]

Engel then developed a model for steel specimens subjected to repetitive compound impacts in the elastic contact stress range to calculate the number of cycles at the zero wear limit [1, 41-43].

The following equation was derived to evaluate the zero wear limit for steel specimens subjected to repetitive compound impacts in the elastic region. It considers wear damage resulting from the surface shear stress,  $\tau_2$ , and the maximum subsurface shear stress,  $\tau_1$ , during each impact.

$$N_0 = \frac{1}{1+\partial} \left( \frac{Y\sigma_y}{P_o} \right)^9 2000 \quad 2.1$$

where  $N_0$  is the number of cycles at which the zero limit is reached;  $\sigma_y$  is the tensile yield stress;  $P_o$  is the peak Hertzian contact pressure and  $Y$  is a material wear factor (approximately 1.1 for carbon and tool steel specimens) [1].

$\partial$  is the ratio of the surface damage  $D_2$  to the subsurface damage  $D_1$ , where:

$$D_1 = \int_0^{t^*} \tau_1^9(t) dt \quad 2.2$$

$$D_2 = \int_0^{\bar{t}} \tau_2^9(t) dt \quad 2.3$$

$$\partial = \frac{D_2}{D_1} \quad 2.4$$

Where:  $\tau_1$  is the maximum subsurface Hertz shear stress =  $0.31 P_o$ ,  $\tau_2$  is the shear stress arising in relative tangential motion during impact =  $\mu P_o$  while  $t^*$  is the contact time and  $\bar{t}$  is the slipping time.

This zero wear model can only be applied when the contact is elastic in nature, but cannot predict the maximum scar depth at the zero wear limit. Additionally, the model can only predict the number of zero wear cycles.

Therefore, the model has three main limitations, first it can only be used to predict the number of cycles at which the zero limit is reached when the contact is elastic in nature and therefore the maximum contact pressure should be below or equal to the yield stress of material. In reality materials in the plastic region will go through a further number of cycles before they start to wear.

## 2.4.2 Extant Impact Wear Models

A number of wear models that claim to be able to predict wear due to impact have been published in literature. They are all empirical and rely on generation of experimental data to produce accurate predictions. The models are introduced here with their relative merits then discussed at the end of Subsection 2.4.2.6.

### 2.4.2.1 Wellinger and Breckel

Wellinger and Breckel [44] studied impact wear in dry conditions of various metallic materials such as steel, aluminum, copper and titanium alloys using three types of impact test rigs (hammering rig, projectile rig and reciprocating rig) using a spherical hard steel striker head and loads producing plastic deformation from the first impact.

The results based on mass loss revealed the following empirical Equation:

$$W = KNV^{n_{Wellinger}} \quad 2.5$$

where:

$W$  represents the wear volume

$K$  is a constant impact wear coefficient, normally in the range  $(15-42) \times 10^{-6}$

$N$  is the number of impact cycles

$V$  the impact velocity (m/s)

$n_{Wellinger}$  is the velocity exponent and vary from 1.5-2.2 according to the tested materials

### 2.4.2.2 Rabinowicz

Rabinowicz [45] suggested that the wear during impact of ductile materials under normal impact in dry conditions for all tested materials except for stainless steel 304 with lubrication was similar to the wear of the same materials during sliding (adhesive wear). In later studies, Montgomery, Bayer, Engel and Sirico, Iturbi, Greenfield and Chou, working on different materials, concluded that impact wear is similar to surface fatigue wear [45].

To study the impact wear experimentally a pendulum tester was built and the impactor made from a hardened steel bearing (Rabinowicz 1995) for testing different types of materials (chromium, aluminum bronze, titanium, stainless steel 304 and nickel) with different number of impacts (up to 2000 impacts).

The results for different materials revealed that the mass loss increase with increasing the number of impacts.

As a quantitative measure of impact wear, Rabinowicz built a model based on the linear model of Archard starting with the relationship [45]:

$$W = \frac{kFx}{H_s} \quad 2.6$$

where:

$W$  is the wear volume

$F$  is the applied Load (N)

$x$  is the sliding distance (m)

$H_s$  is the hardness of the softer materials and  $k$  is a dimensionless sliding wear coefficient.

Load can be represented by  $(F_r/\mu)$  where  $F_r$  is the friction force and  $\mu$  is the coefficient of friction and  $(F_r \times x)$  represents the energy dissipated during sliding. Further, if we define  $\zeta$  as the total impact energy expended during sliding and the term  $(\zeta k/\mu)$  is replaced by a parameter  $K$ , then wear volume would be:

$$W = \frac{KeN}{H_s} \quad 2.7$$

where:

$K$  is non-dimensional impact wear coefficient and  $e$  is the impact energy,  $K$  is related to  $k$  by:

$$K = \frac{k\zeta}{\mu} \quad 2.8$$

### 2.4.2.3 Fricke and Allen

A pivotal impact hammering wear rig with a frequency of 15 Hz was used to study the impact wear of different types of steel: AISI 304, 440C, 431, 817M40, 1210, in dry and distilled water in normal impact conditions and line contact configuration. The line contact configuration used to reflect the impact wear of poppet valves used in mining equipment [22].

The results of repetitive impacts based on mass loss revealed that increase the number of cycles for all materials increases both the contact area and mass loss. The mass loss of materials under dry conditions is almost twice that in wet conditions (distilled water) with dark grey surfaces [22].

The surface examination for all tested materials revealed that two forms of wear damage exist, spalling due to pitting with relatively smooth surface and delamination as a result of cracks that propagate parallel to the surface and eventually material removal and the surface is relatively rough.

The angle between the impactor and the contacting flat surfaces was  $90^\circ$ , in actual valve system, the angle should be less ( $45^\circ$ ) to reflect the actual situation of impact wear and to provide the maximum material constraint at the contact [22].

The impact wear results for AISI 431 stainless steel specimens impacted at energies from 2-5 J can be represented by the following impact wear model [22]:

$$W = KNe^{n_{Fricke}} \quad 2.9$$

where:

$e$  is the impact energy (J)

$N$  is the number of impact cycles

$K$  is the empirically impact wear coefficient, and has a value of  $(2.715 \times 10^{-5})$

$n_{Fricke}$  is the impact energy exponent (2.07)

#### 2.4.2.4 Lewis

Building on more applied work, Lewis [46] developed a new, more general, predictive model to measure the overall compound impact wear that comprises the sum of two wear models. One for predicting impact wear, in the same form that is used in the erosion formula by Fricke [22], and one for sliding wear based on an Archard Equation, [46] [47] and included the contact area ratio to the power  $q$  for changing the contact geometry:

$$W = \left( \frac{k \bar{P} N x}{H_s} + K N e^{n_{Lewis}} \right) (A_i / A)^q \quad 2.10$$

where:

$W$  is the wear volume ( $m^3$ )

$\bar{P}$  = Average load (N) from Engel [48]

$k$  is the sliding wear coefficient (0.001) for dry and (0.00001) for lubricated from Rabinowicz [49]

$H_s$  is the hardness of softer material ( $kg/m^2$ )

$N$  is the number of cycles

$K$  is the impact wear coefficient, normally in the range  $(3.5-5.3) \times 10^{-14}$  from Lewis [6]

$x$  is the sliding distance (m)

$e$  is the impact energy (J)

$n_{Lewis}$  is the impact wear exponent, normally in the range (0.2-1.2) from Lewis [6]

$A_i$  is the initial elastic contact area ( $m^2$ ) from Engel [48]

$A$  is the contact area after  $N$  cycles ( $m^2$ )

$q$  is the exponent of contact area ratio measured experimentally

For validation purposes, the experimental data of Engel [48] where sintered bronze and hard steel plates impacted with steel hammer were used, the initial contact areas  $A_i$  were calculated from the same reference using Hertzian line contact analysis and dynamic load were taken from Engel [48] as the average load during contact.

$K$  and  $n_{Lewis}$  were determined from experimental data under normal impacts through iterative process of Equation 2.10 to wear curve [6]. The exponent of contact area ratio ( $q$ ) were calculated empirically during the iteration process and the effective mass of the striker were taken from Engel [48] for the impact energy calculation. The sliding distance ( $x$ ) that occurs during compound impact was calculated from the sliding velocity and sliding time  $\bar{t}$ , the sliding time was measured by using an electrical

inductance method [48], due to lack of other sliding wear data, the sliding wear coefficient  $k$  were taken from Rabinowicz [49].

The model was validated first with the experimental data of Engel [1] under normal impact where steel striker hit sintered bronze plate and good correlations is achieved. Then the model were further validated with other data of Engel [1] under compound impact between soft steel striker and hard steel specimen and also good correlation is found.

#### 2.4.2.5 Akhondizadeh, Mahani & Rezaeizadeh

The effect of impact parameters on the wear of alloy steel plates has been studied using an impact wear rig. Since the ball size and ball velocity are two important parameters in mill liners, different values of impact velocity (2.5, 5, 7.5, 10) m/s, ball radius (7.5, 12.5, 20, 25) mm and impact angle (10°, 15°, 20°, 30°, 35°, 45°, 60°, 70°) are used. A steel plate is impacted repeatedly by AISI 52100 steel balls and the mass loss is measured after a certain number of impacts (600) [35].

Results showed that the impact wear effectively depends on the impact velocity, impact angle and ball size. Akhondizadeh built a model using design of experiments based on the effective kinematic variables and is presented in the form [35]:

$$W = K V^\alpha R^\beta e^{\theta\gamma} \quad 2.11$$

where:

$V$  is the impact velocity (m/s)

$R$  is the striker ball radius (m)

$\alpha, \beta, \gamma$  are the constant parameters

$K$  is the impact wear coefficient and have a value of 100

$\theta$  is the impact angle

The new model has been found by using the Taguchi method in the design of experiments with level 4 and 16 tests.

While the Taguchi method is useful for working on linear relationships, the results for impact angles obtained in this paper are non-linear, which makes Taguchi unsuitable for use as it would be missing an important interaction between parameters effectively.

Additionally, the number of cycles is not a parameter taken into consideration in this model which may reduce the accuracy of the model especially when all the previous models considered it as a primary parameter effecting on the results under both normal or compound impact.

Also, it is important to mention that the paper defined  $\theta$  as the impact angle and then in the model Equation 2.11, they said that  $e$  is the impact angle, it is most likely a typo and possibly re-write as:

$$W = K V^\alpha R^\beta \theta^\gamma \quad 2.12$$

### 2.4.2.6 Kai, Yang & Wei

A new impact fretting wear model was proposed based on both the Archard model and the energy loss during impacts to reflect actual impact fretting wear occurs in some components such as the interaction between the tubes /supports in steam generators (SG) [50].

The proposed model of Kai has the following form:

$$W = \left( \frac{kF_n x}{H_s} + KN\Delta E \right) \quad 2.13$$

where:

$W$  is the wear volume ( $m^3$ )

$F_n$  is the normal impact force (N)

$H_s$  is the hardness of softer material ( $kg/m^2$ )

$N$  is the number of cycles

$x$  is the sliding distance (m)

$k$  is the sliding wear coefficient

$K$  is the impact wear coefficient

$\Delta E$  is the energy loss (J) and  $= \left( \frac{1}{2} M_{eff} V^2 - \frac{1}{2} M_{eff} V_r^2 \right)$

$V$  is the impact velocity (m/s)

$V_r$  is the rebound velocity (m/s)

$M_{eff}$  is the effective mass (kg)

The proposed model has two components, one is similar to the Archard equation and presents the sliding component while the other one which presents the normal component is based on the energy loss during impact ( $\Delta E$ ).

The major drawback of the new proposed model is that the tangential components  $\left( \frac{kF_n x}{H_s} \right)$  does not take into consideration the number of impact cycles during impacts in a similar fashion to both Rabinowicz (see Equation 2.7) and Lewis (see Equation 2.10). Which means that every time the number of impact cycles has changed it would lead eventually to different value of  $k$  and thus disagree with all the previous models described in Section 2.4.2.

Also, the model which should be built to reflect the sliding impact motion did not take into consideration the role of tangential component (shear force) during impact and on the contrary, it contributed the damage occurs during sliding impact to the normal impact force ( $F_n$ ). The normal component ( $KN\Delta E$ ) also has another drawback, contrary to all the previous extant models which clearly stated that the damage is mainly contributed to impact energy.

This model considers the energy dissipation during impact which is the difference between the impact energy and rebound energy is responsible for the damage. For example, when a body goes into impacts with another one with impact energy 7 J and the rebound energy is 4 J. It means that based on this model the 3 J which presents the energy loss during impacts is responsible for the damage during normal impact which does not make sense.

### 2.4.2.7 Summary of Extant Impact Wear Models

The models described in Section 2.4.2 have different forms and therefore, it leads to different impact wear coefficients being used. Rabinowicz outlined different values of impact wear coefficient taken from his work using Equation 2.6 and the work of others as shown in Table 2.1.

Table 2.1 Impact wear coefficient values extracted from [45]

Reference	Surface Measured	Impact Energy (J)	Number of Impacts (N)	Lubrication	Impact Wear Coefficient, $K$
Rabinowicz, 1952	Copper (hard)	2	1	N	$53 \times 10^{-6}$
	Steel	20	1	N	$67 \times 10^{-6}$
	Steel	20	1	Y	$10 \times 10^{-6}$
Wellinger and Breckel 1969	Copper	60	$5 \times 10^5$	N	$20 \times 10^{-6}$
	Soft Steel	120	$5 \times 10^5$	N	$19 \times 10^{-6}$
	Aluminium Alloy	60	$5 \times 10^5$	N	$42 \times 10^{-6}$
	Titanium Alloy	120	$5 \times 10^5$	N	$15 \times 10^{-6}$
	Hard Steel	160	$5 \times 10^5$	N	$28 \times 10^{-6}$
	Hard Steel	700	$4 \times 10^3$	N	$43 \times 10^{-6}$
	Hard Steel	42	$2 \times 10^4$	N	$104 \times 10^{-6}$
Engel, 1975	Hard Steel	0.36	$6.5 \times 10^4$	N	$14 \times 10^{-6}$
	Hard Steel	0.36	$4.3 \times 10^5$	Y	$1.2 \times 10^{-6}$
	Soft Steel	0.36	$1 \times 10^4$	N	$247 \times 10^{-6}$
	Soft Steel	0.36	$3.2 \times 10^6$	Y	$0.8 \times 10^{-6}$
Engel 1976	Hard Steel	0.48	$10^7$	N	$0.2 \times 10^{-6}$
Rabinowicz 1995	Soft Steel	110	800	N	$930 \times 10^{-6}$
	Nickel	110	1300	N	$850 \times 10^{-6}$
	Titanium Alloy	110	500	N	$99 \times 10^{-6}$
	Aluminium Bronze	110	500	N	$370 \times 10^{-6}$
	Chrome Plate	110	2000	N	$1200 \times 10^{-6}$
	Soft Steel	110	500	Y	$24 \times 10^{-6}$

Table 2.1 shows that the impact wear coefficient  $K$  depends on the material tested, impact energy, number of impact cycles and impact condition (dry or lubricated), in all cases the deviation in the impact wear coefficient was between  $(0.2-1200) \times 10^{-6}$ .

All the models described in Section 2.4.2, with the exception of Lewis where the wear depth of his work validated with the work of Engel, did not validate the wear volume with any other published papers. The parameters were generated directly from their experimental works using either best line fitting such as in the model of Wellinger [44] and Fricke [22] or from the regression of the DOE such as in the Akhondzadeh model [35]. Therefore, there is no paper that developed a model and compared the wear volume with the works of others for the same materials.

The models presented in Section 2.4.2 all share a significant limitation that they are unable to predict the wear loss by taking into account the effect of tangential force (shear force) during compound impact with different angles, especially at lower angles where more shear force than normal force is extant. Additionally, all those models depend on the total applied force, rather than both force components independently during compound impacts, so they are unable to predict as a function of impact angle.

The majority of previous models, with the exception of Lewis, do not consider the role of work hardening or the sliding component directly during impact and thus are more suitably applied to purely normal impacts. The Lewis model attempts to overcome this by means of its Archard-based sliding component, which is dependent on accurate knowledge of the magnitude of the interfacial sliding distance at the point of impact, but does not include the impact angle as an input directly. This is important because where impact wear occurs in many industrial applications, it is typically a compound impact (poppet valves, drilling tools, gears, bearings, linkages), yet as described here, no existing model can successfully predict the wear volume as a function of impact angle, more details in Chapter 7.

### **2.4.3 Impact Wear Numerical Simulation**

Few studies have been carried out to simulate the contact mechanism during normal impact and even fewer during the compound impact. Different commercial software used to model the contact during the wear mechanisms includes programs such as ABAQUS and ANSYS that are based on the FEM.

Numerical modelling using finite element method (FEM) via ANSYS/Explicit was employed to simulate the impact of a hardened stainless-steel ball striker (AISI 420) with diameter of 9 mm on a rubber specimen at impact angle ( $30^\circ$ ) and impact velocity 135 m/s. The effective Von Mises stresses were calculated at different rubber specimen thicknesses 1-16 mm [51] and the numerical results showed highest stresses (Von Mises) with the thinnest rubber plate.

Numerical modelling using commercial software (SPAM) was employed to simulate the impact of a hardened steel ball striker with diameter of 9 mm on a rubber specimen at an impact angle of  $45^\circ$  and impact velocity 37 m/s to study the effect of goods on a conveyor rubber belt. The effective von Mises stresses were calculated during modelling [52].

The results revealed that the Von Mises stresses which has the highest value beneath the surface increases with impact time and the penetration depth increases also with increasing the impact time.

ABAQUS/Explicit was used to model the equivalent stresses (Von Mises) caused by a hardened steel ball bearing striker (52100) according to ASTM A295 upon a specimen of hardened bearing steel under compound impact at ( $45^\circ$ ) and impact velocity of 0.51 m/s. Making the simple assumption that the contact pressures were equal to that of a normal impact with an impact velocity equal to the normal velocity component of the sliding impact [11].

All the previous simulation programs have been used only to predict the amount of surface and subsurface stresses. This would help to predict the location of cracks formation (initiation and propagation) in case of point contact, but were not used to predict the amount of wear loss of different materials under repetitive impact.

## **2.5 Impact Wear Parameters**

### **2.5.1 Role of Impact Angle, High Temperature and Impact Conditions**

In general, reducing the impact angle will lead to more tangential force (shear force), thus likely higher sliding that will potentially lead to more wear loss depending on the mechanical properties of the specimen. There appears to be no consensus in literature as to how impact angle is defined, and in this work the impact angle ( $\theta$ ) is defined as the angle between the direction of impact caused by the impactor and the plane of the specimen, as illustrated in Figure 2.19.

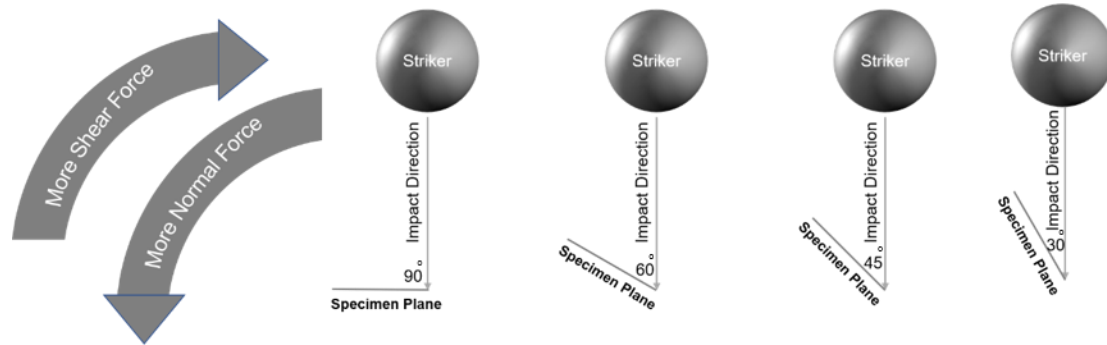


Figure 2.19 Schematic diagram of different impact angles

The impact angle also plays a key role in controlling the type of wear mechanism [53] in ductile materials. A larger impact angle will lead to more normal impact force than from a sliding impact, and damage is therefore more likely to be in the form of plastic deformation and surface fatigue due to spalling by surface cracking or delamination. However, a smaller impact angle will lead to more tangential force and less normal force, causing more sliding impact in addition to spalling and subsurface cracks and leading to delamination and excessive material loss (wear). The experimental work of Akhondizadeh showed that the maximum wear loss occurred at  $30^\circ$  [35].

Further investigation on the role of impact angle was conducted by Tyfour and colleagues [30] who performed impacts in the range  $90^\circ$ -  $40^\circ$  on a low carbon steel (A516-70) with a hardness of 145 HV. They used an in-house built impact hammering wear rig and the results indicated that the mass loss is highly dependent on the impact angle, with the lowest mass loss recorded with normal impact 0.18 mg and highest mass loss at impact angle  $40^\circ$  (0.68) mg after 1000 cycles.

Similar results were also obtained by Zanoria [54] where highest wear volume occurred at  $45^\circ$  and slip length was approximately 0.18 mm at  $45^\circ$  compare with 0.1 mm at  $75^\circ$ . Rigaud & Le Bot [29] results of wear volume of medium carbon steel and austenite stainless steel 304 using spherical cap method showed that no wear found at impact angles  $60^\circ$  and maximum of wear occurred at impact angle  $30^\circ$  with significant increase in wear scar depth and diameter at impact angle  $30^\circ$ .

The above results show that the highest wear loss occurs with lowest impact angle and because there are very few data available on the role of angle during impact and specifically for austenitic stainless steel. Further investigation has been done during this work for both AISI (304, 316) and EN8. This will help in better understanding the impact angle role and eventually connecting it to the new proposed model.

An impact hammering wear rig controlled by electromagnetic field was used by Wang [39] to study the effect of dry and lubricated contacts using PB450 and PB1300 oils on wear rate of 40Cr steel with hardness of 210 HV using steel ball of 25.4 mm diameter and number of impacts up to 100,000.

Results for dry contacts revealed that at short impact durations, a hardened layer is formed on the metal surface that is useful in preventing surface damage and the scar depth is less than in the case of lubrication which means that the existence of lubricant goes against the formation of the hardened layer on the specimen surface. This could be explained by the effect of oil packing, the oil flows into the crevices formed from previous impacts and therefore the crevices are expanded in the following impacts. However, at higher impacts, wear for lubricated contacts is less because the lubricant acts as a protective layer and restrains the impact wear and plastic deformation in addition to the fact that lubricants make the heat generated in the dent transfer quickly to the specimen surface [39].

The boundaries between the new surface and the hardened layer were blurred which indicates the adhesive wear, delamination layer and crack formation can be also seen in specimens under dry contacts, spherical debris is formed in dry contact inside the impact scar as shown in Figure 2.20 [39].

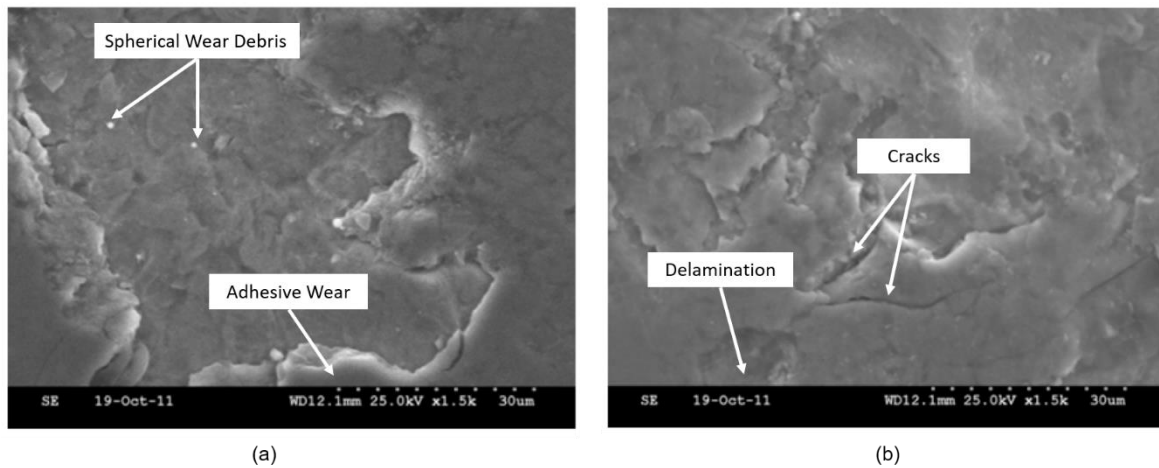


Figure 2.20 SEM image of medium carbon steel wear scar showing (a) the spherical wear debris and adhesive wear while delamination and surface cracks are shown in (b) extracted from [39]

Results of impact wear on AISI 431 steel by Fricke [22] in dry and wet conditions (distilled water) revealed that the rate of mass loss in dry impacting appeared constant, with an increasing number of impacts, and this resulted in more than twice the mass loss after 100,000 impacts compared with that from wet impacting [22].

There are only a few papers where the impact wear is in wet or lubricated conditions because in reality the majority of engineering or industry applications of impact wear have dry contacts and therefore, the work reported in this thesis was done in dry conditions.

Impact wear of components such as engine valves and valve seat inserts are frequently observed for various actual engines, but yet the role of high temperature on their wear rate is still not clarified or studied at present which complicate the understanding to their wear mechanism.

A repetitive impact hammering rig was used by Ootani [33] to investigate the damage that resulted from repetitive impact for both austenitic stainless steel rings (impactor) with hardness of 380 HV and sintered alloy disks (specimen) of 373 HV under room and high temperature (200 and 400 °C) and sliding speed varying from 0.1 m/s to 0.8 m/s.

In normal impact (without sliding) the wear volume measured from mass loss of the disc (specimen) and ring (striker) was very small compared to results obtained for impacts with sliding regardless of temperature, 3 mm<sup>3</sup> for disc and 0.3 mm<sup>3</sup> for the ring after 500,000 cycles.

The results did not reveal a direct correlation between the wear volume and high temperature, at room temperature, increasing the sliding velocity from 0.1 m/s to 0.8 m/s revealed accelerated wear volumes for both specimen and ring, at 200 °C, softening played a role and the wear volume of disc accelerated. However, at 400 °C, the wear volume decreased to less than those of room temperature because oxide layer formed on the surface and had a strong effect on wear of disc and no acceleration of wear volume was observed at any sliding speed.

Results showed that only one paper investigated the role of high temperature (200 and 400 °C) during impact for both stainless steel and carbon steel and only under normal impact. The work reported here

aimed to investigate the role of high temperature for stainless steel and carbon steel but under both normal and compound impact (90° and 45°C) and it will be useful to get some data about the expected wear volume of materials under high temperature.

### 2.5.2 Role of Bulk Hardness and Surface Hardening

The role of both bulk hardness and Young's modulus on impact wear of five metallic materials (Al, Cu, Fe, Cr, W) with point contact has been investigated by Wang [37] using an impact hammering wear rig with point contact configuration and steel chrome ball as an impactor. Specimens were polished to have a surface roughness of  $R_a=1 \mu\text{m}$  and the impact force for all materials was measured during impact by using piezoelectric force sensor.

The results revealed that the impulse and peak impact force slightly increased during impact with increasing cycles from 1000 to 100,000 cycles with a percentage of 7-9 % for the tested materials. For example, the peak impact force of Chromium increased from 211 N after 1000 cycles to 240 N after 100,000 cycles. Also, an increase in the number of cycles for all materials led to an increase in both wear volume and wear depth. The wear mechanism for softer material (Al) was mainly severe plastic deformation and spalling while for moderate hardness materials (Cu and Fe) material flow, limited plastic deformation, spalling and delamination were the wear mechanism. The hardest materials (Cr and W) showed spalling, large delamination and wear debris with no evidence of plastic deformation [37].

Surface hardening is a treatment of metal by either heating or mechanical methods to increase the hardness of the metal surface while the core remains relatively soft. The combination of a hard-upper surface and a soft interior is beneficial in engineering applications because it can lead to improvement of the hardness and strength of the material and increase the wear resistance of metal.

Plastic deformation occurs due to impact and so the wear rate decreases due to the hardening behaviour [32]. So, surface hardening can be useful to improve the material resistance to impact wear and can be done through different methodologies such as:

- **Conventional heat treatment:** It involves heating a specimen in a furnace or electrical oven to austenitizing temperature and kept in furnace for a specific period of time to enable the temperature within the specimen to be uniform. For example, martensitic stainless steel is heated up to 1020 °C and kept there for 10 minutes [12]. The specimen is then quenched by oil to achieve the rapid cooling, for the tempering process, the quenched specimen is put in an electrical oven pre-heated to the required temperature and kept there for 2 hours, then the specimen is naturally cooled inside the oven at room temperature.
- **Induction hardening:** Is a type of surface hardening of steel and other alloys in which a metal part is induction-heated and then quenched. The induction process which uses the principle of electromagnetic induction to produce heat inside the surface layer of a specimen. The quenched metal undergoes a martensitic transformation, increasing the hardness and brittleness of the part and reducing ductility. Induction hardening is used to selectively harden areas of a part or assembly without affecting the properties of the part as a whole.
- **Cryogenic hardening:** the process where the material is cooled to approximately  $-185 \text{ }^\circ\text{C}$ , usually using liquid nitrogen and it is designed to increase the amount of martensite in the steel's crystal structure, increasing its strength and hardness. This treatment is used on tool steels, high-carbon, high-chromium steels to obtain excellent wear resistance.
- **Laser hardening:** the process that aims to improving the wear resistance of ferrous materials suitable for hardening, including steels and cast iron with a carbon content of more than 0.2 %

by heating the surface of a metal part to the hardening temperature above (1000 °C) in a reduced area within a very short period of time and then let it quickly cool down in room temperature to produce martensitic structure.

The role of a ball burnishing process on stainless steel 316 has been investigated by Yilmaz [28] using an impact hammering wear rig under normal impact and point contact geometry with a ball as a striker made of WC with diameter of 13 mm. The results revealed that the burnishing process which led to higher hardness for specimens improved the material resistance to impact wear and reduced the volume loss by between 53–62 %, also increasing the number of cycles led to higher wear volume.

The effect of normal impact wear on compacted graphite iron has been studied using the impact hammering wear rig designed by Slatter [8]. Three sets of specimens were used in this work, an untreated set, and two sets with two levels of induction hardening depth 2 mm and 3 mm.

The results showed a significant increase in hardness from 250 HV for untreated specimens to 650-700 HV for treated, also for a 2 mm induction hardened depth, the specimens showed both more wear resistance and highest hardness, but formation of cracks near the wear scar edge was observed in these specimens. Wear scar depth of induction hardened specimens was about a quarter of that for untreated specimens [8].

The effect of normal impact wear on grey cast iron (EN-GJL-240) has been studied using the impact hammering wear rig designed by Slatter [7]. Three sets of specimens were used, one of which was untreated and the other two sets were laser treated.

The results of set A after 72,000 impacts showed very good wear resistance but also rough surface and surface cracks formation at the melted layer and subsurface deformation occurrence in either the hardened layer or the substrate layer. Results of set B after 36,000 impacts showed good wear resistance and some damage to the hardened layer on the surface, but little subsurface deformation. Specimens of set C, which included untreated specimens, exhibited the highest levels of wear, after only 18,000 impacts, and the wear scar depth was almost double that of Sets A and B [7].

The effect of normal impact wear on martensite stainless steel has been studied by Tianmin [12] using impact hammering wear rig with ball on flat contact geometry, both conventional heat treatment and laser hardening were used in this work. Results after 10,000 impacts showed surface fatigue in the form of spalling for the conventional specimens and only plastic deformation for the laser specimens, but after 50,000 impacts even the laser specimens exhibited surface fatigue (spalling).

EDX showed that laser hardening for stainless steel provides better surface properties regarding oxidation resistance compared with those obtained by conventional heat treatment. Also, SEM analysis and surface roughness measurement suggested that the size of the impact wear scars of steel specimens decreases with the increase of the surface hardness [12].

The effects of normal impact wear on graphitic cast iron (EN-GJL-240) with hardness of 235 HV and low carbon steel with hardness of 175 HV have been studied using the impact hammering wear rig designed by Slatter [9]. Two sets for each material were prepared, one untreated and one with cryogenic treatment.

Cryogenic processing of low carbon steel produced a very clean wear scar edge that was well defined after 4500 impacts, while after 72,000 impacts it became slightly rougher and exhibited cracks formation at the wear scar edge [9]. Meanwhile, cryogenic processing of lamellar graphite cast iron produced a dark ring of wear debris around the wear scar after 72,000 impacts.

Results revealed that the untreated specimens produced large metallic flake debris whereas cryogenically processed specimens produced much finer, darker particles.

Cryogenic processing can thus have a positive effect on the wear resistance of low carbon steel. The lamellar graphite iron showed greater improvement of its ability to resist impact wear compared to the low carbon steel.

The results suggested that in general increasing the bulk hardness of material can lead to a reduction in both wear volume and depth [37], but further investigation on different materials revealed that bulk hardness may not play a primary role on wear loss of materials under repetitive impact such as by Rastegar [21], Fricke [22] and Petrov [24].

Different surface hardening methods revealed an improvement in impact wear resistance for tested materials but it should be noted that these papers either measured the wear volume by spherical cap method or used 3D profilometer to measure the wear volume which is actually the total volume loss not the wear volume and this agreed with results obtained in this study for the zero wear as explained in details in Chapter 4.

### **2.5.3 Change of Surface Roughness during Impact**

Surface profile measurements along two orthogonal lines after 30 min, 1, 2, 4, 8, 16 and 24 h were investigated by Rigaud & Le Bot [29] as shown in Figure 2.21. The surface damaging process can be explained as follows. Below 30 min there is no significant evidence of plastic deformation at the surface, or weight loss of the sample. At 24,000 impacts, which means after 1 h based on a frequency of 6.5 Hz, a slight disturbance of the surface roughness appears due to repeated impact which causes metal fatigue, without generating scar or detectable wear. The initial roughness of the sample of 0.1  $\mu\text{m}$  peak to peak rapidly rises until 3  $\mu\text{m}$  peak to peak [29]. This observation is consistent with the Engel model [43].

Evolution of roughness leads to a modification in the real contact surface. Beyond this running-in period, stress at impact may be sufficient to generate local plastic deformation at asperities and wear proceeds by surface fatigue. Visual observations show that wear debris escapes from the contact zone under the influence of gravity. The scar volume increases almost linearly with the number of impacts [29].

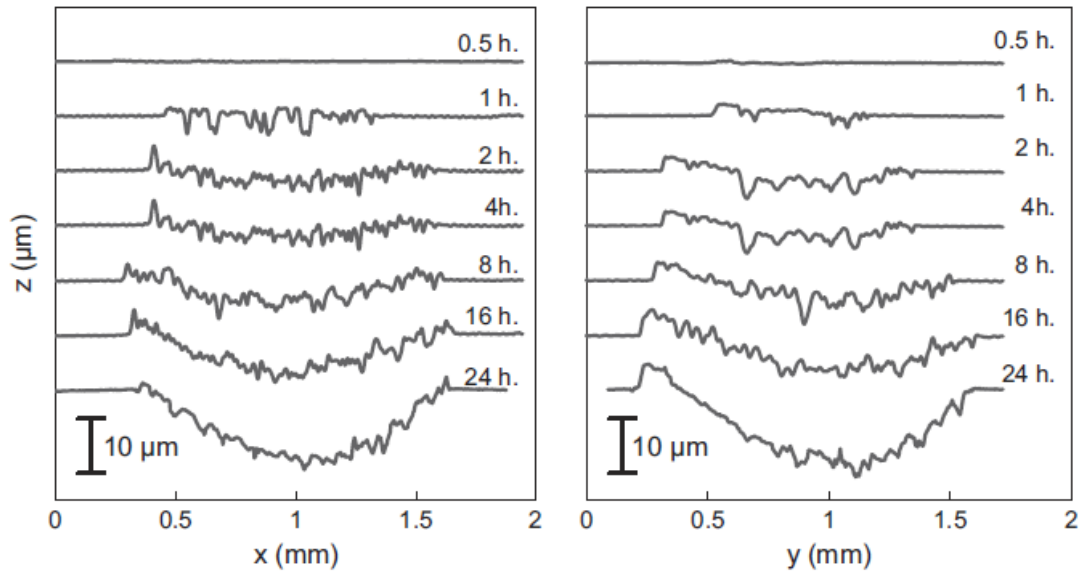


Figure 2.21 Profiles measured along the horizontal and vertical diameters of wear scar extracted from [29]

## 2.6 Research Literature Grading

### 2.6.1 Methodology

In order to evaluate the current status of research on impact wear of different materials that are widely used in industry applications, a grading system was established. It enabled quick identification of the data that is available in relation to this literature review through scoring each reference according to a set of criteria.

This methodology has been used in industry and at The University of Sheffield such as in the field of rail friction by Lewis, Preece, and Ishizaka [55-57].

The criteria that were used to score the papers in the grading system are listed below:

1. Peer reviewed: assessment by experts in the field to determine whether the research satisfies the established standards for such journal papers and industry reports.
2. Scaled test: involves using small scale test rigs to simulate the impact wear and gain control over specific variables.
3. Full scaled test: involves carrying out testing using a full scale test rig to simulate the impact wear with real components.
4. Experimental testing supported by modelling or simulation: to identify whether the testing is supported by empirical equation or by FEM simulation using commercial programs such as ABAQUS, ANSYS.
5. Field test using actual machine (for validation).

The research outputs assessed in the grading system have been given a mark out of 5 as illustrated in Appendix A. They were then categorized into A and B. Category A papers, in green colour, fulfil at least 60 % of the criteria, Category B, in amber colour, fulfil at least 40 % of the criteria. The results are then plotted on a “knowledge map” to highlight the extent and quality of available information on impact wear.

This grading system for research was useful to highlight the availability of data and the status of this research according to the criteria mentioned above. Review papers and handbooks or textbooks or papers

that are not directly connected to impact wear have not been included in this evaluation of the research and also it is necessary to mention that while the research is categorized according to the above criteria, this is not intended as criticism of the research in general.

The grading system has been sorted into primary and secondary groups according to the main areas of the research. The grading system comprised the following four areas related to the impact wear rate of materials:

- General impact wear mechanisms which covered the material removal mechanisms and the impact wear damage of metals (ferrous and nonferrous).
- Experimental impact wear testing which covered all test rigs that have been used widely by papers in the field of impact wear and the method used to measure the wear volume (mass scale and volume loss).
- Impact wear modelling analysis and simulation: It includes all papers that measured either the zero wear or developed a model under different impact factors to measure the wear volume. Lastly FEM analysis throughout commercial software such as ANSYS, ABAQUS and SPAM is performed to calculate the surface and subsurface stresses.
- Different impact wear parameters that have influenced on the material's life such as impact angle, temperature, hardness, et al.

To be included in a peer reviewed journal, the study needs to conduct testing that is supported by modelling or simulation and carry out a scaled test or a full scale test that would give industry confidence that the conclusions of the study paper are accurate.

### **2.6.2 Results**

The chart displaying the results of the grading is shown in Figure 2.22. From the chart, it is obvious that most of the research is marked as Category B, with only 10 papers marked as Category A.

According to the research grading methodology, one research has been achieved to study the effects of high temperature on impact wear. Few models of impact wear are available to date and except for Lewis model, all other models have not validated with any other papers.

Moreover, only one paper available studied the role of zero wear during impact by Engel to calculate the number of cycles at zero wear limit in the elastic region. Two papers were conducted with lubrication conditions and few papers investigated the role of impact angle during impacts for steels with lack of information about stainless steel in general and the austenitic one in specific.

However, the map grading also illustrated that many laboratories have been using different impact wear rigs for studying a variety of materials with majority of tests were conducted using impact hammering wear rig while fewer used the ballistic rig.

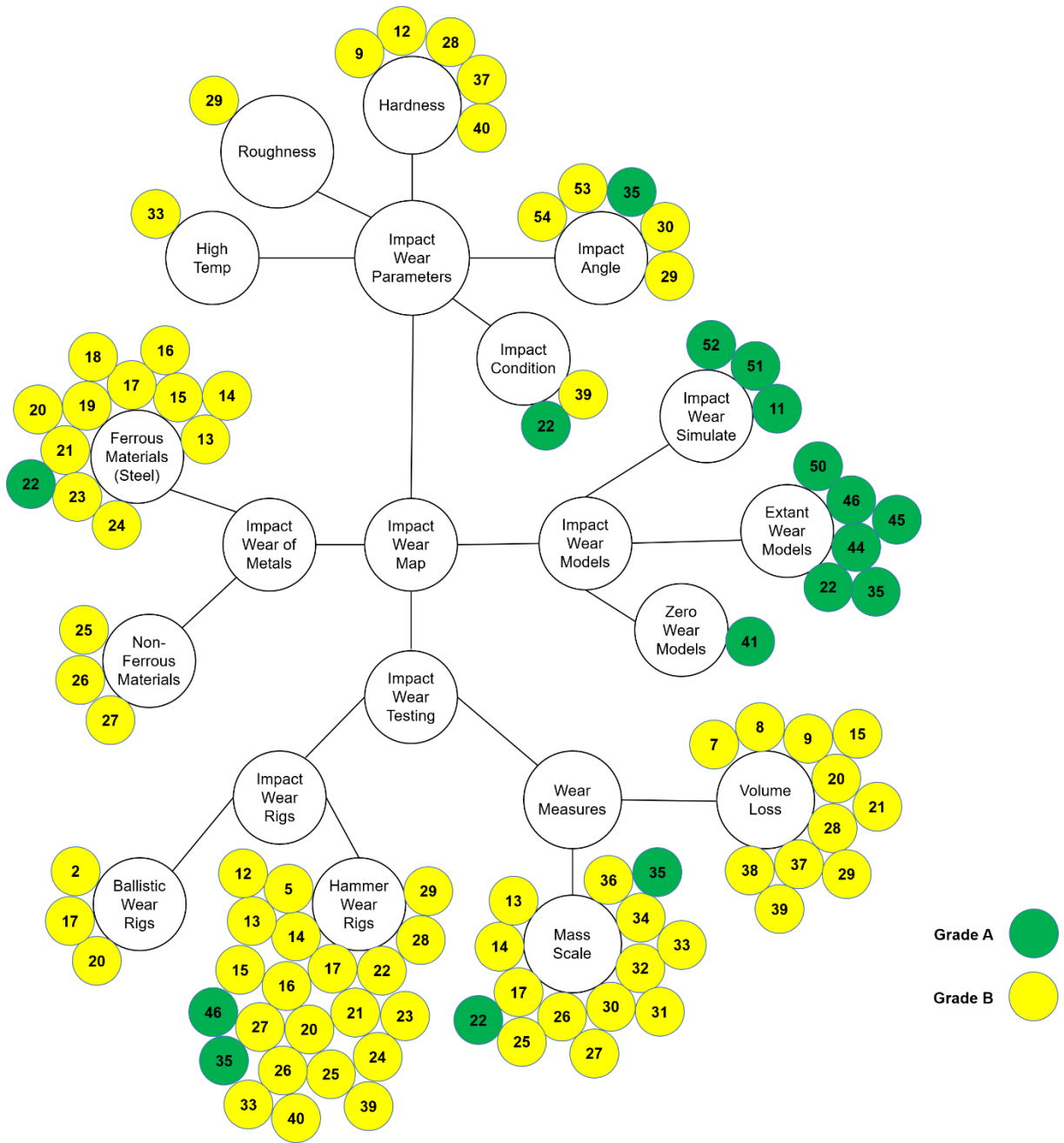


Figure 2.22 Knowledge map of impact wear

## 2.7 Literature Review Summary & Conclusions

A summary of the literature connected to the work achieved in this study has been utilised. This section summarises the importance points and key findings from the literature as follows:

- There is a lack of data about the impact wear damage mechanism for austenitic stainless steel AISI 304 and AISI 316 especially with different impact angles.
- Two body and three body abrasive wear damage during compound impact of ferrous and nonferrous materials has not been studied in the literature.
- It is not obvious if the cracks that initiated and propagated during normal and compound impact occur inside the grains or within the grain boundaries.
- The role of zero wear volume on the total volume loss has not been taken into consideration in the literature especially under normal impact.
- Impact hammering wear rig is the most common type of rigs used in the field of impact wear.
- Both mass scale and volume loss methods are complementary to each other, rather than simple substitution for each other, in order to have an accurate measurement for the impact wear scar.
- The impact wear damage is highly depending on the impact angle and there is a change of wear mechanism from surface fatigue to abrasive wear with lower impact angle.
- There is a lack of data about the correlation between the microhardness measurements for the centre of wear scar and the impact angle in the published work.
- The number of impact cycles, impact energy, impact force and impact angle are important parameters during repetitive impact.
- It is not obvious if the high temperature will lead to more or less wear volume than at room temperature as the only available paper did not reveal a specific pattern.
- The existing models made a good contribution in the field of impact wear, but the role of shear force during compound impact (tangential component of impact force) has not been considered in any of these models despite that highest wear volume occurs with the highest shear force.
- A map grading methodology has been used in this work to summarise the main area of research and give an idea about the potential gaps in the literature.

## Chapter 3 Impact Wear Methodology

### 3.1 Test Equipment and Specimens

#### 3.1.1 Impact Test Rig

In order to ensure that the impact is repeated over the same contact region to reflect the actual impact that occurs in many industrial applications and to study the details of that region under different impact parameters. A modified impact wear rig similar to that used previously by Slatter [40] and later by Bruce [8, 58] has been used for the purpose of work in this study.

Also, based on the previous literature review, the impact wear rig was selected as the most common and reliable type of rig for measuring the wear loss of different materials under repetitive impacts.

The rig was designed by Slatter [40] in a simple form to achieve high quality repeatable and accurate results at low cost. The rig was deliberately designed to allow better understanding of the impact wear characteristics of different materials prior to being used in a particular component, rather than to simulate a specific type of component or system.

A rig schematic is shown in Figure 3.1, illustrating the oscillating striker arm, made from silver steel to improve the stiffness and driven by a spring / cam system comprising a cam and follower with helical stainless steel compression spring. The majority of the rig was made from mild steel, except for the pivotal block and striker block which were made from aluminum alloy to reduce flexural bending of the arm throughout and to reduce the mass at the end of the arm.

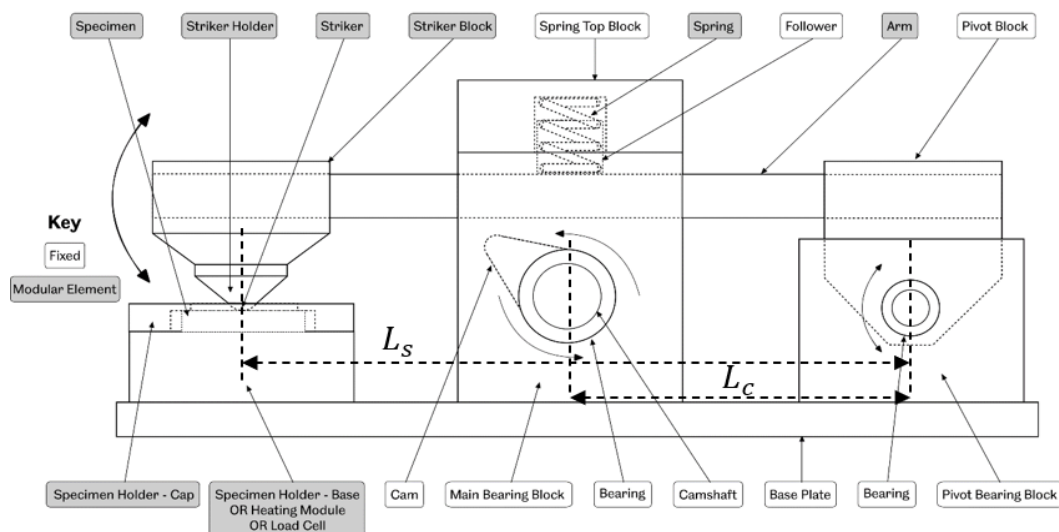


Figure 3.1 Schematic diagram of impact rig

The cam was arbitrarily taken from a 2.4 L (D.O.H.C) diesel engine and would be in direct contact with the hardened face of the silver steel arm, while the other hardened face would be in contact with the follower, inside which a compression stainless steel spring was located to ensure that the arm would stay in contact with the cam during the rotation of the cam.

The rig is driven by a 1.1 KW electrical motor and the speed of the motor is regulated by a variable frequency controller (inverter); steel ball bearings were used to support the camshaft and pivot shaft.

Lubricant oil can be supplied through two small holes in the centre of the top block to avoid friction and wear between the compression spring and the follower.

The striker holder at the end of the lever arm holds a 15 mm diameter series 400 chrome steel ball with a material specification equivalent to AISI 52100 which is used as a striker and contacts the specimen. The selection of this particular striker is arbitrary for the work conducted here, but it has been extensively used in the previous work performed on this apparatus where it was selected to be representative of the contact (s) being studied and shown to consistently reproduce the required levels of measurable wear needed for this study.

The striker ball was made from a very hard steel (AISI52100), much higher hardness and strength than the specimens to ensure that the damage would only occur on the specimens (one-body wear) and to enable the ball to be considered as a rigid body without surface degradation; therefore, any damage to the striker ball has been neglected.

A modified sacrificial plate similar to the one used by Slatter, made from hardened alloy steel, was attached between the ball and the striker block to avoid excessive damage to the striker head, as this plate would be easier to replace than the striker block. However, this modified hardened plate was used for many tests before changing it since there was no evidence of damage or degradation after a few tests.

The rig can be operated with different test parameters; for example, changing the impact frequency will enable the rig to work with different impact velocity/energy and force, while changing both the striker and the specimen holders will allow the rig to work at different impact angles.

The contact geometry (point, line, or elliptical contact) can also be changed if required by varying the form of both striker and specimen. In addition, the rig can be used dry or with lubrication as it is easy to place a gasket between the specimen and the specimen holder to avoid any spillage during tests.

The original design of the rig enabled the tests to be performed at different impact angles by changing the specimen holder base and the striker blocks to simulate the sliding wear occurring during impact. The two designed angles that can be used in addition to the normal impact are 60° and 45°. Further angles, such as 70° or 30°, can be accommodated by using a new specimen holder and new striker holder in this rig.

Both (striker/holder) pairs were designed to ensure that, regardless of the configuration of the test rig, the striker would impact the specimen at the same point in space and with the same effective mass and distance. The specimen holder cap and the striker holder are universal and fit all three of the different specimen holder bases and striker blocks.

The main modifications to the rig completed during the work carried out for the purposes of this thesis and thus make it different from that used by Slatter are:

1. A load cell has been used to measure the impact force during normal impacts.
2. A heater cartridges and controller box have been added to study the effect of high temperature during impact (200, 400) °C for point contact geometry.

The new heater cartridges enable the rig to work with different temperatures to simulate actual conditions of certain components where the operating temperatures approach, or exceed, the hot hardness of the material they are made from.

Three heater cartridges were inserted inside a newly designed block made from medium carbon steel with high thermal conductivity and low thermal expansion in order to ensure rapid heating distribution within a short period, as shown in Figure 3.2.

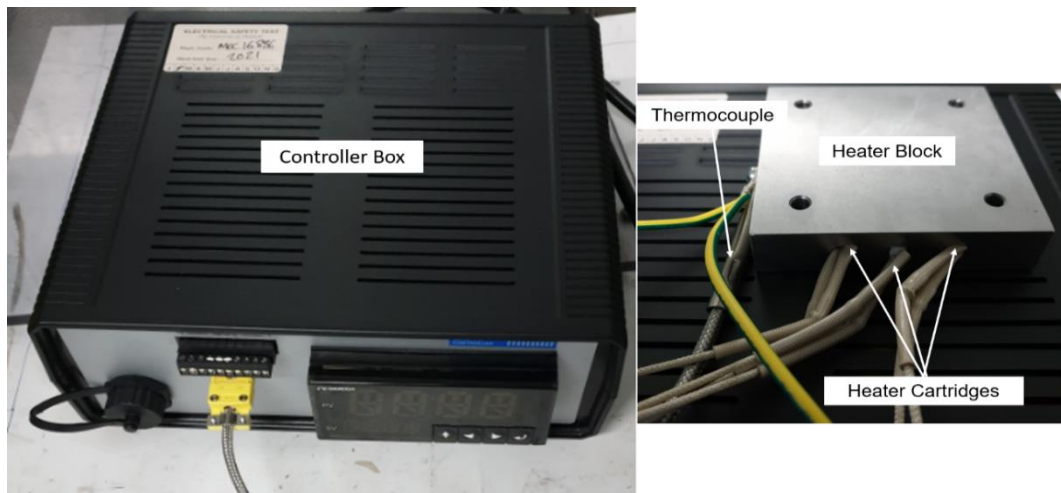


Figure 3.2 Controller box, thermocouple and heater cartridges connected to the designed block for use in high temperature measurements

The location of these heater cartridges was designed in a way such that heat would be evenly distributed to the specimen, with each heater cartridge able to withstand continuous operating temperatures up to 650 °C.

A high temperature Inconel overbraided silica fibre insulated thermocouple that could withstand high temperatures of up to 1038 °C was attached to the heater block from one end, as shown in Figure 3.2. The other end was inserted inside the controller box to measure the temperature on the block, bolted into a hole, square end style, inside the block and secured with a screw.

An infrared thermometer is used to measure the temperature on the specimen surface and compare it with the thermocouple reading on the controller box. Since the specimen was of 10 mm thickness it was expected that the temperature on the block would be slightly less than on the specimen surface and 200 and 400 °C were the actual readings selected for the specimen surface.

The reason for selecting these two temperatures was to compare the wear behaviour of medium carbon steel EN8 and austenitic stainless steel 304 with the only available previous results for the same range of temperatures, from a paper by Ootani [33], and identify any similarities in behaviour.

A Universal Benchtop controller box with 4-digit input display is used to control the temperature on the block, and the desired temperature can be set using manual instructions or software using USB drive before carrying out experimental work.

The temperature as measured by the thermocouple should reach a steady state, which would take some time. Once a steady state of the desired temperature has been reached on the specimen surface as measured by infrared thermometer (200, 400) °C, the experimental work can be carried out. The controller box, thermocouple and heater cartridges, as shown in Figure 3.2, were supplied by Omega Engineering.

### 3.1.2 Materials Consideration and Test Specimens

The different commercial metallic alloy materials used during the experimental work and described in Section 1.1 are widely used in industrial and engineering applications. These materials were manufactured by casting process.

The mechanical and chemical compositions of the tested materials as provided by the supplier (Apollo Metals, Sheffield) in addition to the striker ball provided by Simply Bearings Ltd. are shown in Table 3.1 and Table 3.2.

Table 3.1 Mechanical properties of tested materials and striker ball

Material	Elongation at Fracture %	Yield strength $\sigma_y$ (MPa)	Tensile strength $\sigma_u$ (MPa)	Young's modulus E (GPa)
AISI 304	58	270	581	190
AISI 316	50	332	630	190
EN8	10	628	739	200
EN-GJS-600-3	3	370	600	174
AlSi9Cu3	~1	165	330	70
PB102	12-14	380	460	121
Ball Striker (AISI52100)				
		2000	2300	210

Table 3.2 Chemical compositions of tested materials and striker ball

Material	% wt.													Bal.
	C	Sn	Si	Mn	Cr	Ni	Cu	Mo	Mg	Zn	S	P	N	
<b>Specimens</b>														
AISI 304	0.03	-	0.43	1.04	18	9.36	-	0.42	-	-	0.026	0.029	0.062	Fe
AISI 316	0.024	-	0.35	1.67	16.8	10	0.46	2.04	-	-	-	-	0.076	Fe
EN8	0.43	-	0.2	0.72	0.02	0.06	-	-	-	-	0.021	0.013	-	Fe
EN-GJS-600-3	3.25-3.7	-	2.4-3	0.1-0.3	-	-	-	-	-	-	0.02 max	0.015-0.08	-	Fe
AlSi9Cu3	-	-	10.7	0.022	-	-	2.4	-	0.022	1.1	-	-	-	Al
PB102	-	4.5-5.5	-	-	-	-	-	-	-	0.3 max	-	0.03-0.4	-	Cu
<b>Striker Ball</b>														
AISI 52100	0.95-1.1	-	0.15-0.3	0.25 Max	1.3-1.6	-	-	-	-	-	0.025 Max	0.03 Max	-	Fe

All test specimens were manufactured from as received round bar of 50 mm diameter and 500 mm length. They were cut to individual specimen discs of 10 mm thickness and using the original diameter of 50 mm to fit the existing rig specimen holder.

All specimens were secured and orientated inside the specimen holder in such a way that the surface grinding direction would be parallel to the direction of impact. Once the test was completed, the specimen is removed from the holder and taken to the scale and 3D non-contact profilometer to measure the wear volume and characterise the wear scar. After every test the striker ball is changed.

### 3.1.3 Rig Procedure

The rig was operated at a frequency of 10 Hz, i.e. 10 nominal impacts per second. In terms of the frequency limitation, the rig was found to operate efficiently in a frequency range of 2-10 Hz as mentioned by Bruce [58], as was confirmed later by using the load cell to measure the impact force during impact (see Section 3.3.2).

Based on the work of Slatter [40], the spring that exhibited the highest wear scar diameter throughout those experimental works and for this reason selected for this work, has the specifications shown in Table 3.3.

Table 3.3 Spring specifications used in impact hammering wear rig

Outside diameter (mm)	Free length (mm)	Solid length (mm)	Wire diameter (mm)	Stiffness (N/mm)
20.00	28	16.40	2.80	29.25

## 3.2 Theoretical Characterisation of Impact Wear Test Apparatus

The theoretical performance of the cam can be derived and calculated based on the cam data profile when the rig is working at 600 r.p.m (10Hz) and is described in Figure 3.3.

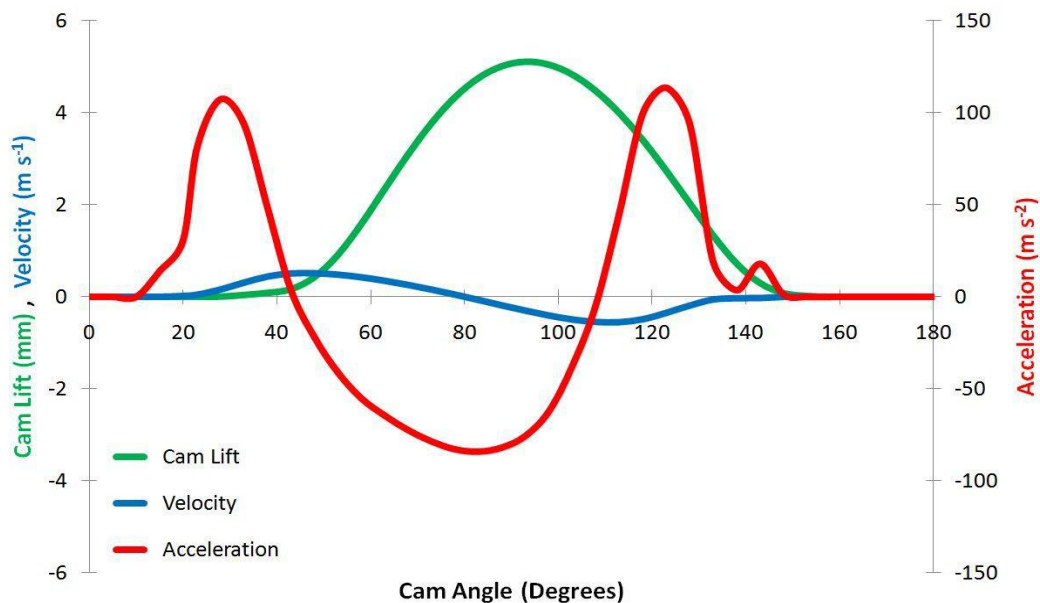


Figure 3.3 The designed correlation between cam lift, cam velocity and cam acceleration relative to cam angle at 10Hz extracted from [40]

For the analytical calculation of the impact, the following assumptions should be considered:

1. The arm and its components, excluding the spring, should be perfectly stiff so any deflections or vibrations can be neglected. In reality there will be some deflection of the arm and striker, especially at impact with the specimen, which may produce multiple rebounds per rotation instead of a single strike. This was previously reported by Slatter [40] using data from a high speed camera.
2. The cam stays in contact with the arm during the rotation of the arm, the inertia of both arm and striker is neglected. In reality, the inertia will cause the arm to temporarily separate from the cam when the cam profile starts to fall and the spring is no longer able to maintain the contact between them.
3. The cam profile remains the same and no change occurs in the profile due to impact (no wear in the cam); in reality, during use the cam profile will undergo a few changes due to repetitive impact wear between cam and arm.

In order to measure the theoretical value of striker velocity/acceleration, the angular velocity of the silver steel arm is assumed to be constant through its length, based on which the following correlation can be established:

$$v_s = v_c \left( \frac{L_s}{L_c} \right) \quad 3.1$$

where:

$v_s$  is the striker velocity,  $v_c$  is the cam velocity,  $L_s$  is the distance between the arm pivot and the point where the striker acts on the specimen (see Figure 3.1) and  $L_c$  is the distance between the arm pivot and the centre of the cam base (see Figure 3.1).

Then,

$$K.E._s = \frac{1}{2} M_{eff} v_s^2 \quad 3.2$$

where:

$K.E._s$  is the kinetic energy of the striker,  $M_{eff}$  is the effective mass of striker calculated by Equation 3.3.

To calculate the effective mass theoretically, moments were taken around the pivot and the effective mass was calculated using Equation 3.3.

$$M_{eff} = \frac{M_1 * d_1 + M * d_2}{d_2} \quad 3.3$$

where:

$M_{eff}$  is the effective mass,  $M_1$  is the mass of the silver steel arm,  $M_2$  is the mass of striker holder,  $d_1$  is the distance from the centre of the arm to the pivot point,  $d_2$  is the distance from the centre of the striker holder to the pivot point.

The effective mass was found to have a value of 1.19 kg which is very similar to the effective mass calculated previously by Slatter 1.1 kg [40], the rig has designed by Slatter in such a way that different striker holders have the same mass irrespective of their angle.

Also, based on Equation 3.1, a similar correlation can be used to calculate theoretically the maximum height that the striker arm reaches before impact and has a value of 9 mm based on the maximum height of the cam lift and arm before impact (5 mm) as shown in Figure 3.3.

Equation 3.1 is used to calculate the average velocity of the striker just before the impact, based on the 2 mm clearance between the cam and arm running at 10 Hz, the theoretical value of impact velocity is 0.51 m/s as described by Slatter [40] and shown in Figure 3.4.

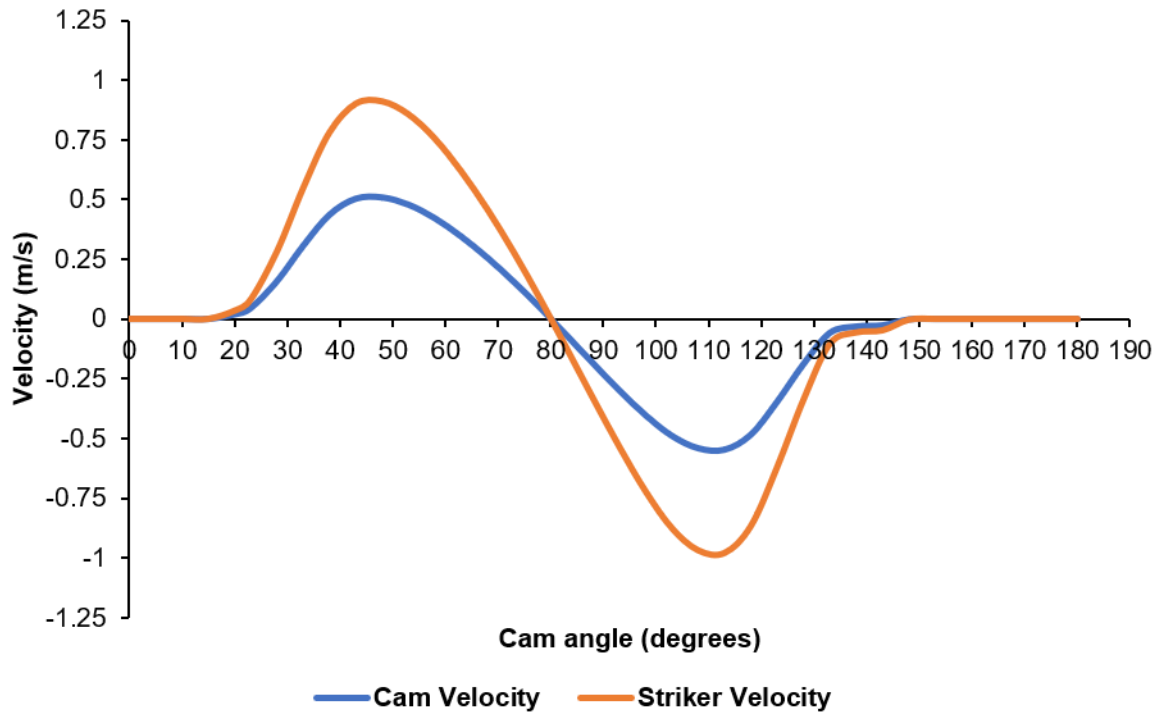


Figure 3.4 Correlation between the velocity of the cam and striker vs the cam angle

Also, it is possible to plot a theoretical relationship between the velocity of impact and the frequency of the rig based on the cam data profile and the results shown in Figure 3.5 were obtained by using the same Equation 3.1 to calculate the striker velocity based on the cam velocity that varies with each frequency. A high-speed camera could be used in future works to validate the theoretical results with different frequencies.

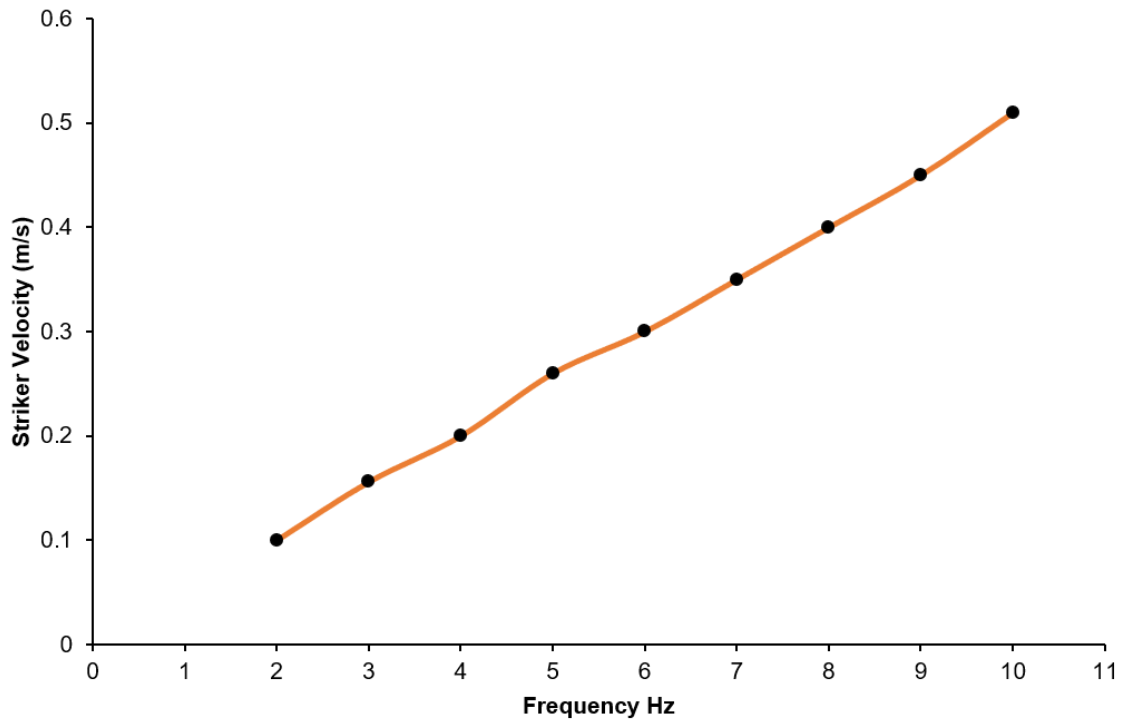


Figure 3.5 Correlation between the theoretical velocity of impact and rig frequency

### 3.3 Experimental Characterisation of Impact Wear Test Apparatus

In order to compare the experimental with the theoretical results, a high-speed camera was used, although it was unlikely that the rig would behave exactly as the theoretical one due to the assumptions listed in Section 3.2.

#### 3.3.1 High Speed Analysis

A high-speed Phantom v210 camera was used to record the actual performance of the test rig in operation. The test parameters were kept constant at 10 Hz, with cam/arm clearance of 2 mm and a spring stiffness of (29.25 N/mm). A flat aluminum alloy block, without a specimen holder, was used to enable the camera to record data on the impact zone clearly without any obstruction and to capture large and obvious wear scars for easy measurement.

Comparable data were recorded for the series of normal and compound impacts and were then analysed using motion-tracking software PC 3.1.

For measurement purposes a defined length (sacrificial plate of 0.007 m) was first calibrated as shown in Figure 3.6 and then the origin was set at the bottom of the striker ball and the options (distance, speed, two points) were activated to measure the distance and impact velocity directly.

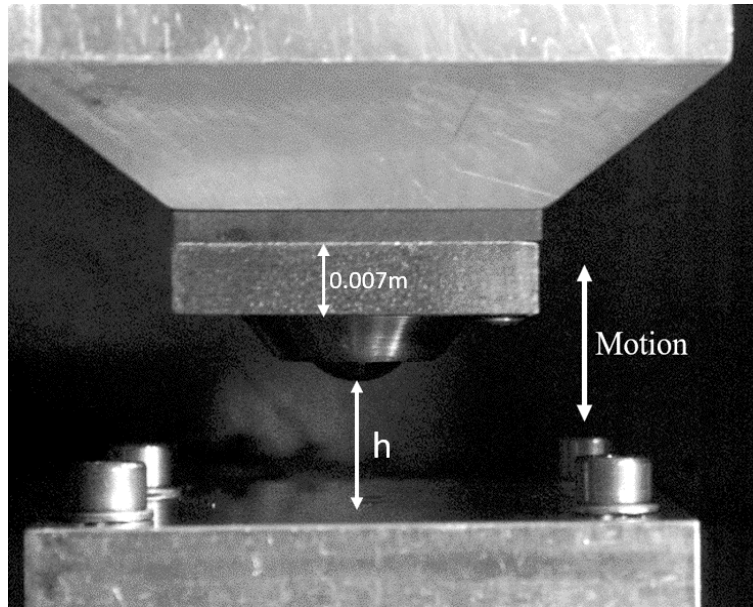


Figure 3.6 High speed camera motion

An average of eight readings were taken under both normal and compound impact from the recorded data and since the experimental differences between normal and compound impact were very small. The averages of these readings were taken for displacement, impact velocity and impact energy are 10 mm, 0.62 m/s and 0.228 J respectively.

As expected, the dynamic response of the system was slightly different from the theoretical response. The velocity of the striker just before impact, taken from the designed data, was 0.51 m/s, while the experimental result, measured by high-speed camera, was 0.62 m/s. The experimental impact velocity value was slightly higher than measured previously by Slatter [40] (0.45 m/s). Which could be explained by the fact that a higher spring stiffness (29.25 N/mm) was used during impact to achieve a larger wear scar compared to the spring with stiffness of (9.48 N/mm) used previously by Slatter.

Within each impact, the high-speed camera was able to capture four rebounds per each cam rotation before the cam lifted the arm again, but since the specimen and striker ball were very close to each other it was difficult to read the fourth rebound. Therefore, a load cell was used to detect the fourth rebound. Table 3.4 shows the mean of six readings for the displacement and rebound velocity ( $V_r$ ) values per each cycle.

Table 3.4 The mean displacement and velocity values per each impact cycle measured by high speed camera

Rebound No	Mean displacement (mm)	Standard Deviation $\sigma$ (STD)	Mean Rebound Velocity ( $V_r$ ) (m/s)	Standard Deviation $\sigma$ (STD)	Mean Rebound Energy ( $E_r$ ) (J)
1	3.68	0.85	0.288	0.052	0.049
2	2.1	0.66	0.195	0.055	0.022
3	0.7	0.057	0.115	0.013	0.0078

### 3.3.2 Impact Force Analysis

The dynamic response of the striker was characterised by using a pancake type load cell placed beneath the specimen to measure the impact force during repetitive normal impact at room temperature. The selected load cell could measure the load within the range (5-5000) N which covered the expected required range for the experimental work and the signal is acquired by digital card with sampling frequency of 50 KHz. The high value of sampling frequency ensuring that the impact force is measured correctly during the impact.

Impact force calculation is crucial for the following reasons:

1. To identify the impact force value and then calculate the surface and subsurface stresses during impact by using the Hertzian equations for both surface and subsurface by means of a MATLAB script.
2. Through identifying the stresses, the nature of contact could be detected (elastic contact, elastic – plastic or fully plastic), which would be helpful in determining whether the number of cycles during the tests starts from the elastic region or from the plastic region.
3. To detect the actual number of cycles during impact at 10 Hz.
4. To measure not only the impact force but also the force at rebounds
5. To calculate the impact force value at different frequencies, from (2-10) Hz and then predict it for other values, by detecting the impact force at different frequencies. Further work could be done to study the effect of different impact forces during impact under certain numbers of cycles.

The load cell was provided by Procter and Chester Measurement (PCM) along with the calibration certification.

Full records of impact force signals of duration 10 sec were regularly collected during the test with sampling frequency of 4.8 kHz which was sufficient to capture the impact and rebounds occurring during impact, as shown in Figure 3.7 and Figure 3.8.

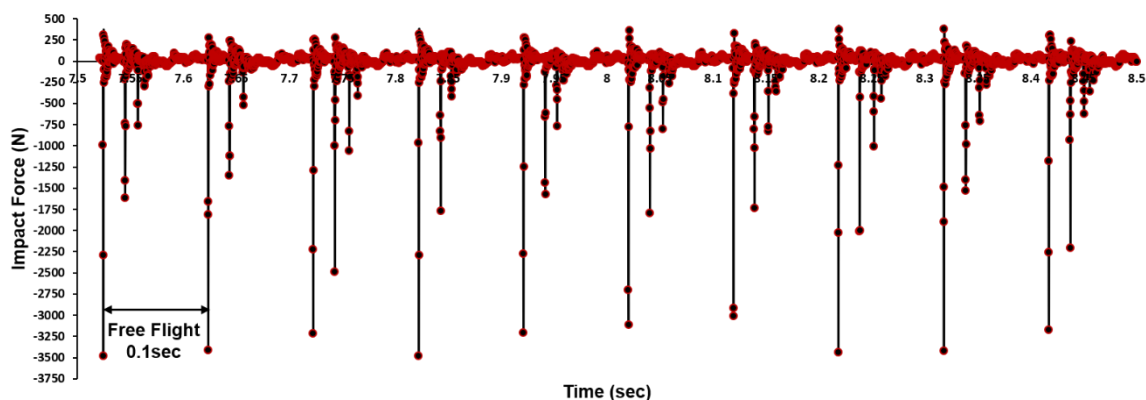


Figure 3.7 Impact force data for a single nominal impact in an apparatus operating for 1s

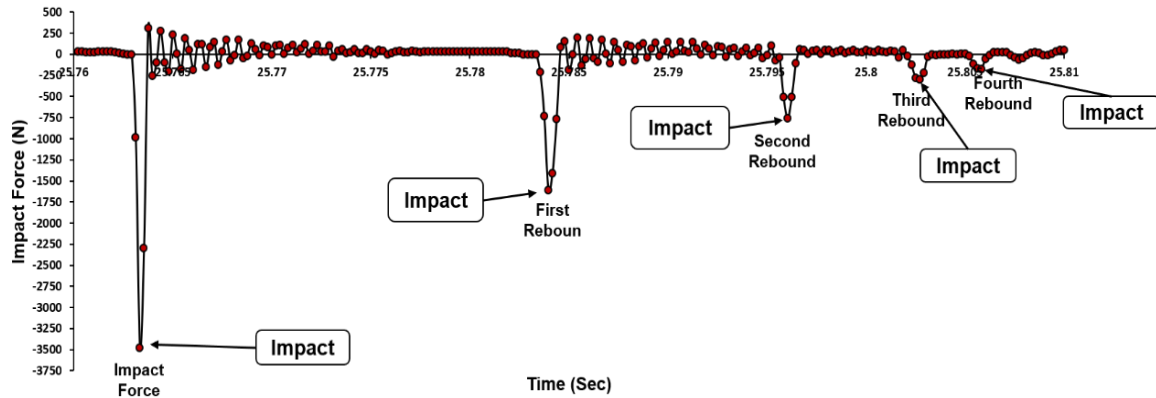


Figure 3.8 Impact force data for 0.1s showing four rebounds recorded for rig operating at 10Hz

Figure 3.7 shows the typical dataset of 10 cycles for every second from 7.5-8.5 sec which verified the nominal operating frequency of the rig. The mean peak value for impact force is 3476 N with standard deviation of 8.8, while the four rebounds value as shown in Figure 3.8 are 1612, 760, 298, 170 N respectively which supported the previous high-speed camera results.

The impact force (3476 N) is the resultant of effective mass (1.19kg) multiply by the acceleration of impact ( $F = M_{eff} \times a$ ), this leads to an acceleration value of ( $2921 \text{ m} / \text{s}^2$ ).

The experimental value of impact force measured by the load cell was verified by using an impact force equation described by Stronge in his “Impact Mechanics book” [59] and has the following form:

$$F = 1.73 k_s^{\frac{2}{5}} \times K. E. s^{\frac{3}{5}} \quad 3.4$$

where  $k_s$  is the stiffness of non-conforming spherical contact and has a value of  $1.29 \times 10^9$ ,  $K. E. s$  is the kinetic energy of the striker.

Using this equation led to an impact force value of 3157 N, this value is very close to the measured one by the load cell (3476 N) with an percentage error of (9.1%).

Regarding the impact force measurements under different frequencies, rig frequency can be modified through the inverter, with the rig, as mentioned before, found to work efficiently in a range of 2-10 Hz and also verified by the load cell tests. Therefore, the load cell was used to measure the impact force under different frequencies. The values of impact force from 2-10 Hz were measured experimentally on AISI 304 specimens and the mean peak value from each frequency test was taken as shown in Figure 3.9.

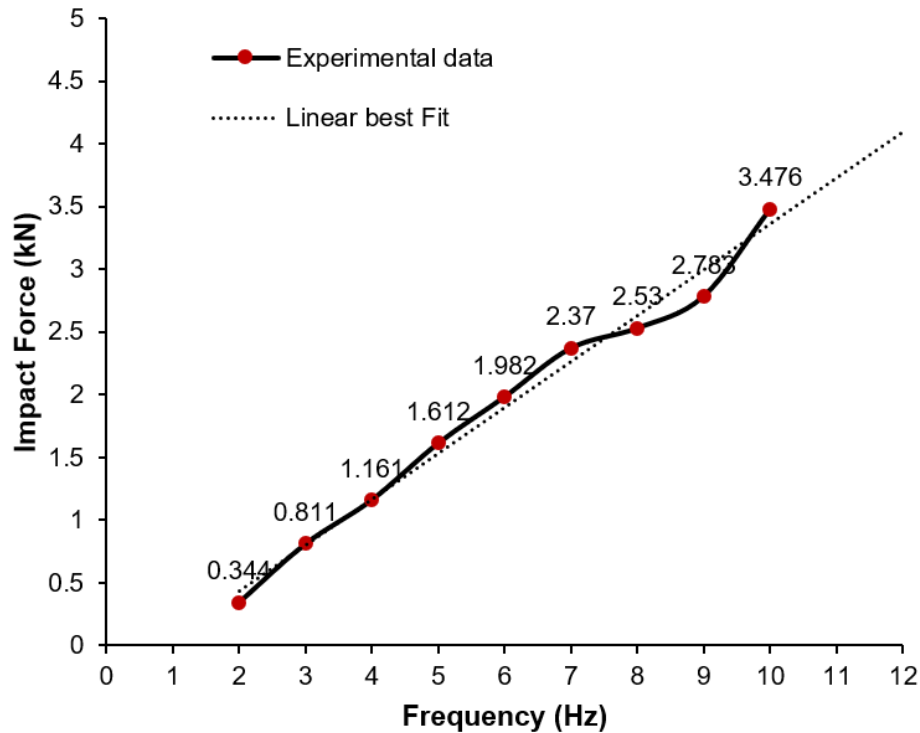


Figure 3.9 Impact force values at different frequencies

Figure 3.9 shows not only the impact force value at different frequencies but also the predictive values (linear best fit) of these frequencies; the difference in error values between the experimental and predictive results varies from 0.2 % (at 3 Hz) to 21 % (at 9 Hz).

All tests under different frequencies show the exact number of cycles per second; the example at 3 Hz frequency shown in Figure 3.10 confirms the stability of the rig within this range.

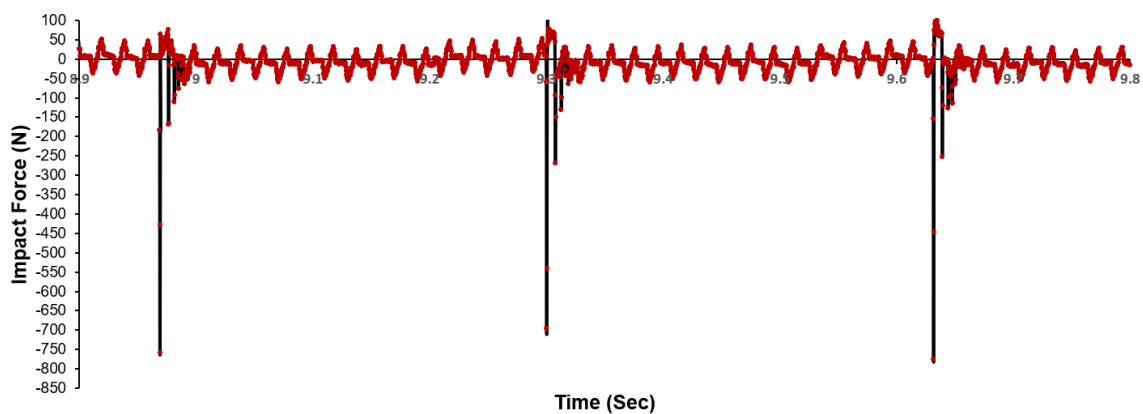


Figure 3.10 Impact force for 1 sec at 3 Hz

### 3.4 Bulk Hardness

Hardness was measured for all specimens during the experimental work using the Vickers hardness test. First, using a Vickers testing machine set at 20 kgf, this load presents the best correlation between the indentation size (diamond shape) and the hardness number. At least 10 readings were taken for each specimen, with five readings obtained from each side to minimise the experimental error, and then the average of these readings was used.

The hardness measurements were taken from different places, but keeping away from the expected location of the wear scar in order to avoid damaging (plastic deformation) in that region.

The experimental results for Vickers testing machine are reported in Table 3.5.

Table 3.5 Hardness measurements of tested materials

Material	Vickers Hardness $HV_{20kgf}$	Standard Deviation $\sigma$ (STD)	Standard Error ( $\sigma_{\bar{x}}$ )	% Standard Error
AISI 304	190	1.84	0.3	0.16
AISI 316	180	0.77	0.388	0.215
EN8	213	2.56	0.64	0.29
EN-GJS-600-3	238	6.9	3.45	1.46
AlSi9Cu3	124	1.73	0.866	0.69
PB102	127	2.5	1.49	1.17

Table 3.5 shows the standard deviation and the standard error results of Vickers hardness for all tested materials, standard deviation is a statistic that measures the dispersion of a dataset relative to its mean and the small value of standard deviation shown in the table indicates that the hardness reading spread closely to the mean.

The standard error of the mean measures how far the mean of the data is likely to be from the true population mean and lower standard error of the mean is the more likely it is that the calculated mean is close to the actual mean. The standard error shown in Table 3.5 for all materials is very small with the highest value of 1.46 % for phosphor bronze which means that these measurements have excellent repeatability and the hardness is distributed uniformly on specimen surface and between different specimens.

Vickers microhardness measurements were also taken for the tested materials by using an automated hardness tester (Struers Durascan) with a load of 0.1 kgf to detect the possible increase in hardness resulting from the impact process after different cycles and angles, additionally to measure the depth of the work hardening layer. This load was chosen as the smallest load that still present reasonable reading close to the one measured by Vickers testing machine and shows obvious indentation as shown in Figure 3.11. Below this value of 0.1 kgf, the indentation size is considered very small and the hardness measurement is too high compare with the bulk material and this increasing the deviation of the results and eventually the error of these measurements become too high.

The microhardness measurements of the bulk materials were taken away from the impacted region (about 5 mm) for polished but not etched specimens according to ASTM E384 [60] as a matrix of 36 points (6×6) in order to establish a guideline for the bulk hardness of each material, with Figure 3.11 showing an example for AISI 316. The experimental results for microhardness measurements are reported in Table 3.6 for bulk materials.

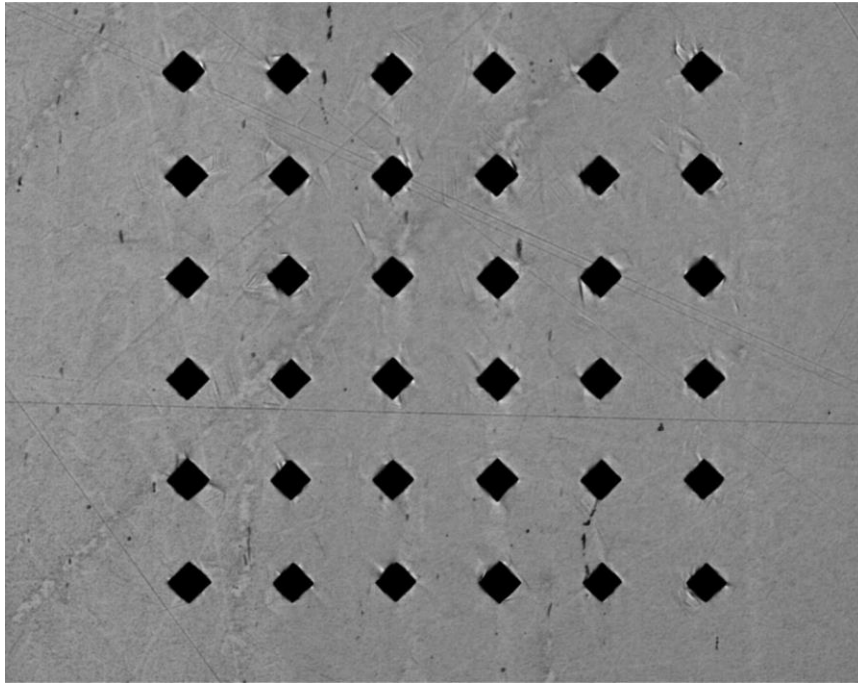


Figure 3.11 Microhardness indentations of AISI 316 specimen as a matrix of 36 points below the impacted region (about 5 mm from the centre of the wear scar)

Table 3.6 Microhardness measurements of tested materials

Material	Microhardness HV <sub>0.1kgf</sub>	Standard Deviation $\sigma$ (STD)	Standard Error ( $\sigma_{\bar{x}}$ )	% Standard Error
AISI 304	185	5.09	0.93	0.5
AISI 316	188	3.25	1.88	0.99
EN8	205	11	2.59	1.26
EN-GJS-600-3	258	3	1	0.422
AISI9Cu3	107	5.2	1.17	1.09
PB102	100	7.7	2.07	2.11

The microhardness measurements shown in Table 3.6 is very similar to the one measured by Vickers testing machine in Table 3.5, the results have good standard deviation and excellent standard error which does not exceed 2 % and indicates very good repeatability.

### 3.5 Hertzian Contact Stresses

Theoretically, when two non-conforming solid bodies are brought into contact under a force, they touch initially at a single point or along a line and under the action of the load they are deformed in the vicinity of their point of first contact so that they touch over an area which is finite small compared with the dimensions of the two bodies [61].

Three dimensional stresses are developed as contact stresses, which is important in calculating strength for many applications like bearings, gears and cam mechanisms, while typical failures of these applications are seen as cracks, pits and eventually debris removed from material. The first satisfactory analysis of the stresses at the contact of two elastic solids was based on Hertzian theory.

Before calculating the surface and subsurface stresses, the following assumptions were made:

1. The strain is small within the elastic limit ( $a \ll R_1$ ).
2. The surfaces are non-conforming ( $a \ll R_1$ ).
3. The surfaces in contact are frictionless, which means that the shear force is considered to be zero.
4. The contacting bodies are at rest and in equilibrium.
5. Contact load is caused by the load which is normal to the contact, which means no tangential forces acting between the two surfaces.
6. Non-adhesive elastic contact.

### 3.5.1 Surface Stress Calculation

In the present work the contact between sphere and flat specimen is point contact and according to Hertz theory the pressure distribution in the contact region is elliptical, with maximum value in the centre of the two contacting bodies and then falling to zero outside the contact area [61, 62].

For the sphere in contact with the flat specimen, the radius of the specimen is infinite and the reduced or relative radius of curvature  $R^*$  and the reduced modulus of elasticity  $E^*$  are shown in Equations 3.5 and 3.6.

$$\frac{1}{R^*} = \frac{1}{R_1} + \frac{1}{R_2} \quad 3.5$$

$$\frac{1}{E^*} = \frac{1-\nu_1^2}{E_1} + \frac{1-\nu_2^2}{E_2} \quad 3.6$$

where  $\nu_1$  and  $\nu_2$  are the Poisson's ratio,  $E_1$  and  $E_2$  are the Young's modulus for the striker and the specimen, respectively.

According to Hertz theory the contact pressure and stress distribution on the surface are shown in the following Equations [61, 62]:

$$a = \sqrt[3]{\frac{3FR}{4E^*}} \quad 3.7$$

$$P(r) = P_o * \sqrt{1 - \frac{r^2}{a^2}} \quad 3.8$$

$$P_o = \frac{3F}{2\pi a^2} \quad 3.9$$

$$P_m = \frac{F}{\pi a^2} \quad 3.10$$

$$\frac{\sigma_r}{P_o} = \left(\frac{1-2\nu}{3}\right) * \left(\frac{a^2}{r^2}\right) * \left\{1 - \left(1 - \frac{r^2}{a^2}\right)^{3/2}\right\} - \left(1 - \frac{r^2}{a^2}\right)^{1/2} \quad 3.11$$

$$\frac{\sigma_\theta}{P_o} = - \left(\frac{1-2\nu}{3}\right) * \left(\frac{a^2}{r^2}\right) * \left\{1 - \left(1 - \frac{r^2}{a^2}\right)^{3/2}\right\} - 2\nu \left(1 - \frac{r^2}{a^2}\right)^{1/2} \quad 3.12$$

$$\frac{\sigma_z}{P_o} = -\sqrt{1 - \frac{r^2}{a^2}} \quad 3.13$$

where:

$a$  is the radius of the elastic contact area,  $P(r)$  is the surface pressure distribution,  $P_o$  is the maximum contact pressure,  $P_m$  is the mean contact pressure,  $\sigma_r$ ,  $\sigma_\theta$ ,  $\sigma_z$  are the stresses on the surface and subsurface in polar coordinate.

### 3.5.2 Subsurface Stress Calculation

A study has shown that subsurface damage (crack initiation and growth) occurs more frequently in comparison to contact surface damage [11].

Fatigue can be distinguished into subsurface initiated and surface initiated. The maximum range of principal shear stress was selected as the critical stress controlling subsurface contact fatigue damage [63], while the normal principal stresses can play a critical role in the propagation of the crack.

The maximum subsurface shear stress has a value of  $(0.31 P_o)$  at a depth of  $(0.48 a)$  beneath the Z axis, which exceeds the shear stress at the origin  $(0.1 P_o)$  and also the shear stress on the surface at the edge of the contact  $(0.13 P_o)$ , which would lead to expectation that plastic yielding would initiate beneath the surface [41, 61].

In order to calculate the principal stresses down the Z axis, the following relationship is used.

$$\frac{\sigma_r}{P_o} = -(1+\nu) \left\{ 1 - \left(\frac{z}{a}\right) \tan^{-1} \left(\frac{a}{z}\right) + \frac{1}{2} \left(1 + \frac{z^2}{a^2}\right)^{-1} \right\} \quad 3.14$$

$$\frac{\sigma_\theta}{P_o} = -(1+\nu) \left\{ 1 - \left(\frac{z}{a}\right) \tan^{-1} \left(\frac{a}{z}\right) + \frac{1}{2} \left(1 + \frac{z^2}{a^2}\right)^{-1} \right\} \quad 3.15$$

$$\frac{\sigma_z}{P_o} = -\left(1 + \frac{z^2}{a^2}\right)^{-1} \quad 3.16$$

The maximum subsurface shear stress  $\tau_{max}$  was not the only critical stress controlling contact fatigue damage; Von Mises stresses  $\sigma_v$  were also involved and can be calculated according to the following equation:

$$\sigma_v = \sqrt{\frac{(\sigma_1 - \sigma_2)^2 + (\sigma_2 - \sigma_3)^2 + (\sigma_3 - \sigma_1)^2}{2}} \quad 3.17$$

where:

$\sigma_1$ ,  $\sigma_2$ ,  $\sigma_3$  are the principal stresses

In the case of a circular contact, like that of a ball on a flat surface, the stresses in X and Y directions are called  $\sigma_r$  and  $\sigma_\theta$  (stress in radial direction) and because of symmetry  $\sigma_r = \sigma_\theta$ , so the Von Mises will be:

$$\sigma_v = \sqrt{\frac{(\sigma_r - \sigma_\theta)^2 + (\sigma_\theta - \sigma_z)^2 + (\sigma_z - \sigma_r)^2}{2}} \quad 3.18$$

$$\sigma_v = \sqrt{\frac{(\sigma_r - \sigma_z)^2 + (\sigma_z - \sigma_r)^2}{2}} \quad 3.19$$

where  $\sigma_r$ ,  $\sigma_\theta$  and  $\sigma_z$  are the stresses at specific depth of  $(0.48a)$  beneath the Z axis.

### 3.5.3 Stresses Analysis Results

The two main parameters controlling the impact wear on the material surface are impact energy and contact stresses caused by the impact force which is dynamic in nature and varies continuously with impact area that varies with the deformation of the surface of a specimen [61].

Based on the measured value of impact force (3476 N), a full analysis for surface and subsurface stresses was carried out by using the previous Hertzian equations throughout MATLAB coding. The results of normal impact as an example are shown in Figure 3.12 for AISI 304 and explained in Table 3.7 for all tested materials. It is important to mention that calculations in Section 3.5.1 and Section 3.5.2 are accomplished using the Hertzian equations in the elastic region and therefore, it is not valid for the plastic regime.

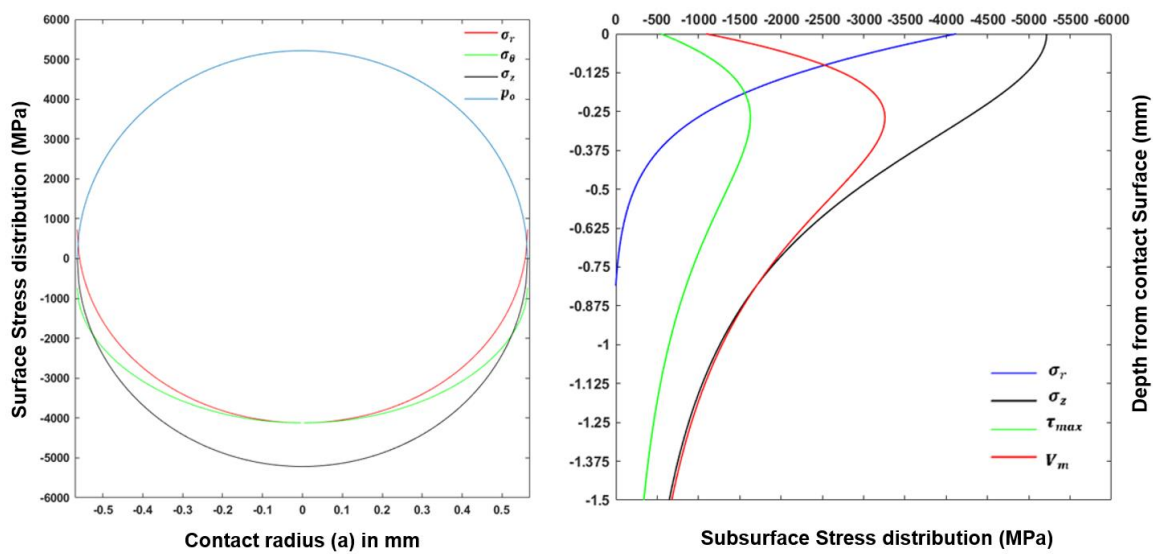


Figure 3.12 Surface and subsurface stresses for AISI 304 under normal impact

Table 3.7 Summary of stresses for tested materials under normal impact

Materials	$\sigma_y$ MPa	$\sigma_u$ MPa	$p_o$ MPa	$p_m$ MPa	$p_m/\sigma_y$	$\sigma_z$ MPa	$\sigma_r$ MPa	$\sigma_\theta$ MPa	$\tau_{max}$ MPa	$V_m$ MPa	Depth of max subsurface stresses from surface mm
AISI 304	270	581	5215	3476	12.9	5215	4119	4119	1628	3257	0.27
AISI 316	332	630	5215	3476	10.4	5215	4119	4119	1628	3257	0.27
EN8	628	739	5308	3538	5.6	5308	4193	4193	1658	3315	0.267
EN-GJS-600-3	370	600	5036	3357	9	5036	3979	3979	1573	3145	0.27
AlSi9Cu3	165	330	3446	2297	14	3446	2722	2722	1076	2152	0.33
PB102	380	460	4444	2963	7.8	4444	3511	3511	1388	2776	0.29

Materials under point contact are considered to be in the elastic region since the mean contact pressure  $P_m$  is less than  $1.1 \sigma_y$  [53] or  $P_o$  is less than  $1.6 \sigma_y$  [61, 62]; at this ratio the material starts to be in elastic-plastic contact and the limit between the elastic-plastic region and fully plastic region can be explained by  $1.1 < P_m/\sigma_y < 2.8$ ; when the ratio of  $P_m/\sigma_y$  exceeds 2.8, the material is considered to be in the fully plastic region [61, 62].

Results revealed that the ratio of  $(P_m/\sigma_y)$  varies from (5.6-16.8); therefore, the nature of the contact could be considered as plastic.

It is important to mention that with compound impact ( $60^\circ$  and  $45^\circ$ ), the normal component decreased theoretically from 3476 N to 3010 N at impact angle  $60^\circ$  and to 2457 N at impact angle  $45^\circ$ ; yet both values that were used to calculate the maximum and mean contact pressure by Hertzian equations show that the nature of contact was plastic from the beginning of impacts ( $P_m/\sigma_y$  exceeds 2.8), as shown in Table 3.8 for impact angle  $60^\circ$  and Table 3.9 for impact angle  $45^\circ$ .

Table 3.8 Summary of stresses for tested materials with impact angle  $60^\circ$  and normal impact force 3010 N

Materials	$\sigma_y$ MPa	$\sigma_u$ MPa	$p_o$ MPa	$p_m$ MPa	$p_m/\sigma_y$
AISI 304	270	581	4970	3313	12
AISI 316	<b>332</b>	<b>630</b>	4970	3313	9.9
EN8	628	739	5059	3373	5.3
EN-GJS-600-3	370	600	4800	3200	8.6
AlSi9Cu3	165	330	3285	2190	13
PB102	380	460	4236	2824	7.4

Table 3.9 Summary of stresses for tested materials with impact angle  $45^\circ$  and normal impact force 2457 N

Materials	$\sigma_y$ MPa	$\sigma_u$ MPa	$p_o$ MPa	$p_m$ MPa	$p_m/\sigma_y$
AISI 304	270	581	4645	3097	11.4
AISI 316	332	630	4645	3097	9.3
EN8	628	739	4728	3152	5
EN-GJS-600-3	370	600	4486	2991	8
AlSi9Cu3	165	330	3070	2046	12.4
PB102	380	460	3959	2639	6.9

The results on the nature of contact during impact were very helpful in revealing that from the beginning all the cycles were already in the plastic region.

The current results of Hertzian stresses clearly represent an idealised analysis and further insight into the contact could be achieved by means of a finite element analysis which would produce a more accurate representation of the plasticity in each of the materials used.

The MATLAB coding used to implement the Equations for both surface and subsurface is shown in Appendix B.

### 3.6 Zero Wear Methodology

Zero wear volume can be defined as geometry change due to material compression that occurs before other mechanisms that cause change through actual material loss which initiated during repetitive impact.

Both mass scales and 3D non-contact profilometer are employed in determining the zero wear volume. Which has not been defined previously as a part of overall volume loss for wear of materials under repetitive impacts.

It should be noted that the following terms are used in the next Chapters (4, 5, 6, 7):

- *Wear Volume* ( $V_w$ ) – volume of material removed from contact zone and detached from the material as wear debris and measured by mass scale and then converted to wear volume through material measured density.
- *Plastic Flow Volume* ( $V_{pf}$ ) – material removed plastically out of the contact zone, and therefore now not part of the material directly supporting a load, as a result of impact. Usually observed as newly formed ridges of material around the circumference of any resulting wear scar and not detected by mass loss methods but by direct measurement by 3D non-contact profilometry.
- *Zero Wear Volume* ( $V_{zw}$ ) – the volume previously occupied by material that appears to have been deformed by impact, causing its surface to be at a different point in space, but remains in the contact zone.
- *Total Volume Loss* ( $V_t$ ) – the sum of these volumes representing the wear volume, plastic flow volume, and zero wear volume previously resided, detected by direct measurement by 3D non-contact profilometry.

The total volume loss was calculated directly from the 3D non-contact profilometer dataset. The zero wear volume was then calculated from 3.21 based on the following assumption of Equation 3.20 as illustrated in Figure 3.13.

$$\text{Total Volume Loss } (V_t) = \text{Plastic Flow Volume } (V_{pf}) + \text{Wear Volume } (V_w) + \text{Zero} \quad 3.20$$

$$\text{Wear Volume } (V_{zw})$$

$$V_{zw} = V_t - V_{pf} - V_w \quad 3.21$$

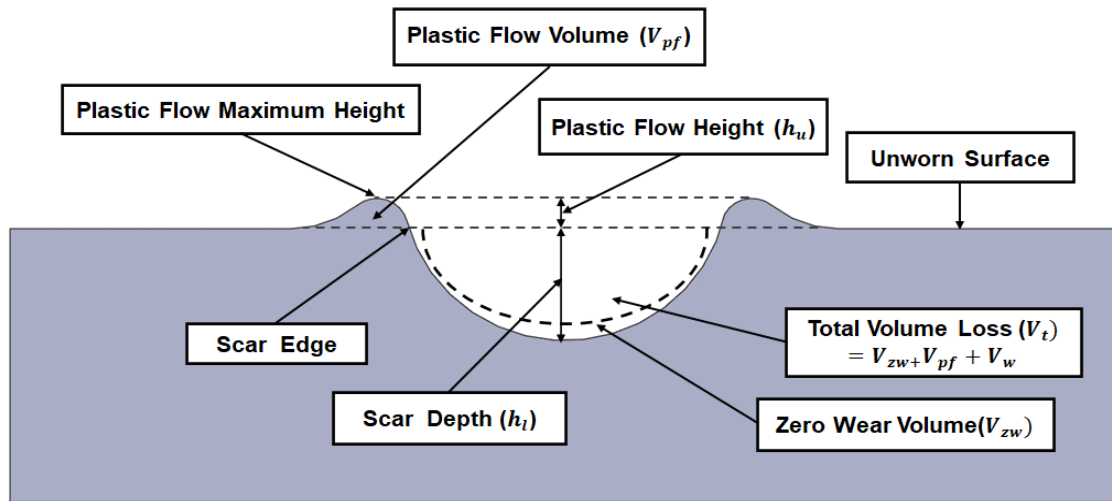


Figure 3.13 Schematic illustrating the total volume loss during impact

### 3.7 Sample Preparation

Sample preparation was carried out during this work in order to investigate the subsurface microstructure damage of tested materials mentioned in Table 3.1.

#### 3.7.1 Sectioning

The Secotom 50 is a high-performance cut-off machine that can be used for cutting a wide range of materials.

The first step of sample preparation was to section the samples into small rectangular pieces using abrasive cutting discs by Secotom 50 with a very slow feed rate of (0.05) mm/sec in order to avoid addition of any further deformation to the sample, especially in the impact region, and to ensure the least amount of heating or changes in the sectioned samples.

Each of the specimens, which were of disc shape, were cut from four directions to obtain the rectangular piece of the impacted region and this was taken away from the centre of the wear scar in order to allow further material to be removed during the grinding process.

The sectioning direction was parallel to the grinding orientation for all samples, as shown in Figure 3.14, since it was expected that the plastic flow formation would be in the direction of impact which is the same as the direction of grinding.

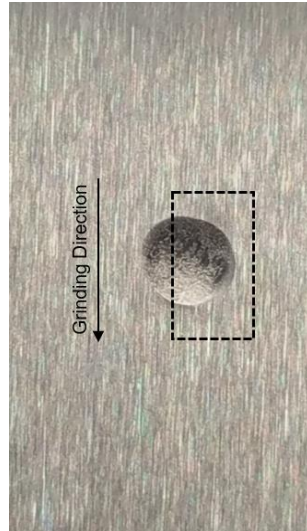


Figure 3.14 Sectioning process

### 3.7.2 Hot Mounting

The samples from the sectioning process were mounted separately in single stubs in order to prepare them for the grinding and polishing process.

Since the steel and the other tested materials would not be directly affected by the temperature and pressure experienced in the Buehler SimpliMET1000 hot mounting press. During the mounting process, specimens were heated up to a temperature of approximately 180 °C and a pressure of 250 bar for 150 seconds and then cooled for 240 seconds, before being used in the grinding and polishing processes.

The samples needed to be viewed by SEM; for this purpose, conductive graphite resin (Bakelite) was used.

### 3.7.3 Grinding and Polishing

Automatic grinding and polishing for surface finishing of all specimens was carried out using the Buehler *AutoMET* machine. The grinding and polishing processes were undertaken after hot mounting to remove any possible deformation that happened during the sectioning stage and also to produce a reflective mirror surface finish for examination by SEM and for taking micro hardness measurements.

The grinding process was carried out in four stages using silicon carbide sandpaper grit lubricated with water on the automated grinding machine. Starting with the rougher grit to remove the scratches and proceeding to the finest one where it is expected that the specimen surface will be flat and uniform without scratches on the sample. Each stage of grinding will remove the distortion from the previous stage and reduce the scratches on the surface.

After mounting and before starting the grinding process, the overall thickness of the specimen was measured by micrometer (rectangular section). Then, after the first stage of grinding, the thickness was measured again and the difference compared to the original thickness represented the thickness removed by the first grinding stage over a specific time. This measurement procedure was repeated up to the end of the fourth stage and the overall thickness removed represented the distance from the centre of the wear scar to the sectioning limit.

A few trials on deformed specimens of AISI Types 304 and 316 in addition to EN8 were carried out for this purpose. The overall thickness removed during the four stages for each of the stainless steels was about 1.1 mm, while it was approximately 0.95-1 mm for EN8.

After the final stage of the grinding was complete, the polishing process was started, which also consisted of four stages. Using diamond suspension, the polishing stages ensure that the surfaces of the specimens will be even and have a mirror like finish ready for the later microhardness examination by SEM. No removal of material was detected as a result of the polishing process.

A summary of the grinding and polishing stages and settings that were found to give a shiny reflective surface, free from scratches, is shown in Table 3.10.

Table 3.10 Grinding and polishing processes

Settings	Grinding Stages (FEPA)				Polishing Stages (FEPA)			
	Stage 1	Stage 2	Stage 3	Stage 4	Stage 1	Stage 2	Stage 3	Stage 4
<b>Grit Size</b>	#320	#500	#800	#1200	6 $\mu$ m	3 $\mu$ m	1 $\mu$ m	0.25 $\mu$ m
<b>Base Speed (r.p.m)</b>	220				150			
<b>Head Speed (r.p.m)</b>	60				60			
<b>Force (N)</b>	20	20	20	20	15	15	10	10
<b>Time (min)</b>	3	2	2	2	12	12	12	12
<b>Motor Rotation</b>	Count	Count	Count	Count	Comp	Comp	Comp	Comp

### 3.7.4 Etching

#### 3.7.4.1 Electro Etching of Stainless Steel

The etching process that produces the best results in terms of revealing the microstructure of AISI types 304 and 316, is electro etching using nitric acid (HNO<sub>3</sub>).

Electro etching of the stainless steel samples first involved immersing them in a solution of 60 % nitric acid and 40 % distilled water to reveal the grains boundary. This technique is based on work described in the paper entitled “Improved metallographic etching techniques for stainless steel and for stainless steel to carbon steel weldments” by Bell and Sonon [64].

This process was performed to reveal the grain boundaries of the stainless steel in order to detect the grain size and area before and after impact, using a standard ASTM E112 [65] on an image scanned by Nikon optical microscope.

The electro etching process was carried out by BASETech BT-305 in the materials department lab. The anode was used to hold in place the stainless steel piece located inside a dish that contained the etching solution, while the cathode was used to etch the samples through wire made from stainless steel. Polished samples of austenitic stainless steel must be immersed in the etchant solution and both the cathode and the anode must be made from stainless steel.

The process took approximately 2 min for each sample and the voltage had to be set at 1V to prevent excessive attack while immersing the sample in the etchant and then adjusted to achieve a current density of approximately 8-9 mA/cm<sup>2</sup>. Increasing this setting leads to production of a lot of over etched spots on the specimens; therefore, this setting was considered as the best option for both types of stainless steel.

The specimens were inspected during the etching time, and when the desired microstructure appeared, the specimens were first washed in water, then rinsed in ethanol, and finally dried using hot air. In the case of AISI 304, as shown in Figure 3.15, the number 8.1 appeared on OM image, based on table 4 of ASTM [E112]. This number is equivalent to an average grain diameter of  $22.5\ \mu\text{m}$  and area of  $504\ \mu\text{m}^2$  for unimpacted specimens; several trials were performed on different etched samples and the results were largely similar.

Figure 3.16 shows the number 6.9 on the OM image of AISI 316, which is equivalent to an average grain diameter of  $32\ \mu\text{m}$  and area of  $1008\ \mu\text{m}^2$  for unimpacted specimens.

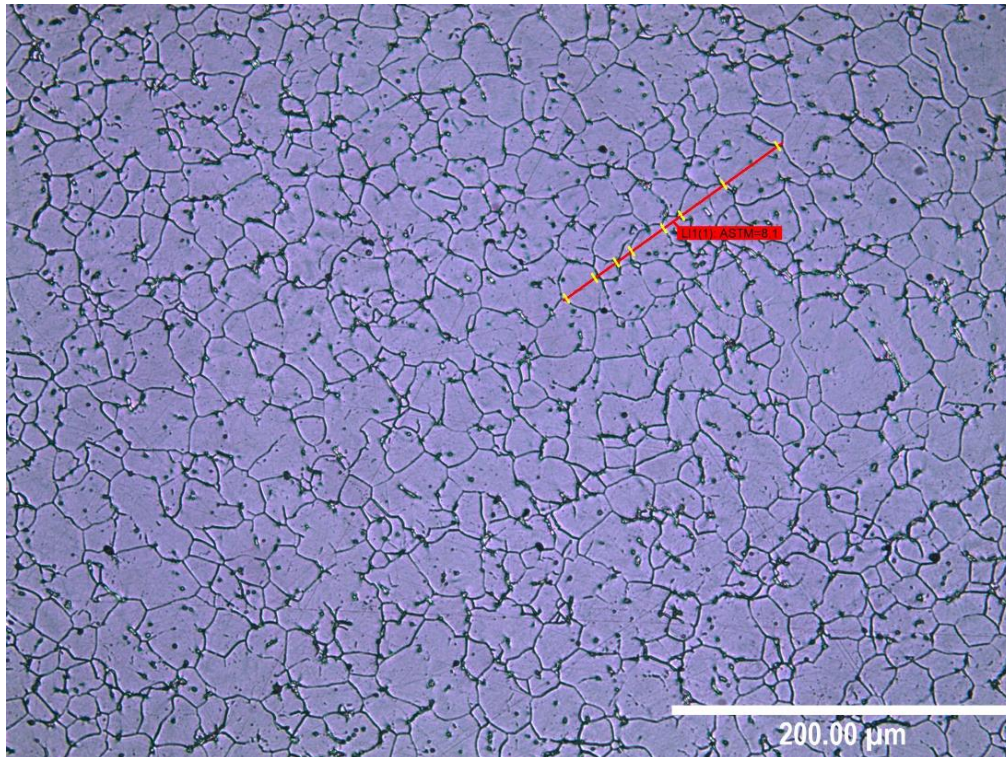


Figure 3.15 ASTM E112 for grain size of AISI 304 before impact

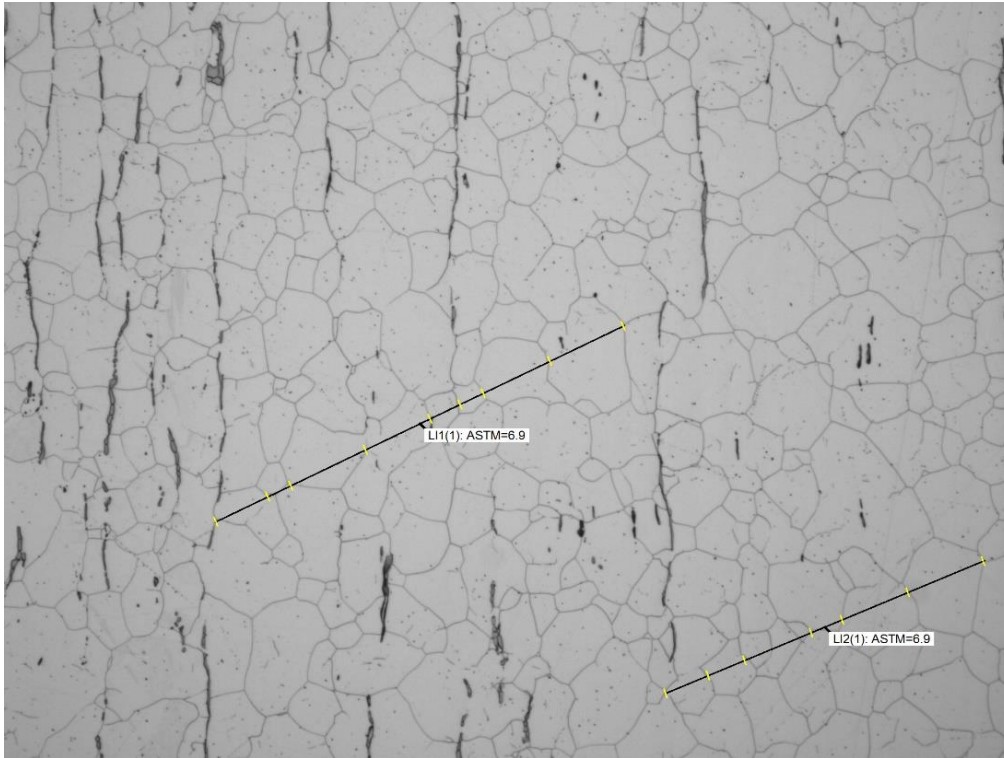


Figure 3.16 ASTM E112 for grain size of AISI 316 before impact

Chemical etching materials such as Vilella's reagent (picric acid) were used during this work according to ASTM E407-15 [66], but they failed to provide good enough results to reveal the microstructure; therefore, the electro etching method was considered the best way to reveal the microstructure of stainless steel.

#### 3.7.4.2 Chemical Etching of Carbon Steel

The most common type of chemical etching of carbon steel is 2 % nital etching which involves the use of 100 ml of industrial methylated spirits (IMS) with 2 ml nitric acid according to ASTM E407-15[66]. The polished samples of carbon steel were immersed in a dish containing the etching solution, using crucible tongs, until the preferred microstructure had developed and the surface became slightly clouded; approximately 20 sec was the time taken to reveal the structure of each specimen ( $\pm 3$  sec). Next, similar to the electro etching procedure, samples were washed in water, then rinsed in ethanol, and finally dried.

It should be noted that etching was performed only on AISI types 304 and 316 and EN8 samples, while other materials (ductile cast iron, aluminum alloy and phosphor bronze) were not etched since they were tested only for zero wear work as explained in detail in Chapter 4. Contrary to the case with the stainless steel and medium carbon steel samples, no more details were required on surface and subsurface damage to these other samples.

The microstructure of medium carbon steel before impact for both phases, pearlite (P) and ferrite ( $\alpha$ ), is shown in Figure 3.17.

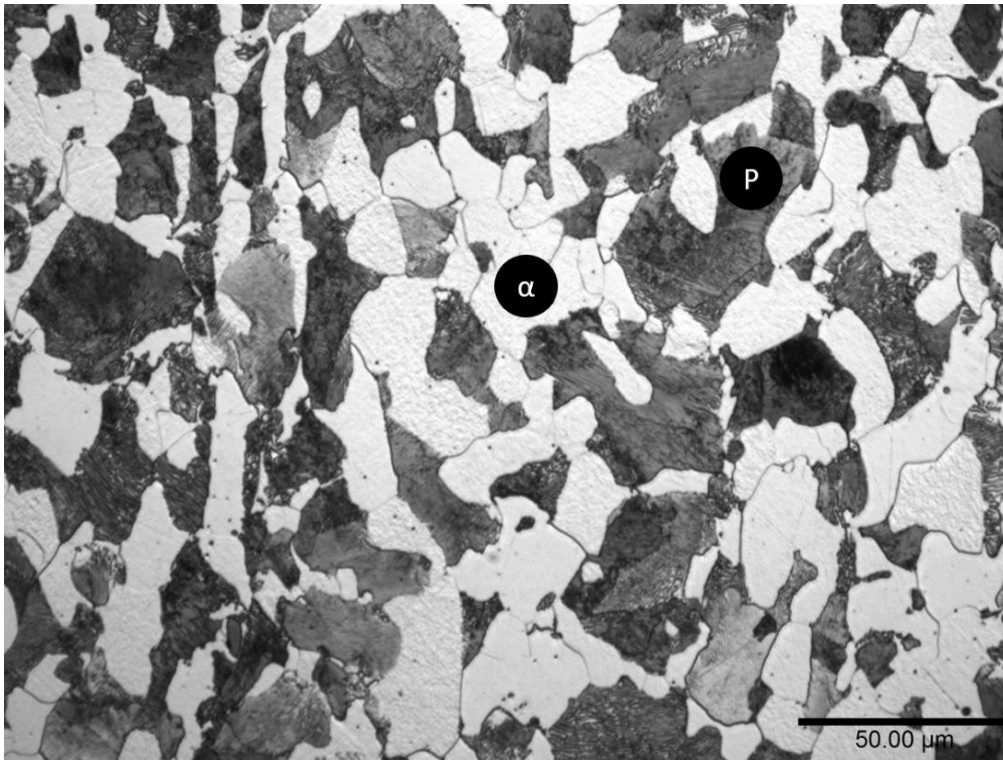


Figure 3.17 Microstructure of EN8 showing both unimpacted phases, pearlite (P) and ferrite ( $\alpha$ )

### 3.8 Wear Observation

Different techniques were used to detect the wear damage mechanisms and features on tested materials under specific impact conditions (load, angle and number of cycles) within a controlled environment (room temperature), including qualitative and quantitative measurements. The qualitative measurement included surface morphology and wear debris (optical microscopy and SEM), while the quantitative measurements included surface roughness and wear features (3D non-contact profilometer) and can be summarised as follows:

#### 3.8.1 Optical Microscopy

Zeiss and Nikon optical microscopes were both used to capture images from the specimen surface or subsurface by using lenses with magnification levels of (50-1000) X, enabling large to small details of the specimens' microstructure to be captured. The microscope was linked to a computer and controlled by a digital camera, allowing measurements to be taken easily using computer software to measure different features such as the scale bar, length of features or even to measure the grain size using ASTM E112.

#### 3.8.2 Scanning Electron Microscopy (SEM)

Surface morphology can reflect different variations which can distinguish different wear mechanisms like fatigue, adhesion and abrasion; therefore, the Hitachi tm3030 plus table model with an acceleration voltage of 15kV and two types of detectors (BSD and SE) was used to capture all the wear damage features on the surface and subsurface. However, it was unable to capture features with higher magnification (more than 3000 X), and any images below this length became blurry and unable to detect the damage features. The current results were found to be sufficient with this SEM and no further details

with higher magnifications were required. The Hitachi SEM was used at the Leonardo Tribology Centre (Sheffield).

### 3.8.3 Surface Profile Measurements

3D non-contact profilometer ( Alicona Infinite Focus SL) was used during this work to measure the surface roughness of the tested materials and to detect all the impact scar features, such as scar diameter, area, depth and volume of both the impact scar and the plastic flow formed on the ridges. Additionally, 3D images of the impact scar were taken by 3D non-contact profilometer, and since the majority of impact scars were large, the image field option was used to scan the impact scar, the number of points, while the sampling distance was not constant and varied depending on the size of the impact scar.

The 3D non-contact profilometer with objective 5 X was used to scan the wear scar on all specimens and the time taken to scan the whole wear scar was around 10 min, while the volume measurements took from (30-40) min depending on the size of the wear scar. The largest sizes of wear scar were found on the aluminum and phosphor bronze specimens and measurement took approximately 40 min, while for the other materials it took about 30 min.

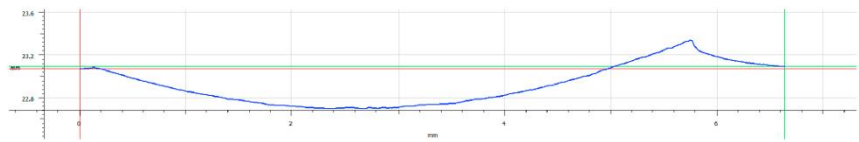
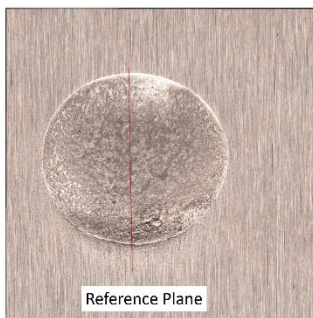
For volume measurements (Figure 3.18 (a)), a reference plane must be created first, to achieve this, three points must be selected, the first point is the reference plane point and it is outside the wear scar (typically 2-3) mm away from the edges of the wear scar. Using profile measurements method by 3D non-contact profilometer revealed that the maximum distance that the edges of the wear scar can be extruded outside the impact region above the reference plane is 1mm as shown for example in Figure 3.18 (b). Then two further points must be selected, one above the reference plane from one of the top wear scar edges and the other one below the reference plane from the other opposite bottom of the wear scar. The maximum height of the plastic flow for all the tested specimens is 770 $\mu$ m while the maximum depth of the wear scar is 572 $\mu$ m. Based on that, these two points were out of focus by 2mm to ensure that all volumes are included in the scanned region and ensure that there was no distortion of the sample outside of the impact area.

Image field measurement option was used to generate the volume for all specimens due to the large size of the wear scar, this option enables the specimen stage to move horizontally and vertically to scan the three selected point and create a 3D image as shown in Figure 3.18 (c). The original points of the 3D non-contact profilometer moved to the reference plane to get accurate measurements, both rectangular and circular scan options were used and the results are the same every time. No filters were used during this procedure and both auto exposure and autofocus options were used during this procedure.

All specimens were designed previously by Slatter [40] to have a thickness of 10 mm to ensure that no distortions or deformation occurs to the other side of the specimen and it has always a flat surface.

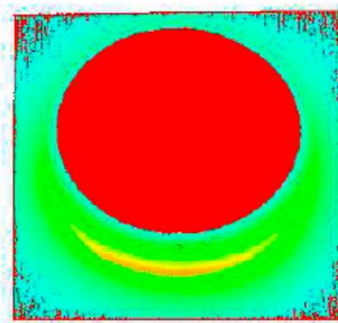
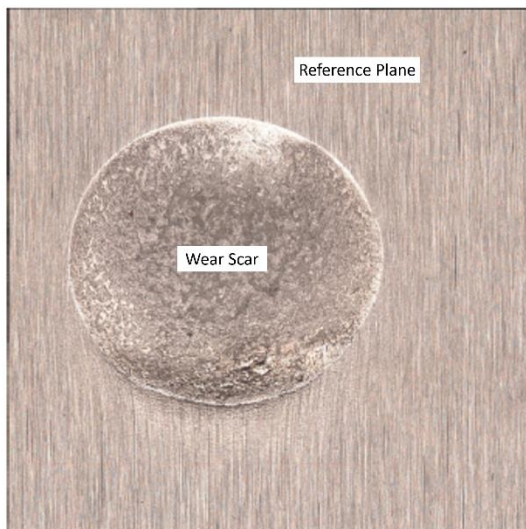


(a)



ReferencePosition	I: 6.645mm	z: 23.092mm
MeasurePosition	I: 0.000µm	z: 23.070mm
RelativeMeasurement	ΔI: -6.645mm	Δz: -21.815µm
	Angle: 180.188°	Distance: 6.645mm
Filter:	No Filter - Primary profile	

(b)



<b>Volume</b>	Reference Plane	
Above Surface:		1.589mm <sup>3</sup>
Below Surface:		3.639mm <sup>3</sup>
Projected Area:		52.375mm <sup>2</sup>

(c)

Figure 3.18 Volume measurements of typical impact wear scar of AISI 304 with impact angle 60° after 72,000 cycles by 3D non-contact profilometer shows (a) the impact wear scar and the reference plane while (b) the distortion outside the wear scar edges and (c) the volume of the wear scar

### 3.9 Surface Roughness

All samples were ground on both faces as recommended by the grinding services company (T&J Smith, Sheffield) to achieve the required surface roughness of approximately  $R_a \leq 0.5 \mu\text{m}$  and this was verified by using the 3D non-contact profilometer (5 X).

At least two readings were taken from each sample on the impact face and the mean of surface roughness was reported in the direction of grinding and in the transverse direction (perpendicular to the grinding orientation) except in the cases of the aluminum alloy and phosphor bronze because they were received with circular grinding marks.

The results of roughness measurements taken by 3D non-contact profilometer before impact are summarised in Table 3.11 and verified the T&J Smith measurements.

Table 3.11 Surface roughness measurements of tested materials by 3D non-contact profilometer Alicona

Materials	Roughness with grinding marks		Roughness against grinding marks	
	$R_a$	$R_q$	$R_a$	$R_q$
AISI 304	0.42	0.54	0.8	1.04
AISI 316	0.48	0.63	0.92	1.2
EN8	0.46	0.6	0.85	1.1
EN-GJS-600-3	0.43	0.56	1.06	1.37
AlSi9Cu3	$R_a$		$R_q$	
	0.47		0.6	
PB012	$R_a$		$R_q$	
	0.44		0.56	

Deviation in the results from one material to another is considered as normal due to the uneven surface finish produced during the grinding process, but it stayed within the required range.

The current work measured the roughness using both  $R_a$  and  $R_q$  since they are the most common types of surface roughness measurements and similar to those used in all the published papers examined in the literature review.

The surface roughness values for all tested materials fell within the required range for many tribology applications and within the range of the previous papers in the literature review (0.1-6)  $\mu\text{m}$ . Despite the fact that the previous papers did not mention in which orientation the surface roughness had been taken or the number of samples tested for surface roughness. Roughness may play a role in the amount of wear and smoother surfaces could possibly have worn less than rougher surfaces [67]; nevertheless, none of the research had studied the effect of different surface roughness on the amount of wear due to impact.

### 3.10 Testing Procedure

A recent study by Watson showed that out of 290 experimental works taken from 379 published papers in the field of tribology for the year 2017, only 3.2 % used randomisation either the tests or the test specimen, while non randomise both, 30 % were repeated 3 times or more, and 86 % of these repetitions were done using single batches [68].

Four random repetitive impacts on the tested specimens were performed during this work. The ductile cast iron, phosphor bronze, aluminum alloy, medium carbon steel and AISI 304 were tested first to detect the zero wear volume under normal impact, as explained in detail in Chapter 4, with a specific number of cycles (36,000) being sufficient to reveal the damage on all specimens.

Then AISI 304 was tested later in more detail to investigate the role of number of cycles and impact angle on wear volume and damage to both surface and subsurface. The experimental tests procedure for the four random repetitive impacts are shown in Table 3.12; the numbers of cycles used during these tests were found to be sufficient for formation of an apparent wear scar with noticeable wear volume.

Table 3.12 Experimental tests for AISI 304 with different impact conditions

Stainless steel 304		
Test Order	Number of cycles (N)	Impact angle ( $\theta$ )
1	72000	60°
2	36000	60°
3	54000	90°
4	54000	45°
5	36000	45°
6	54000	45°
7	36000	90°
8	54000	90°
9	72000	90°
10	36000	90°
11	72000	90°
12	72000	60°
13	54000	90°
14	54000	60°
15	54000	60°
16	54000	45°
17	72000	90°
18	36000	60°
19	36000	45°
20	72000	60°
21	72000	45°
22	54000	60°
23	54000	90°
24	72000	60°
25	54000	45°
26	72000	90°
27	54000	60°
28	72000	45°
29	36000	60°
30	72000	45°
31	36000	90°
32	36000	45°
33	36000	90°
34	72000	45°
35	36000	60°
36	36000	45°

Then, three repetitive impacts were applied on both AISI 316 and EN8 under specific number of cycles (54,000) to further investigate the role of impact angle on these materials. Since the materials were tested under specific number of cycles, the tests were randomised with impact angle only.

One of the most powerful methods for randomising the tests during the experimental work is design of experiments (DOE), but it requires the use of two parameters or more; therefore, it was used only with AISI 304, where both impact angle and number of cycles were adopted as variable parameters, as shown in Table 3.12.

Experimental design has been widely applied in many disciplines, such as science, engineering and economics [69].

Table 3.12 presents the general full factorial method used in design of experiments and with Minitab software. Despite the full factorial method having main disadvantages of being time consuming due to the large number of tests runs and potentially expensive in some applications, it plays an important role in tribology applications.

A full factorial run requires 9 tests to be accomplished for two parameters and three levels ( $B^O$ ), where B and O represent the levels and factors, respectively, and with 4 randomisations, which means that 36 tests should be carried out.

### 3.11 Methodology Summary

A modified impact hammering wear rig similar to the one used by Slatter [40] was developed for the purposes of this work. A new load cell was used to measure the impact force experimentally and accurately during normal impact and to record the actual number of cycles with different frequencies. It revealed the same number of cycles in a range of frequencies from (2-10) Hz which reflected the stability of the rig.

The heater cartridges, controller box and a heater block made from medium carbon steel were designed specifically for this rig to measure the wear loss of different materials under high temperature conditions (200, 400) °C and to simulate the actual impact situations of some components that can be used for a variety of materials. The three heater cartridges inserted inside the heater block (see Figure 3.2) can be used with continuous temperatures of up to 650 °C and therefore the rig could be tested up to this temperature.

Different metallic alloys (ferrous and nonferrous) were selected for this work, to represent the alloys most commonly used in the industry field in terms of different structure and composition. These alloys included: austenitic stainless steel 304; austenitic stainless steel 316; medium carbon steel (EN8); aluminum alloy (AlSi9Cu3); ductile cast iron (EN-GJS-600-3) and phosphor bronze (PB102).

In order to use these alloys in the impact wear rig and other mechanical characterisation testing by such as the Vickers tester machine, 3D non-contact profilometer, SEM and optical microscopy, all specimens were cut into discs of 50 mm diameter and 10 mm thickness. Then smaller rectangular samples were prepared from these discs for other specific tests such as microhardness measurements, SEM and optical microscopy to detect the plastic deformation depth, grain size, surface and subsurface cracks, and cracks orientation.

The MATLAB coding used in this work was very useful to indicate the nature of contact for all tested alloys. Randomisation and repetitions were performed in this work using design of experiments to ensure the accuracy of the results and each set of tests was grouped in a way that would ensure the deviation of hardness measurements would be almost equal for all groups.

## Chapter 4 The Role of Zero Wear Volume in Percussive Impact

### 4.1 Introduction

This chapter presents the results of the impact wear rig tests carried out on five different metal alloys widely used in engineering applications, each with a different bulk hardness. The materials used were; an austenitic stainless steel (AISI 304); a medium carbon steel (EN8); a ductile cast iron (EN-GJS-600-3); an aluminium alloy (AlSi9Cu3) and a phosphor bronze (PB102). The work presented in this chapter is following one of the objectives highlighted in Chapter 1 and Chapter 2 which shows a lack of information and data about the zero wear volume (Volume loss due to compression and material remains in the contact zone as defined in Section 3.6).

The wear scar features were analysed using standard methods described in Chapter 3 including 3D non-contact profilometer (Sections 3.8.3), SEM (Section 3.8.2), microhardness (Section 3.4) and discussed in detail. Then a summary of the main discoveries and the key findings is listed at the end of the chapter.

### 4.2 Test Results

This section presents the results of impact wear rig tests run for 36,000 impact cycles on metal alloys used in this research by using Equation 3.20. The total volume losses for materials under repetitive impact is measured directly by mass scale and 3D non-contact profilometer as described earlier in Chapter 2 (Section 2.3.2) and Chapter 3 (Section 3.6).

#### 4.2.1 Wear Volume

The data for mass lost due to the wear was obtained from mass scale measurements of the specimens and was then used to calculate the mean wear volume by converting those masses to volumes with reference to the measured densities of the materials (measured mass divided by measured volume of specimen), ( $7620 \text{ kg/m}^3$  for AISI 304,  $7820 \text{ kg/m}^3$  for EN8,  $8028 \text{ kg/m}^3$  for ductile cast iron,  $2720 \text{ kg/m}^3$  for aluminium alloy, and  $8970 \text{ kg/m}^3$  for phosphor bronze) and shown in Figure 4.1. The error bars represent the standard deviation of the data from four repetitions on specimens of each material type.

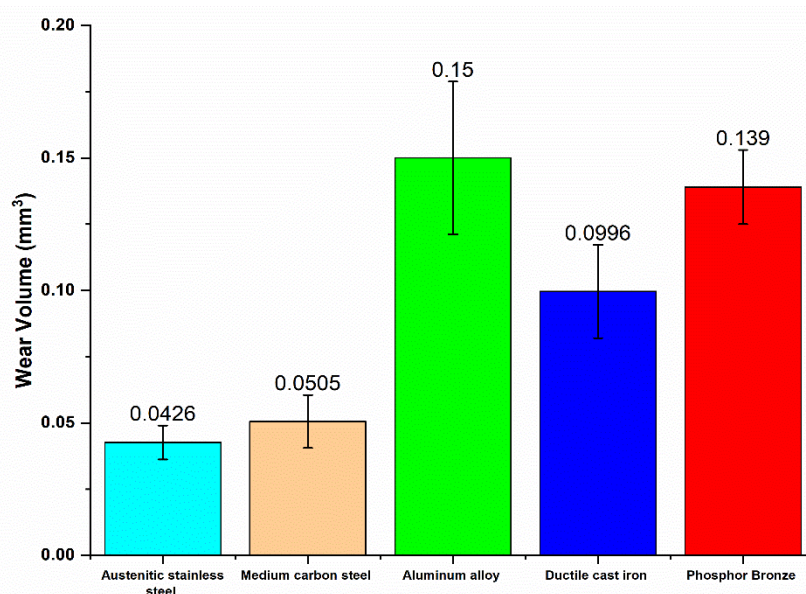


Figure 4.1 – Wear volume of different materials after 36,000 cycles

### 4.2.2 Total Volume Loss

All materials showed a small amount of wear volume under repetitive impact for 36,000 cycles due to the synergistic effect of zero wear volume and plastic flow volume, as illustrated in Figure 4.2.

Figure 4.2 shows that the sum of wear volume and plastic flow volume is significantly less than the directly measured total volume loss, and it is this difference that is defined earlier (Section 3.6) as the zero wear volume. This zero wear volume (the main contributor to the total volume loss) was then calculated using Equation 3.21. For EN8 and ductile cast iron, plastic flow volume also contributed similarly (Figure 4.2).

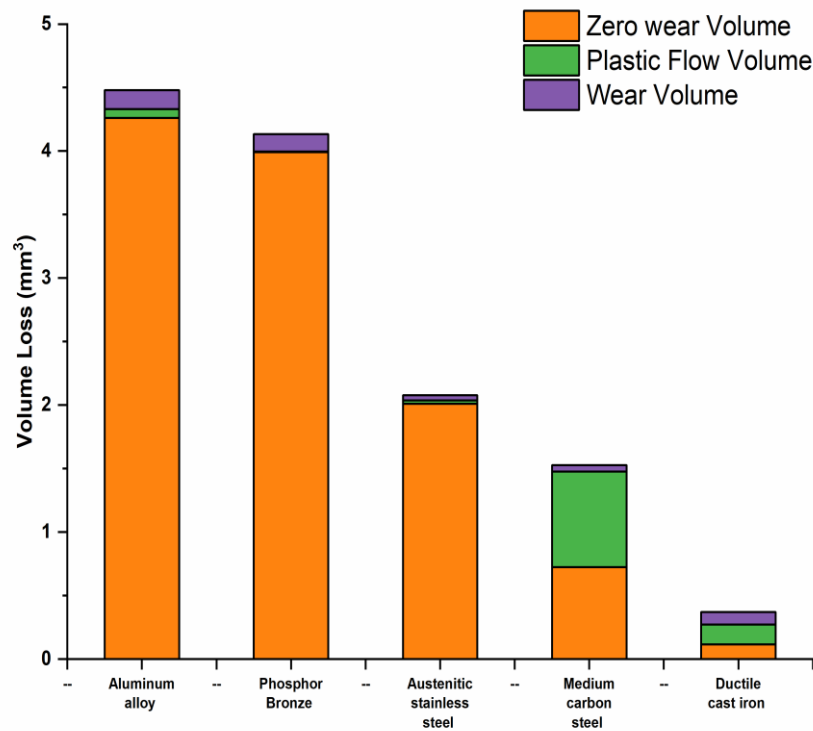


Figure 4.2- Mean total volume loss for materials after 36,000 cycles.

Figure 4.2 illustrates that zero wear volume is almost equal to total volume loss for aluminium alloy, phosphor bronze and AISI 304, while for EN8 and ductile cast iron the volume losses due to compression and plastic flow are approximately equal.

Experimental work on AISI 304 at 10 Hz using the impact wear rig proved that after very small number of cycles (20-30), an apparent deformed contact region formed in the plastic region without any mass loss and also after 16,800 cycles, no mass loss was found, but a large scar was formed as shown in Figure 4.3.

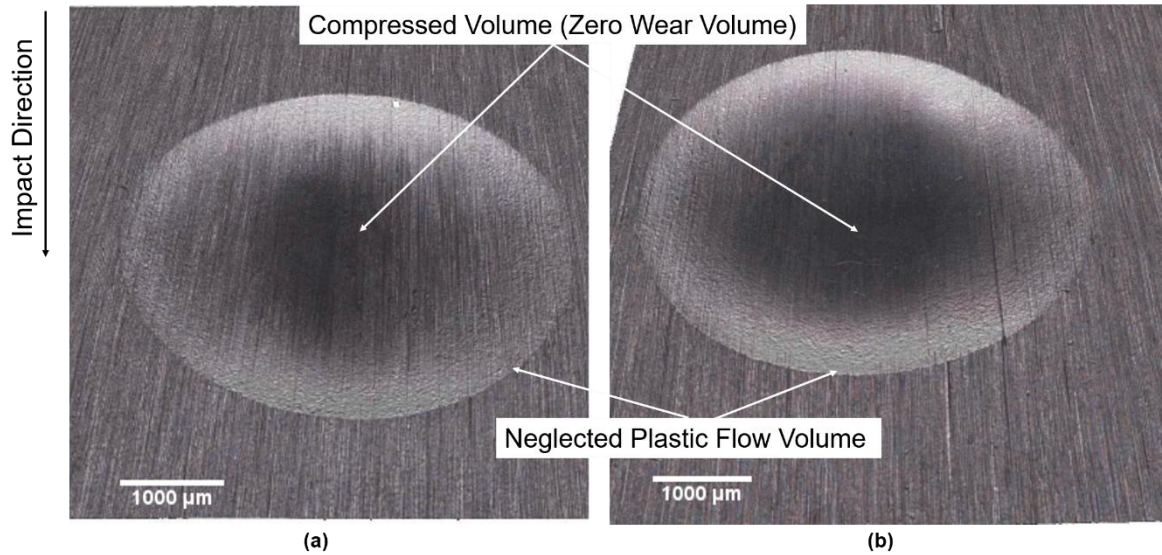


Figure 4.3 Plastic deformation and apparent contact area of AISI 304 under normal impact after (a) 9,000 cycle and (b) 16,800 cycle

The measured size of the plastic flow volume that can be observed as ridges or extruded shoulders around the wear scar edges of AISI 304 for example, Figure 4.4 shows that there was negligible deformation to the surface beyond the edges of the wear scar.

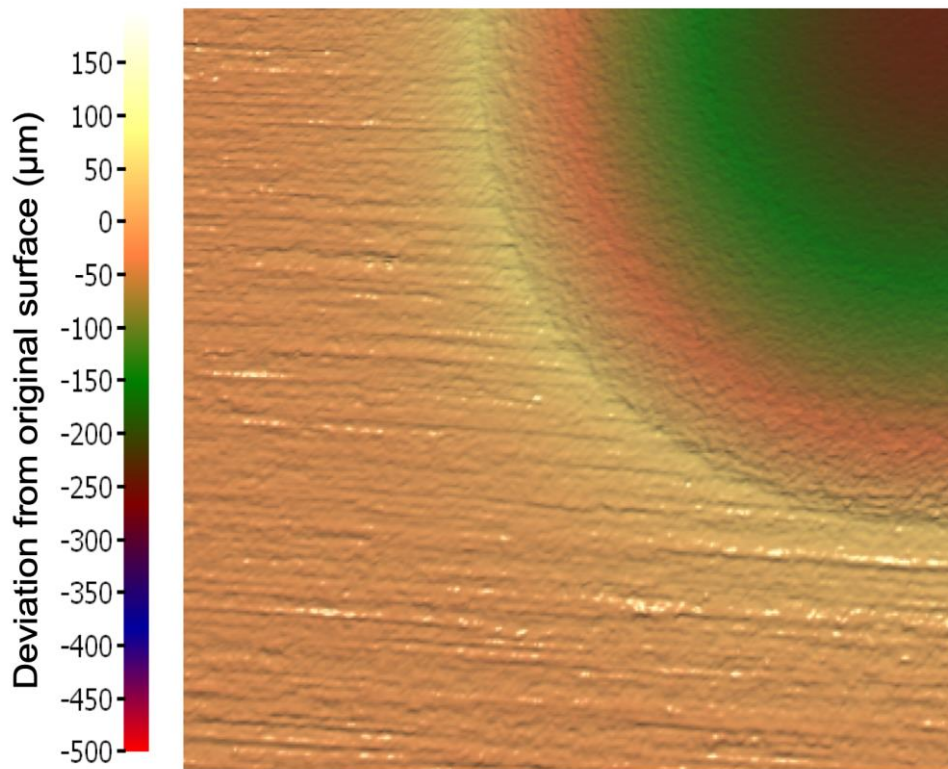


Figure 4.4 Example surface deviation of AISI 304 under normal impact after 36,000 cycles

### 4.2.3 Role of Bulk Hardness During Normal Impact

Despite the fact that AISI 304 is a relatively soft material, it showed the least mass loss among all tested materials which can be connected to its high ductility. Ductile cast iron with the highest hardness (238 HV) showed more mass loss than both EN8 (211 HV) and AISI 304 (190 HV), as shown in Figure 4.5. This agrees with the work of Fricke [22] where AISI 440 with a hardness of (710 HV) has more mass loss under normal impact than AISI 304 (164 HV).

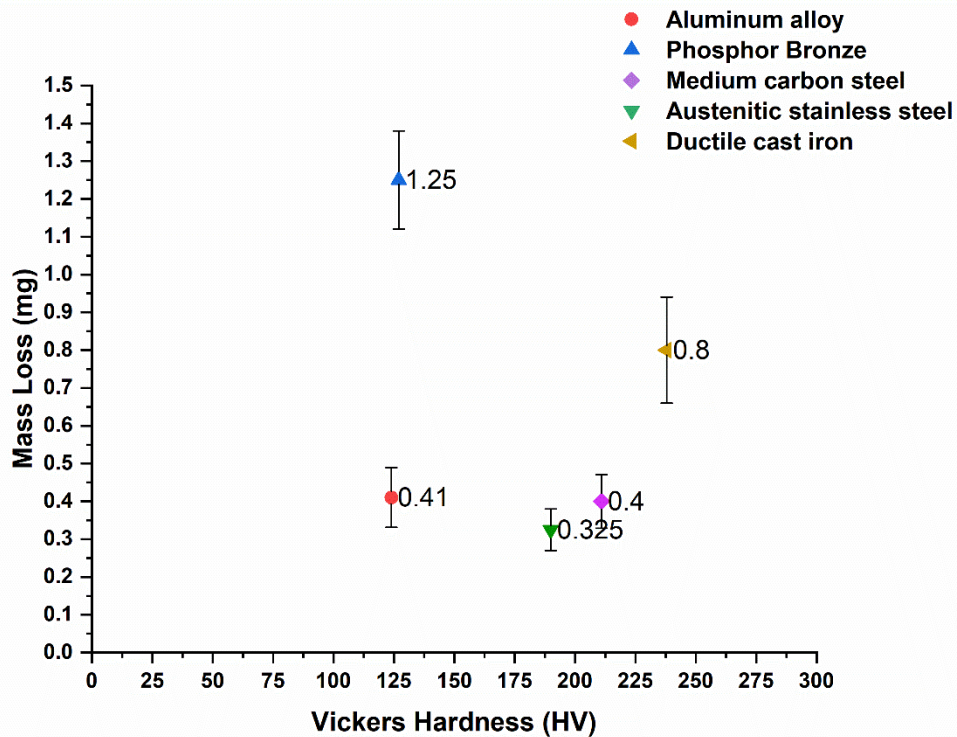


Figure 4.5 Correlation between bulk hardness and mass loss for different materials after 36,000 cycles

The results obtained suggest total volume loss and zero wear volume are all inversely proportional to hardness (see Figure 4.6 and Figure 4.7). The material of highest hardness, the ductile cast iron, gave the minimum indentation and volume loss, contrasting with results for both aluminium alloy and phosphor bronze.

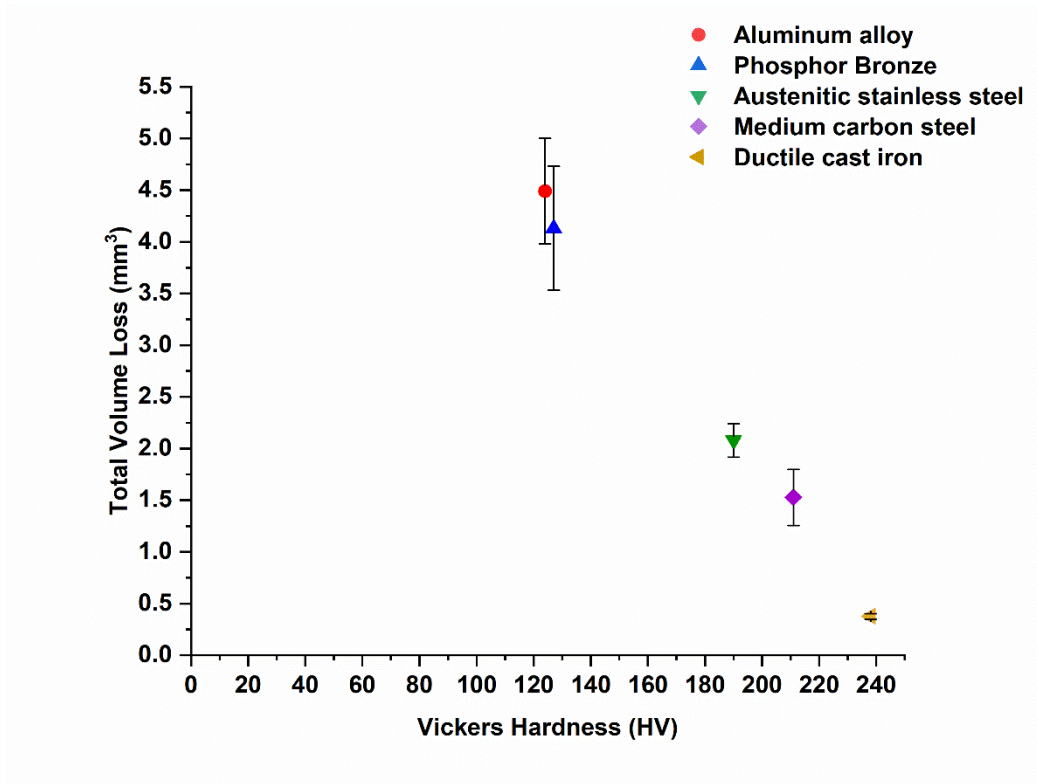


Figure 4.6 Total volume loss of materials after 36,000 cycles

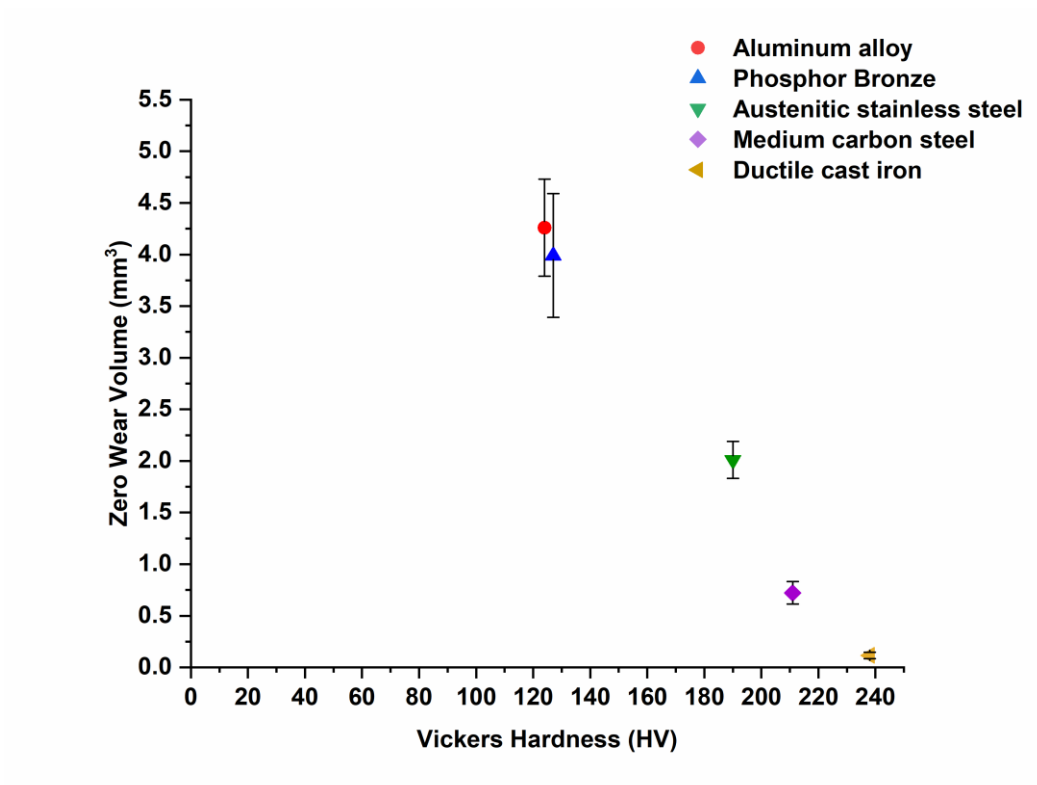


Figure 4.7 Zero wear volume loss of materials after 36,000 cycles

Figure 4.8 shows the scanned surface of the EN8 sample after 36,000 cycles. The red coloured region in the centre of the figure represents the depth of the scar below the reference plane (blue region) and both green, yellow and orange regions represent the plastic flow around the edge of the wear scar above the reference plane.

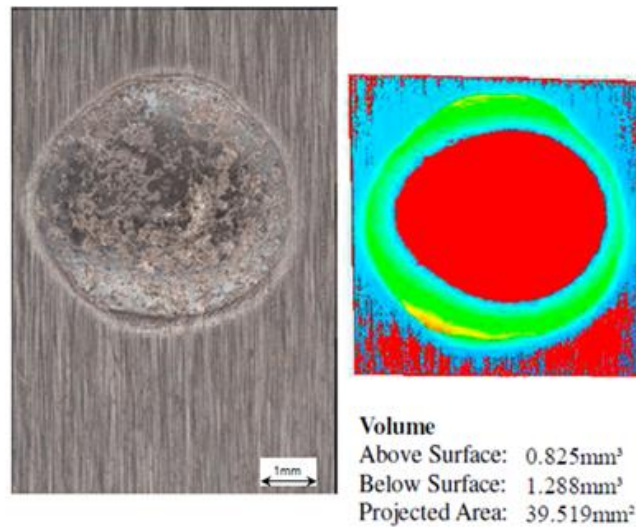


Figure 4.8 Total volume loss on a worn EN8 specimen after 36,000 cycles

These results agree to a great extent with previous results obtained by Wang et al. [37], where a 3D non-contact profilometer was also used to measure wear volume directly. They found that there was more volume loss in a soft aluminium than an iron, but the iron lost more volume than tungsten. However, that study did not use a mass scale to compare between the two methods or identify the ratio of wear volume or zero wear volume to total volume loss, therefore assuming wear volume and total volume loss to be the same.

### 4.3 Wear Scar Morphology

The sizes of the impact wear scars were measured using a 3D non-contact profilometer. Every specimen was measured across three different diametric directions through the centre of the impact wear scar using the software analysis tools. The average for each specimen was recorded and then the averages of four repetitions were plotted as shown in Figure 4.9. This illustrates that the ductile cast iron, which has the highest hardness, has diameter approximately 40 % less than that of aluminium alloy. This figure illustrates the role of hardness, providing approximately similar readings of impact wear scar diameter for aluminium alloy and phosphor bronze or EN8 and AISI 304 due to hardness similarity.

## The Role of Zero Wear Volume in Percussive Impact

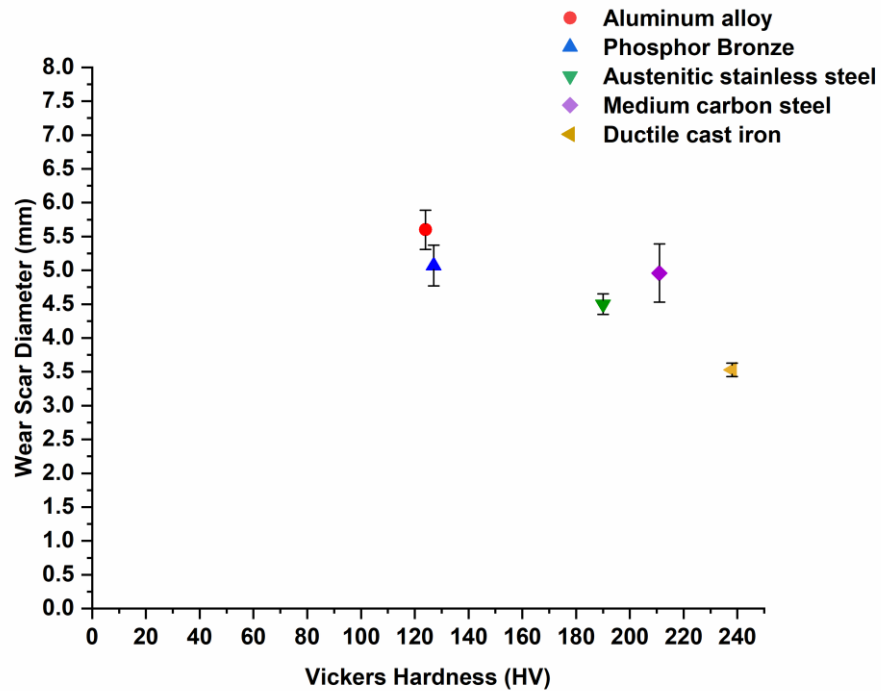


Figure 4.9 Correlation between hardness and impact wear scar diameter after 36,000 cycles

To confirm the results of impact wear scar diameter and to measure the scar depth, the data from every diametric measurement was further analysed to produce geometric profiles of the scars. Measurements of the depth and diameter of the impact scar for every material were taken and a typical profile for each material is shown in Figure 4.10.

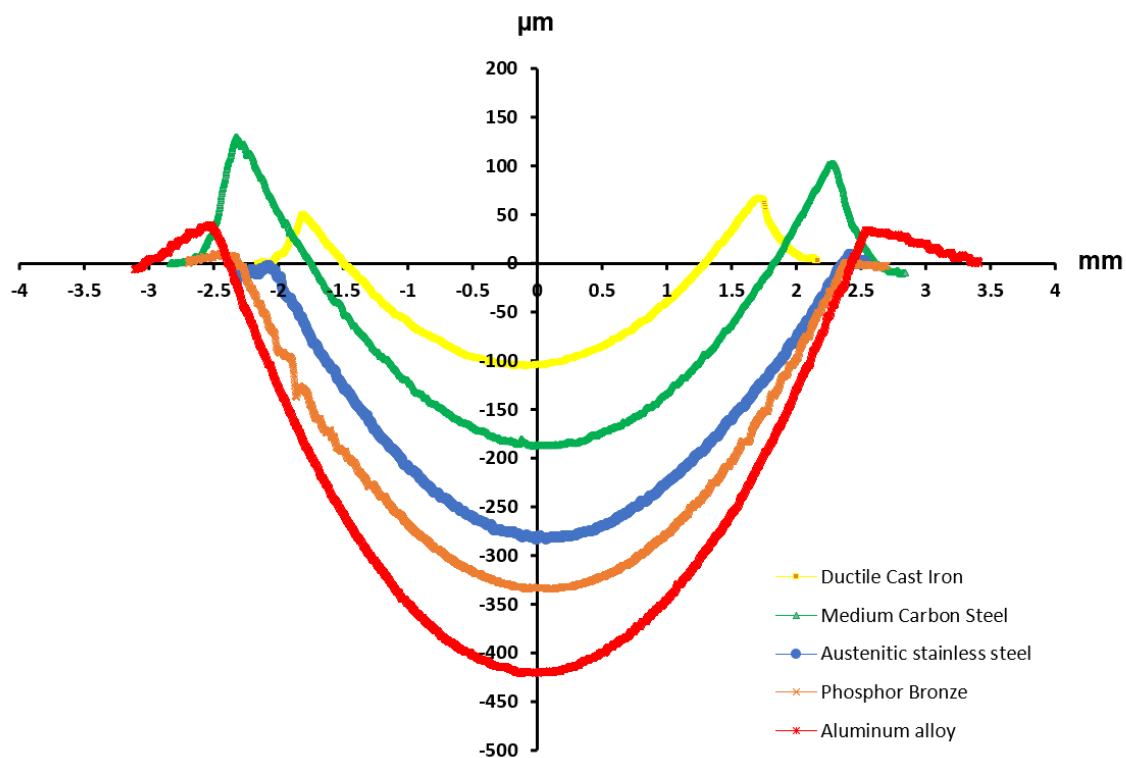


Figure 4.10 Typical wear scar profile after 36,000 cycles for each material tested.

Figure 4.10 reveals, in general, a smooth surface profile for the materials' scars with some obvious roughness near the edges of phosphor bronze. EN8 and ductile cast iron have obvious plastic flow on the edges of the impact scar in addition to some plastic flow for aluminium alloy, while no obvious plastic flow is apparent for either AISI 304 or phosphor bronze.

In terms of the test results recorded for each material, EN8 produced the mean plastic flow height ( $h_u$ ) of 160  $\mu\text{m}$  with mean depth ( $h_l$ ) of 223  $\mu\text{m}$  and the plastic flow volume represents approximately 50 % of the total volume loss. Ductile cast iron produced a similar pattern with mean ( $h_u$ ) of 71  $\mu\text{m}$  and ( $h_l$ ) of 117  $\mu\text{m}$ , with plastic flow volume representing approximately 41 % of total volume loss. Despite the plastic flow formation for the aluminium alloy, this was considered a small amount as the mean plastic flow was only 80  $\mu\text{m}$ , while the mean depth was 426  $\mu\text{m}$ .

The datasets obtained from the 3D non-contact profilometer were also used to perform a 3D analysis and the data for a typical wear scar for each material tested is shown in in Figure 4.11. These illustrate the edges formed by the deformed material and the typical difference in wear scar size between the different materials.

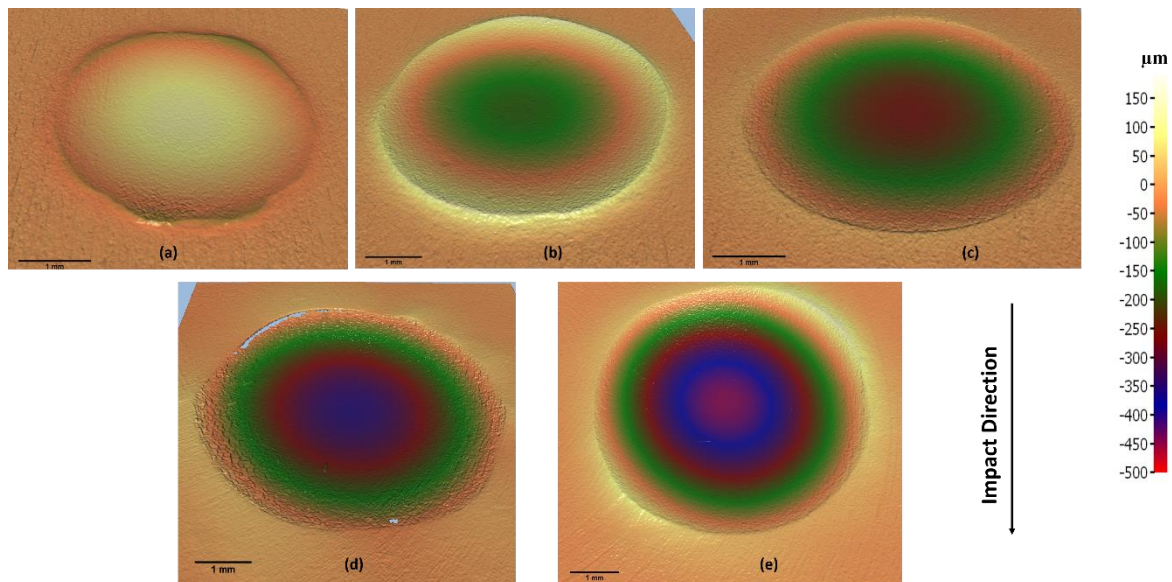


Figure 4.11 Typical wear scars for (a) ductile cast iron, (b) EN8, (c) AISI 304, (d) phosphor bronze and (e) aluminium alloy after 36,000 cycles

As can be seen from Figure 4.11, both the phosphor bronze and aluminum alloy have the maximum depth, shown in blue color, in the centre of the impact scar, while ductile cast iron has the lowest depth, thereby showing the role played by material hardness.

AISI 304 and phosphor bronze (Figure 4.11 (c) and (d)) show a mass loss after 36,000 cycles, but the wear volume is very small compared with the total volume loss and both materials have negligible amount of plastic flow beyond the edges of the wear scar. This confirms the results in Figure 4.10 and again proves that large part of that missing volume has been compressed as zero wear volume.

#### 4.4 Wear Scar Analysis

Despite the relatively low wear volume experienced by all materials tested, due to the dominance of zero wear volume and plastic flow volume in the total volume loss, damage to the surface of all the specimens was clear to the naked eye.

The impact scars were generally circular in shape for all materials although some exhibited some ovality (particularly the AISI 304), which is likely due to the variation in materials properties leading to more plastic deformation or possibly due to random occurrence as explained before by Slatter [8].

The typical wear scars for all materials can be seen in Figure 4.12. Figure 4.13 and Figure 4.14 shows the wear damage mechanism in the centre region of the impact scar of all tested materials.

The main wear damage mechanism after 36,000 cycles was plastic deformation, either in the centre of the wear scar or on the impact edges as both Figure 4.13 and Figure 4.14 reveal plastic flow and surface fatigue. Evidenced to spalling in the centre of the impact scar were expected due to the maximum contact pressure in the middle of the contact region.

The results support the hypothesis that crack initiation at the surface and then propagation beneath the surface leads to surface fatigue and eventual removal of material from the surface as wear debris due to spalling. No obvious delamination or material transfer was detected for any of the materials. Both EN8 and ductile cast iron revealed a significant plastic flow on the ridges of wear scar.

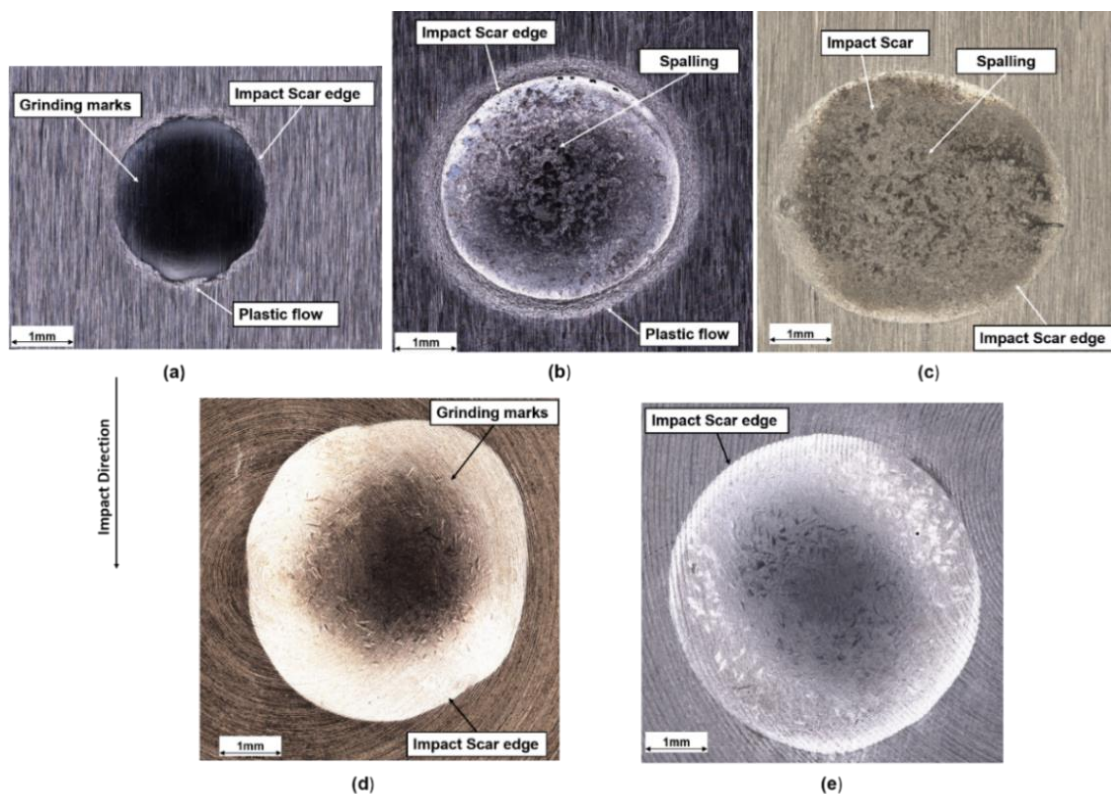


Figure 4.12 Typical impact wear scar for tested materials after 36,000 cycles for (a) ductile cast iron, (b) EN8, (c) AISI 304, (d) phosphor bronze and (e) aluminium alloy

## The Role of Zero Wear Volume in Percussive Impact

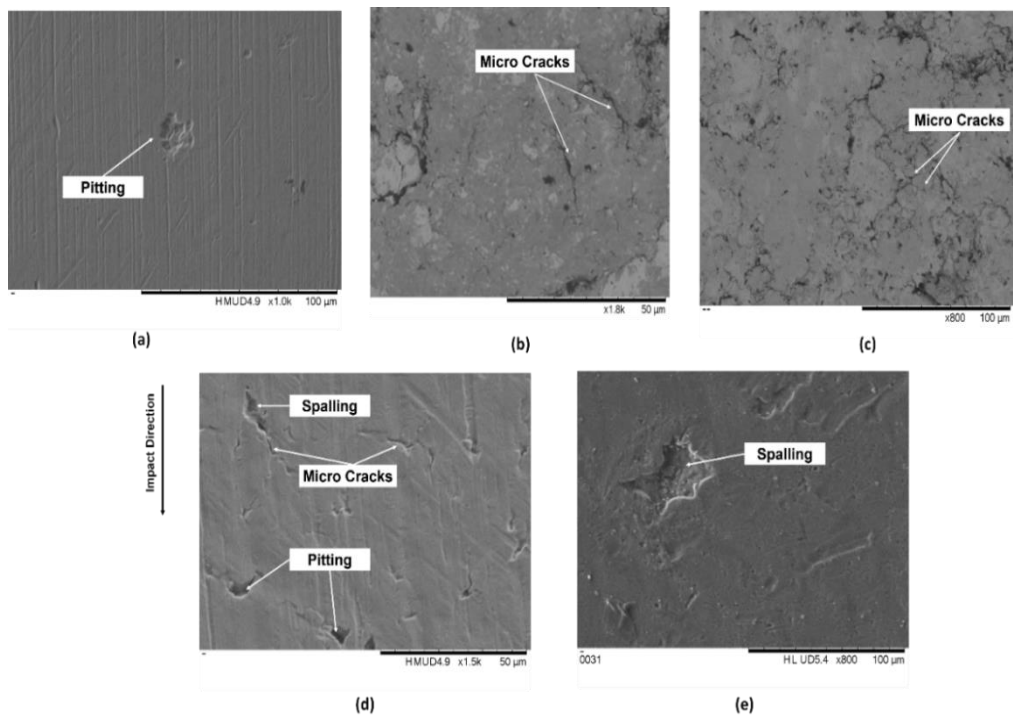


Figure 4.13 Damage mechanism in the centre of the impact scar for tested materials after 36,000 cycles for (a) ductile cast iron, (b) EN8, (c) AISI 304, (d) phosphor bronze and (e) aluminium alloy

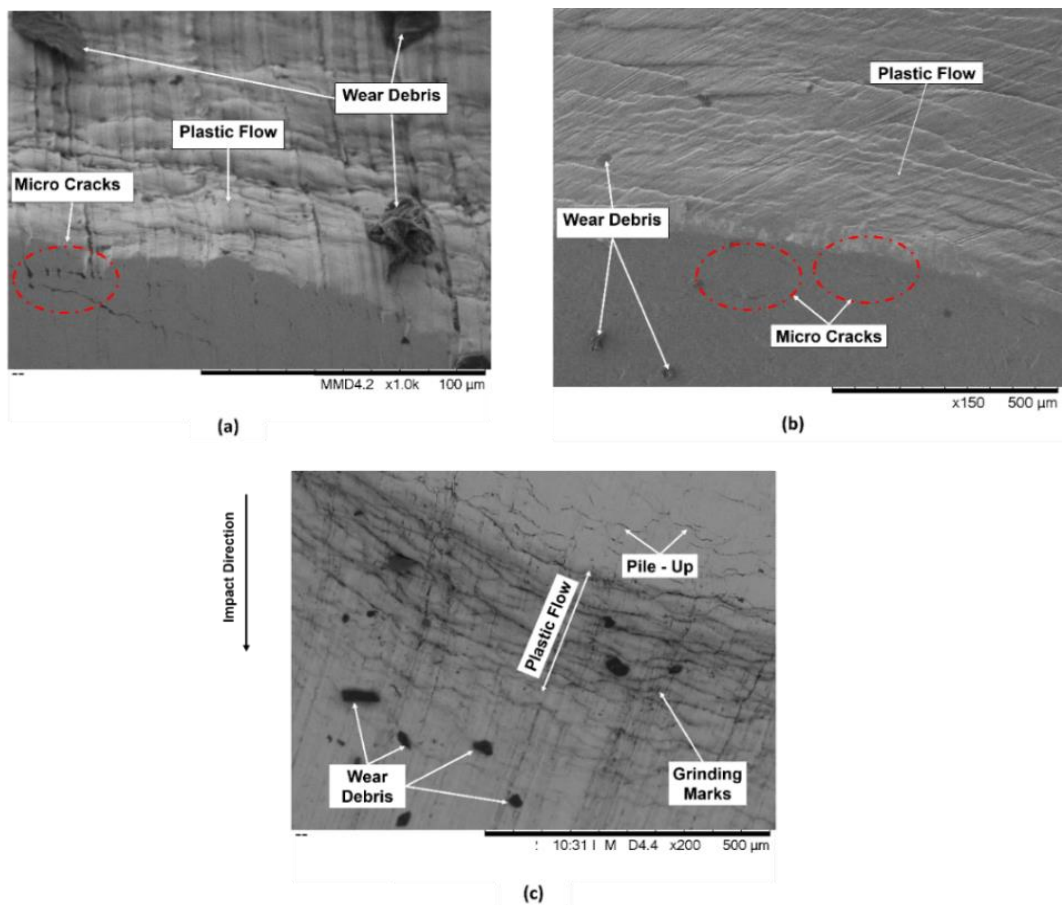


Figure 4.14 Plastic flow formation on the edges and micro-cracks after 36,000 cycles for (a) ductile cast iron, (b) aluminium alloy and (c) EN8

#### 4.5 Microhardness Results

Microhardness profiles of the subsurface material resulting from the impact wear process were obtained by Struers Durascan Vickers indentation at the maximum load of 0.1 kgf for all materials as described in Chapter 3 (Section 3.4). Loading and unloading were performed with a holding period of 10 s and distance between indentations was 2.5d, according to ASTM E384 [70].

Figure 4.15 shows microhardness measurements at a position below the maximum indentation depth of the impact scar and the error bar representing the standard deviation of the data from three repetitions for each distance from the surface.

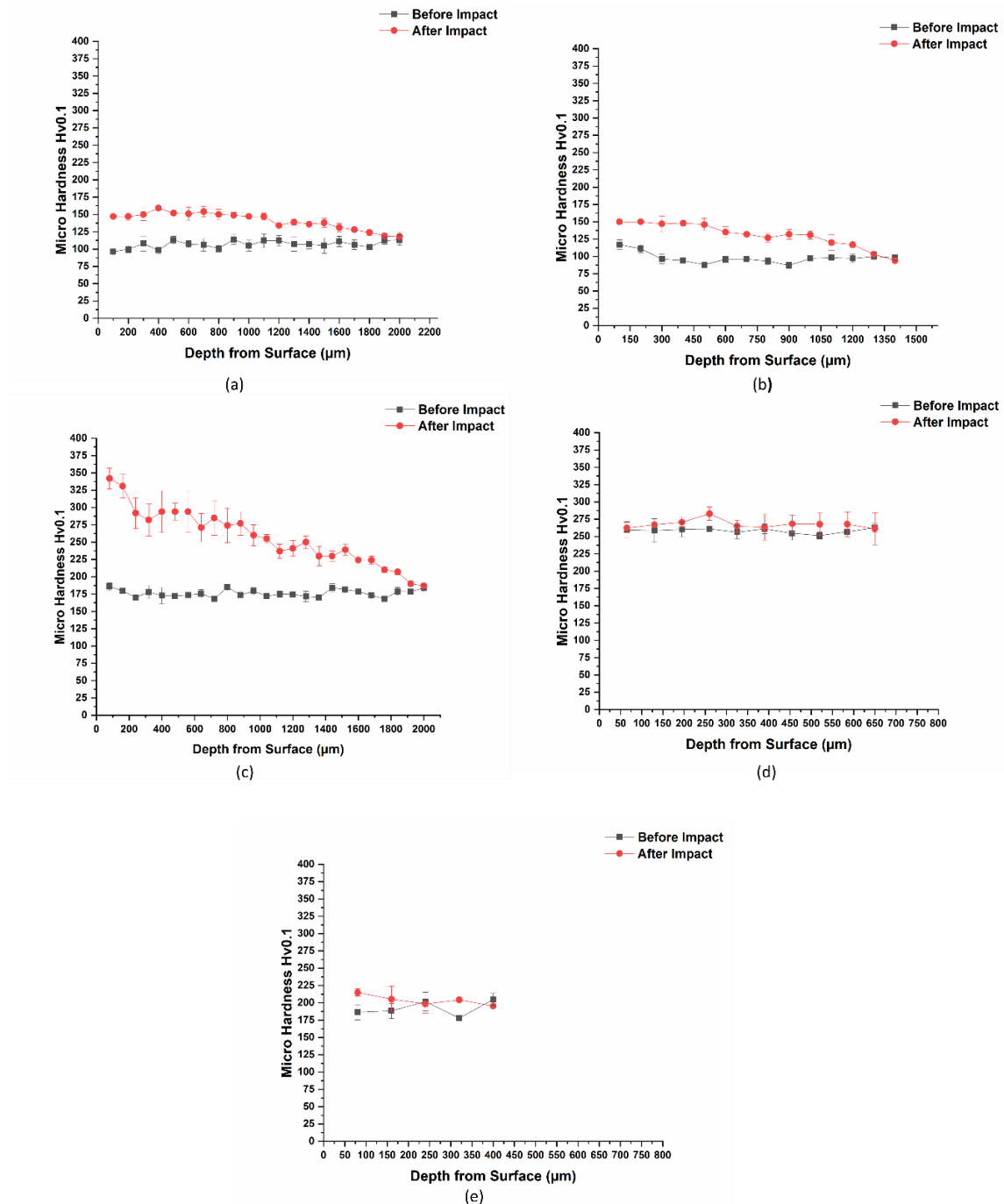


Figure 4.15 Microhardness measurements under normal impact for (a) aluminium alloy, (b) phosphor bronze, (c) AISI 304, (d) ductile cast iron and (e) EN8 after 36,000 cycles

Based on the measurements, aluminium alloy, phosphor bronze and AISI 304 showed a significant increase in hardness after 36,000 cycles of impact due to the role of work hardening resulting from the repetitive impact. While both EN8 and ductile cast iron have more plastic flow on the scar edges with significant increase in hardness of plastic flow and recording an average increase of 24 % for ductile cast iron with a similar pattern for EN8. Both materials did not show a significant increase in hardness for the centre of the wear scar as appeared in Figure 4.15.

The average observed increases in hardness for phosphor bronze, aluminium alloy and AISI 304 were 36 %, 31 % and 39 % respectively and reached depths of approximately 1.4-2 mm from the surface as the microhardness results showed, which indicate work hardening of the materials.

The current results revealed an increase in hardness which agrees with previous results of Rastegar [21] and Yilmaz [28].

An example of the grain deformation that typically occurs near the bottom edge of impact scar for EN8 is shown in Figure 4.16, which reveals the deformed grains of both ferrite ( $\alpha$ ) and pearlite (P). Also visible is a microhardness indentation which represents a value of 257 HV.

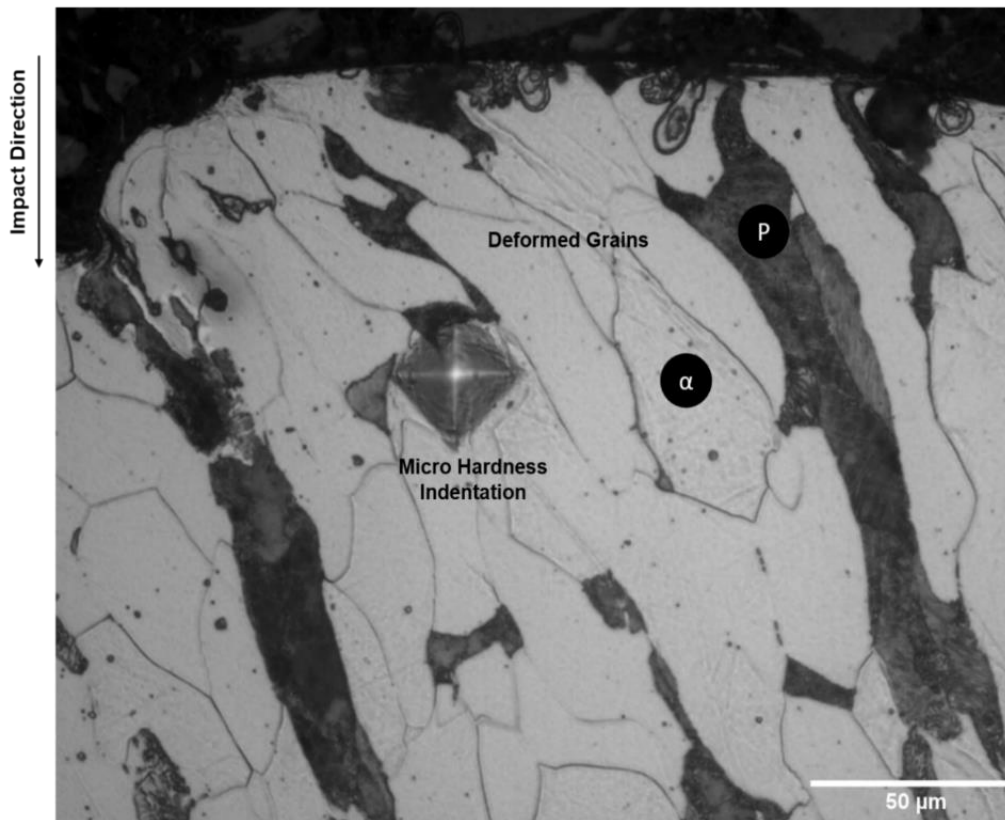


Figure 4.16 Microhardness indentation of EN8 below the bottom edge of wear scar after 36,000 cycles

## 4.6 Discussion

The results of zero wear volume are in agreement with the work of Engel [43] described earlier in Chapter 2 (Section 2.4.1) in that there are a number of wear cycles that a surface can undergo before it starts to wear. The work presented in this Chapter showed that zero wear volume can occur at any point instead of a number of cycles from the initial contact. This is justified by these results demonstrating this not only occurs in the elastic region and the materials can undergo further plastic deformation without any mass loss.

For the case of AISI 304 used in this work there was no mass loss found after up to 16,800 cycles, yet an apparent plastically deformed region formed on the surface of the specimen and large scar after further impacts were accumulated. Further evidence is that the wear volume after 36,000 cycles was very small compared with the total volume loss measured by 3D non-contact profilometer, thus proving that there is a significant volume being compressed rather than being removed from the specimen.

The current results suggest that the previous results of papers that used the 3D non-contact profilometer to calculate the wear volume loss such as by Lindroos [20], Jiang [15] and Rastegar [21], should also have used a mass scale in conjunction with Equation 3.20 in order to find the zero wear volume. This is especially the case when impact occurs normal to the surface and the materials under investigation are expected to be significantly compressed due to their ductility and therefore this volume cannot be neglected when measuring the total volume loss.

The work also suggests that ferrous and non-ferrous materials tested appear to be compressible and this contributes to the total volume lost. This may be due to localised microstructural defects (void nucleation, dislocation, coalescence, internal porosity from ductile failure) and changes (phase transformation, carbide precipitation or hardening).

Surface examination by SEM revealed that the main damage mechanism for tested materials was mainly plastic deformation and surface fatigue due to spalling as a result of the formation of small pits and then subsequent microcracks. There was no obvious delamination observed in any of the materials. The small-scale pitting which led to spalling is expected since the mass loss was very small for all materials and this contributed to the role of zero wear volume during impact.

The current results revealed that the zero wear volume is inversely proportional to the bulk hardness of material. Figure 4.7 shows that ductile cast iron, which has the highest hardness, has the least zero wear volume whereas the aluminum alloy, with lowest hardness, has the greatest zero wear volume.

Hardness, however, appears not to be a primary parameter affecting the mass loss of materials under normal impact. Figure 4.5 shows that ductile cast iron has more mass loss than both EN8 and AISI 304 despite its relatively higher hardness. This agrees with the previous findings of Fricke [22]. The results also showed no direct correlation between the Young's modulus or bulk hardness of the materials and wear volume for any materials which is accounted for by the zero wear.

The current results showed that AISI 304 has a greatest propensity to work harden as shown in Section 4.5 (see Figure 4.15) among other tested materials and the increase in hardness near the surface for the centre of impact scar is almost twice the original bulk hardness. Similar results for the same materials were also observed by Fricke [22] where the surface microhardness results of AISI 304 increased from 242 HV to approximately 650 HV which indicates the great capacity of work hardening. This could explain the greater propensity of AISI 304 to appear to be compressed as zero wear volume. With similar consideration of the relative material properties of the other materials studied here, it could be concluded

that the material with the largest ability to work hardening is more likely to have more zero wear volume than other materials.

Results in Figure 4.2 reveals possible correlation between material ductility and plastic flow formation for ferrous materials. Higher ductility leads to greater zero wear volume and eventually reduced both plastic flow and wear volumes. Both EN8 and ductile cast iron showed more plastic flow at the wear scar edges compared to AISI 304. Since the nature of impact is compression under normal impact therefore, microhardness examination revealed work hardening as expected for all materials under repetitive impacts.

#### 4.7 Zero Wear Summary

A summary of the findings derived from the experimental work on materials discussed in this chapter is presented below:

- Neither Young's modulus or bulk hardness has a direct correlation with wear volume resulting from repetitive normal impacts for the materials examined in this chapter.
- Bulk hardness is inversely proportional to both zero wear volume and maximum indentation resulting from single repetitive normal impacts for the materials considered here.
- All materials show relatively very small amounts of wear volume loss compared with zero wear volume or plastic flow volume, in their total volume loss.
- Depending on the route and quality of manufacture there may be some subsurface imperfections that could account for some localised compression of the material.
- Ferrous materials with high ability for work hardening tend to have more materials being compressed as zero wear volume (sink in) rather than plastically flow to the edges of the wear scar compared with other ferrous materials that have low propensity for work hardening (pile-up).

## Chapter 5 Investigation on Impact Wear and Damage Mechanism of Austenitic Stainless Steel 304

### 5.1 Introduction

This chapter presents the results of experimental work using the impact wear rig on AISI 304, following one of the objectives described in Chapter 1 and outlined in Chapter 2 which shows lack of information and data about the surface and subsurface damage of AISI 304 with different impact angles and the role of shear force during impact.

The wear scar features were analysed using standard methods described in Chapter 3 including 3D non-contact profilometer (Sections 3.8.3), OM and SEM (Sections 3.8.1 and 3.8.2), microhardness (Section 3.4) and discussed in detail. Then a summary of the main discoveries and the key findings is listed at the end of the chapter.

### 5.2 Impact Test Results

This section presents the summarised results of impact wear rig tests with different number of cycles (36,000, 54,000, 72,000) and different impact angles ( $90^\circ$ ,  $60^\circ$ ,  $45^\circ$ ) and an impact force of 3476 N on wear damage of AISI 304. The wear volume was measured directly by converting those masses measured by Sartorius electronic balance with precision to the nearest 0.1 mg to volumes with reference to the measured density of the material ( $7620 \text{ kg/m}^3$ ). While total volume loss was measured by 3D non-contact profilometer (volume change) as the two standard methods described earlier in Chapter 2 (Section 2.3.2) and in Chapter 3 Section 3.6.

#### 5.2.1 Wear Volume

Before and after testing, each specimen was cleaned with compressed air and isopropanol to remove any dust and to remove the remaining wear debris on the specimen after test. Two measurements represent the mass loss; each specimen was weighed before and after testing on the same day to minimise any possible error in reading from the scale.

Figure 5.1 presents the effect of impact conditions on wear volume of AISI 304. The error bars represent the standard deviation of the data from four repetitions on specimens, and the repeatability of the rig was very good as the impacts hit the same contact area. These results showed very good consistency and similarity to previous results obtained by Slatter [8, 9] and Yilmaz [28].

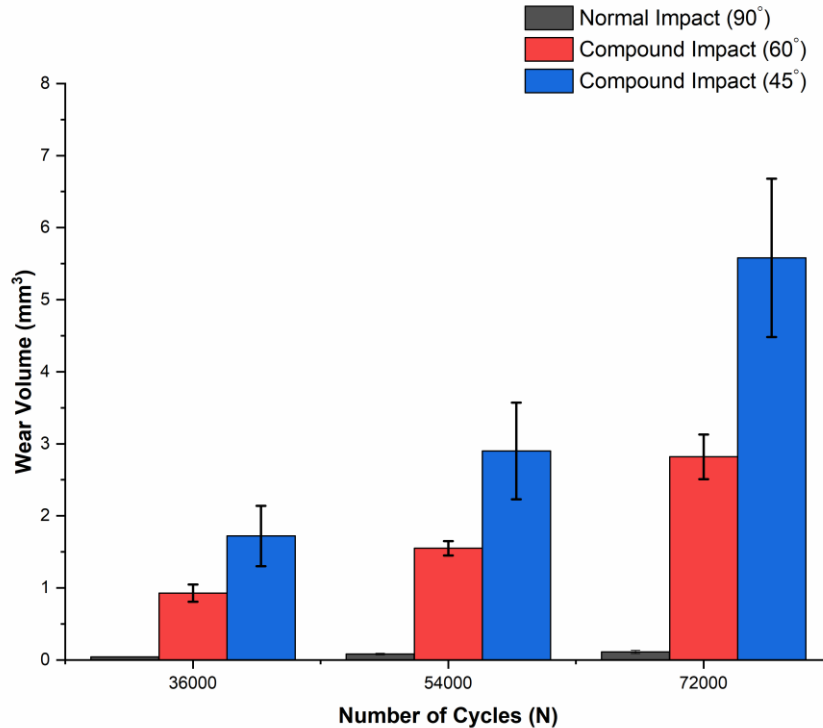


Figure 5.1 Mean wear volume for AISI 304 as a function of impact conditions

### 5.2.2 Total Volume Loss

The total volume loss during impact, as defined earlier in Section 3.6 and the plastic flow volume (above surface) were calculated by using the 3D non-contact profilometer for direct volume measurements since it takes better account of the actual volumetric changes during impacts as described in Section 3.6. The whole wear scar region was selected and then the total volume loss was recorded as can be seen, for example, in Figure 5.2 where the turquoise region represents the reference plane. Regions above are green, yellow and orange and regions below are red.

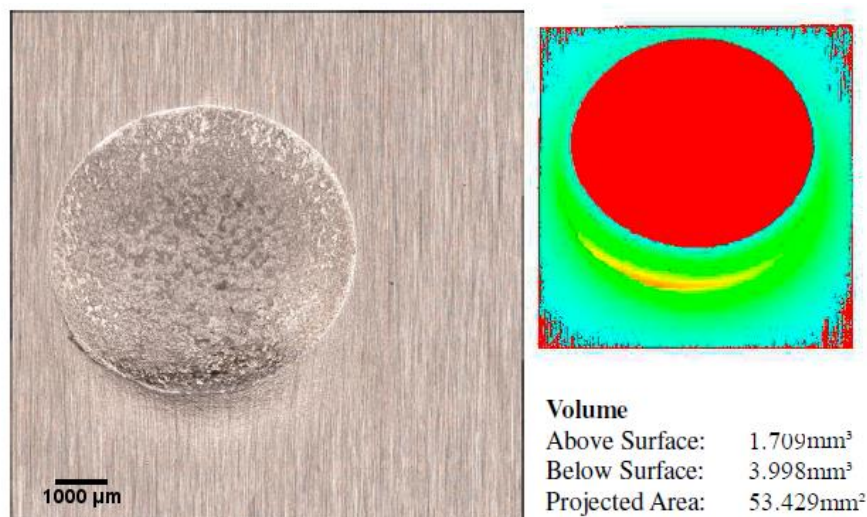


Figure 5.2 Total volume loss as measured on a worn surface (reference plane (turquoise), 'above surface' (green, yellow and orange) = plastic flow volume and 'below surface' (red) = total volume loss) at impact angle 60° after 72,000 cycles

Figure 5.2 shows the contour map after 72,000 cycles with an impact angle of 60°. It can be seen that the surface is regular and circular in shape, with obvious uniform plastic flow on the bottom edge of the impact wear scar.

The total volume loss measured by 3D non-contact profilometer was plotted against the impact angles with different number of cycles is shown in Figure 5.3.

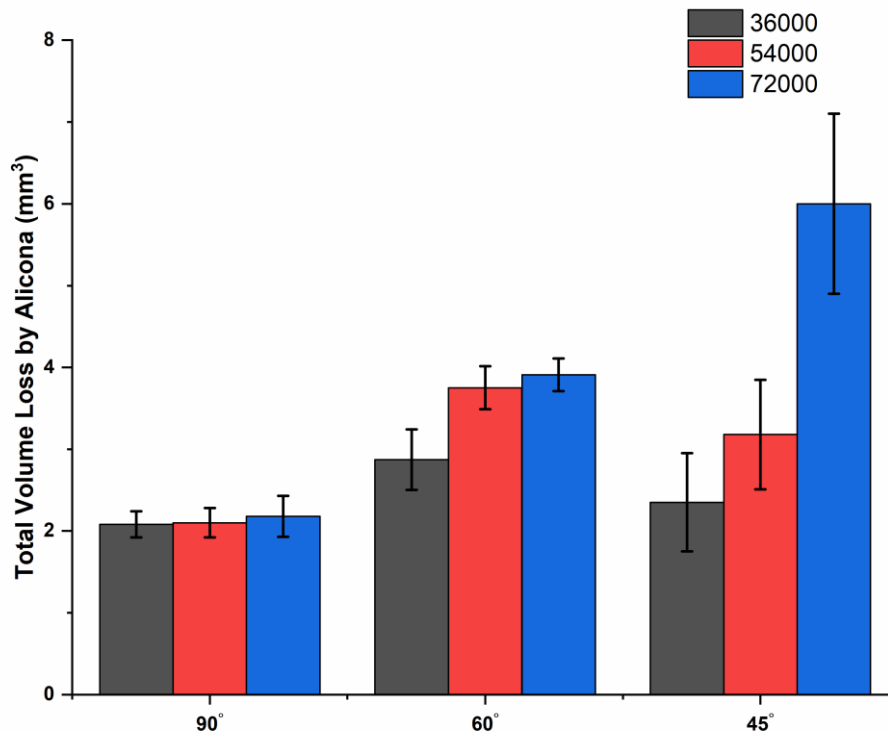


Figure 5.3 Mean total volume loss for AISI 304 Vs impact angles and number of impact cycles

Figure 5.3 shows that the total volume loss scanned by 3D non-contact profilometer increased with the compound impact and the impact angle had an obvious effect on total volume loss. For example, changing the impact condition from normal to compound impact with 60° led to an increase in volume loss in a range varying from 37-80 %, while changing the angle to 45° led to a significant increase in total volume loss, reaching 175 % compared with normal impact after 72,000 cycles.

Figure 5.3 also revealed that the total volume loss with an impact angle of 60° is less than with an impact angle of 45° after 36,000 and 54,000 cycles. However, the total volume loss for an impact angle of 45° is higher than with an impact angle of 60° after 72,000 cycles. This attributed to the synergistic effect of both plastic flow volume and wear volume, with lower number of cycles (36,000 and 54,000), the total volume loss for both angles (60° and 45°) are approximately similar but the plastic flow volume is higher with an impact angle of 60°. While after 72,000 cycles the plastic flow volume of an impact angle of 45° is still less than with an impact angle of 60° but the the wear volume increased significantly (twice the wear volume after 54,000 cycles) and this explain the significant increase in total volume loss with an impact angle of 45° after 72,000 cycles.

Figure 5.4 shows the total volume losses defined in Section 3.6 after 72,000 cycle where highest damage occurs to the material.

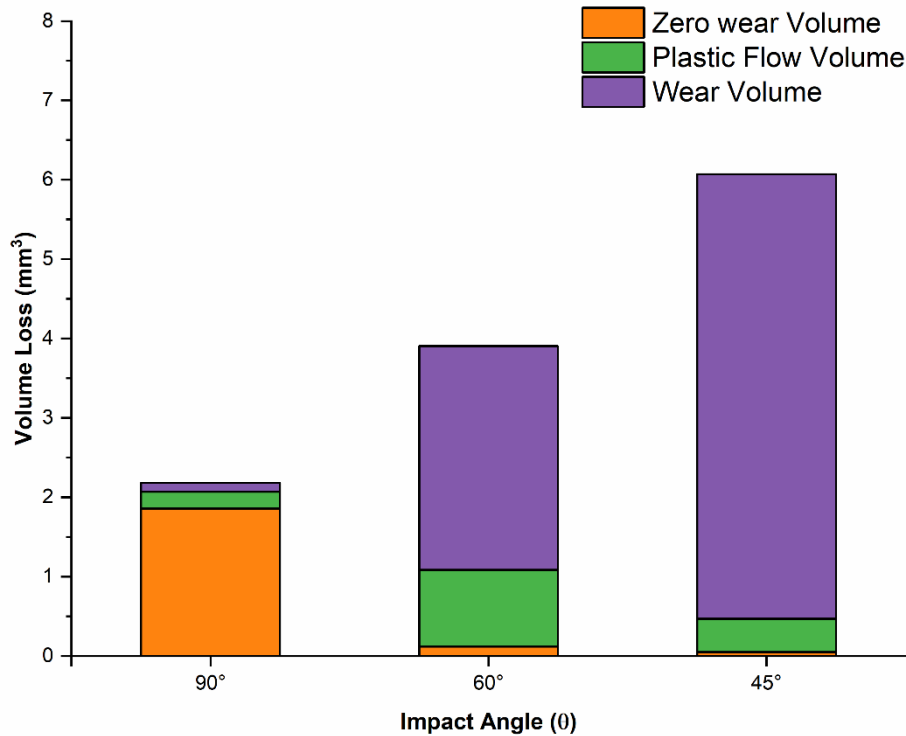


Figure 5.4 Mean total volume loss, and of each component of the volume loss, for AISI 304 after 72,000 cycles with different impact angles

Figure 5.4 showed a small amount of wear volume under repetitive normal impact for 72,000 cycles due to the synergistic effect of zero wear volume and plastic flow volume and this agrees with the previous results shown in Figure 4.3. The sum of wear volume and plastic flow volume is significantly less than the directly measured total volume loss, and it is this difference that has been previously defined as the zero wear volume [71]. One of the main findings of Chapter 4 was that the zero wear volume (calculated by using Equation 3.21) is the main contributor to the total volume loss (the total height of the bars) under normal impact. For compound impact it can be neglected because, as shown in Figure 5.4 for impact at 60° and 45° there are noticeable increases in wear volume and plastic flow volume. Table 5.1 shows the mean total volume losses of each component described in Figure 5.4 and their standard deviations.

Table 5.1 Mean total volume loss of AISI 304 after 72,000 with standard deviation for each component

Conditions (cycles, angle, temp.)	Mean Wear Volume $V_w$ ( $mm^3$ )	Standard Deviation $\sigma$ (STD)	Mean Plastic Flow Volume $V_{pf}$ ( $mm^3$ )	Standard Deviation $\sigma$ (STD)	Mean Zero Wear Volume $V_{zw}$ ( $mm^3$ )	Standard Deviation $\sigma$ (STD)	Mean Total Volume Loss $V_t$ ( $mm^3$ )	Standard Deviation $\sigma$ (STD)
72000, 90°, RT	0.111	0.02	0.209	0.03	1.86	0.17	2.18	0.2
72000, 60°, RT	2.82	0.3	0.966	0.1	0.119	0.02	3.91	0.2
72000, 45°, RT	5.6	1	0.421	0.08	0.05	0.008	6.07	1.1

It should be noted that increases the number of cycles led to slight increase in plastic flow volume and wear volume and therefore, the zero wear volume decreased according to Equation 3.20 and shown in Figure 5.5 for AISI 304 with impact angle  $45^\circ$ , but the main factor that play a primary role during impact is the impact angle (Figure 5.4).

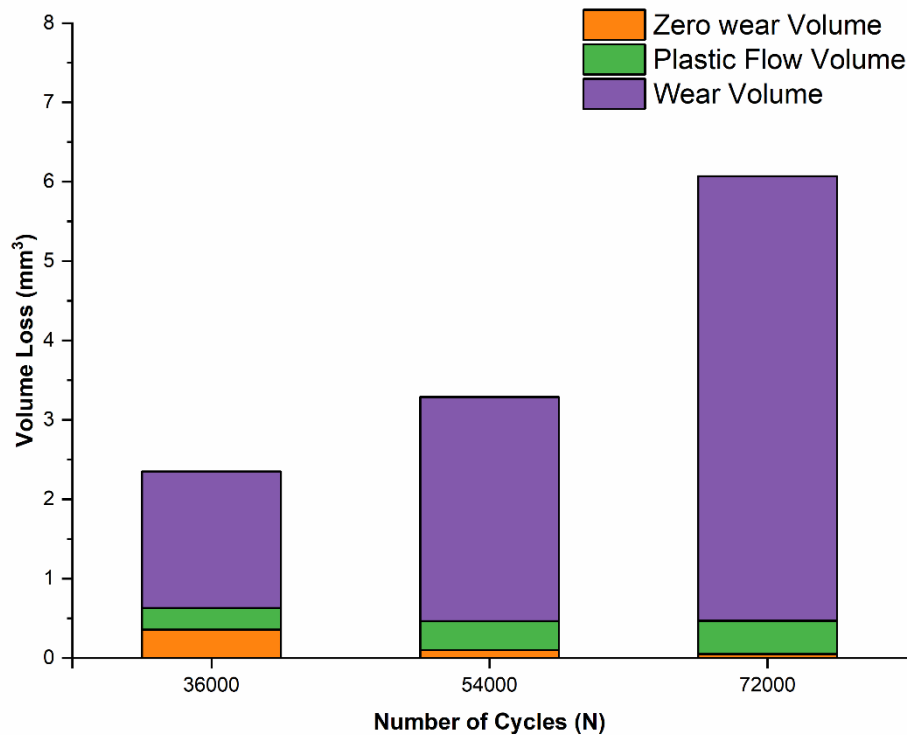


Figure 5.5 Mean total volume loss, and of each component of the volume loss, for AISI 304 with compound impacts  $45^\circ$  and different impact cycles

Table 5.2 shows the mean total volume losses of each component described in Figure 5.5 and their standard deviations.

Table 5.2 Mean total volume loss of AISI 304 with standard deviation for each component with impact angle  $45^\circ$  and different number of cycles

Conditions (cycles, angle, temp.)	Mean Wear Volume $V_w$ ( $mm^3$ )	Standard Deviation $\sigma$ (STD)	Mean Plastic Flow Volume $V_{pf}$ ( $mm^3$ )	Standard Deviation $\sigma$ (STD)	Mean Zero Wear Volume $V_{zw}$ ( $mm^3$ )	Standard Deviation $\sigma$ (STD)	Mean Total Volume Loss $V_t$ ( $mm^3$ )	Standard Deviation $\sigma$ (STD)
36000, $45^\circ$ , RT	1.72	0.4	0.27	0.03	0.36	0.2	2.35	0.6
54000, $45^\circ$ , RT	2.82	0.67	0.36	0.069	0.1	0.018	3.28	0.7
72000, $45^\circ$ , RT	5.6	1	0.421	0.08	0.05	0.008	6.07	1.1

As described before in Section 2.3.2.2, the total volume loss can be directly measured through 3D non-contact profilometer techniques or by using the spherical cap method.

This (Figure 2.17) has been used widely before by Slatter [8, 9], Riguard [29] and Shipway [72] to predict the total volume loss of materials when the configuration of impact is a point contact. The following equation was used to represent the total volume loss estimation:

$$V_t = \pi h_l^2 \left( R - \frac{h_l}{3} \right) \quad 5.1$$

where  $V_t$  is the total volume loss,  $h_l$  is the scar depth measured by 3D non-contact profilometer and  $R$  is the ball radius of the striker.

Then, by using Equation 5.1, the total volume loss estimated by spherical cap method was plotted against both number of cycles and impact angles as shown in Figure 5.6

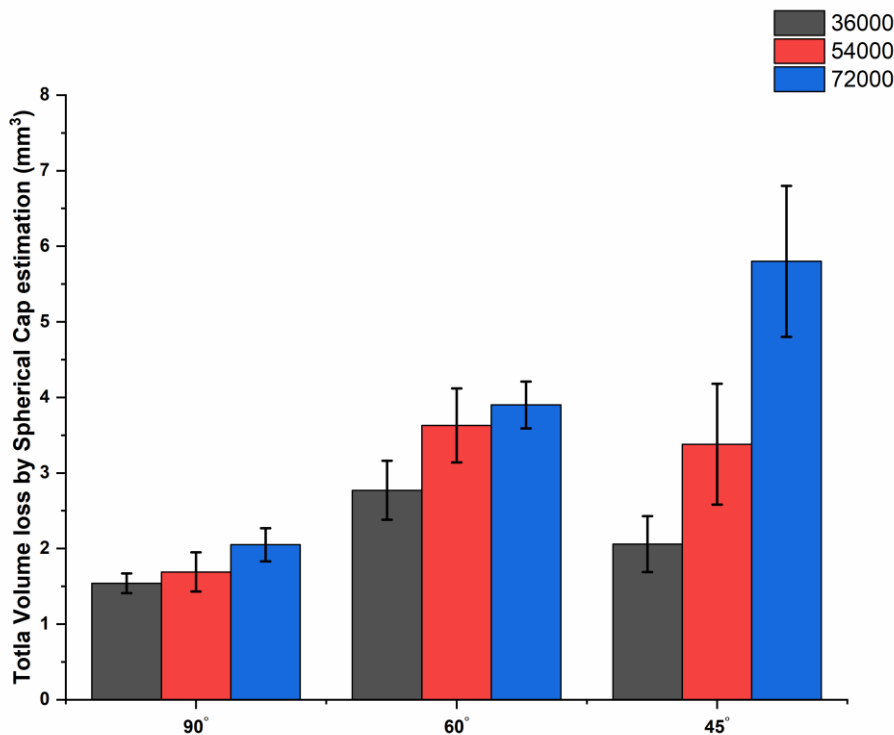


Figure 5.6 Total volume loss for AISI 304 calculated by spherical cap estimation Vs impact angles and number of impact cycles

The total volume loss measured by the spherical cap method revealed good agreement with the total volume loss measured by a 3D non-contact profilometer (Figure 5.3) under both normal and compound impact with different number of cycles and could therefore be used to predict the total volume loss of an impact wear scar for a point contact geometry.

A summary of total volume loss results by both methods is illustrated below in Table 5.3.

Table 5.3 Comparison of total volume loss measured by two different methods with different number of cycles and angles

Number of Cycles (N)	Impact Angle ( $\theta$ )	Mean Total Volume Loss by Alicona ( $\text{mm}^3$ )	Mean Scar Depth $h_1$ (mm)	Ball Radius R (mm)	Total Volume Loss by Spherical cap method ( $\text{mm}^3$ )	Error to Alicona %
36000	90°	2.08	0.257	7.5	1.54	26
54000	90°	2.1	0.269	7.5	1.69	19
72000	90°	2.18	0.297	7.5	2.05	5.9
36000	60°	2.87	0.345	7.5	2.77	3.78
54000	60°	3.75	0.395	7.5	3.63	3.86
72000	60°	3.91	0.41	7.5	3.9	0.5
36000	45°	2.35	0.294	7.5	2.06	14.4
54000	45°	3.28	0.38	7.5	3.38	-1.97
72000	45°	6.07	0.5	7.5	5.8	5.1

Table 5.3 shows that total volume loss measurements obtained by the spherical cap method achieved very good agreement with the 3D non-contact profilometer volume measurements, especially in the case of compound impact where the zero wear volume is at a minimum.

### 5.2.3 Impact Wear Scar Measurements

Dimension of the impact wear scar reflects the deformation level on the material surface and can be considered as one of the major parameters for determining the impact wear resistance of a material.

A 3D non-contact profilometer with 5 X objective was used during this work to examine the impact wear scar of specimens after impact under different impact conditions.

A typical profile measurement for the maximum depth of the wear scar was taken from typical specimens and plotted with different number of cycles and different impact angles as shown in Figure 5.7.

The profile trace was taken from the top to the bottom edge through the centre region of the scar for all specimens, where the bottom edge is on the right side in the figures and the top edge is on the left side in the figures. To ensure that the profile trace goes through the centre of the wear scar, a horizontal line was plotted first from right to left (maximum curve of the circle from right and left) just to mark the midpoint distance. Then a line was plotted from the point of maximum upper curve of the circle (top edge) goes through the marked midpoint in the centre to the bottom edge.

## Impact Wear and Damage Mechanism of Austenitic Stainless Steel 304

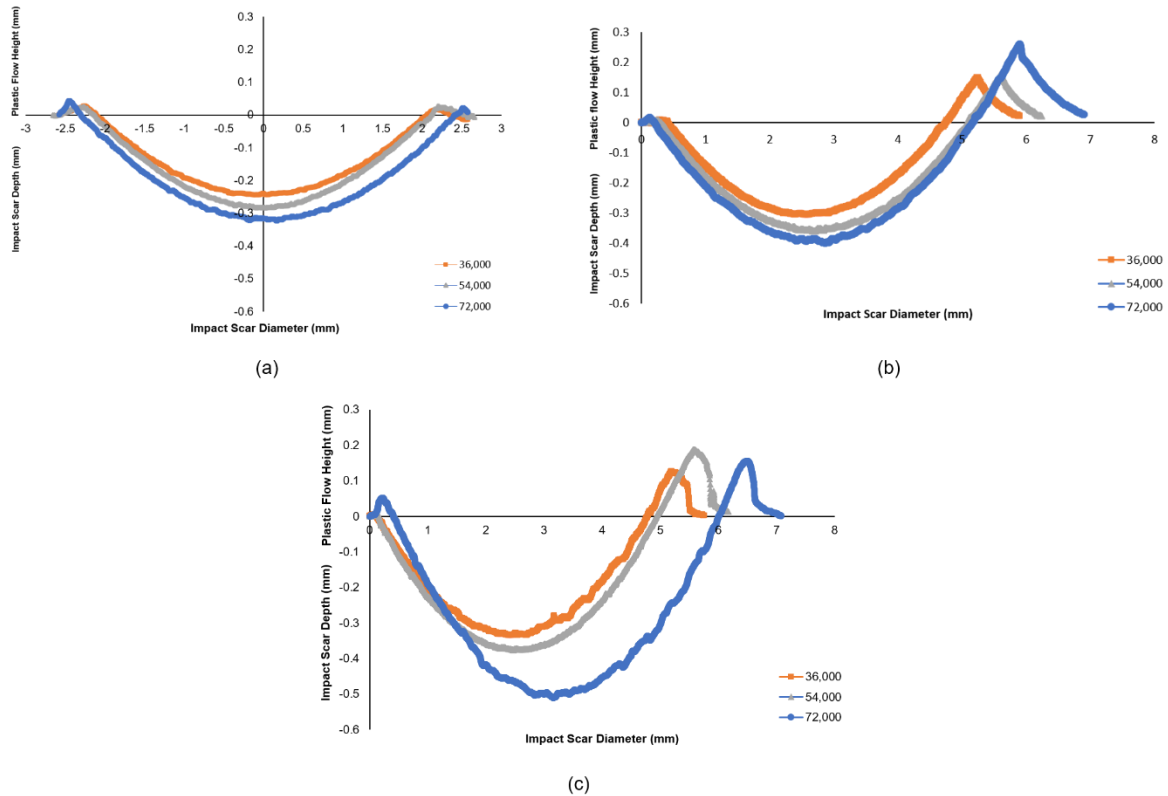


Figure 5.7 Typical diametric and depth of the wear scar with different cycles for AISI 304 under (a) normal impact, (b) compound impact 60° and, (c) compound impact 45°

Figure 5.7 (a) shows that the typical impact scar diameter and depth increased slightly with increasing number of cycles under normal impact due to the good mechanical properties that made the surface's hardened layer more resistant to wear. The surface structure became rougher after 72,000 cycles across the scar, and a small amount of pile up material (plastic flow) had formed on both edges of the impact wear scar with increasing the number of impact cycles, but the height did not exceed 50  $\mu\text{m}$ .

Figure 5.7 (b) reveals that the impact wear scar diameter and depth increased with increase in the number of cycles under compound impact 60°. The bottom edge of the impact scar was elevated by significant amount of plastic flow (shoulders) with height exceeding 200  $\mu\text{m}$ , indicating significant plastic deformation with the direction of impact. The amount of plastic flow increased in line with the number of cycles, and a rough surface was obvious after the 54,000 and 72,000 cycles.

Figure 5.7 (c) is similar to Figure 5.7 (b) except that a significant increase in impact wear scar diameter and depth occurred between 54,000 cycles and 72,000 cycles with an impact angle of 45° due to surface degradation. It seems that fracturing of the material's surface layer and material shearing off led to excessive wear loss, and a very rough and uneven surface can be seen at both the 36,000 cycles and 72,000 cycles across the scar, with a relatively smooth surface after 54,000 cycles. The plastic flow height was less than with compound impact at 60° and did not exceed 180  $\mu\text{m}$ , regardless of the impact angle.

The impact wear scars after testing could be easily seen by the naked eye. In general, across all tested specimens, the wear scars were regular in shape (circular) regardless of the number of cycles and the impact angle.

The three-dimensional morphology of typical impact wear scar is summarised in Figure 5.8 which shows the resulting impact wear scar of AISI 304 impacted by a steel chrome ball at impact force of 3476 N and impact velocity of 0.62 m/s with different number of cycles (36,000, 54,000, 72,000) and different impact angles ( $90^\circ$ ,  $60^\circ$ ,  $45^\circ$ ). The 3D images illustrate the typical depth of the scar (up to  $600\ \mu\text{m}$ ) as well as the plastic flow (up to  $300\ \mu\text{m}$ ).

Differences could be observed in all the scars among the range of applied parameters, with increase in the number of cycles leading to a slight increase in the amount of plastic flow on the impact wear scars in addition to a small increase in the impact wear scar size.

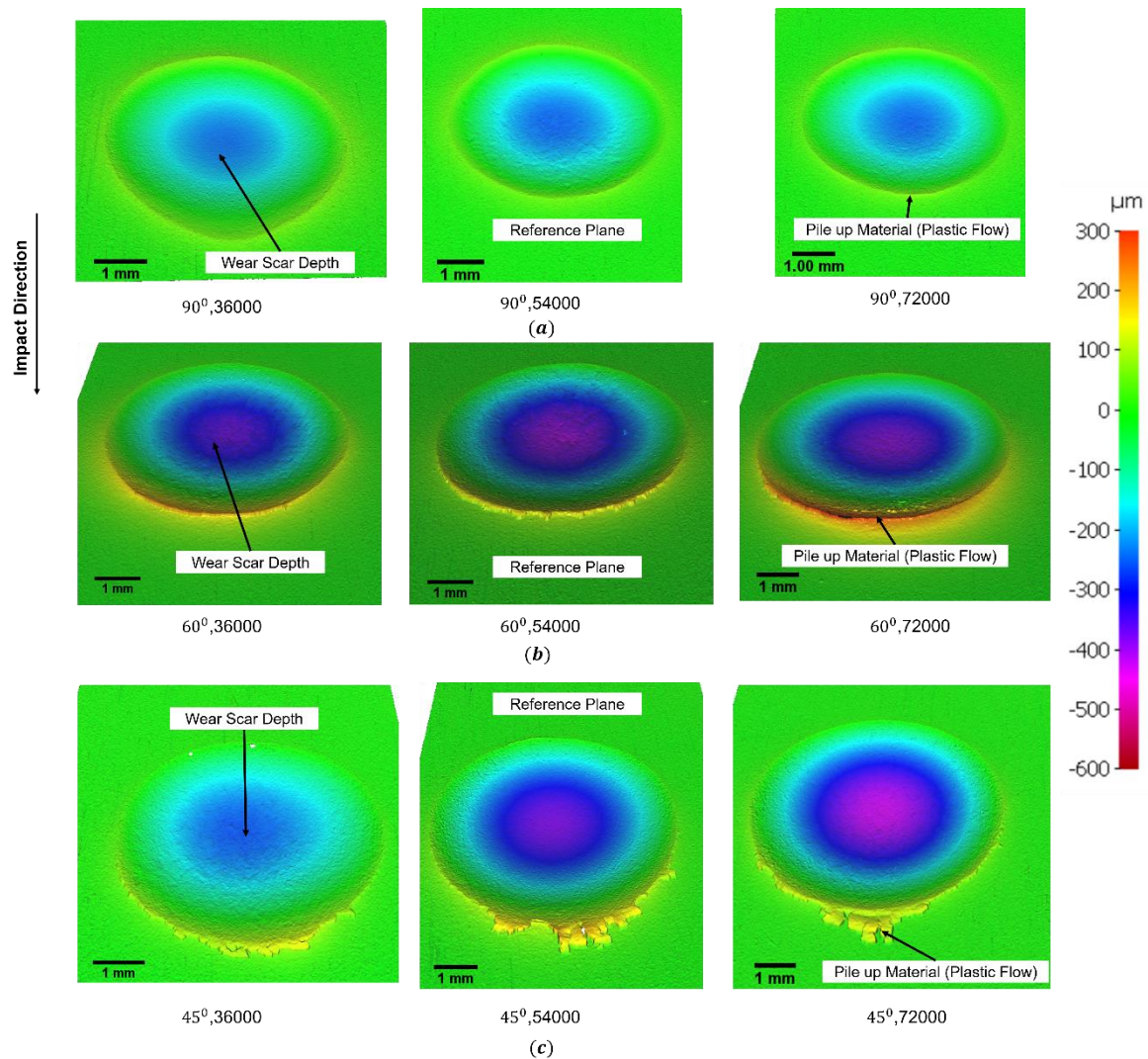


Figure 5.8 3D Image of typical depth and pile up profile of impact scars for material with different impact conditions: (a) under normal impact  $90^\circ$ , (b) with impact angle  $60^\circ$ , (c) with impact angle  $45^\circ$

Figure 5.8 shows that increasing the number of cycles led to a slight increase in both depth and pile up of scar materials under normal impact, while changing the impact condition from normal to compound impact caused a significant amount of plastic flow to form at the bottom edge. As explained earlier, this was due to plastic deformation and impact direction and accompanied by a noticeable increase in wear scar depth.

It should be noted that the impact scar matches with the striker ball which implies that the ball did not break or move during impact, as was confirmed when inspecting the ball after testing.

The green regions in Figure 5.8 indicate the reference plane of the scanned surface, while the positive surface above the reference plane (yellow and orange regions) represents the pile up materials and the negative surface below the reference plane (turquoise, blue and purple regions) represents the depth of impact wear scar.

Figure 5.8 shows that the pile up materials (plastic flow) are uniform in shape at the bottom edge with an impact angle of  $60^\circ$ , while with an impact angle of  $45^\circ$  it was extruded outside the contact region. by the effect of higher shear forces. Two different measurement techniques were used to detect the 3D results by 3D non-contact profilometer (spherical and rectangular plane) and both methods consistently produced the same results.

### 5.3 Wear Scar Analysis

#### 5.3.1 Surface Examination

The wear and deformation behaviour were studied by using a SEM (Hitachi TM3030 Plus) to investigate the surface damage of worn specimens with different number of cycles and angles. The centre of the wear scar was investigated during this work in addition to further regions of interest. The lack of data about the surface damage of austenitic stainless steel in general and AISI 304 in specific with different impact angles as described in Section 2.2.2.1 was the motivation for this investigation. Figure 5.9 which presents the typical impact wear scar of AISI 304, shows the regions described in this thesis.

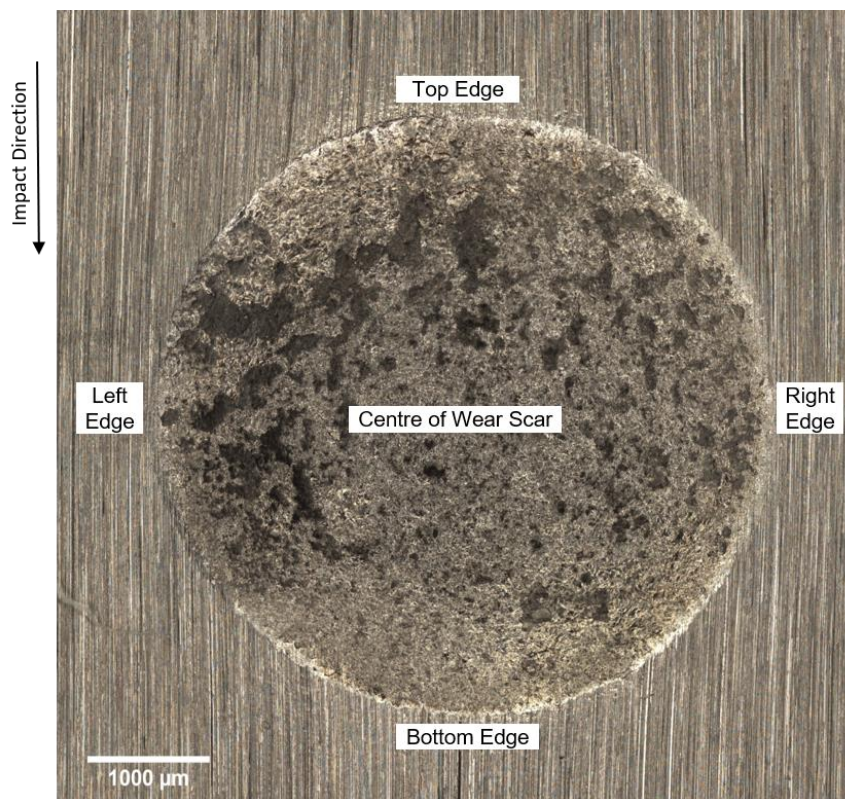


Figure 5.9 Typical 2D image of AISI 304 shows the centre and the edges of wear scar

### 5.3.1.1 Normal Impact (90°)

The main wear damage mechanism after 36,000 cycles was plastic deformation as explained earlier in Chapter 4 (see Figure 2.14 (c) and Figure 4.15 (c)). Figure 5.10 presents the SEM micrograph of a typical worn surface of an impact wear scar after 54,000 cycles under normal impact at the centre region.

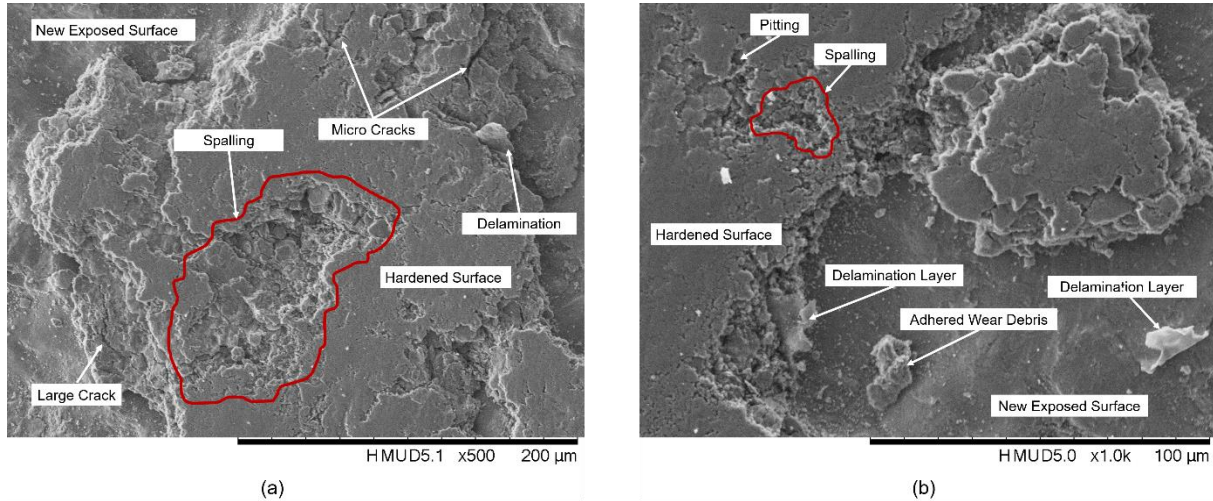


Figure 5.10 SEM micrograph of worn surface for material after 54,000 cycles under normal impacts reveals the centre of impact wear scar

Referring to Figure 5.10, SEM examination of the selected regions revealed spalling, in addition to plastic deformation. Micro pitting was found on the worn surface and delaminated hardened surface layers appeared. These layers would eventually form a new fresh substrate with clear boundaries and visible hardened layer.

The edges between the hardened surface and new exposed surface, regardless of location, underwent severe damage and spalled into small particles. It seems that crushing occurred on these surface regions that led to further surface failure as can be seen in Figure 5.11 which shows the centre of the wear scar with higher magnification.

A possible explanation for crushed particles phenomenon is that these regions underwent severe plastic deformation and a transition from being ductile to brittle happened during impact as the surface hardened, which reflect trends found by Tianmin [12].

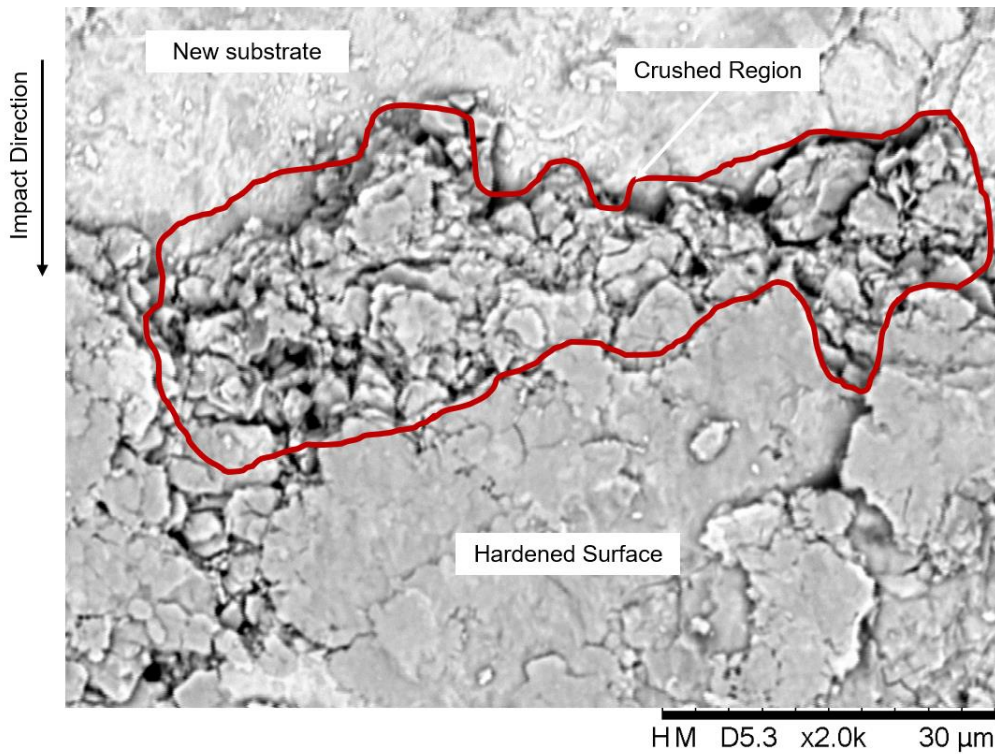


Figure 5.11 Crushed region between the hardened surface and new substrate in the centre of impact wear scar for material after 54,000 cycles

Further increase in the number of cycles to 72,000 led to further damage in the hardened surface as shown in Figure 5.12 (a) and Figure 5.12 (b) for the same region with higher magnification at the centre of the impact wear scar.

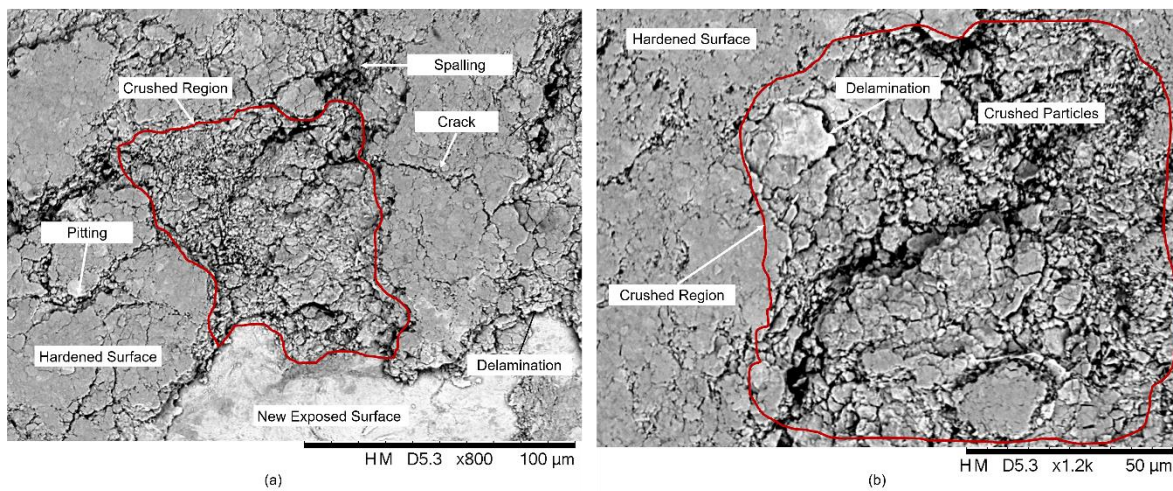


Figure 5.12 SEM micrograph of worn surface for material after 72,000 cycles under normal impacts reveals (a) the centre of impact wear scar and (b) higher magnification of (a) showing the crushed region highlighted in red

Figure 5.12 presents the damage to the impact wear scar region. Besides delamination, significant increase in the crushed region can be seen in Figure 5.12 (b) as a result of a series of micro cracks in the hardened surface due to continuous repetitive impact. The delaminated layers on the surface were highly deformed and extensively fragmented after 72,000 cycles as shown in Figure 5.13.

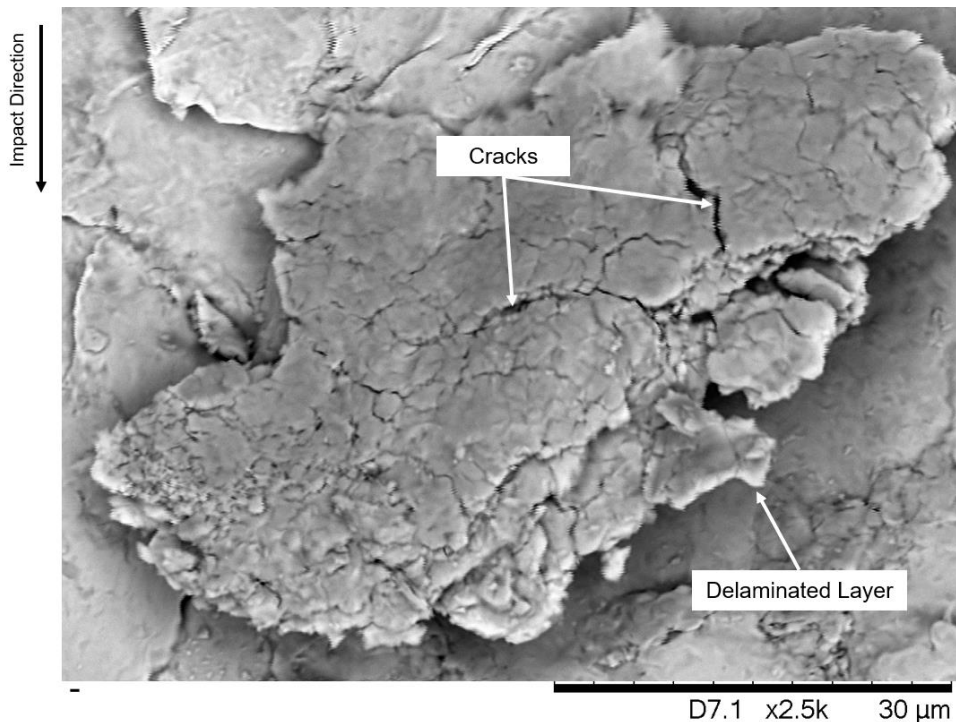


Figure 5.13 Extensively fragmented layer for material after 72,000 cycles

Since the increase in the number of cycles did not highly influence the amount of wear volume or the wear depth, it is likely that the strain hardened layer formed on the specimen surface is beneficial in prevention of further surface degradation. Examination of all the wear scar edges did not reveal any significant plastic flow volume, as shown in Figure 5.7 and Figure 5.8 under normal impacts and therefore have not been examined further.

### 5.3.1.2 Compound Impact (60°)

The surface damage to the material surface with compound impact was investigated in a similar way to normal impact. Figure 5.14 and Figure 5.15 present SEM micrographs of a typical worn surface of impact wear scar after 36,000 cycles under compound impact (60°).

Figure 5.14 shows that a different impact wear mechanism occurred in the case of the hardened surface, due to various features in the centre of the wear scar. The wear damage mechanism for the centre of wear scar is explained separately in Figure 5.14, while the plastic flow near the bottom edge is covered in Figure 5.15. All other edges did not show any noticeable amount of plastic flow and therefore, so have not been examined similarly to the normal impacts.

## Impact Wear and Damage Mechanism of Austenitic Stainless Steel 304

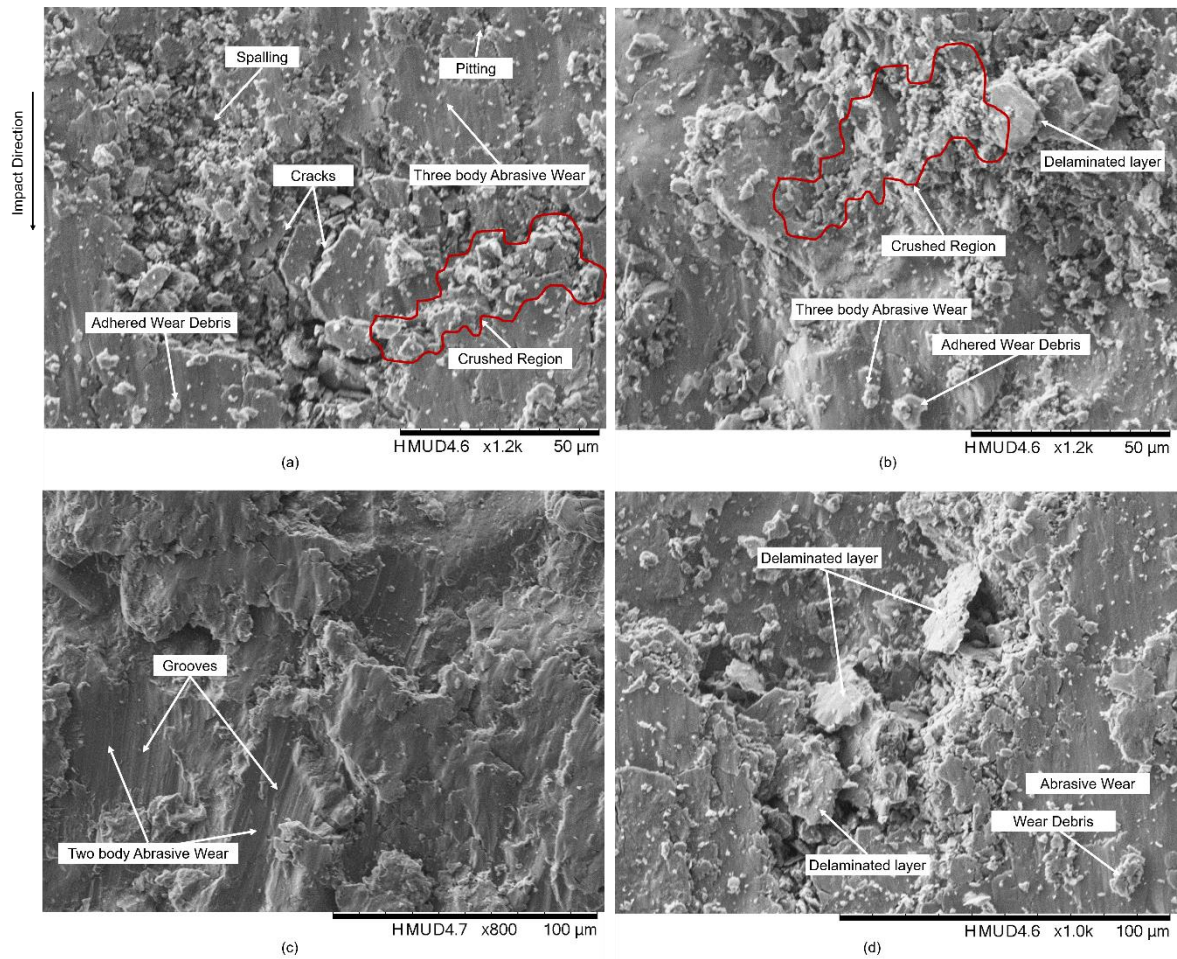


Figure 5.14 Wear damage mechanism for the centre of wear scar for material after 36,000 cycles under compound impact  $60^\circ$  where (a) and (b) show the abrasive wear and the crushed region, (c) and (d) show the ploughing process due to abrasive wear

Figure 5.14 shows that the main wear damage mechanism is surface fatigue (spalling and delamination), while abrasive wear also occurs during compound impact as two body and three body abrasive wear with obvious grooves apparent on the surface, as shown in Figure 5.14 (c), which explain the further increases in mass loss.

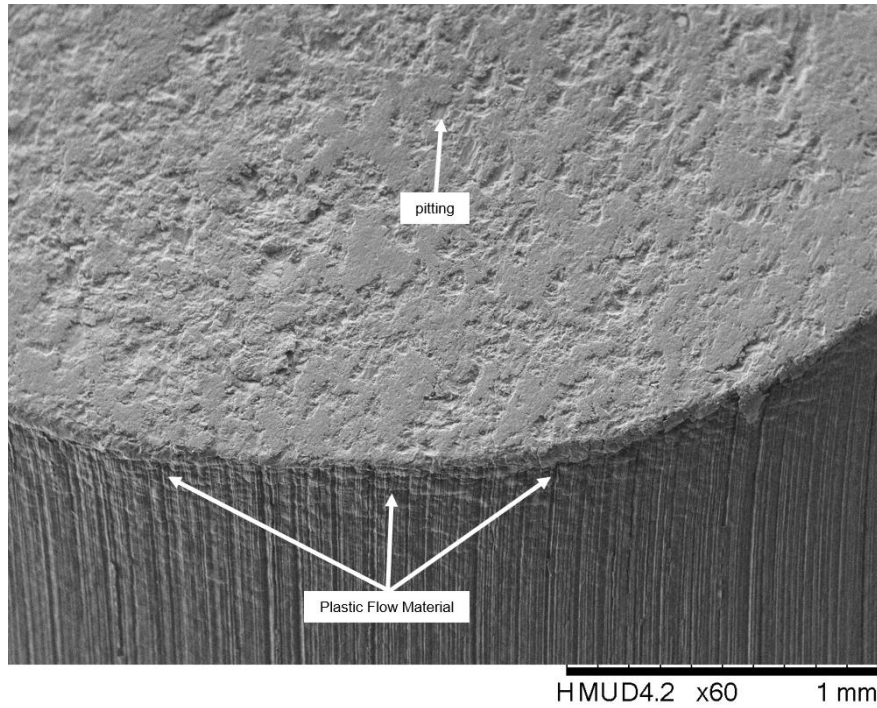


Figure 5.15 SEM micrograph of worn surface for material after 36,000 cycles under compound impact  $60^\circ$  reveals the bottom edge of the wear scar

Figure 5.15 shows a significant amount of plastic flow, the bottom edge revealed plastic flow distributed uniformly due to the effect of shear force with the direction of impact. Figure 5.16 shows the wear damage for the centre region of wear scar after 54,000 cycles while Figure 5.17 shows the plastic flow accumulated near the bottom edge.

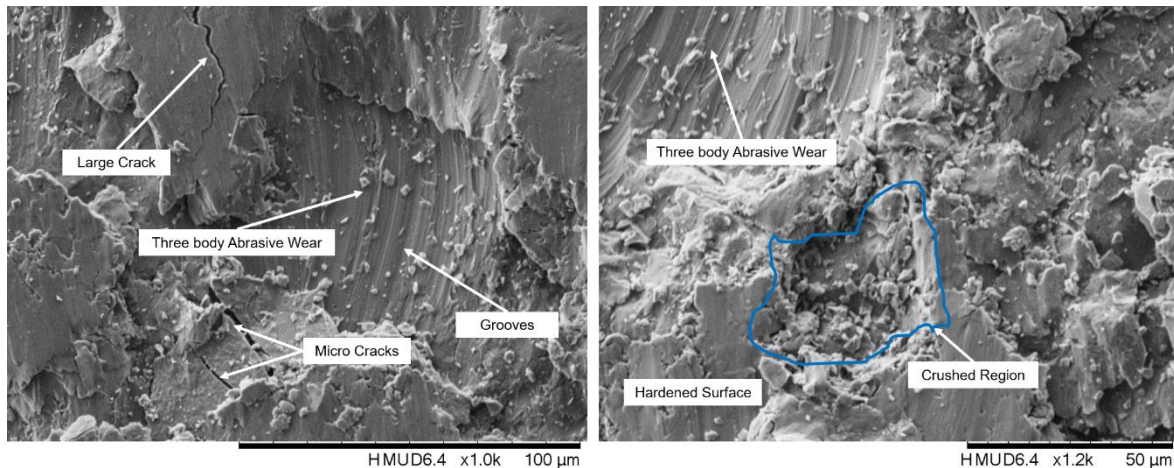


Figure 5.16 SEM micrograph reveals the worn centre regions of wear scar after 54,000 cycles under compound impact  $60^\circ$

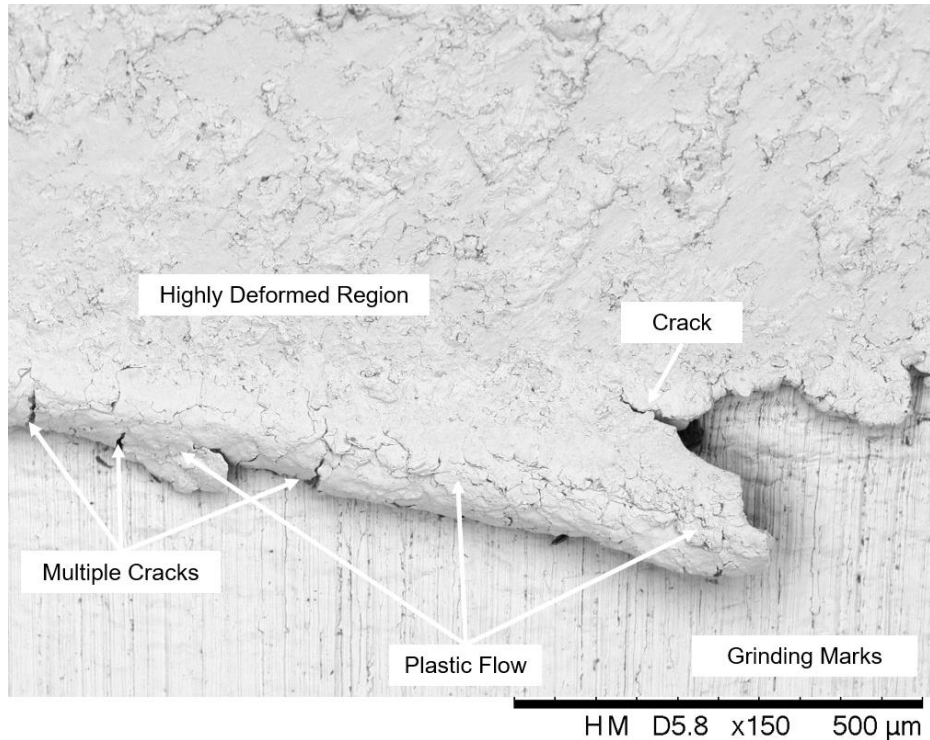


Figure 5.17 SEM micrograph reveals the accumulated plastic flow near the bottom edge of wear scar after 54,000 cycles under compound impact  $60^\circ$

Increasing the number of cycles to 54,000 led to occurrence of deeper three body abrasive wear on the surface of the worn specimen, with obvious grooves indicating the ploughing mechanism. Figure 5.16 revealed an obvious deep groove and three body abrasive wear as a result of small crushed particles trapped between the striker and the worn surface. Also, the crushed region, highlighted in blue, is apparent between the hardened surface and the new exposed surface.

Plastic flow ( Figure 5.17) had formed on the bottom edge with a series of cracks inside the plastic flow, indicating that with further number of cycles these cracks would propagate and eventually delamination would cause removal of layers from the bottom edge. None of the other edges exhibited significant amounts of plastic flow material.

The total number of cycles (72,000) showed no further features other than those described above and it is worth mentioning that all SEM images at  $60^\circ$  revealed noticeable layers of delamination on the surface of the wear scar between the centre and the bottom edge of the wear scar and closer to the bottom edge. The number and size of these delamination layers were increased significantly by increasing the number of cycles and became very obvious after 72,000 cycles, as seen in Figure 5.18.

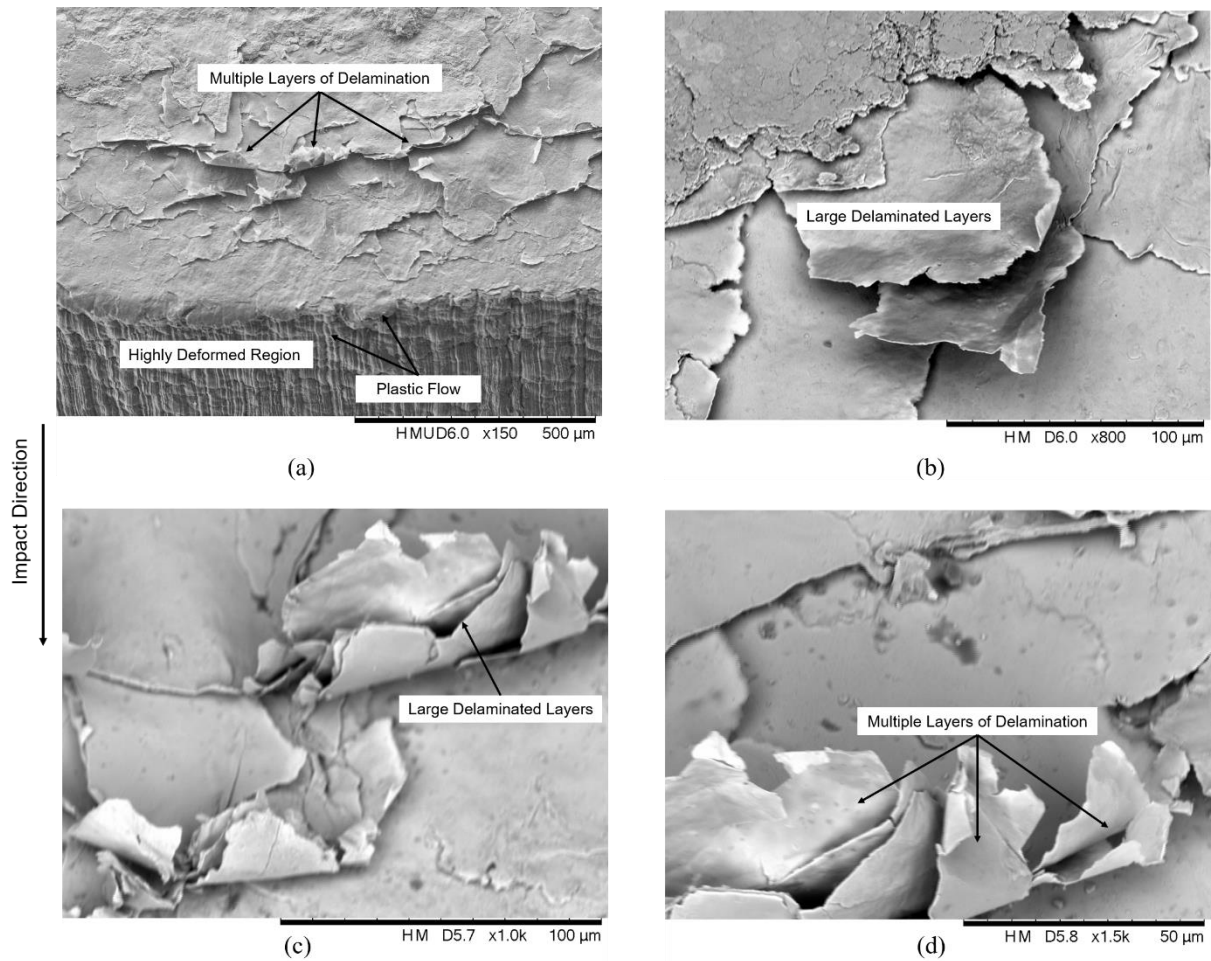


Figure 5.18 Multiple layers of delamination near the bottom of the wear scar for material after 72,000 cycles under compound impact  $60^\circ$  with different magnifications

Figure 5.18 presents the delaminated layers on the worn surface near the bottom edge with different magnifications. These multiple layers of delamination that remained on the surface can be explained as the role of friction force in resisting the motion between the striker and the worn surface, the friction resistance being highest at  $60^\circ$  when compared with an impact angle of  $45^\circ$ . These delaminated layers do not exist with normal impact near the bottom edge as the contact is frictionless.

### 5.3.1.3 Compound Impact $45^\circ$

SEM images of worn surfaces for the specimen with an impact angle of  $45^\circ$  were investigated with different number of cycles as shown in Figure 5.19 after 36,000 cycles for the centre of the wear scar, while the bottom edge is shown in Figure 5.20.

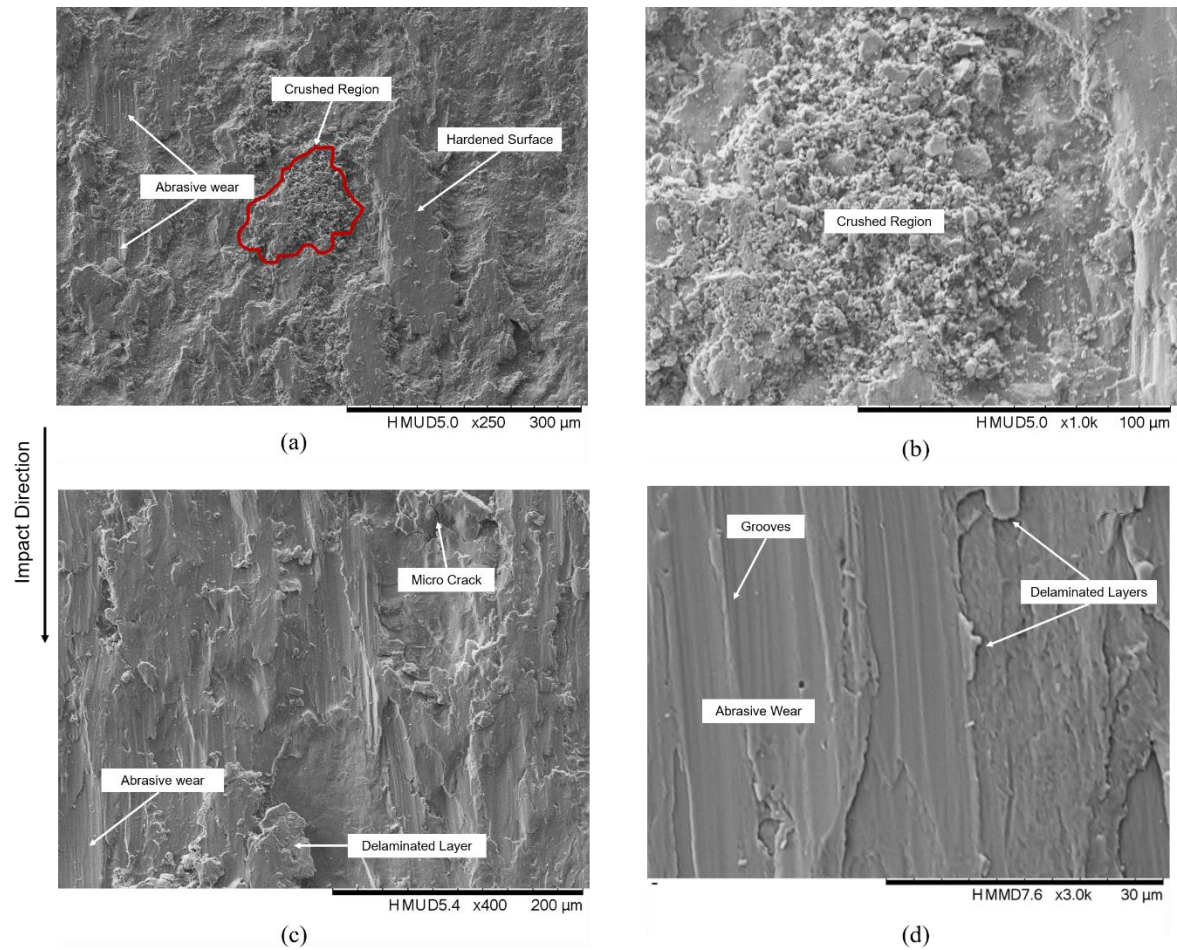


Figure 5.19 SEM micrographs of worn surface for material after 36,000 cycles under compound impact  $45^\circ$  revealing the different wear damage mechanisms for the centre of wear scar where (a) and (b) shows the crushed particles while (c) and (d) reveals the abrasive wear and grooves

Figure 5.19 shows that after 36,000 cycles, the abrasive wear is the predominant type of wear damage that occurs to the worn surface besides surface fatigue. Crushed regions that cause pitting and eventually spalling are obvious in (b) which shows the crushed regions in (a) at higher magnification, (c) reveals the abrasive wear and delamination, (d) shows higher magnification of the eventual abrasive wear with obvious grooves and delaminated layers.

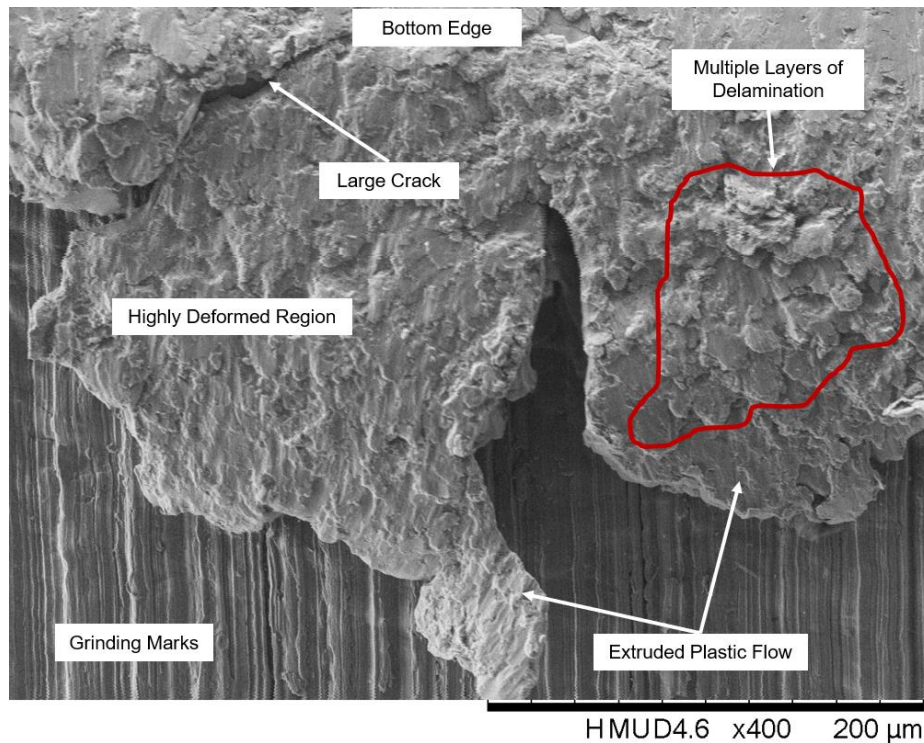


Figure 5.20 SEM micrograph of worn surface for material after 36,000 cycles under compound impact  $45^\circ$  revealing the bottom edge of the wear scar

Figure 5.20 shows that the pile up of materials on the bottom edge gives a slightly different result. Rather than being distributed uniformly as with  $60^\circ$ , it seems that higher shear force led to extrusion of the piled up materials parallel to the direction of impact outside the contact region.

These highly deformed materials had undergone multiple layers of delamination on a small scale, highlighted with a red line in Figure 5.20, and also large cracks were obvious on the bottom edge that would lead eventually to a large chunk of material leaving the surface. This trend was not observed with the other impact angles of  $90^\circ$  and  $60^\circ$  and explains the further damage and the increase in mass loss that occurred to the material.

As the number of cycles increased to 54,000, further degradation (with slightly less rate as in normal impact) to the surface occurred, as shown in Figure 5.21; however, the wear damage mechanism was quite similar to that shown previously in Figure 5.19 for the centre of the wear scar and shown in Figure 5.22 for the bottom edge.

Figure 5.21 shows the main wear damage mechanisms for the centre of the impact wear scar are surface fatigue (spalling and delamination) in addition to two and three body abrasive wear as a result of small particles trapped between the striker and the surface.

Impact Wear and Damage Mechanism of Austenitic Stainless Steel 304

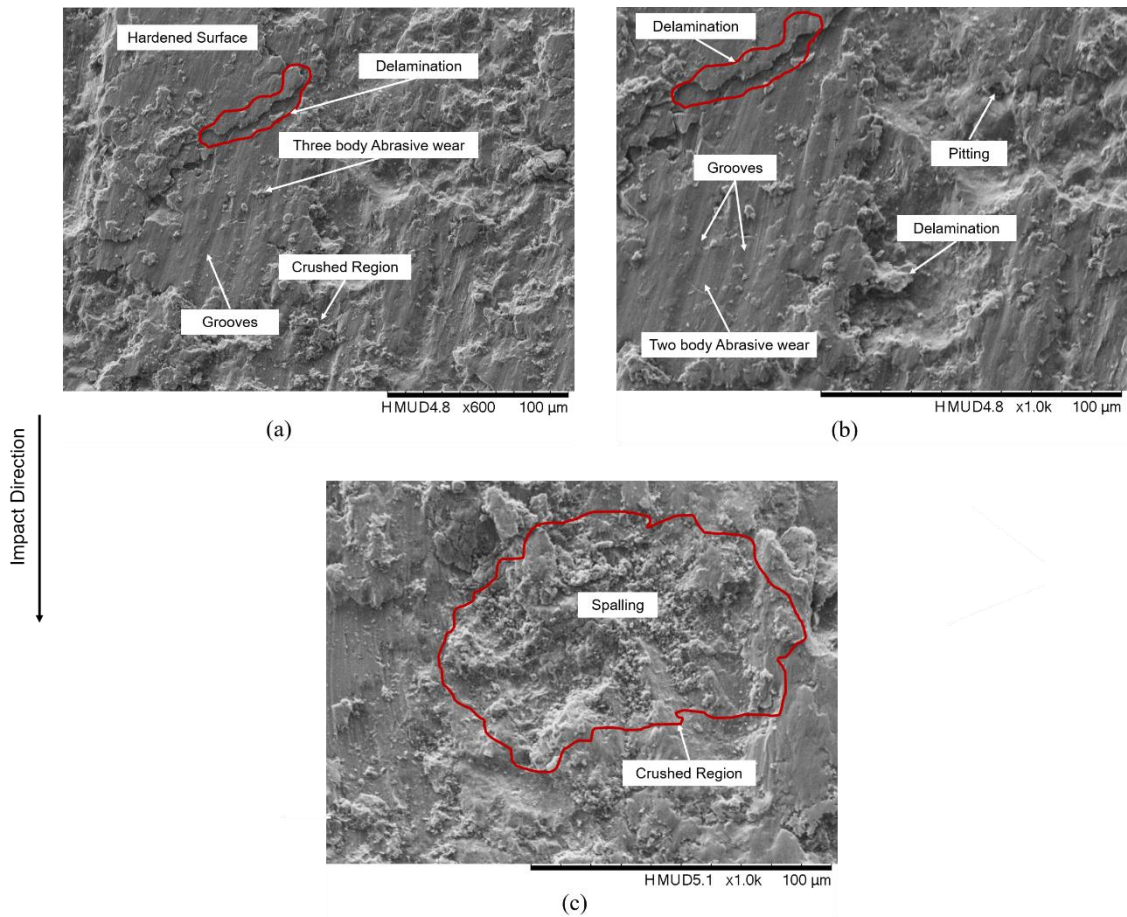


Figure 5.21 SEM micrograph of worn surface for material after 54,000 cycles under compound impact 45° revealing different wear damage mechanisms for the centre of wear scar

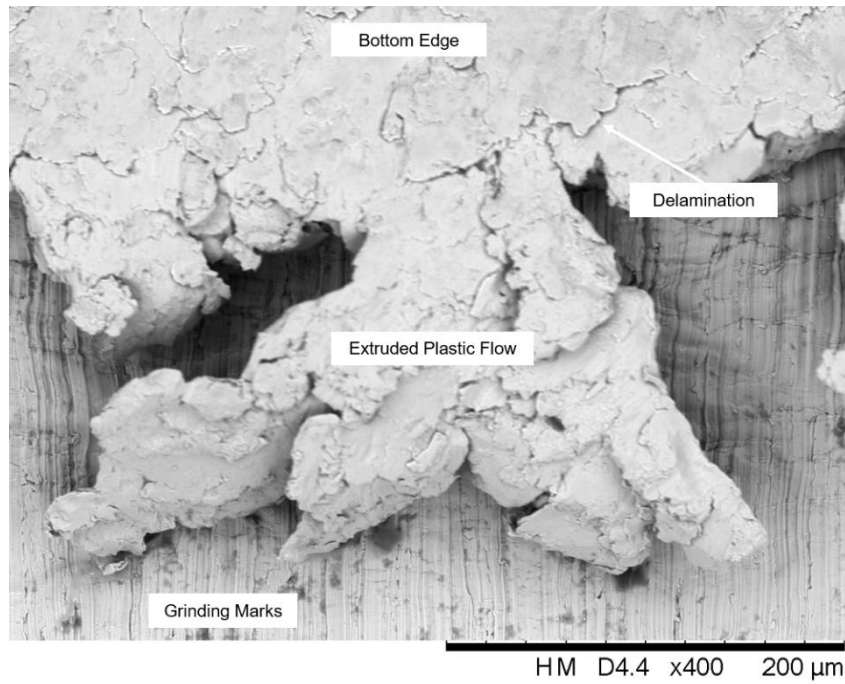


Figure 5.22 SEM micrograph of worn surface for material after 54,000 cycles under compound impact 45° revealing the bottom of wear scar

Figure 5.22 shows that all edges underwent abrasive wear similar to the previous number of cycles and the bottom edge has a little delamination and extruded plastic flow outside the contact region. From 54,000 cycles to 72,000 cycles the surface suffered further degradation (with a higher rate than in normal impact) as can be seen in Figure 5.23.

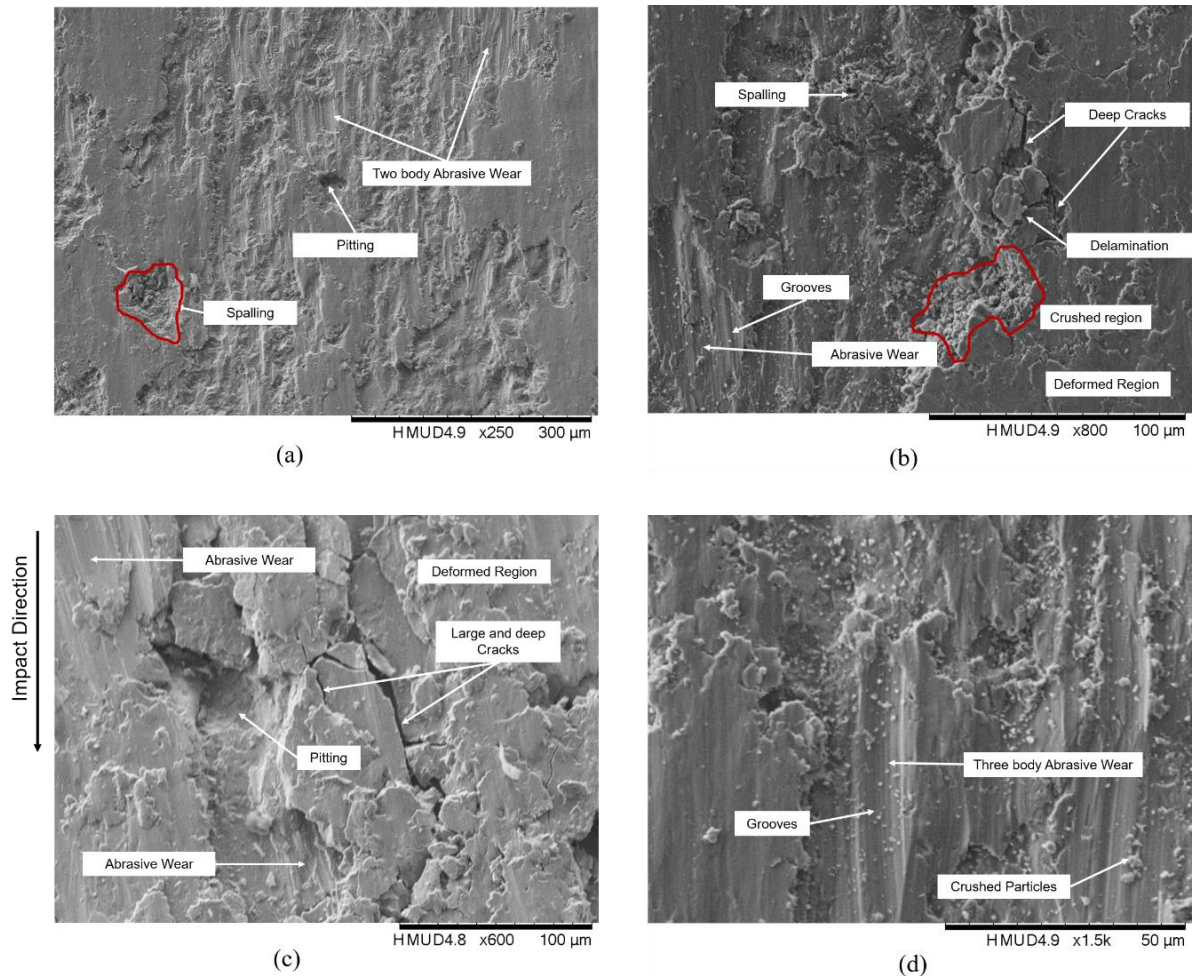


Figure 5.23 showing wear damage mechanism for the centre of wear scar of for material after 72,000 cycles under compound impact 45° where (a) shows pitting and two body abrasive wear, (b), (c) and (d) shows an obvious multiple cracks, crushed particles and abrasive wear with grooves

The centre of wear scar underwent further surface degradation, the presence of more crushed particles trapped on the surface accelerated the three body abrasive wear across a wider range and caused further damage, while the large and deep cracks on the surface indicate that larger and thicker layers of materials were delaminated from the surface. This explains the dramatic increase in wear loss from 54,000 cycles to 72,000 cycles as shown in Section 5.2.1 (Figure 5.1); and all edges showed the same features as explained above in relation to Figure 5.20 and Figure 5.22.

### 5.3.2 Subsurface Examination

Section 2.2.2.1 and Section 2.5.1 described that information is lacking about the likely subsurface damage of AISI 304 with different impact angles including; the crack initiation and propagation, their orientation, grain size, grain orientation during impact and the depth of plastic region. This section addresses this that and broadens the understanding of repetitive impact wear for AISI 304.

### 5.3.2.1 Crack Initiation and Propagation

During impact on a material specimen, high deformation occurs to both the surface and subsurface which affects the microstructure of these regions. The initiation, propagation and coalescence of cracks during the wear process are important processes to be investigated.

All samples were centrally cross sectioned parallel to the direction of impact as shown in Figure 3.14 and metallographically prepared to reveal the damage on the subsurface microstructure. Since the surface examination shows clearly the cause of wear damage with different impact angles and the number of cycles did not change the nature of wear damage mechanism. Therefore, the crack initiation and propagation was examined after 72,000 cycles, where the maximum wear loss occurs, and to confirm the surface examination results.

Well-polished, but not etched samples, were examined first by SEM to detect the damage to the subsurface for different number of cycles and different angles, in order to reveal mechanisms of interest and support the surface examination.

The crack initiation and propagation was examined on the subsurface of the specimen in the centre regions of the wear scar, where maximum impact force and stresses occur, to detect the damage mechanisms in addition to further regions of interest. The purpose was not to study the crack growth in terms of fracture theories, rather to identify the crack location and their propagation under different impact angles. Figure 5.24 shows the cross-section morphology of a specimen after 72,000 cycles under normal impact.

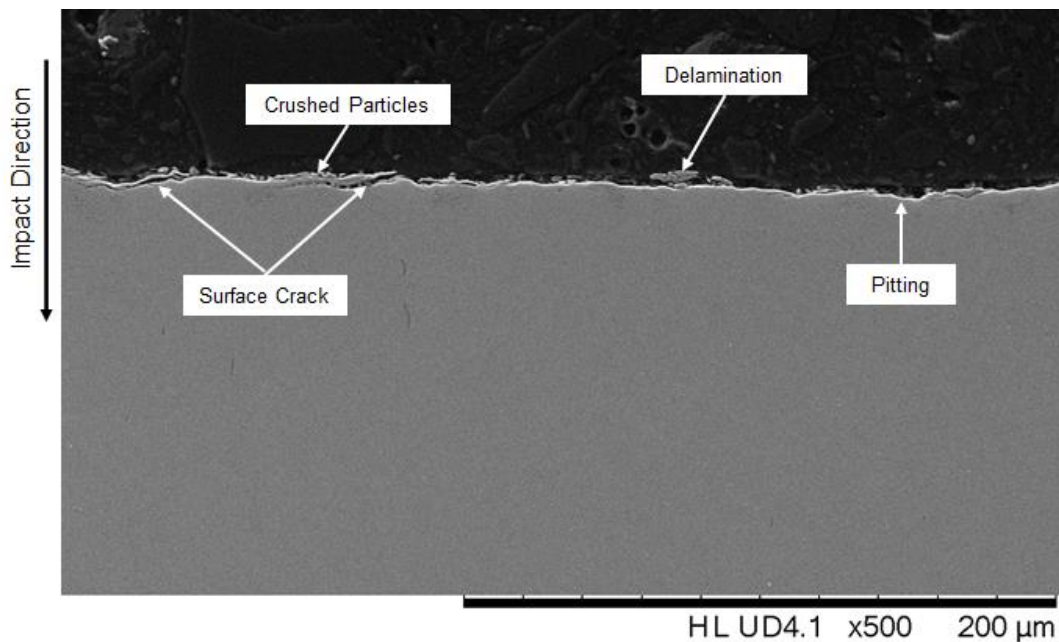


Figure 5.24 SEM image for material after 72,000 cycles under normal impact showing delamination and pitting

Figure 5.24 shows that the delamination of layers started with surface cracks (initiated at the surface, propagating beneath the surface at a steep angle and then turning parallel to the surface), with joining up of several cracks possibly leading to loss of materials as delamination layers and pit formation. These surface cracks are similar to the one found in welded rail and steel materials (see Figure 2.3-d and Figure 2.8) under normal impacts. Crushed particles were also found on the worn surface of AISI 304, these particles happened due to reduce in ductility and became more brittle.

The impact angle, as explained in Figure 5.1 and Section 5.3.1, highly affected the wear loss results and the change from normal impact of  $90^\circ$  to compound impact of  $60^\circ$  led to an increase in mass loss. Subsurface examination of the centre region of the wear scar at the compound impact of  $60^\circ$  showed a noticeable increase in the length of the delaminated layers after 72,000 cycles, represented by larger subsurface major cracks connected together by minor surface cracks, in addition to a large crushed region, as shown in Figure 5.25.

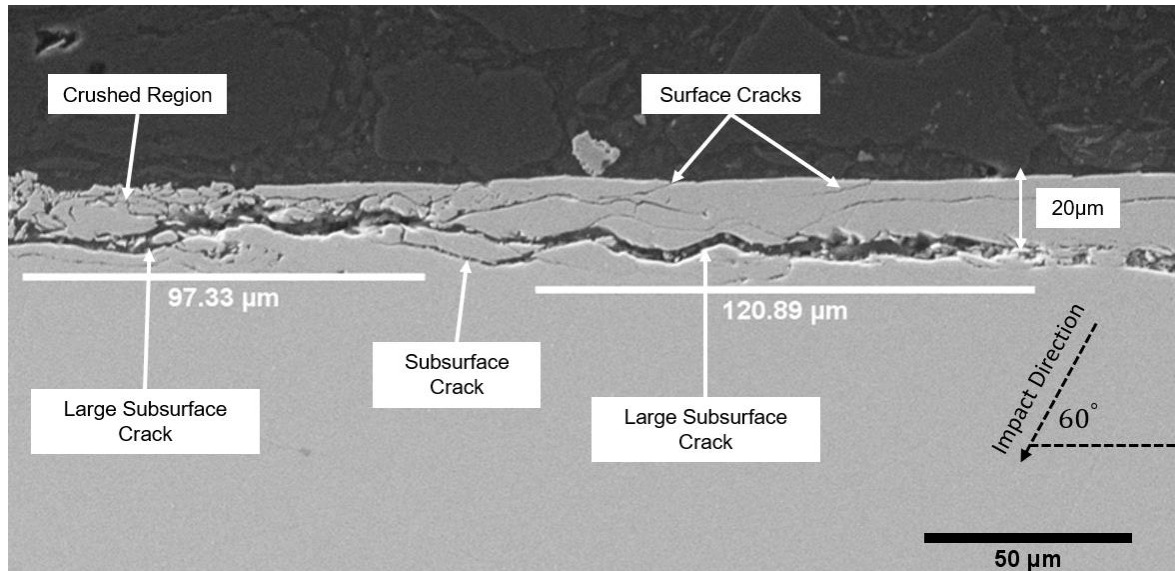


Figure 5.25 SEM image of subsurface damage for material after 72,000 cycles under compound impact  $60^\circ$

Figure 5.25 reveals that two large subsurface major cracks have connected together to cause a large delamination. In addition to these two large cracks within the delamination, minor surface cracks have initiated and propagated beneath the surface of the delaminated layers and these subsurface cracks have joined up to cause further damage. The surface and subsurface crack initiation and propagation are similar to the one found for medium carbon steel with compound impact (see Figure 2.7 (a)).

The obvious crushed region shown on the left side of Figure 5.25 and in higher magnification in Figure 5.26 can be explained as a reduction in ductility in these regions which were highly deformed because of work hardening. These crushed regions started within the delaminated layer in all cases, with small cracks initiating mostly from the surface and then propagating both normal to the plane (spalling) and parallel to the plane (delamination), and eventually these particles left the surface as wear debris or adhered to the surface.

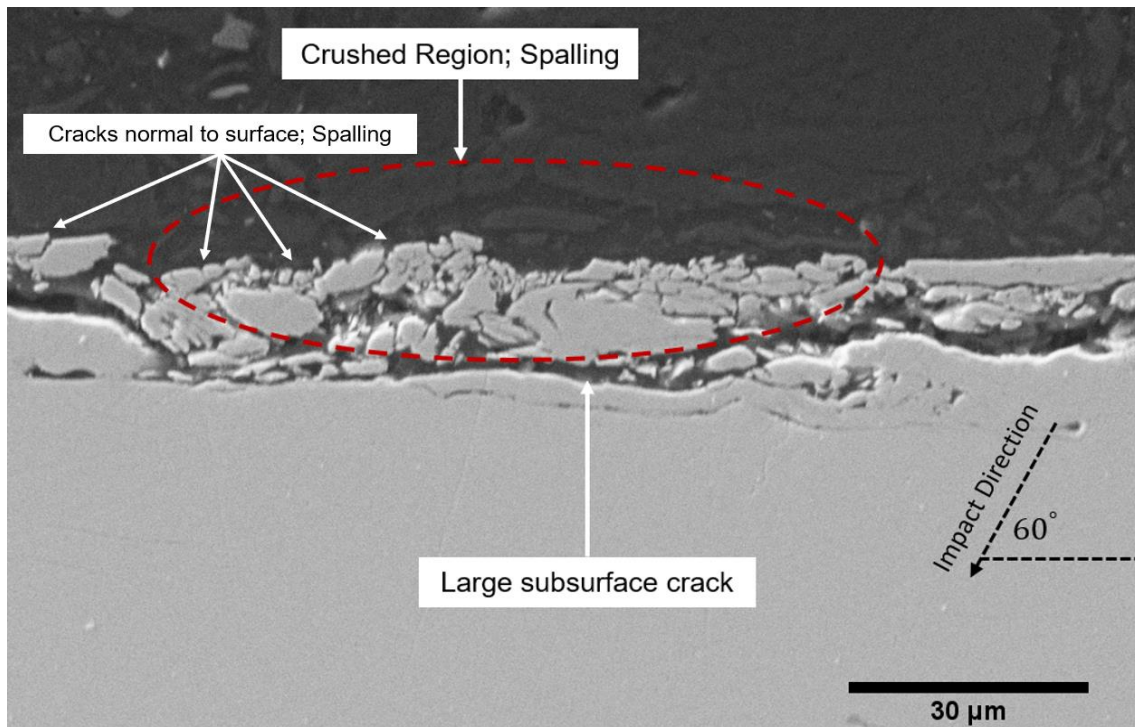


Figure 5.26 SEM image of subsurface damage for material after 72,000 cycles under compound impact  $60^\circ$  showing the crushed region in the centre of the wear scar

Significant layers of delamination were found during subsurface examination near the bottom edge and this supports the previous surface examination (see Figure 5.18), in addition to crushed particles within these delaminated layers after 72,000 cycles, as seen in Figure 5.27. Figure 5.28 shows the multiple layers of delamination that occurred near the bottom edge.

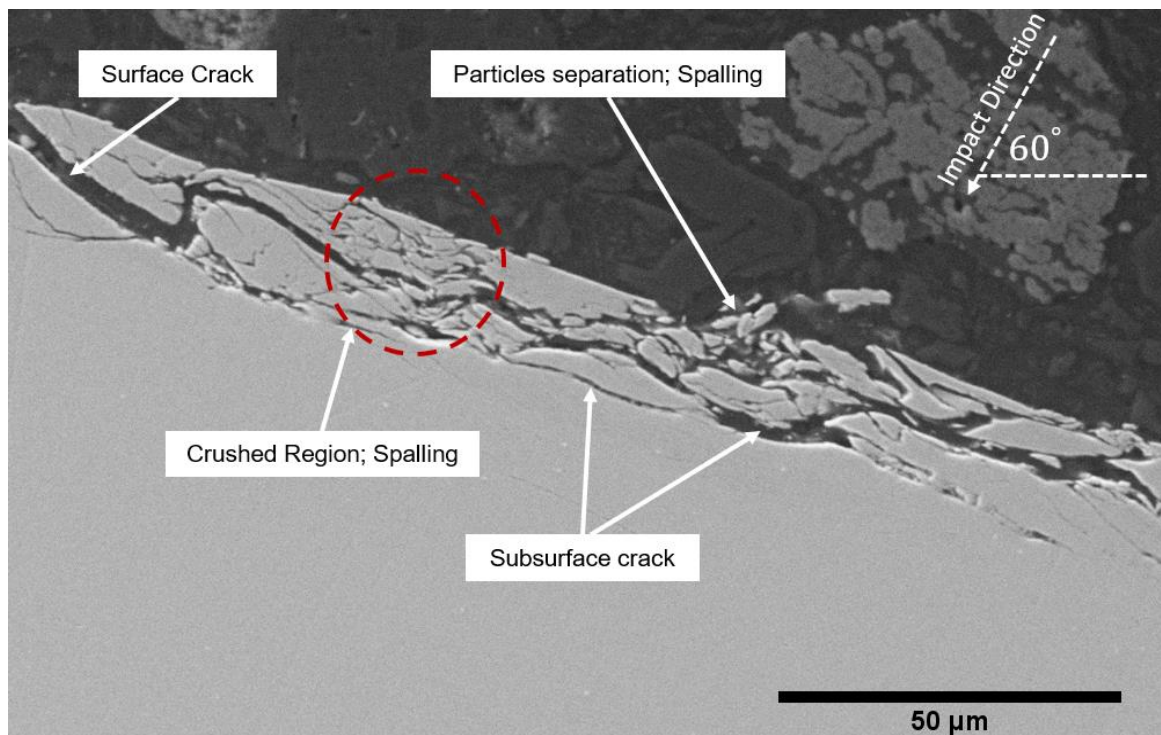


Figure 5.27 SEM image of large delamination layer due to subsurface crack for material after 72,000 cycles under compound impact  $60^\circ$  with crushed particles

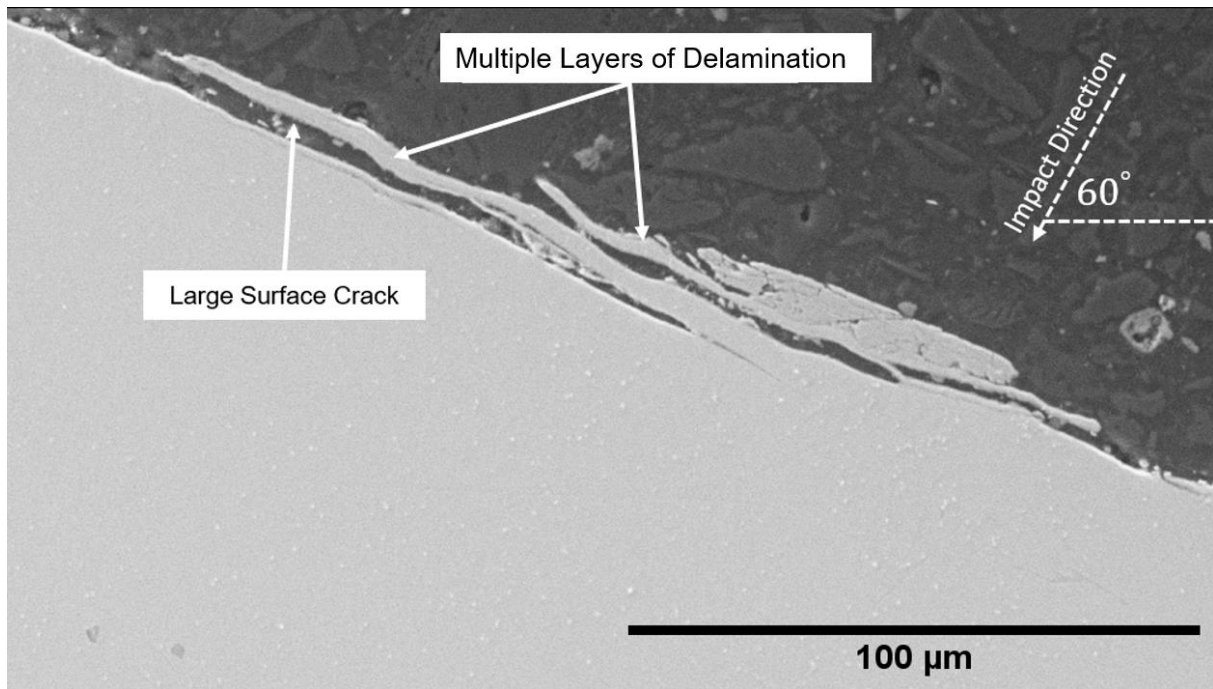


Figure 5.28 SEM image showing multiple layers delamination for material after 72,000 cycles under compound impact  $60^\circ$  near the bottom edge

Figure 5.27 shows the separation of particles from the delaminated layer which is extensively deformed in a region falling between the centre of the wear scar and the bottom edge. These particles would cause spalling as a result of micro pitting. The accumulation of plastic flow at the bottom edge, shown in Figure 5.29, was caused by the tangential force and sliding that occurred during impact.

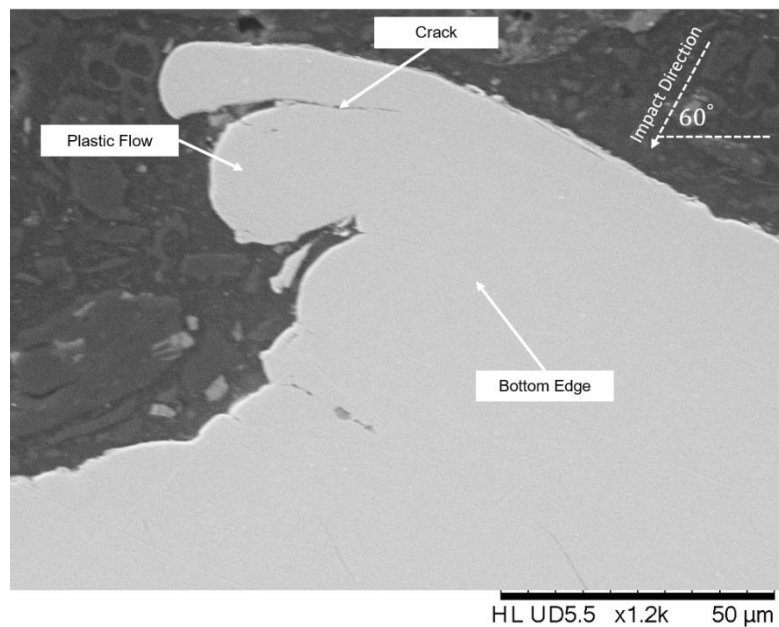


Figure 5.29 SEM image of plastic flow on the bottom edge of the wear scar for material after 72,000 cycles under compound impact  $60^\circ$

At an impact angle of  $45^\circ$ , more hardened layers were removed from the surface by the effect of higher shear force compared with an impact angle of  $60^\circ$  after 72,000 cycles, with delamination occurring due to crack propagation parallel to the surface, as shown in Figure 5.30.

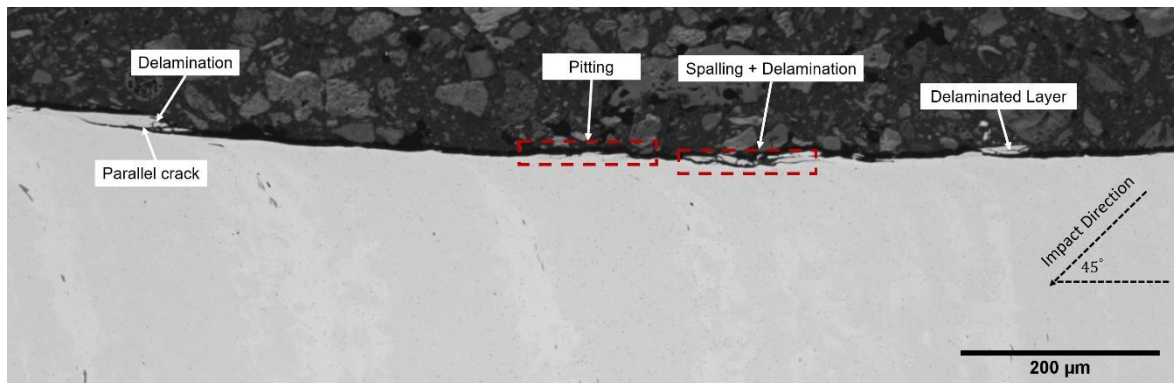


Figure 5.30 Optical microscope image showing the wear damage mechanism for material after 72,000 cycles under compound impact  $45^\circ$

Figure 5.30 shows moderate delamination with crack network which may not alone be responsible for the significant increase in mass loss compared with normal impact or with impact angle of  $60^\circ$ . As a result of an increase in the tangential force with an impact angle of  $45^\circ$ , more plastic flow was extruded outside the wear scar rather than being deformed uniformly as with an impact angle of  $60^\circ$ . Figure 5.31 shows an example of pile up materials that were extruded outside the wear scar after 72,000 cycles.

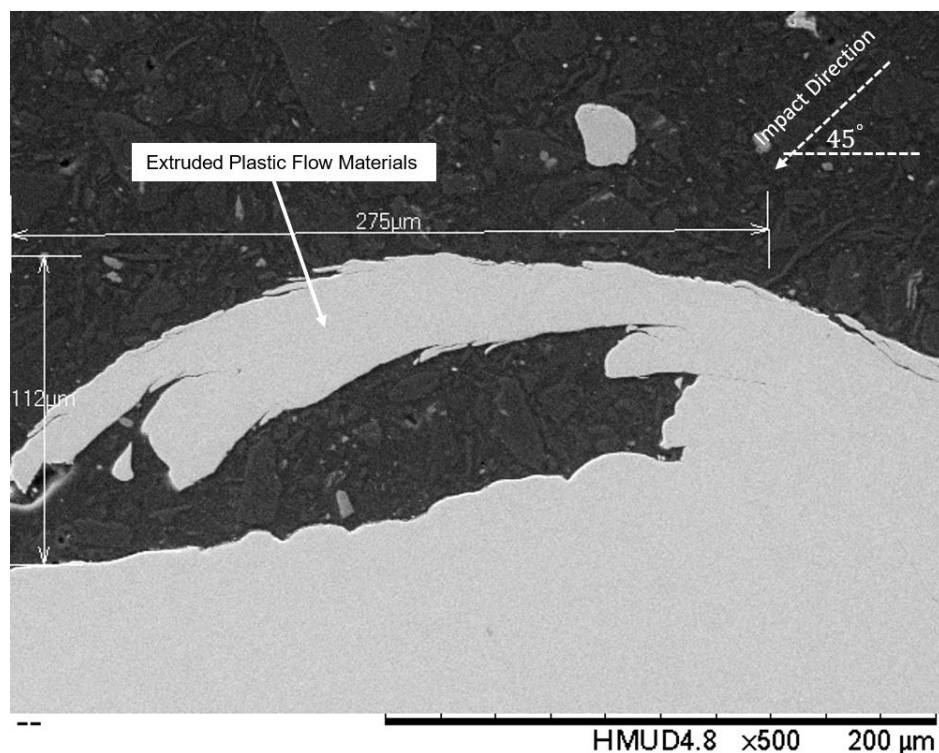


Figure 5.31 SEM image of pile up materials extruded outside the wear scar for material after 72,000 under compound impact  $45^\circ$

Surface examination revealed that abrasive wear at both impact angles ( $60^\circ$  and  $45^\circ$ ) highly influenced the results (see for example Figure 5.16 and Figure 5.23) and since the initial sectioning was parallel to the surface, the abrasive wear damage was not detected during subsurface examination.

Therefore, further work was carried out on three typical specimens subjected to different impact angles ( $90^\circ$ ,  $60^\circ$ ,  $45^\circ$ ) after 72,000 cycles by sectioning perpendicular to the impact direction, to attempt to detect the abrasive wear that occurs during compound impact as shown in Figure 5.32.

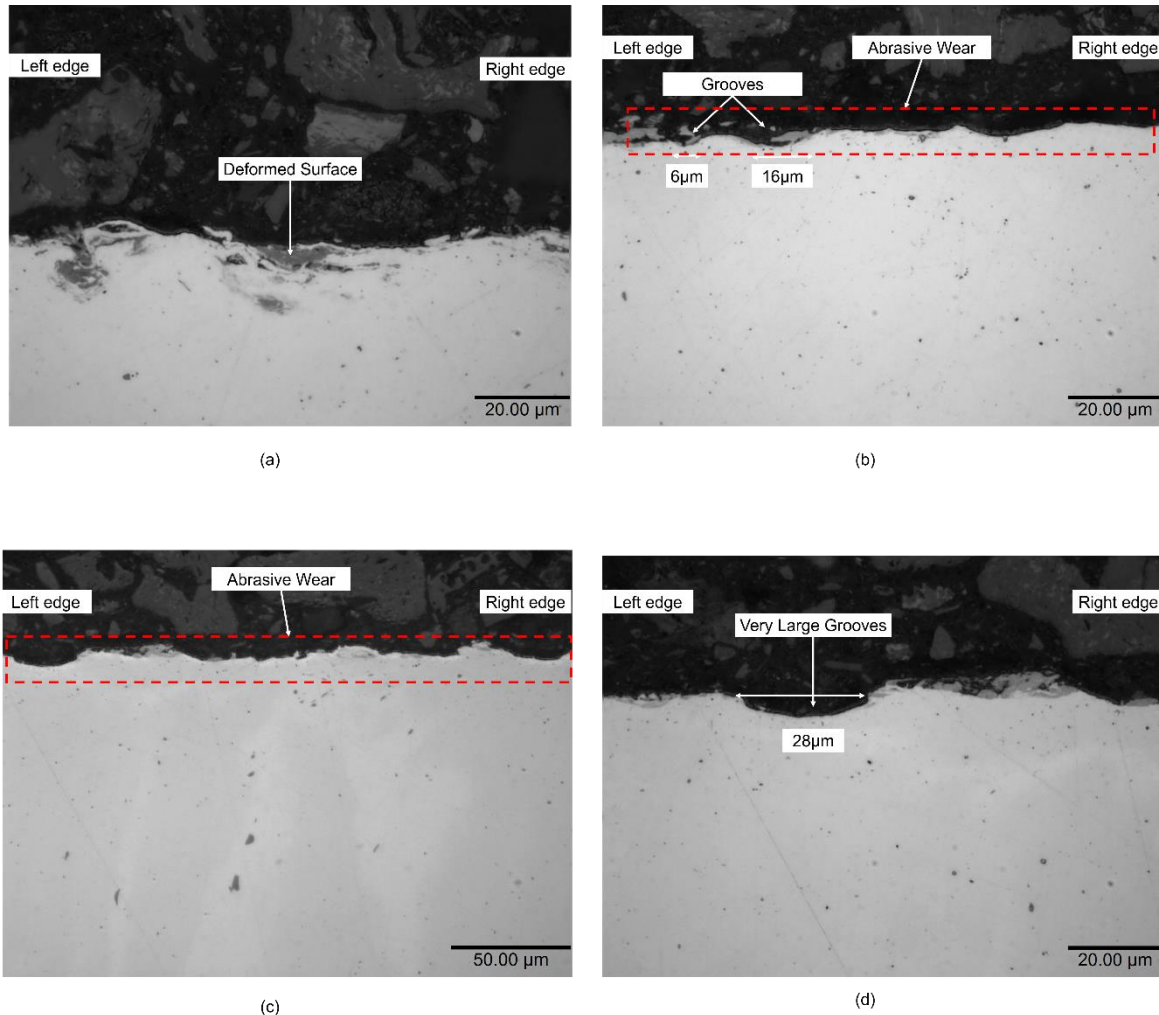


Figure 5.32 Optical microscope images with perpendicular sectioning to the impact direction for the centre of wear scar of three specimens showing the wear damage at: (a) normal impact  $90^\circ$ , (b) compound impact  $60^\circ$ , (c) and (d) compound impact  $45^\circ$  after 72,000 cycles

The results of perpendicular sectioning revealed, as expected, that no abrasive wear occurred with normal impact since there is no tangential component during impact and the contact is purely compressional in nature. For an impact angle of  $60^\circ$ , abrasive wear occurred (Figure 5.32 (b)) with a series of grooves that tended to be small in general compared with an impact angle of  $45^\circ$ , where the highest shear forces occurred, a significant increase in the width and depth of grooves resulted from abrasive wear of those at  $60^\circ$ , as shown in Figure 5.32 (d). These large grooves at an impact angle of  $45^\circ$  explain the further damage and mass loss that happened during impact and contributed to the abrasive wear and supporting the surface results (see Figure 5.19; Figure 5.21; Figure 5.23).

### 5.3.2.2 Electro Etching

Electro etching was carried out during this work for AISI 304 which has an austenite microstructure with average grain size diameter ( $22.5 \mu\text{m}$ ), as explained in Section 3.7.4.1, to detect the grain orientation, deformed grains and the depth of plastic region during impact with different impact angles, such investigation has not been reported before in the literature.

Figure 5.33 shows an image of the wear scar which, due to the scar's large size, was taken by an optical microscope, after 72,000 cycles under normal impact. It was necessary to cover the centre regions of the wear scar which showed the most important features, and reflect the subsurface examination for normal impact (see Figure 5.24).

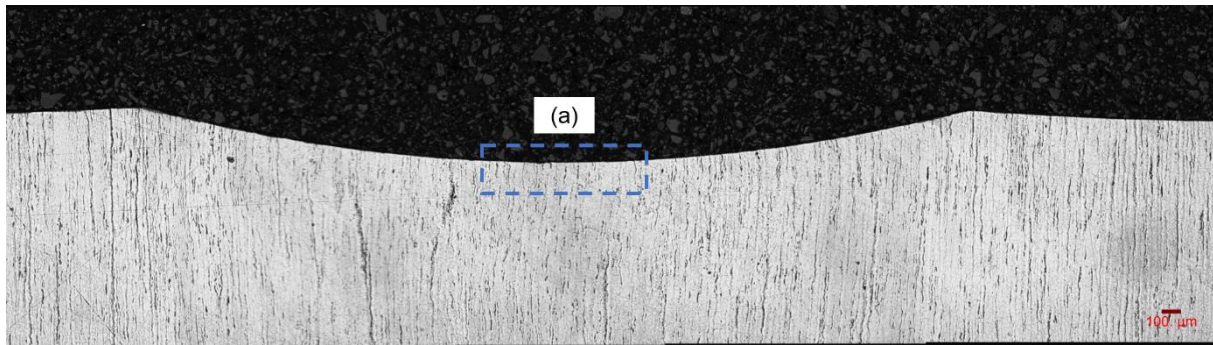


Figure 5.33 Cross sectional optical microscope image for AISI 304 after 72,000 cycles under normal impact showing centre region of wear scar

Both an optical microscope and SEM were used to detect the wear damage on the samples. Figure 5.34 shows that after 72,000 cycles, the microstructure has been deformed by the effect of the impact wear process and the deformed grains have reached a depth of approximately  $65 \mu\text{m}$ . Below this depth the effect of the impact wear process (IW) has decreased with increase in distance from the surface.

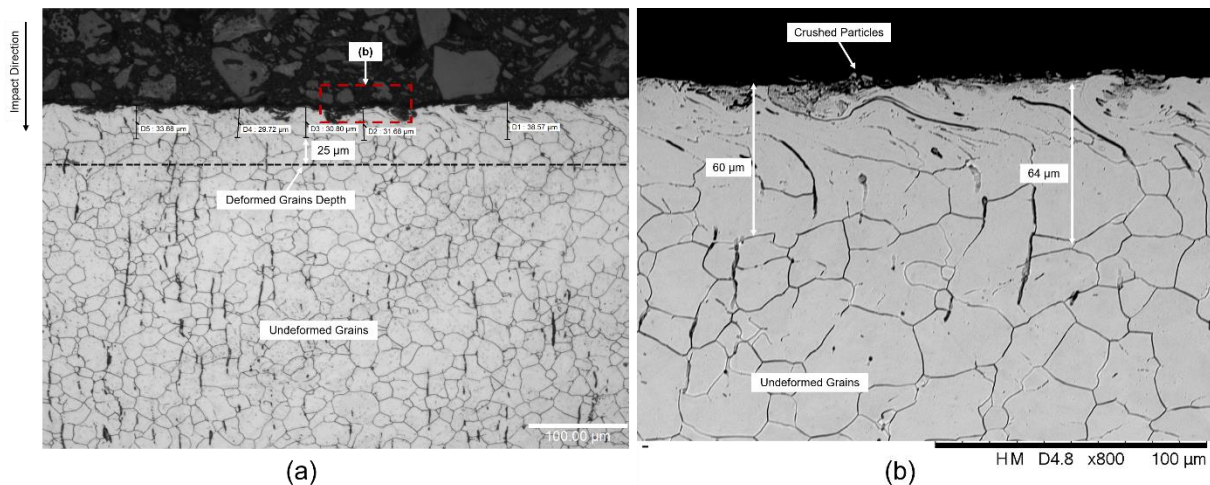


Figure 5.34 Electro etching for material under normal impact for the centre of the wear scar: (a) after 72,000 cycles showing the deformed and undeformed grains, (b) showing the red dotted region in (a)

Figure 5.7; Figure 5.8; Figure 5.29; and Figure 5.31 showed clearly that only the bottom edge of the wear scar accumulated a significant amount of plastic flow for both impact angles ( $60^\circ$  and  $45^\circ$ ), while at the other edges there was no noticeable accumulation of plastic flow. Therefore, two regions (centre and bottom edge) were investigated during the etching process for both angles. Electro etching revealed

three obvious regions in the centre of the wear scar after 72,000 cycles at impact angle  $60^\circ$ , as seen in Figure 5.35.

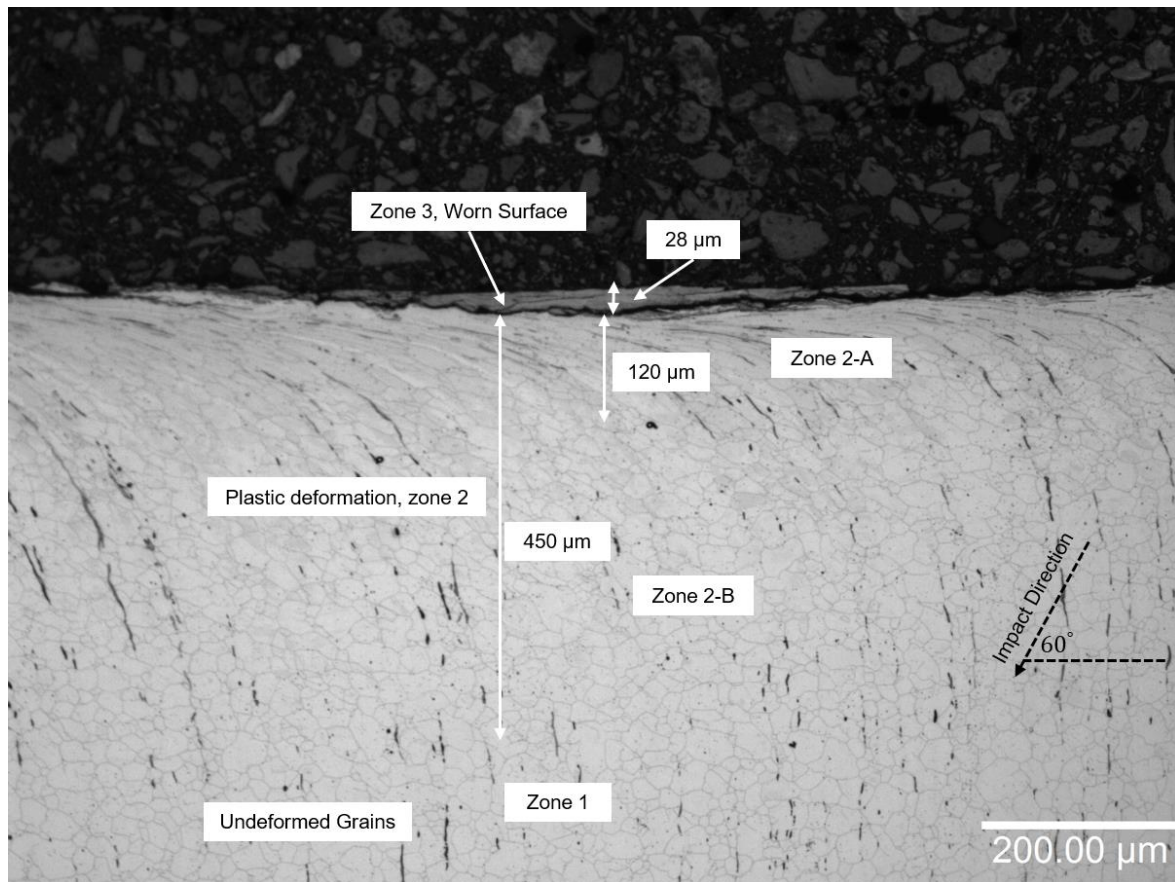


Figure 5.35 Optical microscope image of electro etching for material under compound impact  $60^\circ$  showing the centre of the wear scar after 72,000 cycles showing the impact wear zones

Figure 5.35 reveals three characteristic regions similar to those revealed previously in Figure 2.9. The deepest part of the substrate consists of undeformed grains (zone 1); the second region is the plastic deformation region (zone 2) and the worn surface layer is zone 3.

The plastic deformation region extends to approximately  $450\ \mu\text{m}$  depth and consists of two parts: zone 2-B is the less deformed region, where the grain boundaries can be revealed. Above this region there is an area of highly deformed grains (zone 2-A) where an obvious change in grain orientation has occurred with sliding direction due to the effect of tangential force (shear force) and confirming its role during compound impact. It extends to approximately  $120\ \mu\text{m}$  in depth and the grain boundaries are not easy to detect by etching because of the higher level of deformation compared to zone 2-B. Zone 3 is the worn surface layer and has been severely deformed by the impact wear process. Cracks can be seen in this region and it can be easily distinguished from zone 2-A because of the large parallel cracks. The grain boundaries were not detected by etching since this region has the highest level of deformation. Figure 5.36 shows the wear damage mechanisms that could affect the worn surface layer of the material at an impact angle of  $60^\circ$ . It shows that the worn surface layer (zone 3) about to separate from the surface by the effect of large parallel surface cracks that led to large delamination layer. Within this delaminated layer, the normal cracks and the small parallel cracks will lead eventually to further surface fatigue damage (delamination and spalling).

## Impact Wear and Damage Mechanism of Austenitic Stainless Steel 304

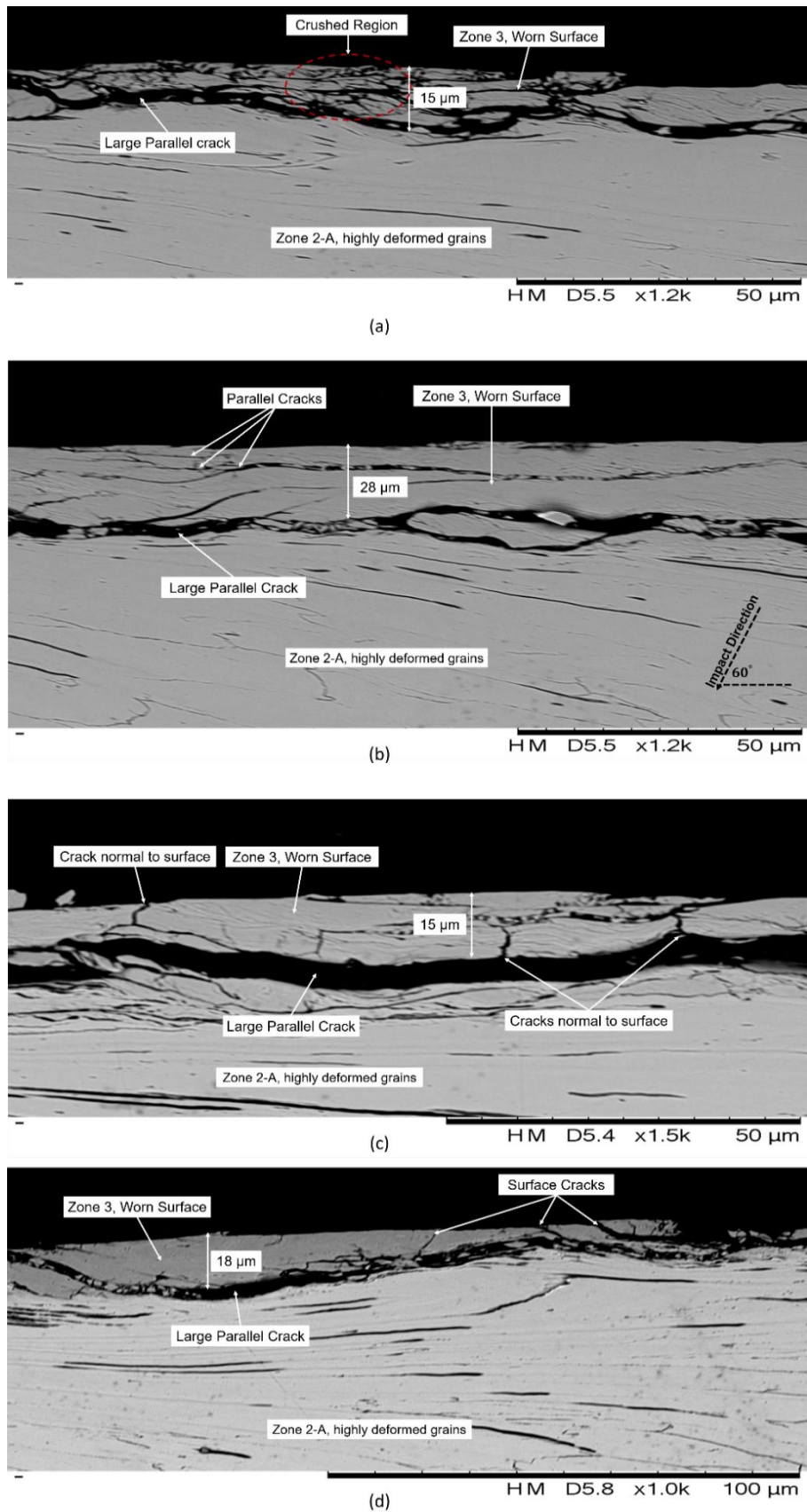


Figure 5.36 SEM images revealing wear damage mechanisms affecting the worn surface layer (zone 3) for material under compound impact 60° where (a) shows the crushed region, (b) reveals the parallel cracks while (c) shows cracks normal to the surface and (d) shows the large parallel crack that separate the worn layer

The worn surface layer which is separated from the original surface has undergone significant deformation due to the impact wear process. Cracks were propagated both parallel to the surface with the direction of impact due to the role of shear force and normal to the surface plane. The small parallel cracks connected with the small normal cracks and caused crushing leading to spalling, while the large parallel cracks led to delamination and eventually separation from the surface.

The worn surface layer can prevent excessive damage to the surface and it is expected to be more brittle than any other zones because of the effect of repetitive impacts. Below this layer there is another region (zone 2-A) which will eventually also become detached from the surface after a specific number of cycles.

SEM examination revealed that at the bottom edge, after 72,000 cycles, gross plastic deformation has occurred and produced a uniform wear lip on the trailing edge of the specimen as seen in Figure 5.37.

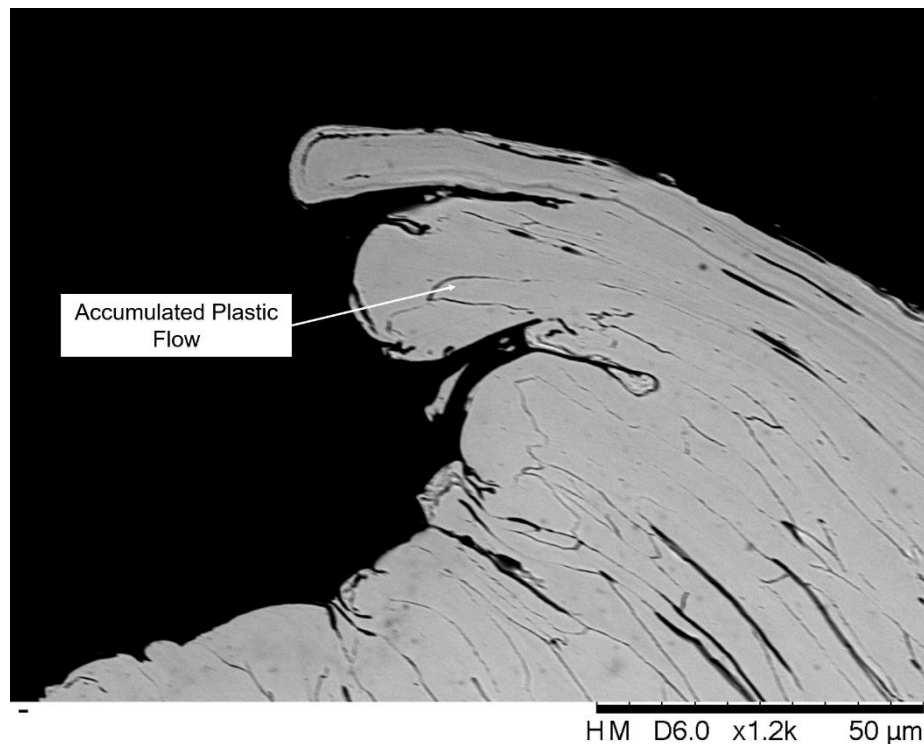


Figure 5.37 SEM image of pile up materials on the bottom edge after 72,000 cycles under compound impact  $60^\circ$  as revealed by electro etching

Figure 5.38 shows the typical impact wear scar with an impact angle of  $45^\circ$  after 72,000 cycles, while the impact wear zones after the same number of cycles are shown in Figure 5.39.

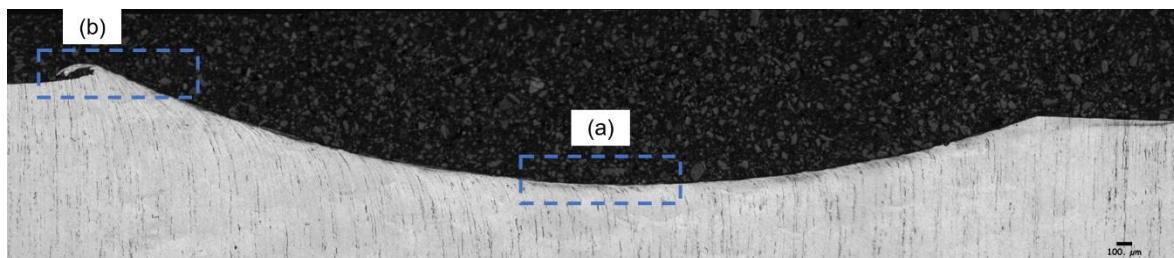


Figure 5.38 Cross sectional optical microscope image for material after 72,000 cycles under compound impact  $45^\circ$  for (a) centre of wear scar and (b) the bottom edge

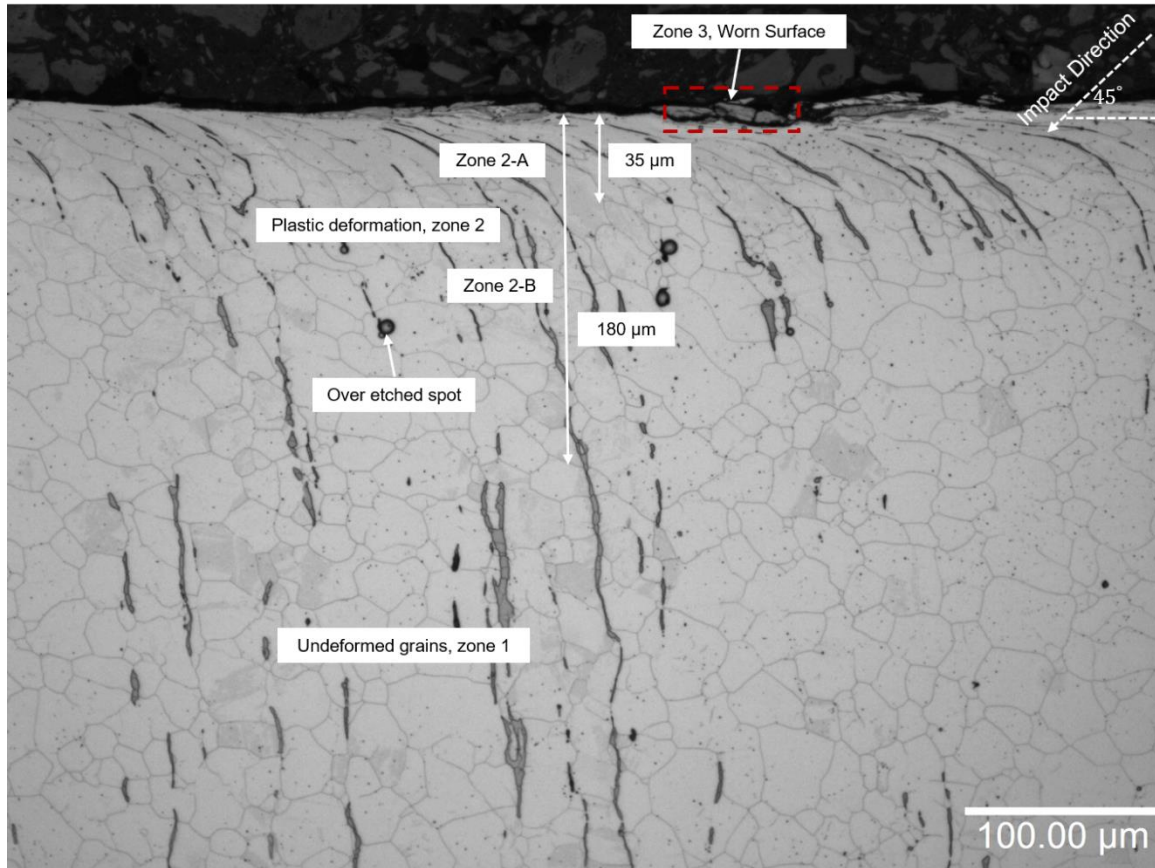


Figure 5.39 Optical microscope image of electro etching for material under compound impact  $45^\circ$  for the centre of wear scar after 72,000 cycles showing the impact wear zones

Figure 5.39 shows that the deformed regions (zone 2) extend to approximately  $180\ \mu\text{m}$  which is less than with an impact angle of  $60^\circ$  ( $450\ \mu\text{m}$ ); zone 2-A extends to approximately  $35\ \mu\text{m}$  compared with ( $120\ \mu\text{m}$ ) for an impact angle of  $60^\circ$ . The red dotted line in Figure 5.39 highlights the worn layer and is plotted with higher magnification in Figure 5.40.

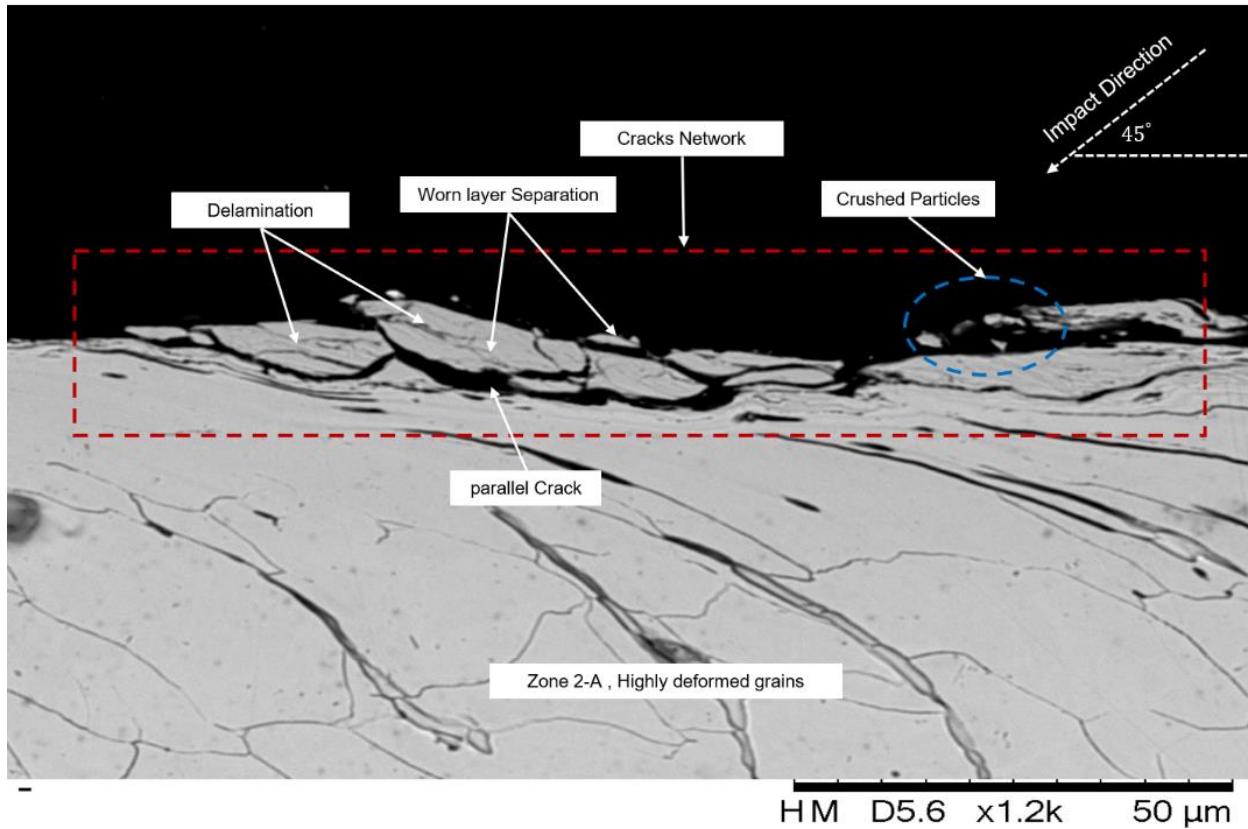


Figure 5.40 SEM image reveals the wear damage mechanisms occurring in the worn surface layer for material after 72,000 cycles under compound impact  $45^\circ$

Figure 5.40 shows feature similar to those found with an impact angle of  $60^\circ$  in Figure 5.36. The worn surface (zone 3) is separated from the impact region by parallel cracks, having undergone significant deformation due to the impact wear process. The small parallel cracks connected with the small normal cracks and caused crushing leading to spalling (blue colour), while the large parallel cracks led to delamination and eventually separation from the surface; therefore, surface fatigue occurred as a result of both spalling and delamination. Electro etching revealed the extrusion of plastic flow outside the wear scar region from the bottom edge by the effect of highest shear force and also the highly deformed and elongated grains as shown below in Figure 5.41.

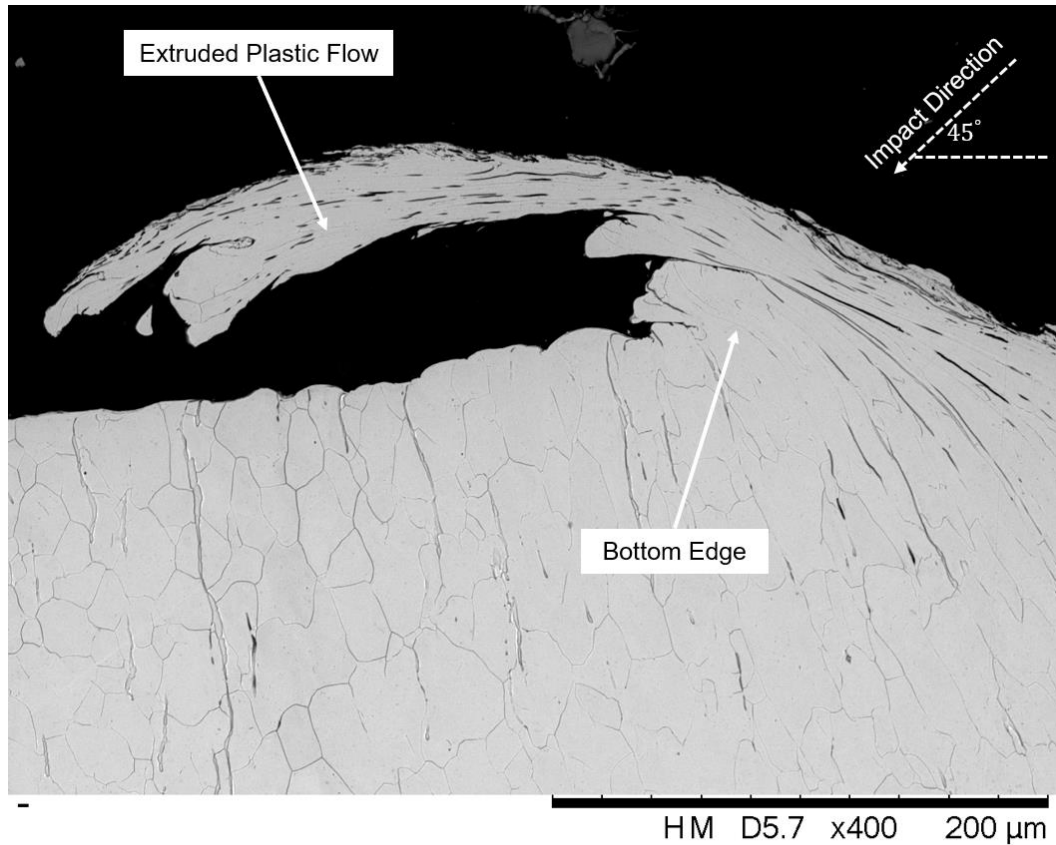


Figure 5.41 SEM image after electro etching for material reveals the deformed grains on the bottom edge and the extrusion of pile up materials outside the wear scar of specimen after 72,000 cycles under compound impact  $45^\circ$

### 5.3.3 Microhardness Results

The hardness of the material was measured using a microhardness test machine (Struers Durascan), as described in Section 3.4, using a load of 0.1 kgf. This was performed in order to detect the possible change in hardness resulting from the impact wear process after different number of cycles and at different impact angles and also to measure the depth of the work hardening layer. The microhardness measurements with different impact angles for AISI 304 or any other material has not been studied in the literature and therefore, it has been covered in this chapter.

There is always a tradeoff between the number of individual measurements required and the accuracy of final hardness value. In this case it was deemed realistic to get a single hardness measurement for the impacted tested specimens to represent the different impact angles at a position below the maximum indentation depth where the highest impact force occurs, similar to Rastegar [21] and Fricke [22]. The results of three microhardness measurements described in Section 4.5 (see Figure 4.15) have an error range of (10-15) %, therefore, the results of a single microhardness measurement of AISI 304 are expected to have a similar range.

The microhardness measurements for the impacted regions were taken first about  $80\ \mu\text{m}$  away from the centre region of wear scar below zone 3 toward zone 1. Which represented about 2.5 times the diagonal size of the indents, whereas  $30\text{-}32\ \mu\text{m}$  was used for the unimpacted region based on ASTM E384 [60].

## Impact Wear and Damage Mechanism of Austenitic Stainless Steel 304

Figure 5.42 shows the variation of microhardness results with different impact conditions along the maximum penetration depth, while Table 5.4 summarises the results for the effect of impact force and angle with both hardening value and depth below the surface.

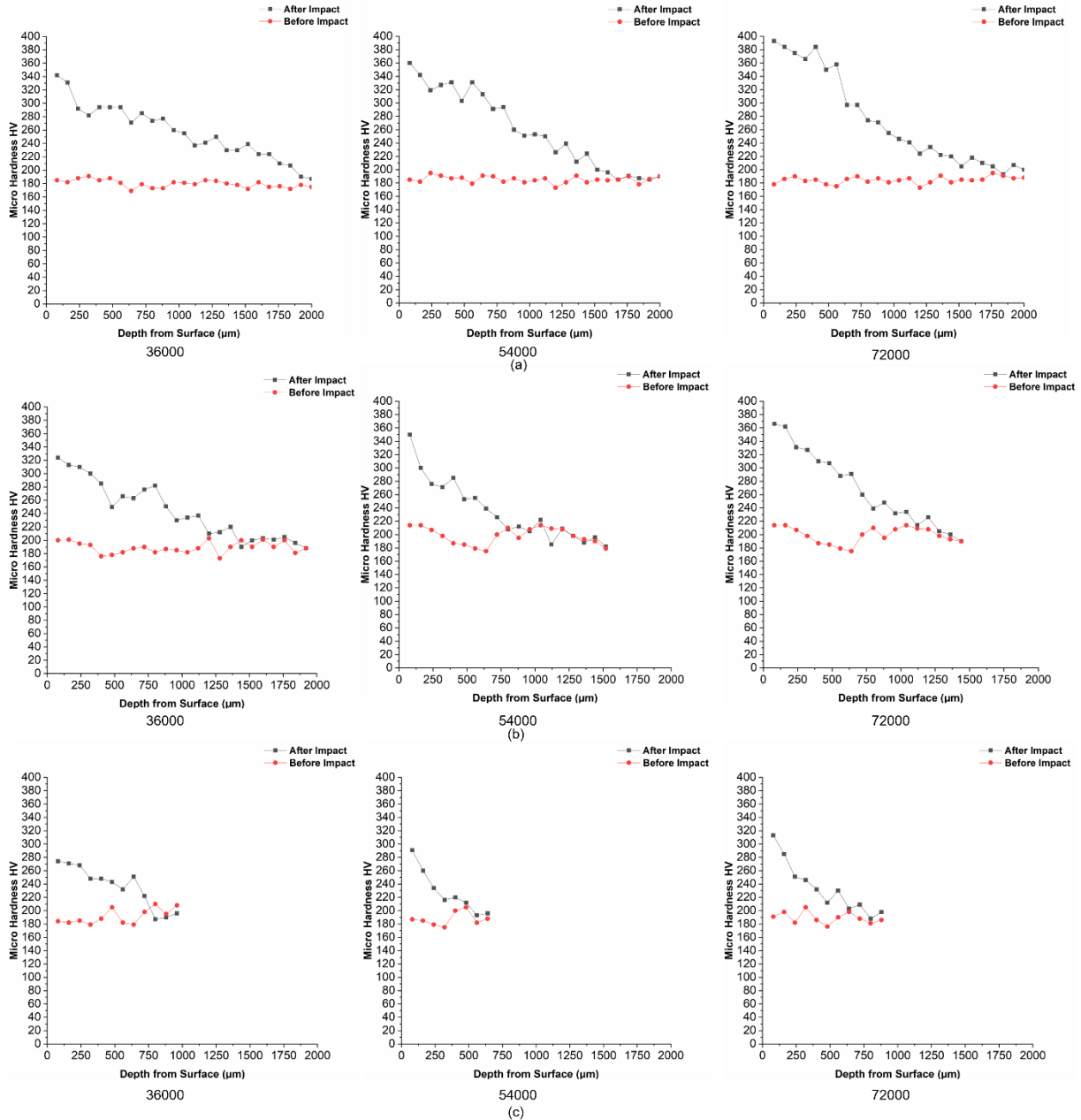


Figure 5.42 Microhardness profile of original and impacted austenitic stainless steel samples at impact force of 3476 N with different impact conditions where (a) is normal impact  $90^\circ$ , (b) is compound impact  $60^\circ$  and (c) is compound impact  $45^\circ$

Table 5.4 Correlation between the impact force and surface hardening of AISI 304

Number of cycles (N)	Normal Impact Force (N)	Tangential Impact Force (N)	Impact angle ( $\theta$ )	Surface Hardening (HV <sub>0.1</sub> )	Location of Hardening from surface ( $\mu\text{m}$ )	Hardening Depth (mm)
36000 54000 72000	2457	2457	45°	274 291 313	80	0.75
36000 54000 72000	3010	1738	60°	324 354 366	80	1.5
36000 54000 72000	3476	0	90°	342 360 393	80	2

Figure 5.42 and Table 5.4 show that, as expected, the maximum increase in surface hardness and depth occurred after 72,000 cycles with normal impact and extended to approximately 393 HV and 2 mm in depth, then at an impact angle of 60° with a hardness of 366 HV and 1.5 mm depth, while at an impact angle of 45°, a lower hardness of 313 HV was achieved and 0.75 mm depth.

This could be explained by the significant decrease in normal impact force from 3476 N to 3010 N at 60° to 2457 N at 45° and change in the wear mechanism from being pure compression under normal impact to abrasive wear with compound impact. These results support the previous findings and explanation presented in Section 5.3.2.2 (see Figure 5.35 and Figure 5.39).

The normal impact force caused more compression and led to creation of a hardened layer, whereas reducing this component and increasing the shear force component led to more materials being removed from the surface and less deformation. The increased hardness at the centre of the wear scar can be explained as the role of work hardening resulting from repetitive impacts.

The results above of microhardness were accomplished according to the standard ASTM [E384] regarding the distance from surface. Also, further work carried out to detect the expected increase in hardness very close to the surface with obvious diamond indentation and without any deformation to the indentation or the surface. After a few trials, it was found that the minimum distance from surface to get accurate microhardness measurement is about 35 $\mu\text{m}$  below the worn surface which revealed a significant increase in hardness compared with the results in Table 5.4. A summary of these results is shown in Table 5.5 which presents the value of microhardness above the previous indentations and about 35 $\mu\text{m}$  from surface.

Table 5.5 shows significant increases in hardness with all impact angles for AISI 304 compare with results obtained in Table 5.4 which is realistic since these results are found from indentations very close to the surface (35  $\mu\text{m}$ ). An example for the microhardness indentation inside the deformed grains (35 $\mu\text{m}$  from surface) can be presented in Figure 5.43 with impact angle 45° after 54,000 cycles.

## Impact Wear and Damage Mechanism of Austenitic Stainless Steel 304

Table 5.5 Correlation between the impact force and surface hardening of AISI 304 at a distance of approximately 35 $\mu\text{m}$  below the impact surface in the centre of the wear scar

Number of cycles (N)	Normal Impact Force (N)	Tangential Impact Force (N)	Impact angle ( $\theta$ )	Surface Hardening (HV <sub>0.1</sub> )	Location of Hardening from surface ( $\mu\text{m}$ )
36,000	2457	2457	45°	398	35
54,000				418	
72,000				457	
36,000	3010	1738	60°	403	35
54,000				423	
72,000				469	
36,000	3476	0	90°	413	35
54,000				434	
72,000				475	

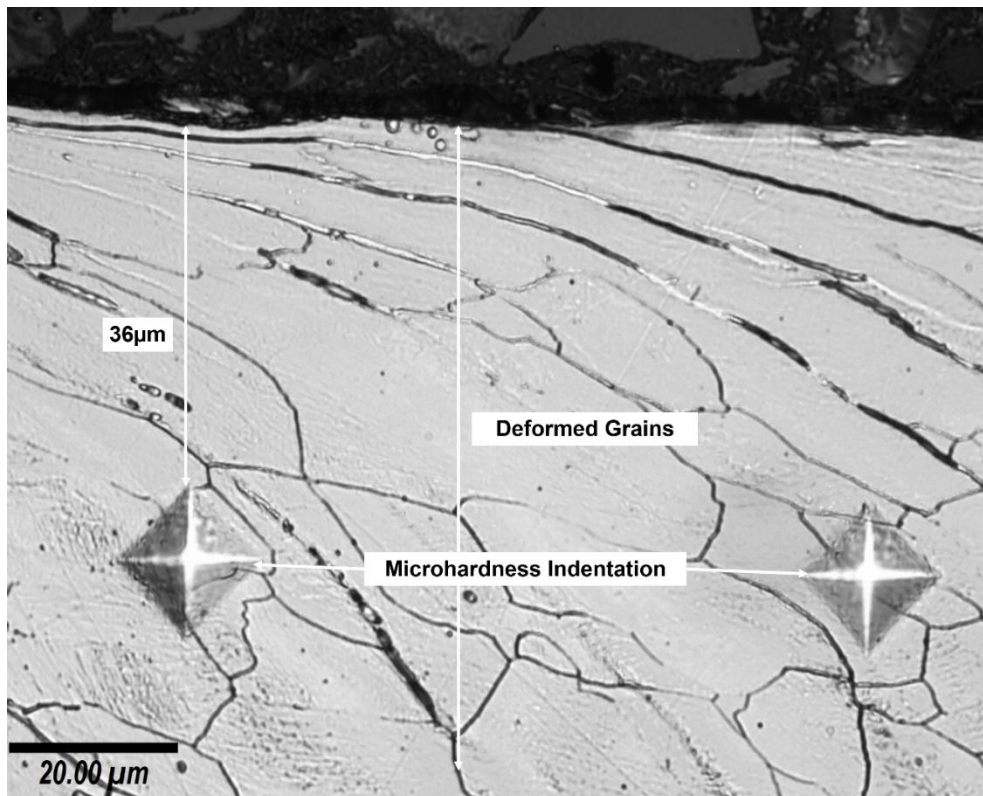


Figure 5.43 Optical microscope image for the microhardness indentation inside the deformed grains of austenitic stainless steel 304 for compound impact 45° after 54,000

### 5.3.4 Crack Orientation

Following one of the objectives described in the literature in Section 2.2.2.1 as a key trend is to identify the nature of crack during repetitive normal and compound impact (intergranular or transgranular). Such work has not been studied before for any material.

The results of this chapter for AISI 304 revealed that cracks initiated either on the surface or subsurface based on the impact condition and this supports and agrees with previous literature review findings by such as Cheng [23], Jiang [15] (see Figure 2.2 (d)), Yang [17] (see Figure 2.7 (a)), Zhang [23] (see Figure 2.8) and Rice [25] (see Figure 2.10). Further investigation was then carried out to detect if cracks propagated within the grain boundaries (intergranular cracks), or within the grain itself (transgranular cracks), or even a combination of both.

After thorough examination of each region of all the subsurface samples used in this work, the cracks in the majority of the examined regions were indeed found to be a combination of both. However, due to the highly deformed grains near the impacted surface it was very difficult to know if the cracks in these regions were intergranular or transgranular.

In the specimen under impact, compression of the grains will occur and cracks will propagate through the grains themselves, or if there are any voids or inclusions inside the materials then the cracks will follow the grain boundaries. The crack will continue to grow under repetitive impacts until it reaches a critical size where the remaining uncracked section of the material can no longer support the applied stress and fracture occurs.

Figure 5.44 shows an example of crack propagation inside the grains under normal impact after 54,000 cycles. The grain diameter within an unimpacted region is typically  $22.5\ \mu\text{m}$  as explained in Section 3.7.4.1 compared with the much smaller size of the crushed particles (see Figure 5.36 and Figure 5.40). This leads to the conclusion that all these crushed regions were the result of transgranular cracks that propagated inside the grains.

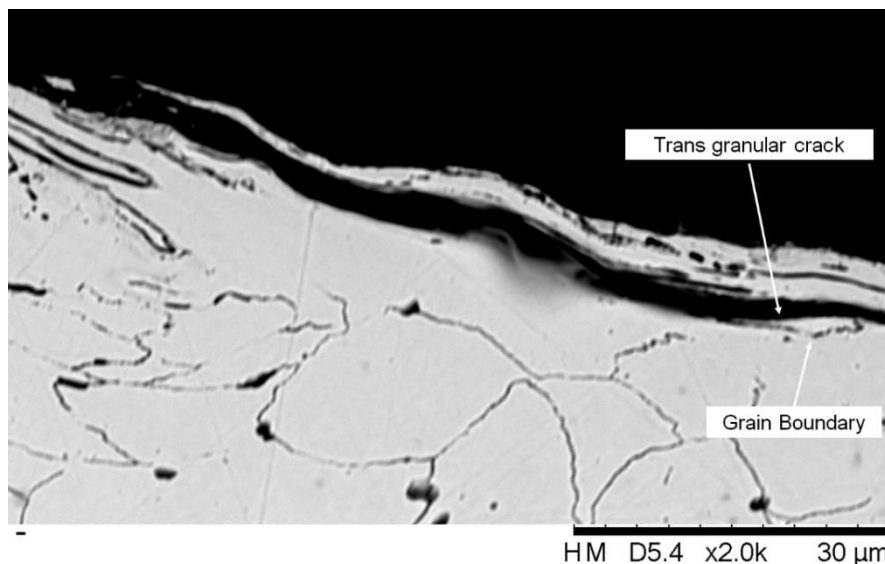


Figure 5.44 SEM image of transgranular crack propagation inside the grains for material under normal impact after 54,000 cycles

Further investigation showed that both types of cracks can exist at the same time as shown in Figure 5.45.

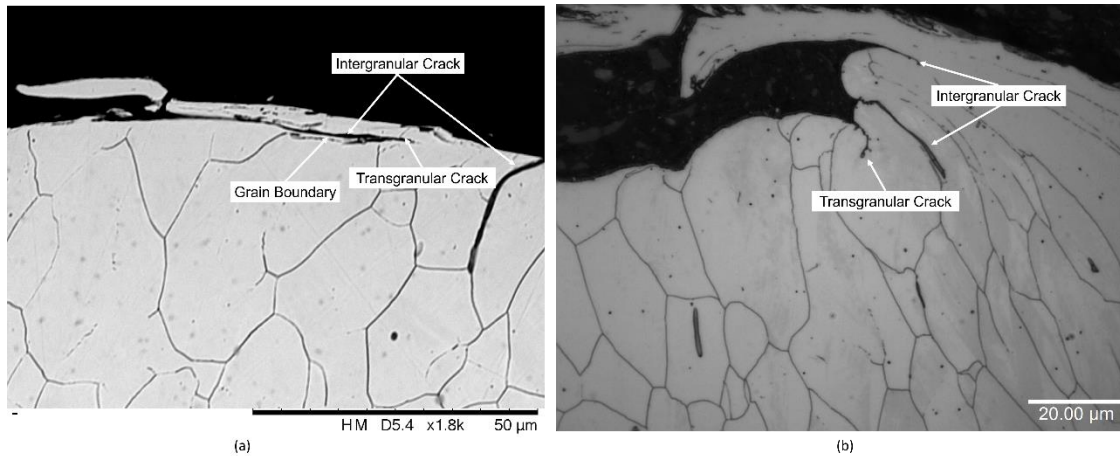


Figure 5.45 SEM images showing transgranular (within the grains) and intergranular (inside the grain boundaries) crack propagation for material under (a) normal impact  $90^\circ$  after 54,000 cycles and (b) compound impact  $45^\circ$  after 36,000 cycles

Figure 5.45 shows that regardless of the impact angle transgranular and intergranular cracks propagated inside the grains and within the grain boundary in the same region, since the centre of impact wear is highly deformed, it is difficult to detect the nature of the crack propagation except in the case of the crushed particles which indicate transgranular cracking.

#### 5.4 Wear Debris

Investigation of collected wear debris from the worn specimens of AISI 304 has been carried out during this work in order to identify the shape and size of the wear debris under different impact conditions. The aim was not to analyse the wear debris, but rather to obtain a simple explanation on how the wear debris can reflect the wear damage mechanism.

Wear debris is generated due to contacted asperities shearing off from one or two of the surfaces that have undergone rolling, rubbing, impact, sliding, metal transfer from one surface to another or cutting action. At microscope level the contact regions are seen to be distributed over the asperities of the contacted surfaces and this is different from the apparent contact area, so the actual contact area is the sum of the asperity contact regions [73, 74].

Under impact, contact regions are created at the asperity levels due to the applied load. With continuous impact for a specific number of cycles and slight increase in load during impact, the contacted regions of asperities start to deformed plastically and eventually degradation of the surface occurs which leads to material loss (wear debris).

Investigation of wear debris analysis using different techniques indicated that different sizes, shapes and colours of wear debris could provide information about which wear damage mechanisms are involved [75]. Additionally, the wear debris can reflect different types of wear mechanisms and wear severity. Since the mass loss was very small in general with normal impact, it was realistic to expect only a small amount of wear debris after 72,000 cycles. SEM examination revealed some adhered wear debris in the centre, edges and outside the edges of the specimen as seen in Figure 5.46.

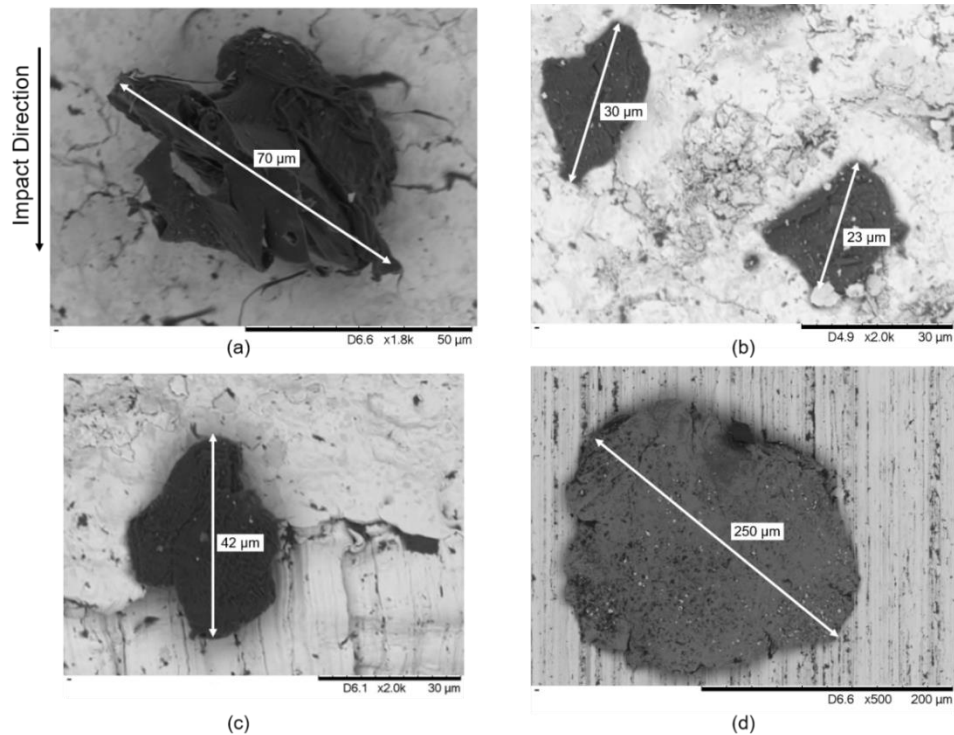


Figure 5.46 SEM image of wear debris for material after 72,000 cycles under normal impact where (a) and (b) show the centre of the wear scar, (c) the bottom edge of the wear scar, (d) outside of the wear scar

Figure 5.46 shows the wear debris to be black in colour (by SEM) and of platelet shape (b and c), with this wear debris shape indicating the high possibility of surface fatigue [75], while (d) tended to be spherical in shape, which also indicates surface fatigue [75, 76]. The major length of wear debris varies from 23-250  $\mu\text{m}$ , while the absence of any sliding marks indicates that no sliding wear happened during impact since the nature of the contact was frictionless.

Under compound impact ( $60^\circ$ ), wear debris accumulation was found on the specimen below the bottom edge of the wear scar during all tests, due to impact direction, as seen in Figure 5.47. Further examination revealed different wear shapes among these wear debris accumulations, as seen in Figure 5.48.

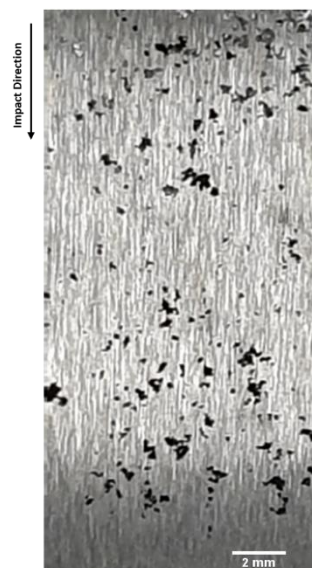


Figure 5.47 OM of wear debris below impact wear scar for material after 72,000 cycles under impact angle  $60^\circ$

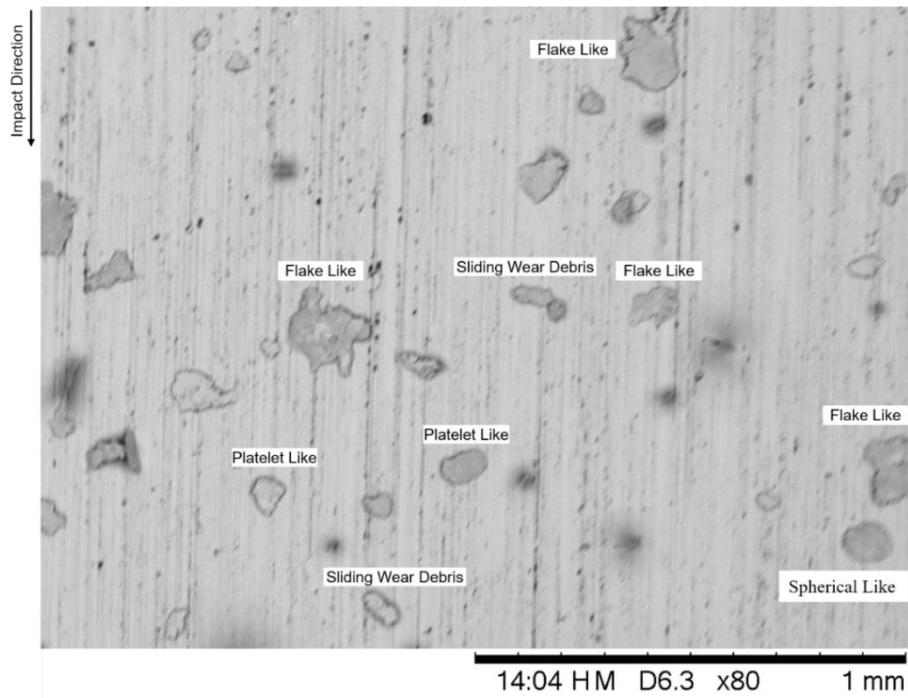


Figure 5.48 SEM image of wear debris from worn surface after 72,000 cycles under impact angle  $60^\circ$

Figure 5.48 shows four different types of wear debris (platelet, flakes, spherical and sliding wear debris). The flake wear debris has the largest length, 120-180  $\mu\text{m}$ , the platelet debris is approximately 100  $\mu\text{m}$  in length, and the sliding debris has the smallest length, about 80  $\mu\text{m}$ . The sliding wear debris again demonstrates and explains the increases in mass loss with an impact angle of  $60^\circ$  and indicates abrasive wear during impact [75, 76], while the platelet, spherical and flake wear debris indicate surface fatigue.

Examination of the surface of worn specimens with compound impact  $45^\circ$  revealed a significant increase in the amount of wear debris at the bottom of the sample, below the wear scar, as shown in Figure 5.49, which indicates the significant increase in mass loss for this material.

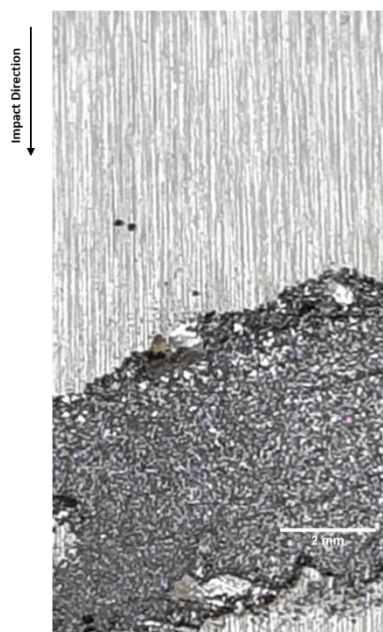


Figure 5.49 OM of wear debris below impact wear scar for material after 72,000 cycles under impact angle  $45^\circ$

The collected wear debris after 72,000 cycles, where significant mass loss occurs, is shown below in Figure 5.50-52, Figure 5.50 shows the mixture of debris types that resulted from repetitive impact after 72,000 cycles.

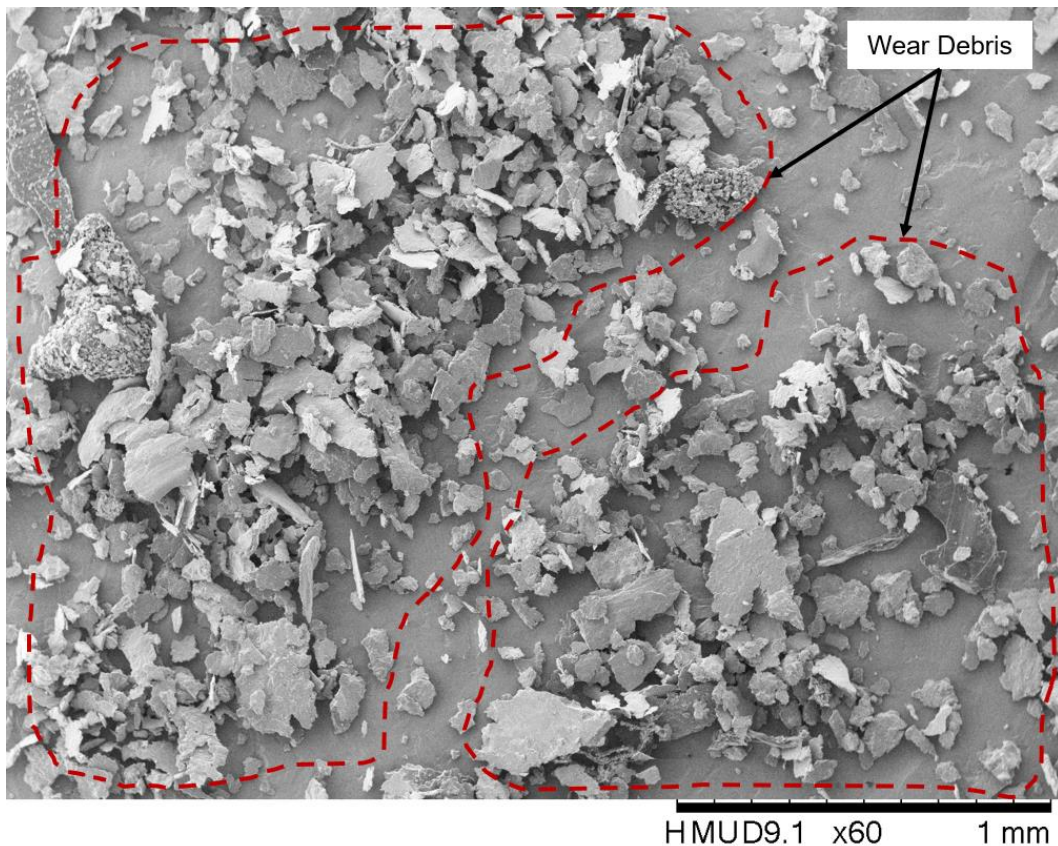


Figure 5.50 Collected wear debris from worn surface for material under compound impact  $45^\circ$  after 72,000 cycles

Figure 5.51 identifies three different types of wear debris under compound impact of  $45^\circ$ : flake, platelet wear debris with average length of  $60\ \mu\text{m}$ , and sliding wear debris with average length of  $150\ \mu\text{m}$ , which is also larger than with impact angle  $60^\circ$ .

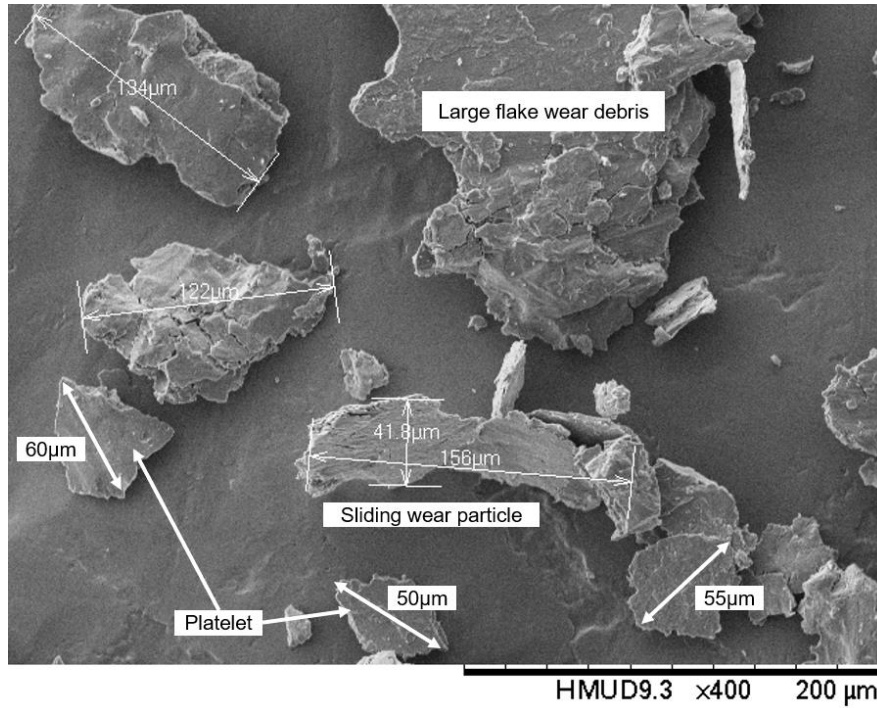


Figure 5.51 Differences in shapes and sizes of wear debris from worn surface for material under compound impact  $45^\circ$  after 72,000 cycles

Figure 5.52 shows large flake reaching around  $450\ \mu\text{m}$ , which has the largest length among the other tested angles ( $90^\circ$  and  $60^\circ$ ).

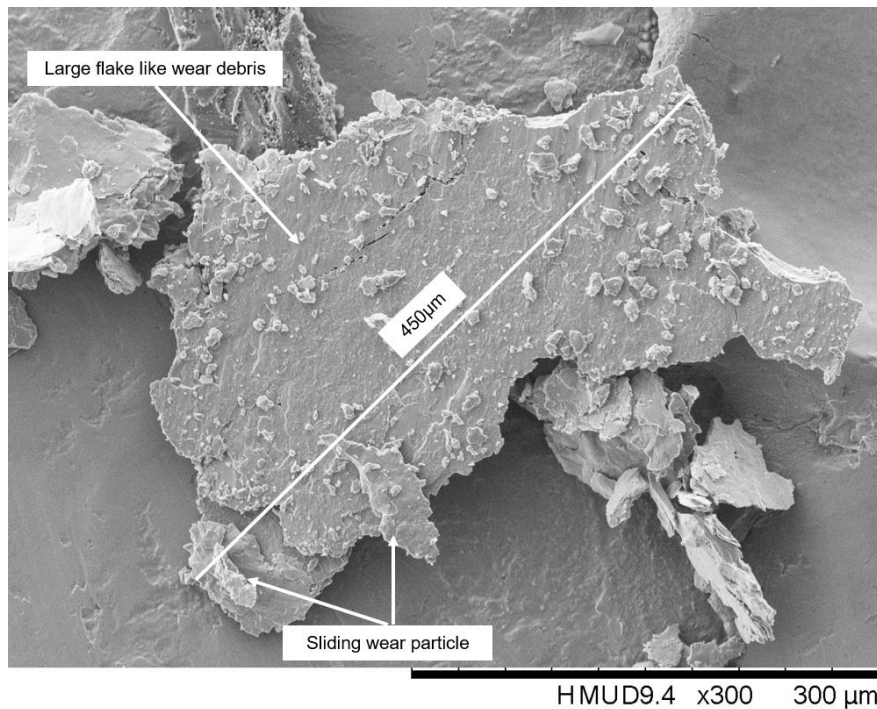


Figure 5.52 Flake wear debris from worn surface for material under compound impact  $45^\circ$  after 72,000 cycles

Figure 5.53 shows an excessively fragmented specimen of flake wear debris with a length of 460  $\mu\text{m}$  which reveals the following wear features:

- abrasive wear as a result of ploughing grooves, with the sliding wear marks indicating the impact direction which is parallel to the sliding direction
- crushed particles between two surfaces (hardened and new exposed) which confirm the previous results of surface examination.
- Multiple layers of delamination in different locations and surface cracks perpendicular to the impact direction which indicate that the cracks also initiated and propagated in a plane normal to the impact direction.

The sliding marks on the wear debris of Figure 5.53 which indicates the sliding wear (abrasive wear) is quite similar to the marks found on the wear debris of medium carbon steel shown in Figure 2.7-b with impact angle  $45^\circ$ , so these results are supporting the previous one of Sections 5.3.1 and 5.3.2.

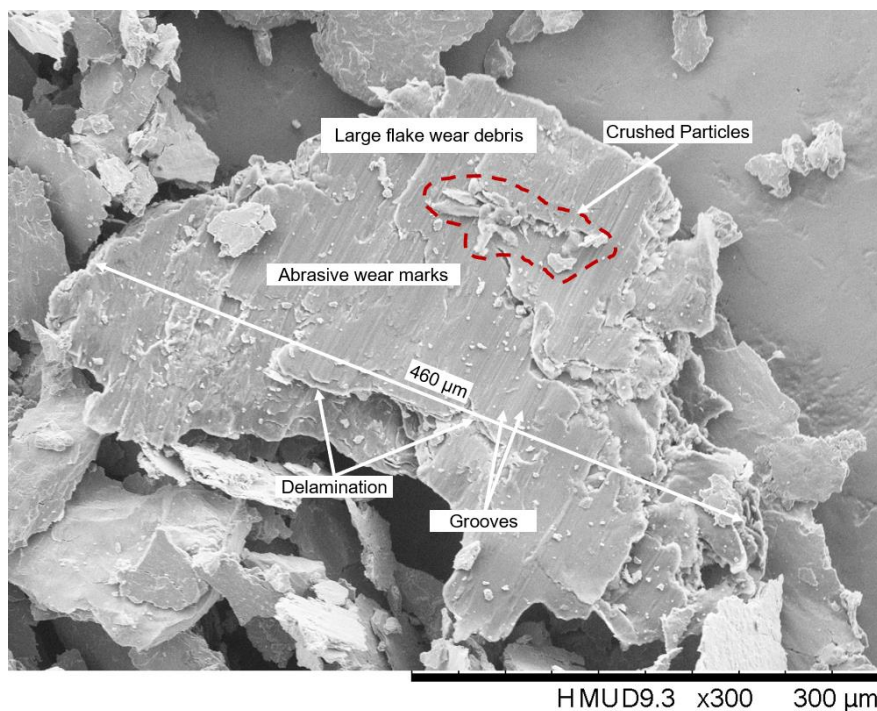


Figure 5.53 Sliding wear marks on large flake wear debris of worn surface for material under compound impact  $45^\circ$  after 72,000 cycles

Chunks of wear debris larger than platelet, spherical and sliding wear debris were found on the worn surface of specimens with an impact angle of  $45^\circ$ , a feature not observed with other tested angles; one such chunk is shown in Figure 5.54.

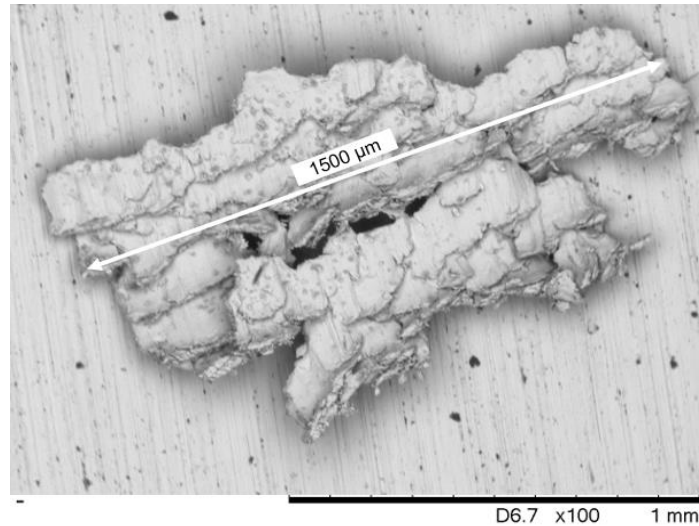


Figure 5.54 SEM image of a chunk of wear debris from worn surface for material after 72,000 cycles under compound impact  $45^\circ$

The chunk shown in Figure 5.54 is very large, up to  $1500\ \mu\text{m}$  in length, rough, dissimilar in length and width (uneven dimensions), extensively fragmented, and has a jagged boundary profile. These chunks are usually metallic and normally generated by combined fatigue and sliding wear that cause severe damage [75]. The presence of these chunks of material provides support for the previous finding revealed in Figure 5.20 and Figure 5.22 that large cracks were obvious on the bottom edge that would lead eventually to large chunks of material leaving the surface, thus explaining the further increase in mass loss that occurred with an impact angle of  $45^\circ$ .

## 5.5 Discussion

### 5.5.1 Wear Volume and Wear Measurements

The mass loss measurements after different numbers of impacts clearly indicate that the wear volume of the specimens increased linearly with number of impacts for both normal and compound impact regardless of the impact angle. The results are consistent with studies using either mass scale or volume loss methodology as described in the literature by Slatter [9], Fricke [22], Zhang [23], Lindroos [20], Ootani [33], and Roncery [31] et al.

However, it should be noted that the total material loss under normal impact in all cases was very small compared with the compound impact. This is attributed to the improvement of surface strength caused by work hardening in addition to the role of zero wear volume during normal impact.

Figure 5.1 also indicates that changing the impact angle resulted in a progressive increase in material loss, suggesting that the wear conditions became more severe. This means that more tangential force led to more mass loss during compound impact, the highest material loss occurring at an impact angle of  $45^\circ$  with different number of cycles. The significant increase in wear volume at  $45^\circ$  from 54,000 cycles to 72,000 cycles could indicate weakening of the material's surface and loss of the capacity to work harden the material.

For example, increases the number of cycles from 36,000 to 72,000 led to an increase in wear volume by 164 % for normal impact  $90^\circ$ , 202 % with compound impact  $60^\circ$ , and 225 % with an impact angle of  $45^\circ$ . While changing the impact angle from normal  $90^\circ$  to  $45^\circ$  at any number of cycles such as 54,000 led to an increase in wear volume by 3340 %. This indicates that the impact angle strongly affects the wear volume loss of the material and often has more influence than the number of cycles (i.e. the total wear volume is more sensitive to impact angle rather than impact cycles).

The profilometry results clearly demonstrate that increasing the number of cycles leads to an increase in the impact wear scar depth, diameter and volume. The 2D profile results (see Figure 5.7) reveal that the increment in impact wear scar depth with different number of cycles was small under the normal impact compared with compound impact. This could be explained as the role of zero wear during normal impact where, since the nature of the impact is dynamic compression, it is expected that more materials will be compressed rather than being removed from surface.

Considerable differences were observed in the impact wear scar depth after 72,000 cycles, with an increase of 33 % from normal impact to compound impact  $60^\circ$ , rising to 67 % at impact angle  $45^\circ$  due to the effect of shear force by compound impacts and eventually excessive wear damage to the material surface.

The 3D profilometer results were very useful for detecting the amount of both plastic flow (volume, height) and the lower volume and depth of the impact scar while also showing the distribution of plastic flow with different impact angles (Figure 5.8).

The results revealed that the highest wear volume, as measured by mass scale, and total volume loss, as measured by 3D profilometer, always increase with decreasing the impact angle regardless of the number of impact cycles. These results support the previous findings of Rigaud & Le Bot [29], Tyfour [30], and Zanolria [54]; additionally, these results agree with the findings of several studies [77-79] that reported that impacts with a sliding component showed significantly more wear loss.

It is important to mention that except for the studies conducted by Lewis [46] and Slatter [7-9], the majority of work in the literature does not randomise or replicate either the tests or specimens so no error bar was present in their results, which reduces the confidence of such results.

Finally, a set of simple criteria such as randomisation, use of control and repeated tests can be considered as a baseline for any research to follow in order to enhance the study design and increase the accuracy of the results [68].

## **5.5.2 Wear Scar Analysis**

### **5.5.2.1 Wear Damage and Crack Propagation**

The deformation and wear behaviour were investigated in two impact conditions including different number of cycles and three different angle impacts.

Based on the observed wear behaviour, the damage mechanism caused by repetitive impacts could be divided into two main forms of failure: plastic deformation and wear degradation.

In general, due to good mechanical properties and high ductility, the work hardening of AISI 304 after repetitive normal impact was sufficient to maintain the structural integrity when the material was exposed to external load beyond the yield and to prevent excessive material loss and damage to the surface. The striker has much higher hardness and therefore the greater deformation occurs to the specimen rather than the striker and the contact surface of the softer body will conform to that of the harder body.

The two main mechanisms of damage to the specimen surface under normal impact are plastic deformation and surface fatigue (spalling and delamination). Plastic deformation, which absorbs kinetic energy and results in permanent deformation, is the main damage mechanism of the specimen surface under normal impact regardless of the number of impact cycles, thereby explaining the small amount of material loss that occurs during repetitive normal impact.

Surface fatigue due to spalling and delamination as a result of microcracking and micro pitting on the surface of the impact wear scar in addition to crushing of particles were also found by Yilmaz [28], Fricke [22], Jiang [15], Wang [37, 80], and Mahoney [13] et al.

The crushed particles, regardless of the location of the examined region, fall between the edges of the hardened surface and the new exposed surface (see Figure 5.11) and their number is increased by increasing the number of impact cycles (see Figure 5.12). These edges of the hardened surface are under concentrations of fatigue stresses that will result in initiation and propagation of microcracks and severe deformation due to the excessive work hardening will result from the effect of compressive impact force. The impact zone becomes brittle, which facilitates the initiation and propagation of fatigue cracks and causes near surface areas to become spalled; similar patterns were found by both Yilmaz [28] and Suh [81].

The highly deformed layers found on the surface of worn specimens with different impact conditions will begin to crack after a specific number of cycles and will eventually detach from the surface, as shown in Section 5.3.1 (Figure 5.13). Below this layer is another less deformed surface which will also begin to crack and detach.

Delamination occurs on the impact surface with both normal and compound impact. In the case of normal impact as described in Section 5.3.1 (see Figure 5.10 and Figure 5.13) microcracks develop from surface and propagate below the surface at a certain depth and then become parallel to the surface, finally

turning toward to the surface. These results agree with Jiang [15] which revealed that delamination of rail welded joints and rail materials under normal impact occurs as a result of microcracks that initiate originally from surface and propagate parallel to the worn surface as described earlier in Section 2.2.2.1 (see Figure 2.3). Eventually, fracture occurs due to a network of microcracks that either become detached from the surface as wear debris or the wear debris adhered to the surface by the effect of compression.

The wear damage developed more quickly for compound impact than normal impact, highlighting the great importance of shear force as represented by the tangential component of impact force which also accelerated the wear volume and eventually caused severe surface degradation to happen with compound impact. Also, the material was not capable of maintaining its structural integrity when subjected to compound impact, making it highly possible that cracks in Section 5.3.1.2 (Figure 5.14-a) and (Figure 5.16-a) would propagate beneath the surface and cause excessive damage to the material.

In general, the morphological characteristics and surface degradation for compound impact were found to be different from those for normal impact; the wear mechanisms for compound impact, besides plastic deformation, are surface fatigue (delamination and spalling) and abrasive wear.

Abrasive wear occurs during compound impact by a ploughing process, with deep and shallow grooves forming on the surface. Two body abrasive wear is caused by adhered particles that transferred from the specimen to the striker during impact, these adhered particles forced to slide against the specimen surface and also indicates that adhesive wear occurs during impact (in small scale) as shown in Figure 5.55. While three body abrasive wear is caused by crushed particle trapped between the striker and the specimen and these particles slides between surfaces during compound impact (see Figure 5.14; Figure 5.16; Figure 5.19 and Figure 5.21).

Adhesive wear occurs when shear starts in the weakest material (specimen) and the fragment of a surface (wear particle) is detached from one body (specimen) and transferred to another (striker), wear particles detach at the areas where a strong junction between contacting asperities is formed between the surfaces sliding relative to one another

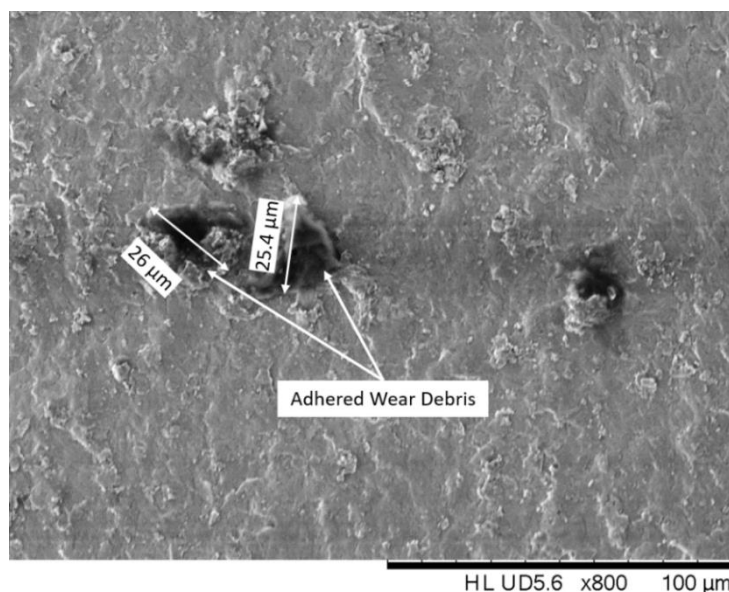


Figure 5.55 SEM image shows the adhered wear particles transferred from the specimen surface to the striker surface with impact angle  $60^\circ$

It is obvious that the existence of crushed particles caused spalling as a series of pitting resulting from micro cracks with normal impacts. These particles play further role during compound impacts ( $60^\circ$  and  $45^\circ$ ), it became trapped between the striker and the worn surface. When sliding occurs between the specimen and the striker during impact, three body abrasive wear happened and thus accelerated the mass loss. The severity of damage to the worn surface depends on the sliding distance and the number of these particles trapped during impact.

The pile up materials (plastic flow) on the bottom edge of the wear scar were also subjected to different damage mechanisms. At an impact angle of  $60^\circ$  the materials were built up and distributed uniformly on the bottom edge (see Figure 5.15), whereas with an impact angle of  $45^\circ$ , the plastic flow was extruded outside the bottom edge of the wear scar. Many of these flow materials had large cracks which would eventually cause chunks of material to detach from the surface (see Figure 5.20 (d) and Figure 5.54), providing further explanation for the excessive material loss that occurred with an impact angle of  $45^\circ$ .

The surface topography of the bottom edge exhibited highly strained materials as pile up material which had been extruded from the centre of the wear scar to the bottom edge with the direction of impact. The extruded plastic flow near the bottom edge of the wear scar in Section 5.3.1 (see Figure 5.31) reflects the high level of deformation is similar to the results previously obtained by Lindroos [20, 82]. The results of Lindroos revealed that the worn surface of steel materials was deformed and removed during compound impacts, and accumulated on the bottom edge of the impact scar as plastic flow, due to shear deformation that had localised in these regions.

The initiation, propagation and coalescence of surface and subsurface micro cracks on the worn surface are important processes; due to the work hardening, the specimen under repetitive impact becomes harder and more brittle, leading to more stresses at the crack tip.

Subsurface examination of AISI 304 under normal impact showed that the majority of cracks were initiated from the surface and propagated beneath the surface in a parallel plane to cause delamination (see Figure 5.24). Similar patterns of cracks were found by Rastegar [21] and Jiang [15] under normal impacts.

Surface fatigue occurred due to surface microcracks that propagated either normal or parallel to the surface (delamination and spalling) in addition to large subsurface cracks that initiated and propagated rapidly, parallel to the surface under the shear stress, finally leading to removal of larger delamination layers from the surface. These results agree with Yang [17] and Zhang [23] which revealed that delamination of medium - high carbon steel under compound impact ( $45^\circ$ ) and low carbon steel occurs as a result of microcracks that initiated originally from surface and subsurface and then propagate parallel to the worn surface as explained in Section 2.2.2.1 ( see Figure 2.8).

Long, thin and thick layers were delaminated from the worn surface as described in Section 5.3.2.1(see Figure 5.25-29) as a result of surface and subsurface cracks. The delaminated layers' length and height depended on the location of both surface and subsurface cracks which is controlled by both normal and tangential stresses [21].

The perpendicular sectioning results of Section 5.3.2.1 (Figure 5.32) identified the abrasive wear during compound impact and explained the significant increase in wear volume of austenitic stainless steel at impact angle  $45^\circ$ .

The trailing edge exhibited the greatest build up due to the role of shear force during impact and sliding which occurred with the direction of impact.

Examination of the electro etching of AISI 304 in the centre of the wear scar, where the maximum contact pressure occurs and leads to maximum indentation, revealed three morphological zones within the impact scar. Zone 3, the surface layer, had undergone severe degradation deformation and shearing off by the impact wear process, resulting in the formation of very thin and elongated grains. These elongated grains were also observed in the plastic deformation region, zone 2, beneath which was the region of undeformed grains (zone 1).

Higher shear force with impact angle  $45^\circ$  led to removal of the hardened surface layer by the effect of abrasive wear and work hardening was unable to prevent further damage to the surface; therefore, it showed less deformation depth compared with an impact angle of  $60^\circ$ .

Intergranular cracking occurs at the grain boundaries in metals that suffered reduction in ductility and became more brittle (crushed particles) and the grain boundaries is weaker. These particles provide a pathway for cracks to grow and propagate at the grain boundaries and therefore, it reduces the toughness of material [83, 84].

Intergranular cracking can be considered as intergranular fatigue fracturing which occurs as a result of cyclic loading that leads to fatigue and severe weakening of the grains [85].

Transgranular fractures are caused by strain localisation and cracking does not follow grain boundaries; instead transferring from one grain to another grain, which indicates fatigue cracking. The grain boundaries have more strength than the grains.

#### **5.5.2.2 Microhardness Analysis**

The results presented in this chapter show that the AISI 304 has great ability in terms of work hardening as discussed in Section 4.6. Results of subsurface examinations revealed that among all the etched samples, zone 1 appeared not to be affected by the impact wear process, but there was an increase in hardness. For example, with normal impact, it reached a depth of 2 mm, as Figure 5.42 shows, and the deformed grains extended to approximately  $65\ \mu\text{m}$ , as shown in Figure 5.34, while the grains below this depth seemed to be unaffected.

These results, which agree with previously obtained by Recep [28] and Cassar [86] could be explained as the role of residual stresses induced and remaining in the contact region area that resulted from the contact stress caused by the high impact force; in particular, previous results on stresses described in Section 3.5.3 have demonstrated that the nature of impact is plastic from the early cycles.

These residual stresses, which are compressive in nature, continue to increase with repetitive impact and the contact stress, which is a function of the contact region area, depends on the deformation resistance of the materials which changes dynamically. Therefore, the work hardening layer that occurs under the stress contact area accumulates in the structure lattice with each subsequent impact cycle.

In the current study, the effects of plastic deformation on the wear behaviour became more clearly observable at high impact angle  $90^\circ$ , the surface of material work hardened in a manner that prevented further damage, results which agree with a previous investigation by Lindroos [20].

### 5.5.2.3 Wear Debris

Despite normal impact revealing only very small amounts of material loss, a little wear debris was found on the worn specimens in the centre of the impact, near the edges and outside the wear scar under normal impact. There is limited possibility for material under compression to leave the contact region and there is a high possibility that wear debris will adhere to the surface of specimens. Platelet, spherical and flake wear debris were the main types of debris found on the surfaces of all examined specimens.

In general, all the collected wear debris from compound impact revealed deformation, cracks and sliding wear marks with different density depending on the impact angle and number of cycles.

With an impact angle of  $60^\circ$ , platelet, spherical and flake wear debris indicated surface fatigue, with the flakes tending to be larger than the platelets, while the elongated particles of the wear debris indicated that sliding wear occurred during impact, which explains the further increase in mass loss under compound impact [75].

With an impact angle of  $45^\circ$ , investigation of the collected wear debris revealed an increase in the number and size of the platelet and flake wear debris in addition to sliding wear debris. Much of these sliding wear debris was extensively fragmented and showed sliding wear marks which reflect the severe level of damage as explained earlier by Dan [75].

## 5.6 Austenitic Stainless Steel 304 Summary

The summary of the findings derived from the experimental work on AISI 304 in this chapter are shown below:

- A series of tests on AISI 304 clearly demonstrated that the wear damage process effectively depends on the nature of impact (normal or compound), with highest material loss occurring at impact angle  $45^\circ$  and the impact wear is greatly influenced by the sliding component.
- Wear volume increases linearly with number of cycles and inversely with impact angle.
- The zero wear as a volume slightly decreases with number of cycles but significantly with impact angle.
- Plastic deformation and surface fatigue due to spalling and delamination are the main forms of wear damage for material under normal impact, while a transition in wear mechanism occurs with compound impact; additionally, to plastic deformation and surface fatigue, adhesive and abrasive wear were also observed.
- Surface fatigue failure occurs due to,
  - Delamination when microcracks propagate along the path parallel to the worn surface
  - Spalling when microcracks propagate normal to the surface inside the worn surface
- Regardless of the impact angle, the current results indicate that delamination of the worn surface is the primary type of surface fatigue, since the size of debris is much bigger than that from micro pitting resulting from spalling.
- The worn surface (zone 3) is an intensely deformed layer. The microcracks, which initiate originally inside it, cause severe wear when the crack inside the worn surface is propagated.
- The characterisation of the wear surfaces revealed that during compound impacts material was removed, especially from the piled up regions formed in front of the impacting region, and shear deformation had localised in these regions.
- The increases in hardness value and depth were inversely proportional to the impact angle and reduced significantly from normal impact  $90^\circ$  to compound impact  $60^\circ$  and  $45^\circ$ .
- Both intergranular and transgranular cracks occur during normal and compound impact wear, regardless of the number of impact cycles and the impact angle.

## Chapter 6 Role of Impact Angle on Surface and Subsurface Deformation of Alloy Steels

### 6.1 Introduction

The work presented in this chapter aims to prove the role of impact angle during compound impact for two metal alloys (AISI 316 and EN8) and support the previous results on AISI 304 using impact wear rig. Also, this work investigated the surface and subsurface damage to these alloys following one of the objectives described in Chapter 1 and outlined in Chapter 2 regarding the lack of information and data about the role of impact angle and shear force for these alloys.

This chapter also reveals the importance of detecting the crack initiation and propagation without etching and the importance of perpendicular sectioning to reveal the abrasive wear during impact. Lastly, the microhardness measurements of these alloys with different impact angles are discussed.

The wear scar features were analysed using standard methods described in Chapter 3 including 3D non-contact profilometer (Sections 3.8.3), OM and SEM (Sections 3.8.1 and 3.8.2), microhardness (Section 3.4) and discussed in detail. Then a summary of the main discoveries and the key findings is listed at the end of the chapter.

### 6.2 Impact Test Results

This section summarises the results on wear damage of impact wear rig tests with different impact angles ( $90^\circ$ ,  $60^\circ$ ,  $45^\circ$ ) and specific number of cycles (54,000) for the AISI 316 and EN8 metal alloys used in this research. This number of cycles (54,000) was selected to obtain measurable wear volume. Nevertheless, the wear volume due to normal impact was still a very small proportion of the total wear, as shown in Section 5.2.1 (Figure 5.1), at an impact force of 3476 N due to the role of zero wear volume during normal impact, especially for AISI 304 [71].

The wear volume was determined by converting measured masses to volumes using the mean measured materials density of  $7860 \text{ kg/m}^3$  and  $7820 \text{ kg/m}^3$ , respectively. While the total volume loss was measured by 3D non-contact profilometer (volume change) using the two standard methods described earlier in Chapter 2 (Section 2.3.2) and in Chapter 3 (Section 3.6).

#### 6.2.1 Wear Volume

Specimens of AISI 316 and EN8 were cleaned using a similar procedure to that described in Section 5.2.1. The wear volume is shown in Figure 6.1, the error bars represent the standard deviation of the data from three repetitions on specimens, and the repeatability of the rig were very good as the impacts hit the same contact area with high precision. These results showed good consistency and similarity to previous results obtained by Slatter [8, 9] and Yilmaz [28].

The number of repetitions is less than for AISI 304 because the work presented in this chapter aims to support and prove the previous results on AISI 304 regarding the impact angle.

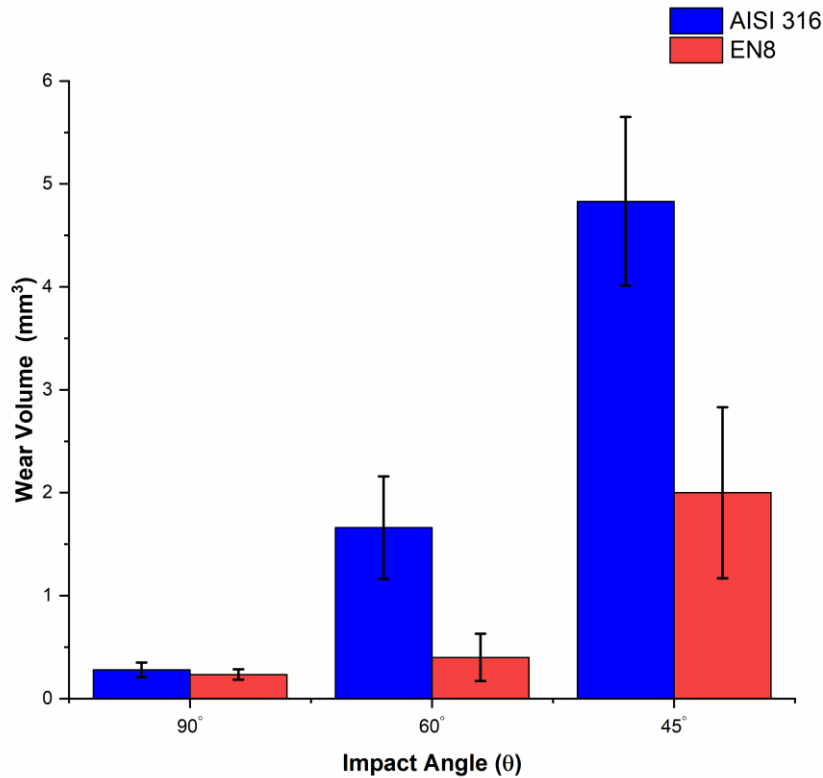


Figure 6.1 Mean wear volume for materials vs different impact angles after 54,000 cycles

Figure 6.1 indicates that changing the impacts from normal (90°) to compound (60° and 45°) led to an increase in material loss. The sliding component plays an important role in material loss as the highest material loss occurred at an impact angle of 45°, similar to the results for AISI 304 presented in Section 5.2.1 (see Figure 5.1).

The results showed no significant difference in the amount of wear volume under normal impact, despite the two materials having relatively different values of hardness (213 HV for EN8, 180 HV for AISI 316). EN8 showed less wear volume than AISI 316 and AISI 304 ( Figure 5.1) for both 60° and 45°, which can be explained as the role of hardness during compound impact and as following the Archard equation [67] prediction that materials with higher hardness will have less wear volume than softer materials.

### 6.2.2 Total Volume Loss

In order to measure the total volume loss and the plastic flow volume (both defined earlier in Section 3.6), a 3D non-contact profilometer was used. The impact wear scar was scanned first by a 3D non-contact profilometer to create a reference plane which was considered as the region outside the impact scar and marked with a turquoise colour, then any upper volume (green, yellow and orange regions) or lower volume (red region) was measured by using the 3D non-contact profilometer as shown in Figure 6.2.

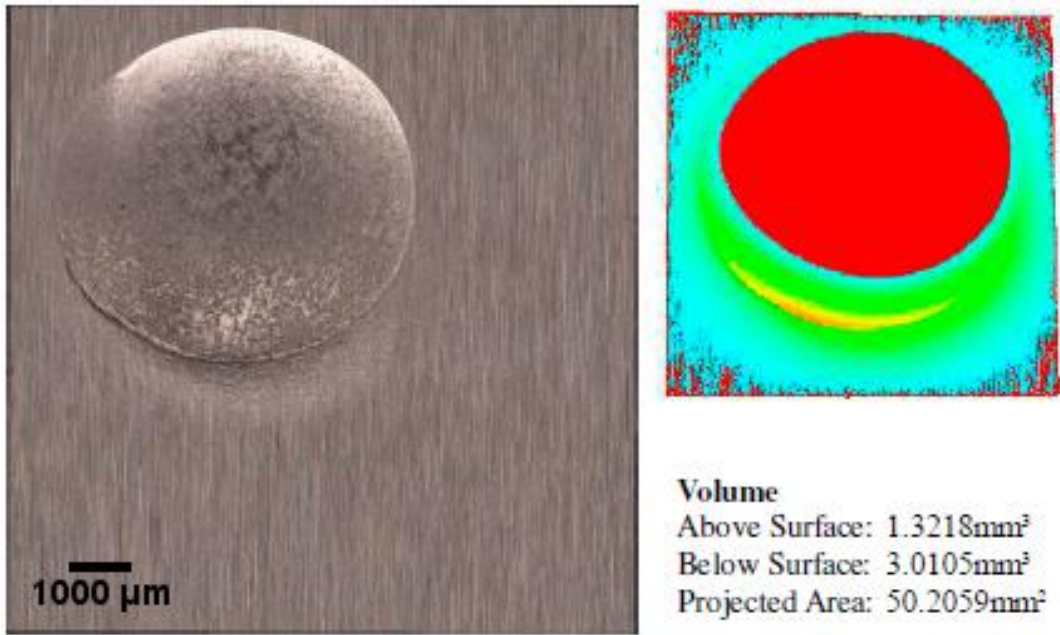


Figure 6.2 Total volume loss as measured on a worn AISI 316 surface (reference plane shown in turquoise), ‘above surface’ (green, yellow and orange region) is plastic flow volume and ‘below surface’ (red region) is total volume loss, at impact angle 60° after 54,000 cycles

Figure 6.2 shows the contour map after 54,000 cycles and at impact angle 60°; it can be seen that the surface is a regular circular shape with obvious plastic flow at the bottom edge of the impact wear scar. The total volume loss for both materials, measured by 3D non-contact profilometer, is plotted against the impact angle after 54,000 cycles in Figure 6.3.

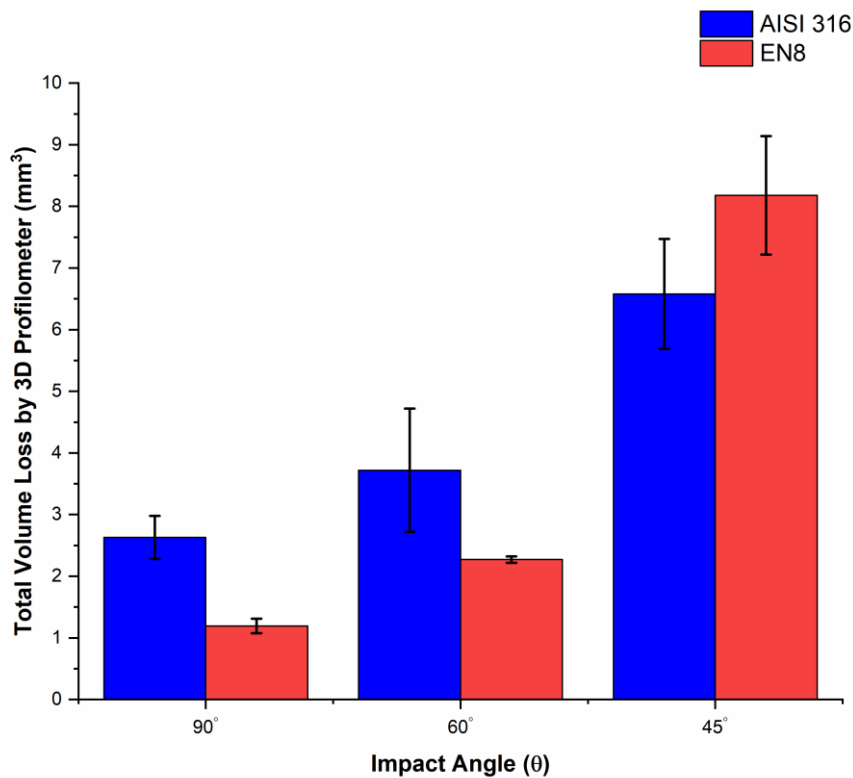


Figure 6.3 Mean total volume loss for both materials vs impact angles at 54,000 cycles

Figure 6.3 shows that the total volume loss for AISI 316 under normal impact is higher than for EN8 due to its relatively lower hardness and this supports the previous results in Chapter 4 (see Figure 4.6).

Similar to the work reported in Section 5.2.2, Figure 6.4 shows an example for the total volume loss and zero wear volume (both defined in Section 3.6) of AISI 316 after 54,000 cycles. Next, Table 6.1 shows the mean total volume loss and the volume loss for each component described in Figure 6.4 and its standard deviation. Similar trends and behaviour were also found for EN8.

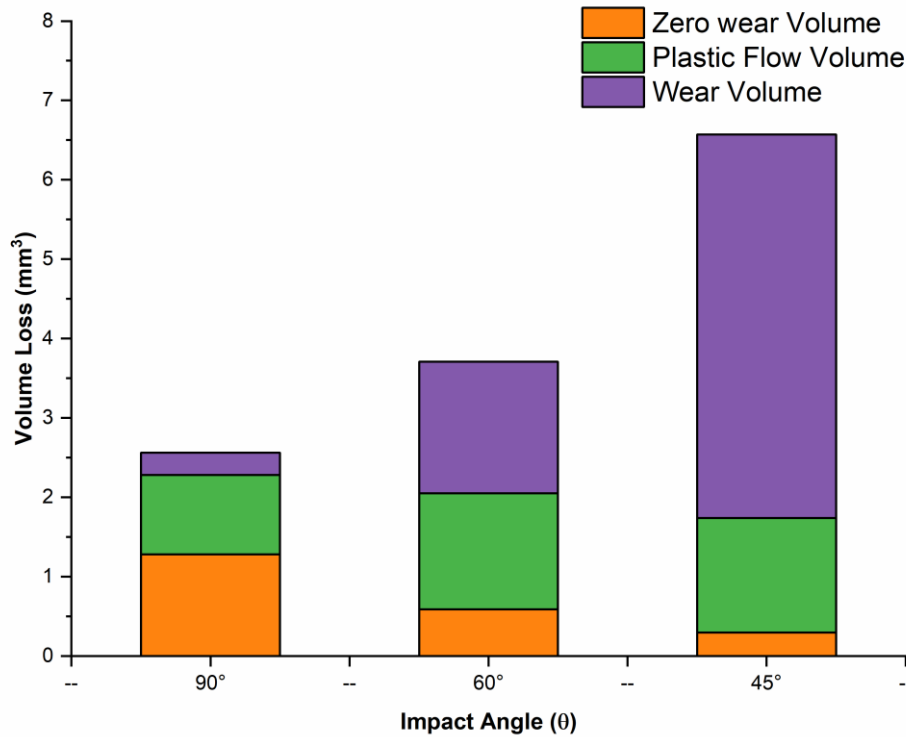


Figure 6.4 Mean total volume loss and volume loss for each component for AISI 316 after 54,000 cycles with different impact angles

Table 6.1 Mean volume loss for AISI 316 after 54,000 cycles with standard deviation for each component

Conditions (cycles, angle, temp.)	Mean Wear Volume $V_w$ ( $mm^3$ )	Standard Deviation $\sigma$ (STD)	Mean Plastic Flow Volume $V_{pf}$ ( $mm^3$ )	Standard Deviation $\sigma$ (STD)	Mean Zero Wear Volume $V_{zw}$ ( $mm^3$ )	Standard Deviation $\sigma$ (STD)	Mean Total Volume Loss $V_t$ ( $mm^3$ )	Standard Deviation $\sigma$ (STD)
<b>AISI 316</b>								
54000, 90°, RT	0.283	0.07	1.07	0.36	1.28	0.36	2.63	0.35
54000, 60°, RT	1.66	0.5	1.46	0.2	0.6	0.3	3.72	1
54000, 45°, RT	4.83	0.82	1.44	0.12	0.3	0.1	6.58	0.89

Figure 6.4 shows a small amount of wear volume under repetitive normal impact after 54,000 cycles due to the synergistic effect of zero wear volume and plastic flow volume, which agrees with the previous results presented in Figure 4.2 and Figure 5.4. The sum of wear volume and plastic flow volume is approximately equal to the directly measured total volume loss (defined earlier in Section 3.6) for

AISI 316. Also, Figure 6.4 shows noticeable increases in wear volume and plastic flow volume with compound impacts ( $60^\circ$  and  $45^\circ$ ), while the zero wear volume has significantly decreased to a potentially negligible level, especially with impact angle  $45^\circ$ , similar to previous results for AISI 304 (see Figure 5.4).

Spherical cap method, as described in Section 2.3.2.2 (Figure 2.17) and used for AISI 304 in Section 5.2.2 (see Figure 5.6), is used again in this chapter to predict the total volume loss of AISI 316 and EN8 with different impact angles by applying Equation 5.1 and the results are plotted in Figure 6.5.

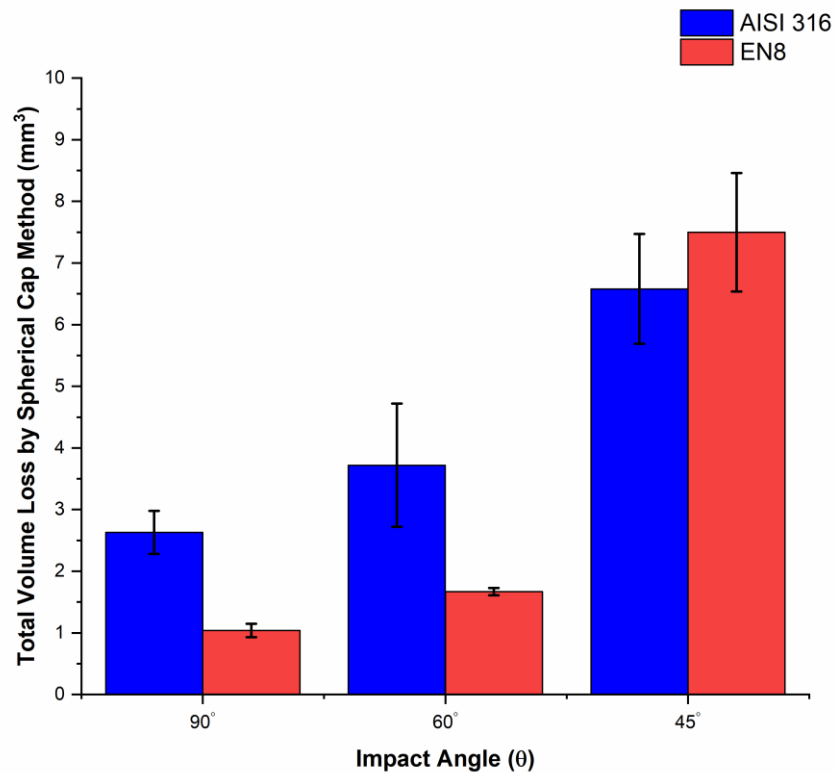


Figure 6.5 Mean total volume loss of AISI 304 and EN8 as calculated by spherical cap method Vs impact angles at 54,000 cycles

The results for total volume loss measured by spherical cap method in comparison with the total volume loss measured by 3D non-contact profilometer under both normal and compound impact are summarised below in Table 6.2.

Table 6.2 Comparison of total volume loss as measured by two different methods for AISI 304 and EN8 with different impact angles and after 54,000 cycles

Conditions (cycles, angle, temp.)	Mean total volume Loss by Alicona (mm <sup>3</sup> )	Mean scar depth $h_1$ (mm)	Ball radius R (mm)	Total volume by spherical cap estimation (mm <sup>3</sup> )	Error to Alicona %
<b>AISI 304</b>					
54000, 90°, RT	2.63	0.316	7.5	2.32	11.79
54000, 60°, RT	3.72	0.377	7.5	3.292	11.48
54000, 45°, RT	6.58	0.517	7.5	6.15	6.48
<b>EN8</b>					
54000, 90°, RT	1.19	0.212	7.5	1.04	11.8
54000, 60°, RT	2.27	0.268	7.5	1.67	26
54000, 45°, RT	8.18	0.572	7.5	7.51	8.15

There is a significant difference between the total volume loss measured by 3D non-contact profilometer or spherical cap method (see Figure 6.3 and Figure 6.5) and the wear volume measured by mass scale (see Figure 6.1), especially under normal impact. This reflects that the previous literature studies that used 3D non-contact profilometer or spherical cap methods, such as those by Jiang [15], Wang [37] and Rigaud & Le Bot [29], were actually measuring the total volume loss rather than wear volume. This can be attributed to the role of zero wear volume during normal impacts, whereas it can otherwise be neglected with compound impacts, especially with lower impact angles such as 45° [71] (see Figure 5.4 and Figure 6.4).

### 6.2.3 Impact Wear Scar Measurements

The wear scar of specimens was examined during this work after impacts at different angles, applying the same procedure as described in Section 5.2.3 and shown in Figure 6.6 for typical 2D profile of impacted specimens.

## Role of Impact Angle on Surface and Subsurface Deformation of Alloy Steels

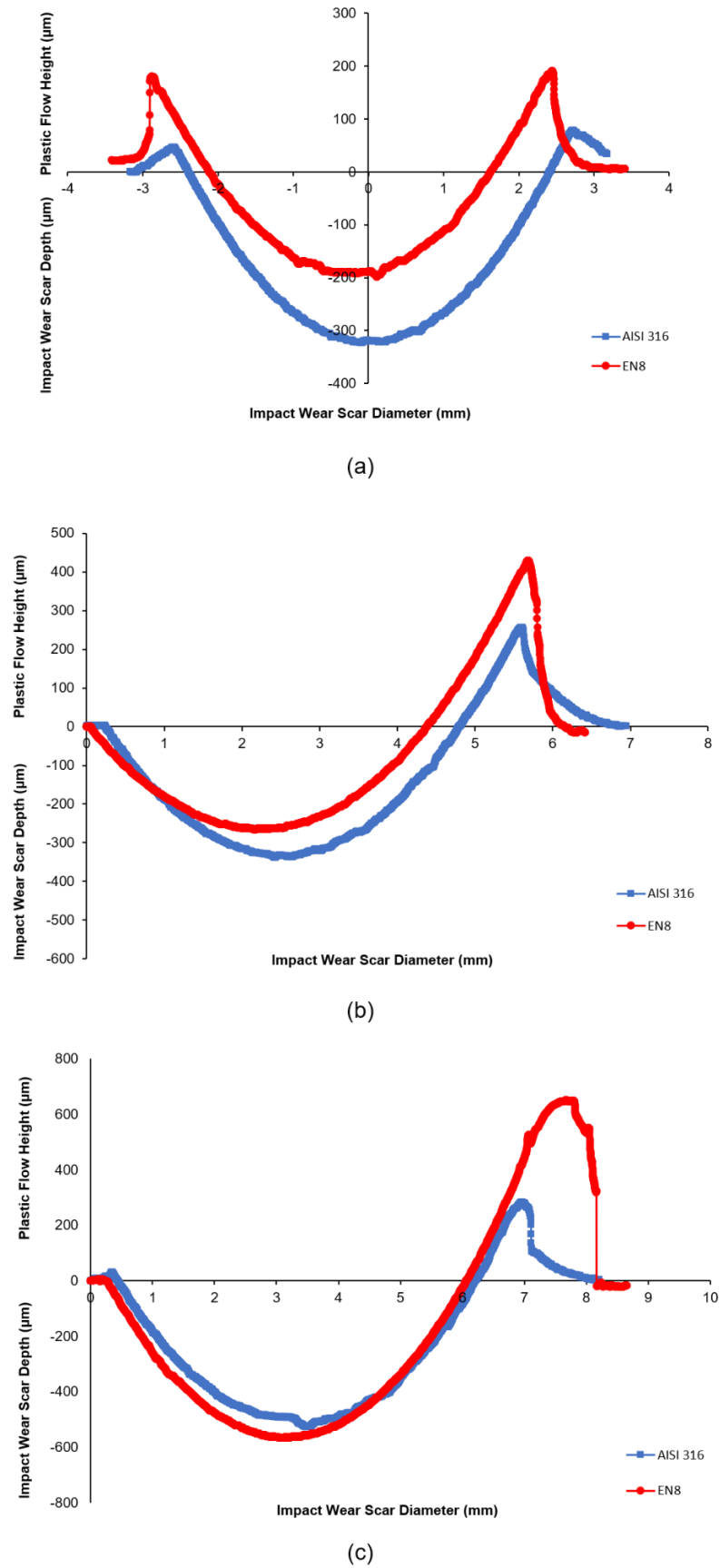


Figure 6.6 Typical diameter and depth of the wear scars for AISI 316 and EN8 after 54,000 cycles under (a) normal impact, (b) compound impact 60°, and (c) compound impact 45°

Figure 6.6 (a) shows that AISI 316 has a small amount of plastic flow on both edges (top and bottom) that reaches up to 80  $\mu\text{m}$  for a normal impact, higher than for AISI 304, in which it reached approximately 40  $\mu\text{m}$ , as shown in Figure 5.7 (a). This proves that in materials with high ability for work hardening (generally soft), more material tends to be compressed rather than plastically flow (with harder materials and low propensity for work hardening) as explained by Tabor [87] or removed from the surface as wear debris.

On the other hand, EN8, due to its lower ductility, shows a significant amount of plastic flow on both edges, reaching up to 200  $\mu\text{m}$ , while the impact wear scar depth of AISI 316 under normal impact is obviously higher than that of medium carbon steel. This is connected to the role of hardness on total volume loss of materials and supports the previous results presented in Section 4.3 (see Figure 4.10).

With an impact angle of 60° (Figure 6.6 (b)), both materials show higher wear scar depth. A noticeable amount of plastic flow material has been removed from the impact region to the bottom edge of impact scar in the cases of both materials, with the tendency for EN8 to exhibit more plastic flow, reaching up to 490  $\mu\text{m}$  as compared with 256  $\mu\text{m}$  for AISI 316.

The accumulation of plastic deformation on the bottom edge of the impact wear scar could be explained as the role of the tangential component of the impact force, which has a value of 1738 N at 60°.

Figure 6.6 (c) presents an obvious increase in the impact wear scar diameter and depth in addition to the amount of plastic flow on the bottom edge of the scar for both materials after 54,000 cycles, EN8 still exhibits higher plastic flow, reaching up to 770  $\mu\text{m}$  compared with 300  $\mu\text{m}$  for AISI 316.

The reason for this noticeable increase in the amount of plastic flow materials at the bottom edge of the impact scar is the higher effect of shear force during impact which caused the removal of further material from the impact region toward the bottom edge; at an impact angle of 45° the shear force is 2457 N which is higher than at 60°.

The results clearly indicate that the shear force (tangential force) plays an important role in impact wear scar depth, diameter and the amount of plastic flow accumulated on the bottom edge.

It is also important to mention that the other edges (right and left) of the impact wear scar did not reveal any significant amount of plastic flow under different number of cycles and impact angle, therefore these have not been analysed further.

## 6.3 Wear Scar Analysis

### 6.3.1 Surface Examination

The impact wear and deformation behaviour at the surface of AISI 316 and EN8 with different impact angles and specific number of cycles 54,000 were studied during this work by using SEM (Hitachi TM3030 Plus). The lack of data about the surface damage to both materials with different impact angles, as one of the main key trends described in Section 2.2.2.1, was the motivation for this investigation.

The centre region of the wear scar was investigated in addition to the other regions of interest. Additionally, the bottom edge was examined during compound impact, while the other edges did not show significant amounts of plastic flow or any other important features and were therefore not analysed in this work.

The wear damage mechanisms of AISI 316 in the centre of the wear scar with different impact angles are shown in Figure 6.7.

## Role of Impact Angle on Surface and Subsurface Deformation of Alloy Steels

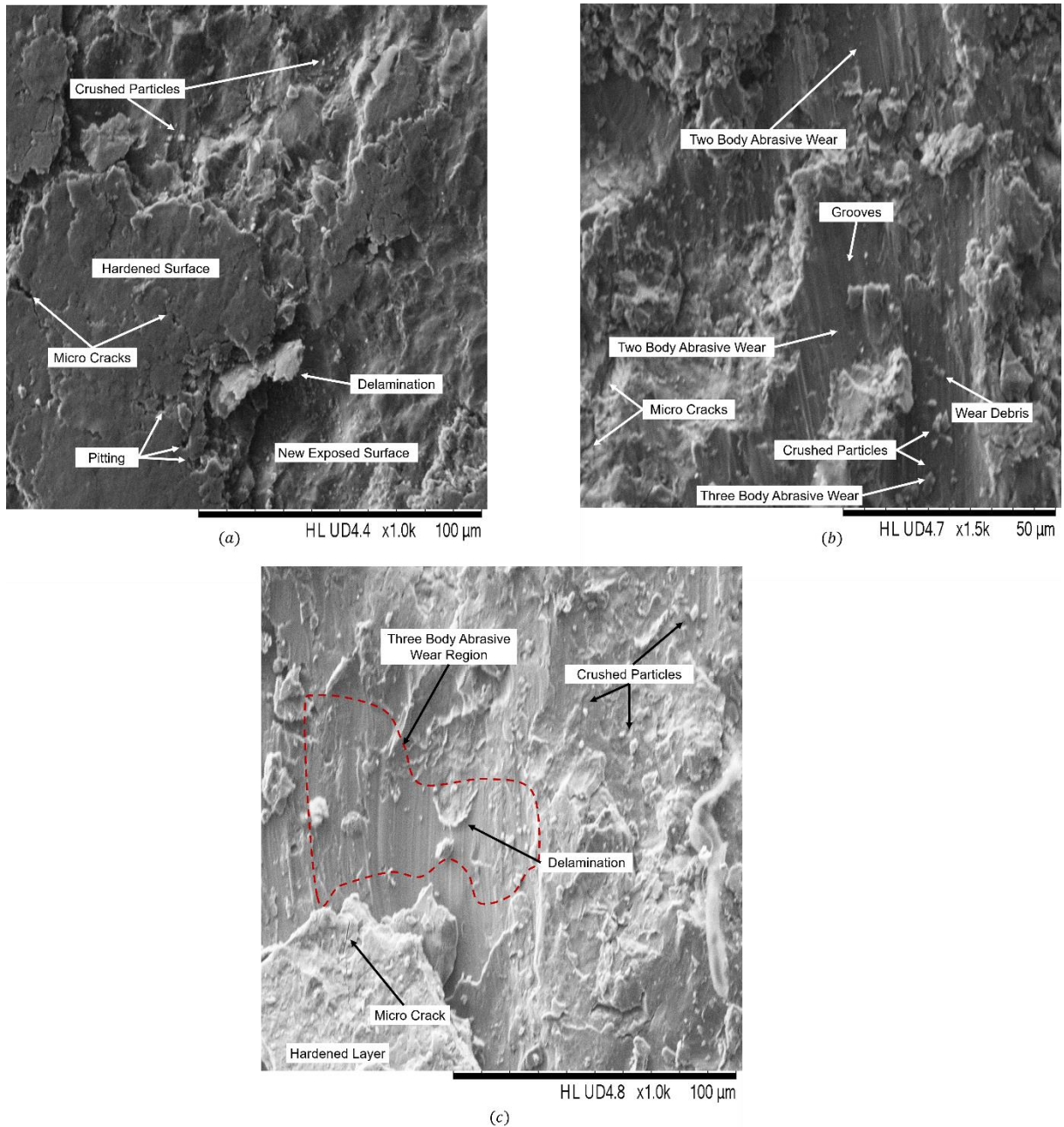


Figure 6.7 SEM image of the worn surface of AISI 316 showing the wear damage mechanism in the centre of the scar after 54,000 cycles under: (a) normal impact  $90^\circ$ , (b) impact angle  $60^\circ$  and (c) impact angle  $45^\circ$

The wear damage under normal impact, as revealed in Figure 6.7 (a), is mainly plastic deformation (hardened surface) with microcracks in addition to surface fatigue as a result of both delamination and spalling resulting from micro pitting. The hardened surface edge underwent severe damage and reduction in ductility that led to crushing of these edges into small particles. The new exposed surface under normal impact will be another hardened surface similar to the adjacent one and then a series of crack will appear and crushed particles that will be removed from the surface and the process will be repeated again.

Figure 6.7 (b) and (c) show the wear damage mechanism under compound impact for angles  $60^\circ$  and  $45^\circ$ , respectively. In addition to surface fatigue, two and three body abrasive wear (defined in Section 5.5.2.1) occurred during impact which explains the increase in mass loss with both angles. The small crushed particles that were trapped inside the abrasion region, between the striker and the worn surface of specimens indicates three body abrasive wear, while other regions without these particles underwent two body abrasive wear (see Figure 6.7 (b) and (c)). Therefore, the surface examination showed that the hardened layers were removed not only by surface fatigue but also due to abrasive wear.

As expected, the AISI 316 surface underwent multiple layers of delamination near the bottom edge of the wear scar at impact angle  $60^\circ$  as shown in Figure 6.8, similar to AISI 304, shown in Figure 5.18, and as explained in Section 5.3.1.2. Meanwhile, Figure 6.9 shows the bottom edge of the wear scar with different angles.

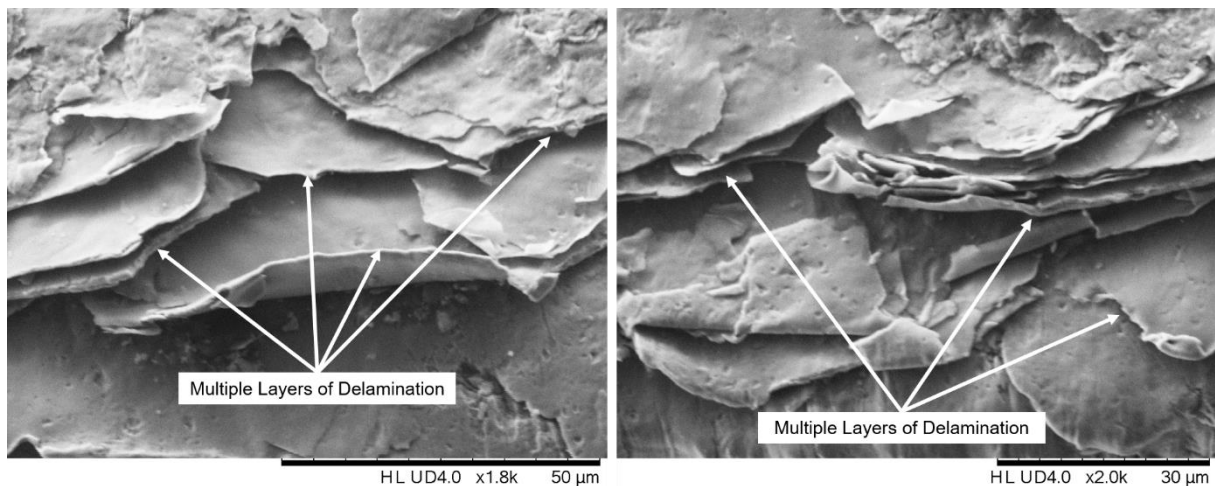


Figure 6.8 Multiple layers of delamination near the bottom edge of the wear scar for AISI 316 after 54,000 cycles under compound impact  $60^\circ$  with different magnifications

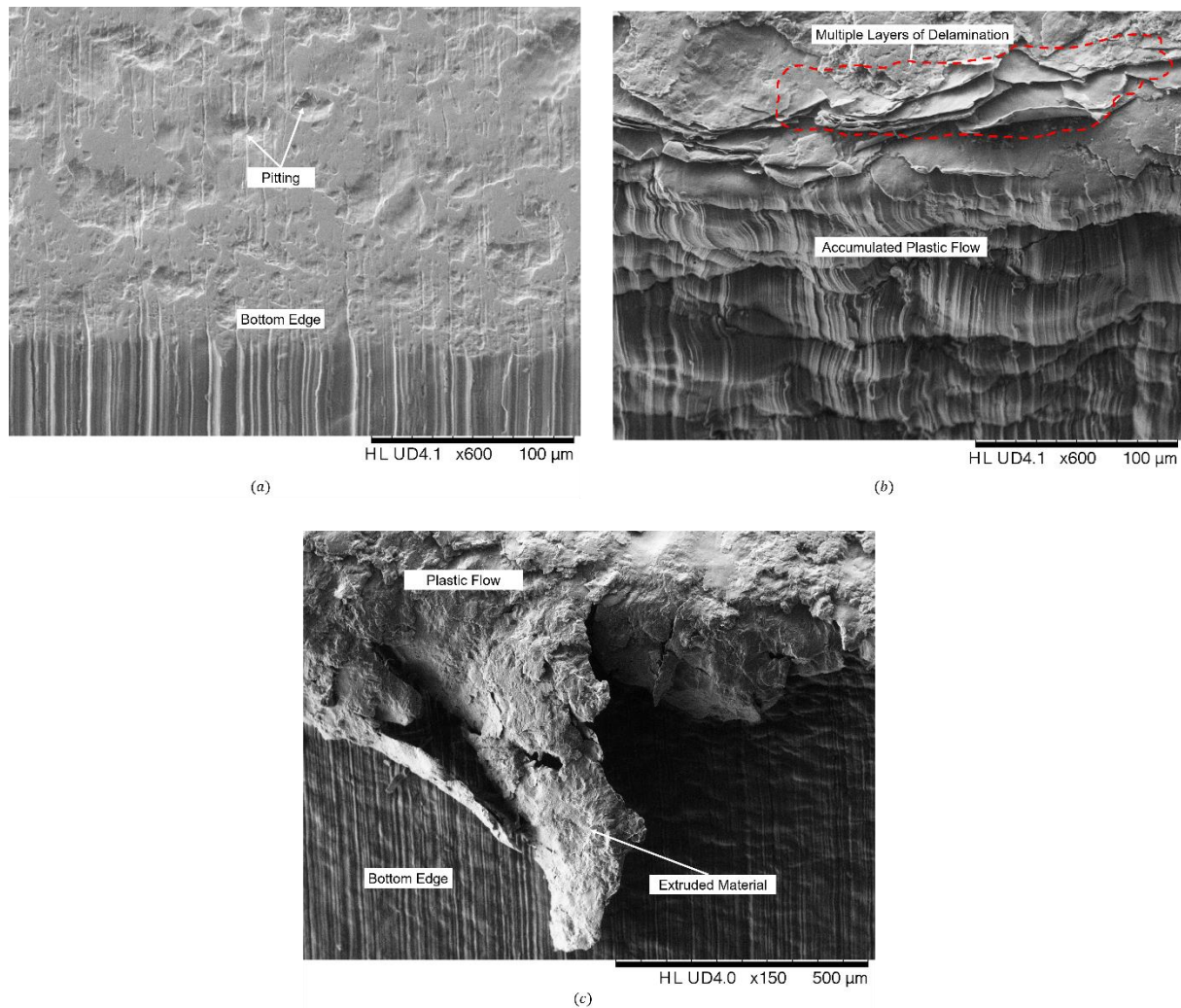


Figure 6.9 SEM image for the bottom of the wear scar for AISI 316 after 54,000 cycles showing the accumulation of plastic flow materials on or outside the bottom edge under: (a) normal impact  $90^\circ$ , (b) impact angle  $60^\circ$ , and (c) impact angle  $45^\circ$

Figure 6.9 shows the important role of shear force regarding the amount of plastic flow near the bottom edge that leads to material being extruded outside of the wear scar. This is obvious by SEM with impact angles of  $60^\circ$  and  $45^\circ$  ((b) and (c)), but not apparent with a normal impact ( $90^\circ$ ) (a). These results are in agreement with the previous data for AISI 304 (see Figure 5.15 and Figure 5.20).

### 6.3.1.1 Medium Carbon Steel

The wear damage mechanisms for EN8 are not very different from those for AISI types 304 and 316, as shown in the images in Figure 6.10 of the centre regions of the impact wear scars.

## Role of Impact Angle on Surface and Subsurface Deformation of Alloy Steels

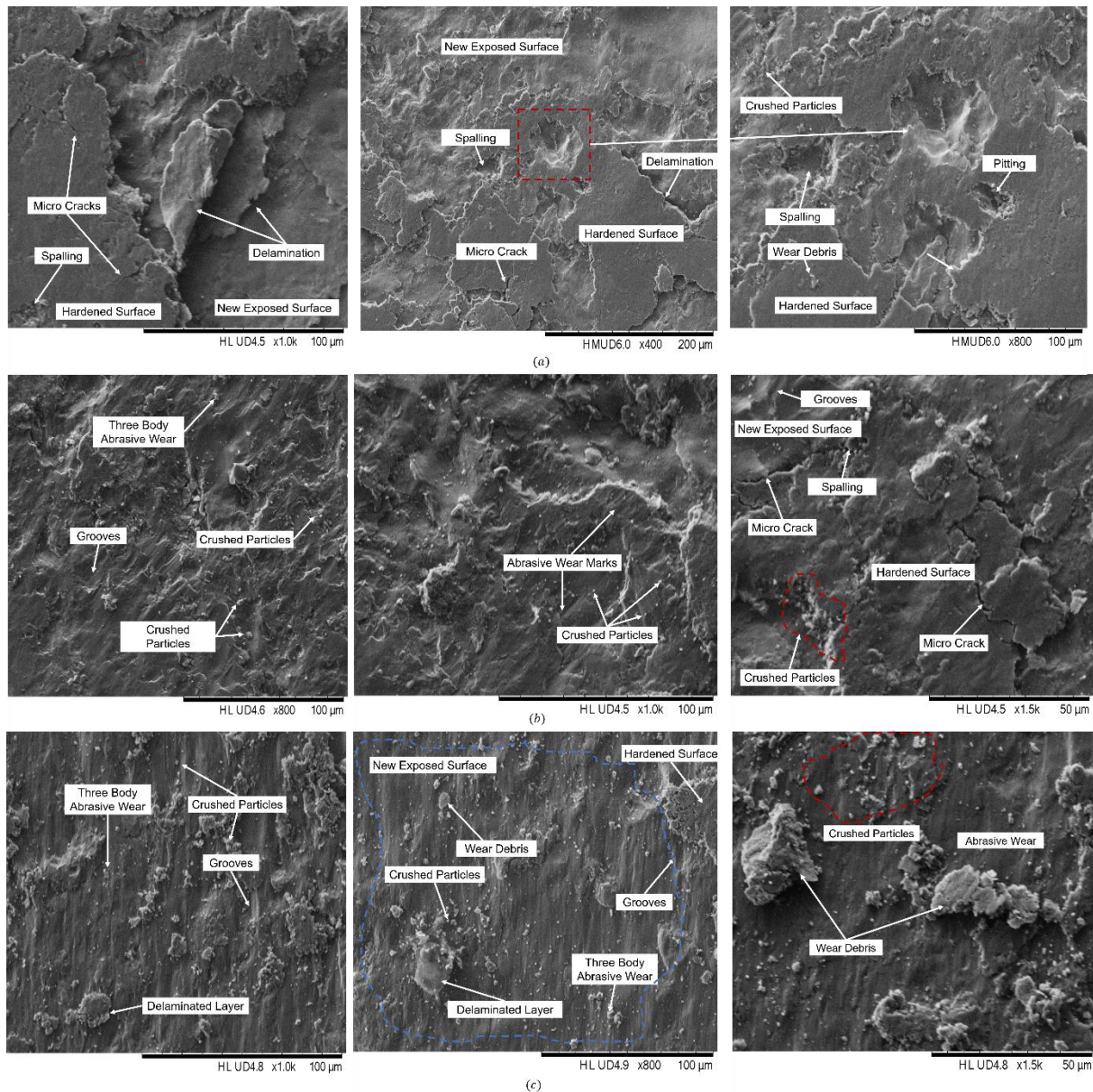


Figure 6.10 SEM images of the worn surface for EN8 showing the wear damage mechanism in the centre of the scar after 54,000 cycles under: (a) normal impact  $90^\circ$  showing the delamination and pitting, (b) impact angle  $60^\circ$  showing the abrasive wear, crushed particles and micro crack, and (c) impact angle  $45^\circ$  showing the abrasive wear, crushed particles and adhered wear debris

Figure 6.10 (a) presents the normal impact after 54,000 cycles and reveals that the main wear damage mechanisms are plastic deformation (hardened surface) and surface fatigue which results in both delamination and spalling.

Additionally, abrasive wear with obvious grooves occurred with both impact angles,  $60^\circ$  (Figure 6.10 (b)) and  $45^\circ$  (Figure 6.10 (c)), after 54,000 cycles in a similar way to both AISI types, 304 and 316. It is clear that abrasive wear is the predominant type of wear damage occurring on the worn surface, especially with impact angle  $45^\circ$  (highlighted in a blue colour) where higher shear force occurs. The trapped crushed particles between the striker and the worn surface cause three body abrasion that is more obvious in Figure 6.10 (c). Multiple layers of delamination occur with both impact angles  $60^\circ$  and

45° near the bottom edge of the impact wear scar as shown in Figure 6.11, while Figure 6.12 shows the distribution of plastic flow near the bottom edge of the wear scar.

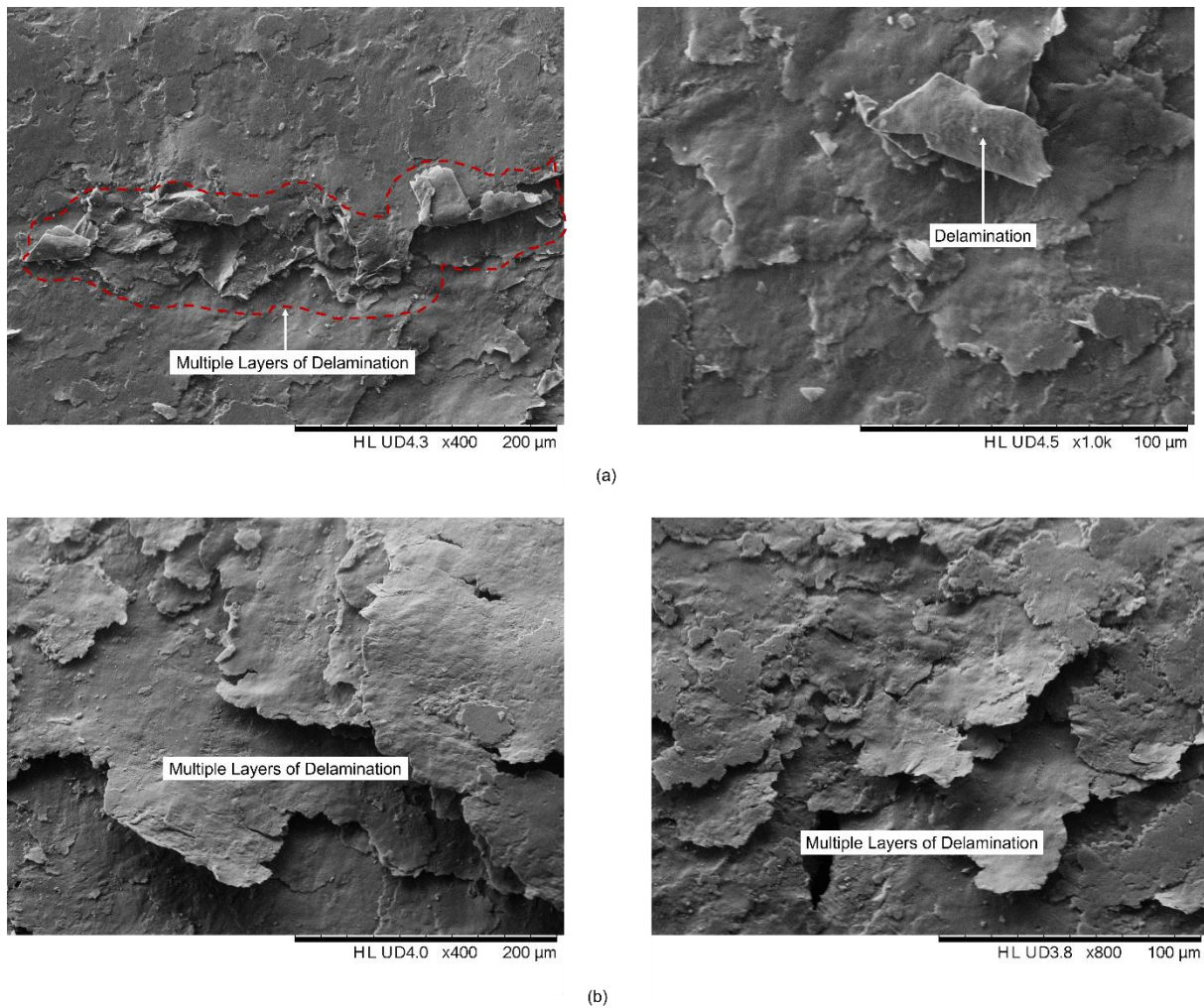


Figure 6.11 Multiple layers of delamination of the wear scar for EN8 after 54,000 cycles near the bottom edge under: (a) impact angle 60° and (b) impact angle 45°

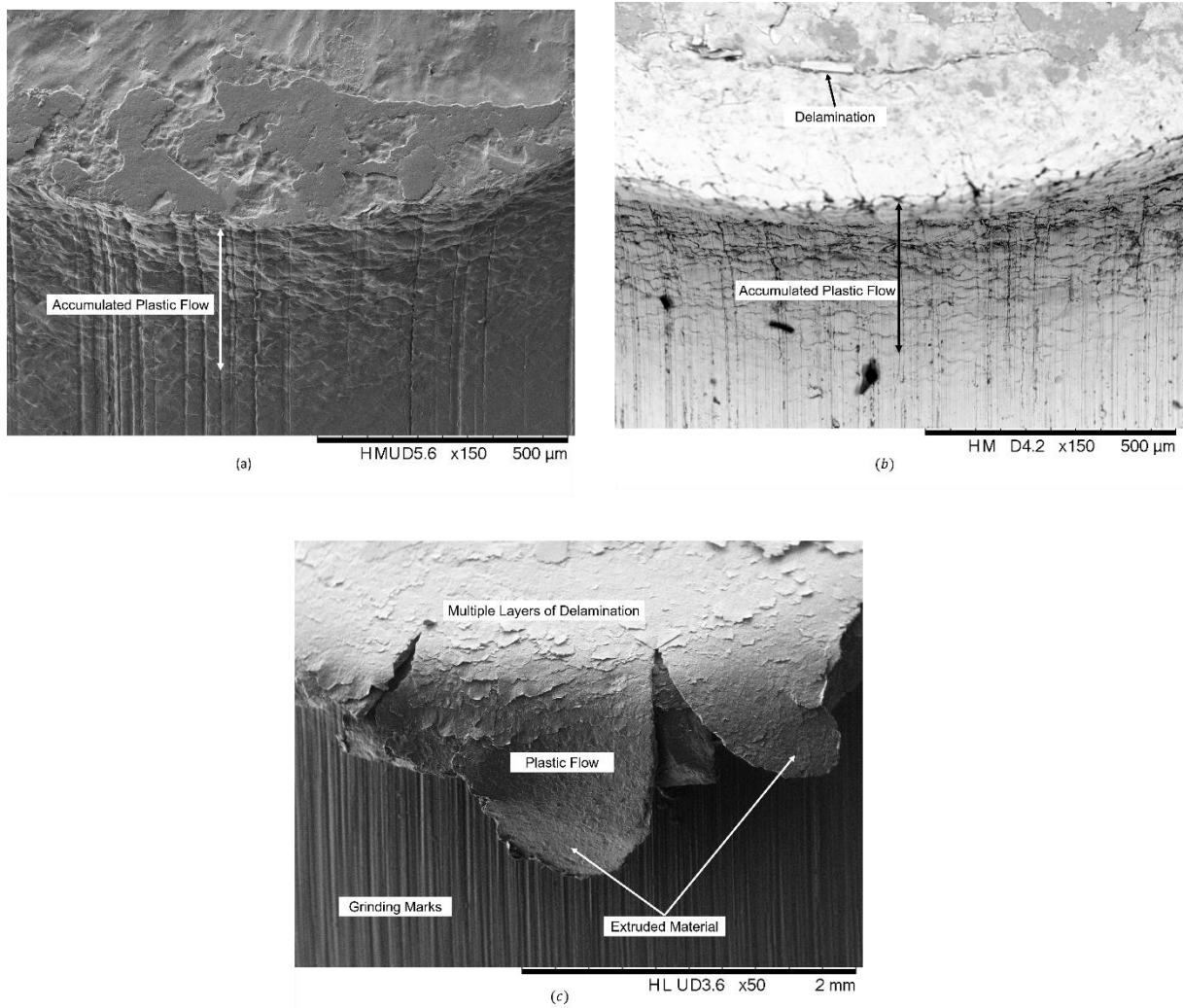


Figure 6.12 SEM image for the bottom of the wear scar for EN8 after 54,000 cycles showing the accumulation of plastic flow materials on or outside the bottom edge under: (a) normal impact 90°, (b) impact angle 60°, and (c) impact angle 45°

Figure 6.12 shows plastic flow was distributed uniformly on the bottom edge with both normal impact (contrary to AISI 304 and 316) and an impact angle of 60° (similar to AISI 304 and 316). With an impact angle of 45°, plastic flow was extruded outside the impact wear as occurred with both AISI types, 304 and 316 (see Figure 5.20 and Figure 6.9 (c)).

### 6.3.2 Subsurface Examination

Section 2.2.2.1 and Section 2.5.1 revealed that subsurface damage to AISI 316 and EN8 with different impact angles is a topic that has not been covered in depth. There is a lack of data about crack initiation and propagation, their orientation, grain size, grains orientation during impact and the depth of the plastic region. Therefore, this section addresses these gaps in order to broaden the understanding of repetitive impact wear for these alloys and support the previous results for AISI 304.

The process of sample preparation was described in Section 3.7 and explained further in Section 5.3.2.1; the examination was conducted for both materials after 54,000 cycles.

### 6.3.2.1 Crack Initiation and Propagation of AISI 316

Figure 6.13 shows an SEM image for the centre region of a wear scar for AISI 316 under normal impact.

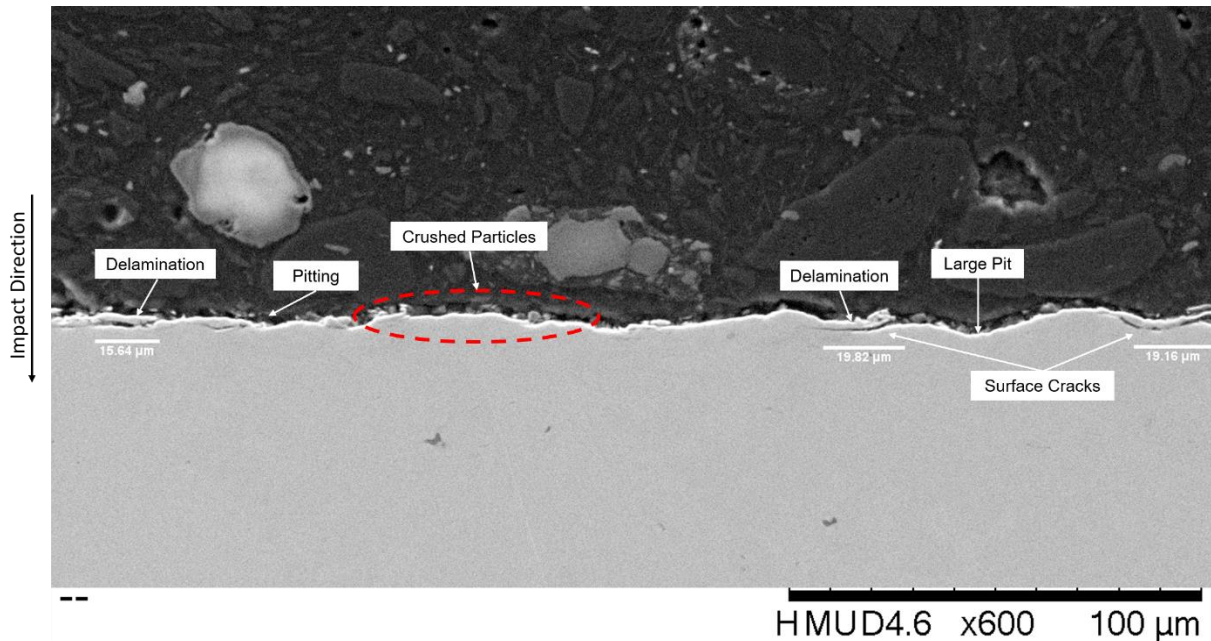


Figure 6.13 SEM image for AISI 316 after 54,000 cycles under normal impact

Figure 6.13 reveals that delamination layers resulted from microcracks that initiated from the surface and propagated beneath the surface at a steep angle and then turned parallel to the surface, a process quite similar to that found for AISI 304 (see Figure 5.24) and steel materials [15] (see Figure 2.3 (d) and Figure 2.8). These delamination layers then leave the surface and a large pit is created, the size of the pit depending on the delamination layer size. Crushed particles were also found on the worn surface of AISI 316, which were formed due to reduction in the ductility of materials and their becoming more brittle.

The top and bottom edges did not show a significant amount of plastic flow and therefore no further features were examined.

Subsurface examination of the centre region of the worn surface with an impact angle of  $60^\circ$  showed, as expected, a larger delamination layer that resulted from larger subsurface major crack connecting together with minor surface crack as shown in Figure 6.14, which is quite similar to the results for AISI 304 in Figure 5.25.

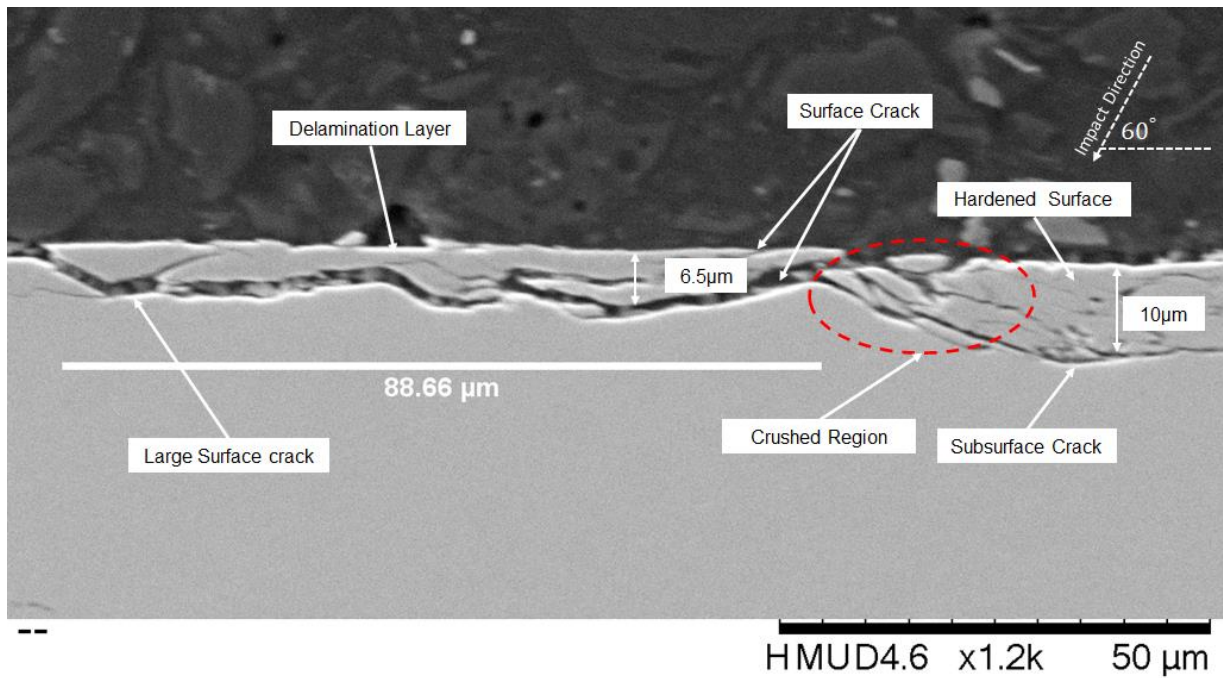


Figure 6.14 SEM image of subsurface damage for AISI 316 after 54,000 cycles under compound impact 60°

Figure 6.14 shows a large surface crack on the left side of the image that has caused delamination and this delaminated layer, which also forms the hardened surface, will eventually leave the surface and leave behind multiple pits. The hardened surface on the right side of the image has undergone a series of surface and internal subsurface microcracks in different directions and these cracks will lead to removal of small particles from the hardened surface (highlighted in a red colour).

Figure 6.15 shows multiple layers of delamination near the bottom edge of the impact wear scar similar to those found in AISI 304 (see Figure 5.28) and supporting the previous results of surface examination presented in Section 6.3.1 (Figure 6.8).

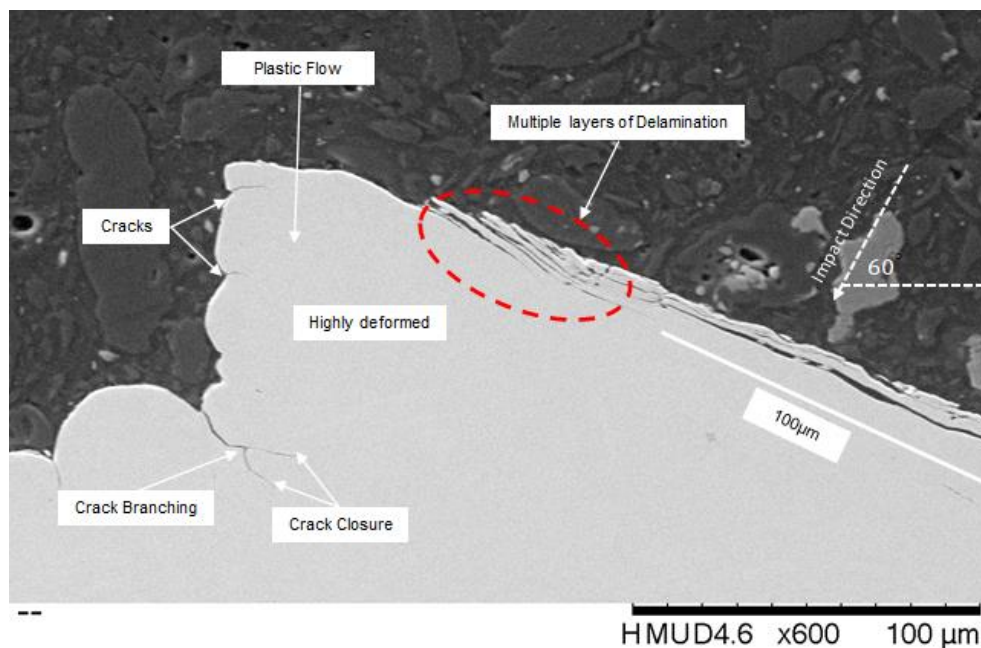


Figure 6.15 SEM image of plastic flow on the bottom edge of the wear scar for AISI 316 after 54,000 cycles under compound impact 60° and multiple layers of delamination near the bottom edge

The wear damage mechanism with an impact angle of  $45^\circ$  revealed removal of more hardened layers from the surface by the effect of higher shear force compared with an impact angle of  $60^\circ$  and obvious removal of delaminated layers from the surface. Multiple cracks occurred in these delaminated layers in different directions and created smaller delaminated layers and also crushed particles as highlighted in a blue colour. These features are similar to those found with AISI 304 (see Figure 5.30), highlighted in a red colour.

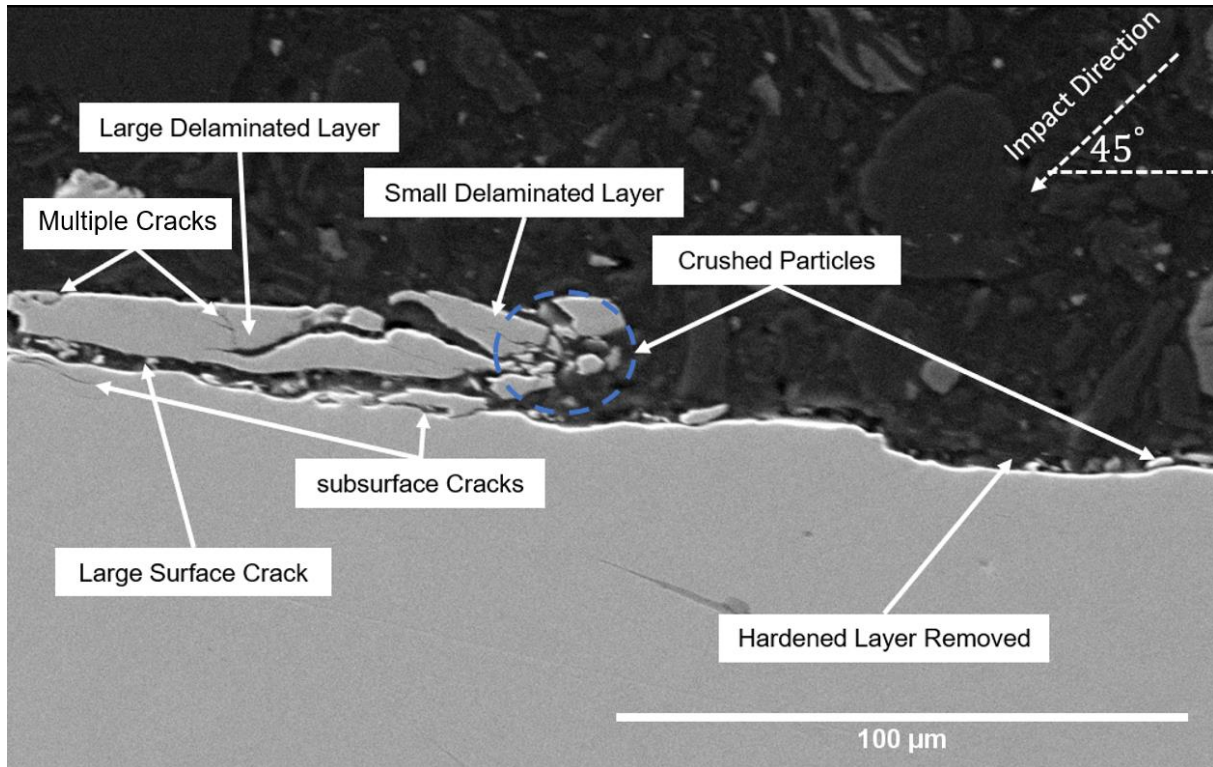


Figure 6.16 SEM image showing large subsurface cracks inside the worn surface for AISI 316 after 54,000 cycles under compound impact  $45^\circ$

Figure 6.17 shows a region away from the centre of the impact scar and towards the bottom edge, where multiple microcrack in different directions have led to surface fatigue in the form of multiple delamination layers and spalling resulting from crushed particles.

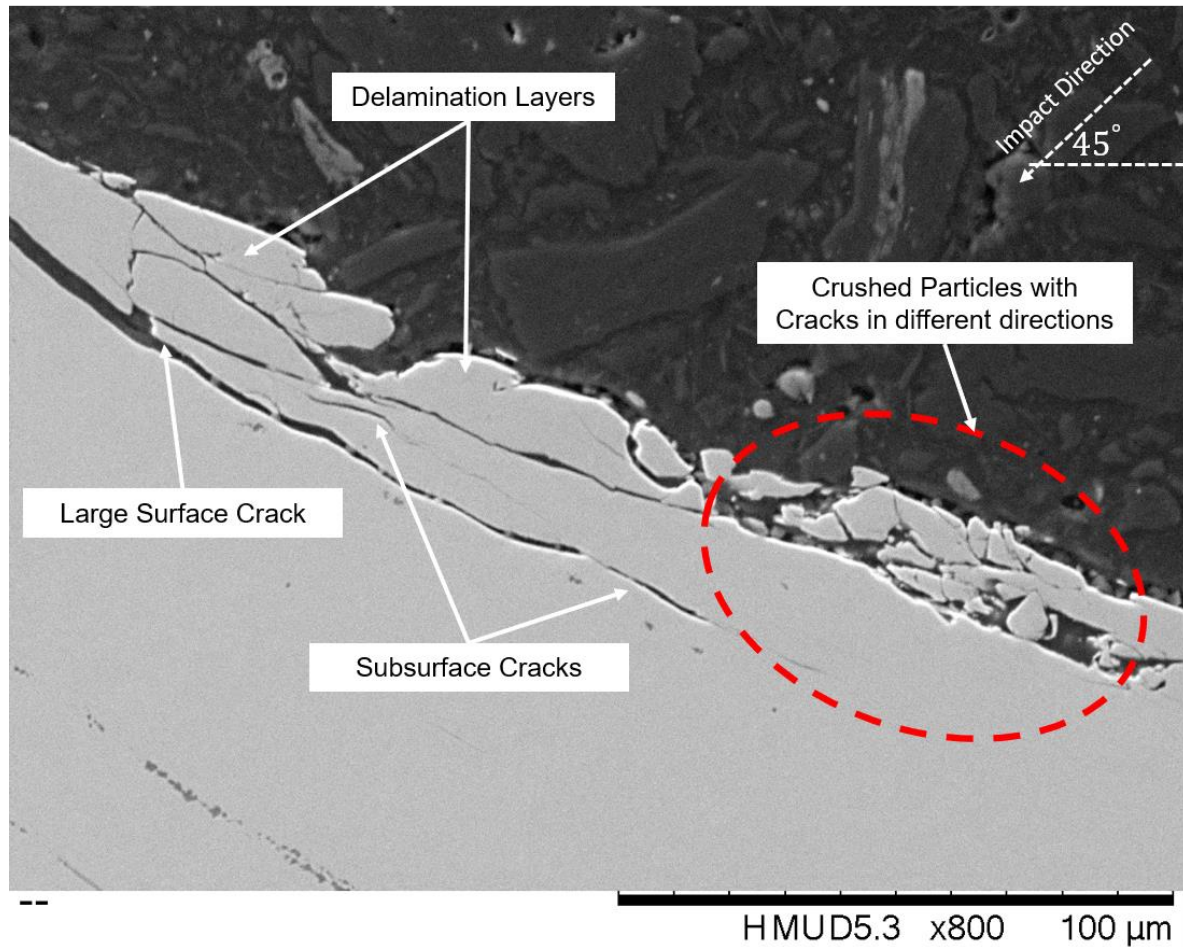


Figure 6.17 SEM image of large delamination layer due to surface and subsurface cracks in AISI 316 after 54,000 cycles under compound impact  $45^\circ$ , with crushed particles to the right side of the image

The left side of Figure 6.17 shows an obvious large surface crack that has connected with subsurface cracks and caused a large delamination layer. Within this large delamination layer, there are microcracks that have propagated in different directions; some of these will cause crushed particles and others will cause small delamination layers within the same large delamination layer. As a result of the increase in tangential force at  $45^\circ$ , more plastic flow has been extruded outside the impact scar rather than being deformed uniformly as with an impact angle of  $60^\circ$ . Figure 6.18 shows an example of pile up materials that have been extruded outside the impact scar in addition to multiple layers of delamination near the bottom edge.

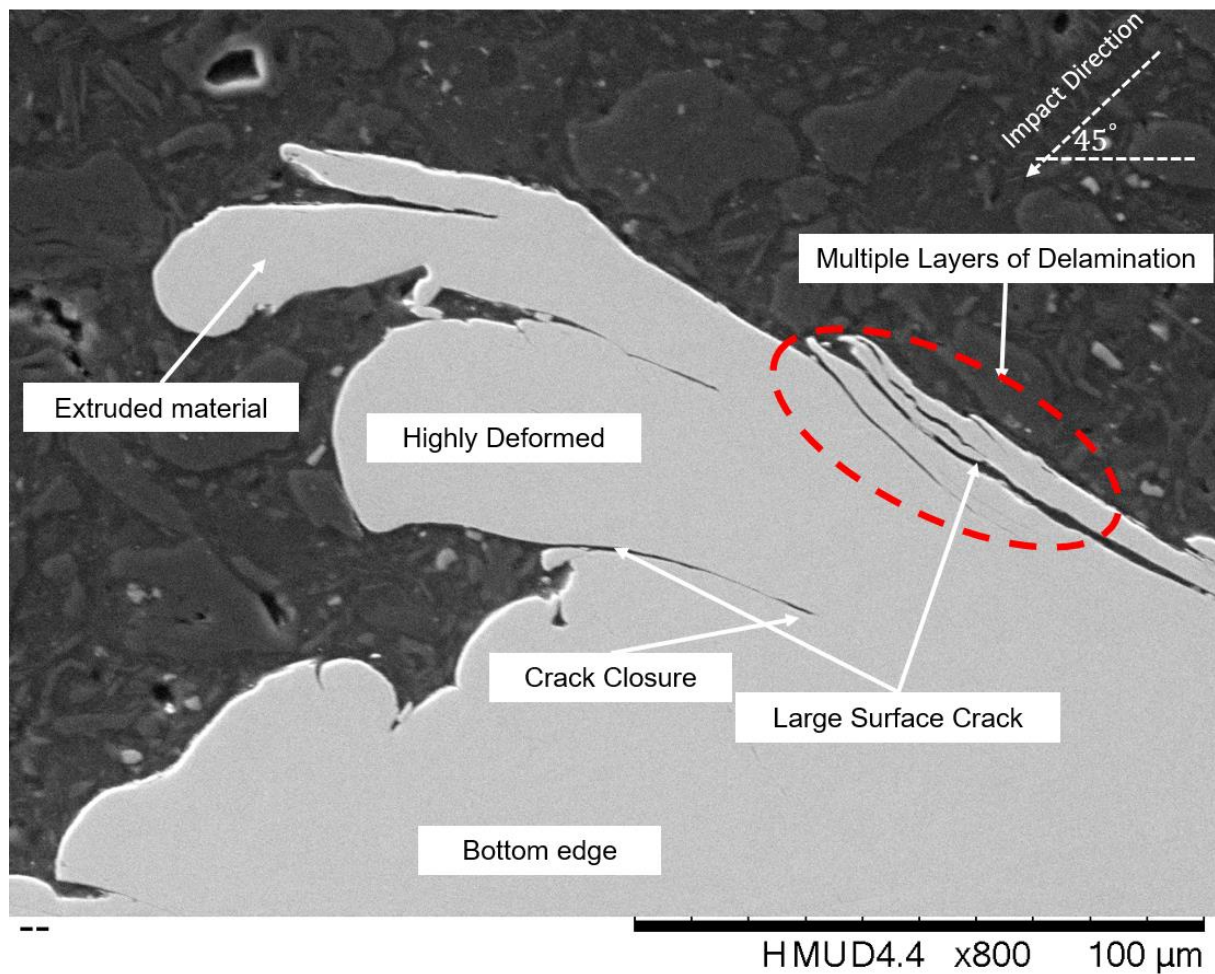


Figure 6.18 SEM image of pile up materials extruded outside the impact scar of AISI 316 after 54,000 cycles under compound impact  $45^\circ$

### 6.3.2.2 Medium Carbon Steel

The subsurface damage for the centre region of the impact wear scar showed no great differences from the two AISI types, 304 and 316. Plastic deformation and surface fatigue due to multiple layers of delamination resulting from surface microcrack were the main wear damage under normal impact after 54,000 cycles, as shown in Figure 6.19. Due to low ductility of EN8 compared with AISI 316, both the top and bottom edges exhibit significant amounts of plastic flow as shown in Figure 6.20.

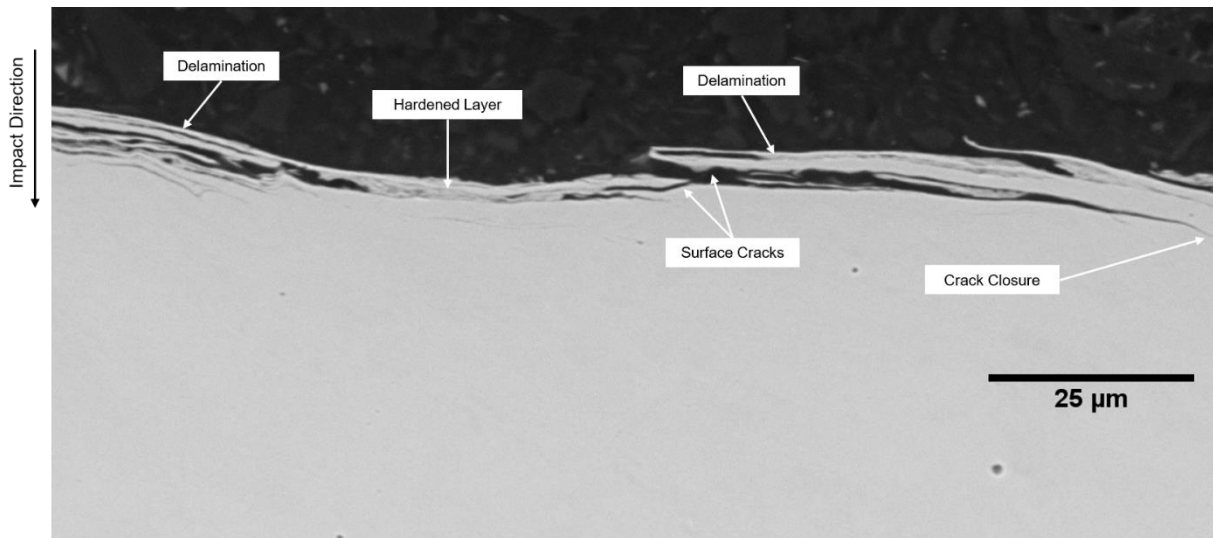


Figure 6.19 SEM image for EN8 after 54,000 cycles under normal impact showing multiple layers of delamination

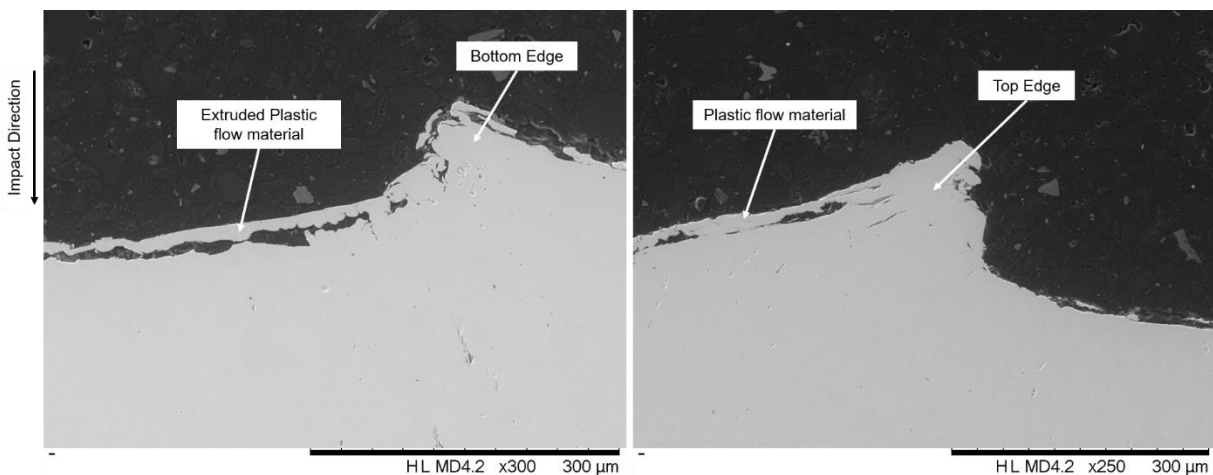


Figure 6.20 Accumulated plastic flow materials on both the top and bottom edge of the impact scar for EN8 after 54,000 cycles under normal impact

Figure 6.19 reveals multiple delamination layers that resulted from microcrack initiated from the surface and propagated beneath the surface and then turned parallel to the surface, a result similar to those found for AISI 304 (see Figure 5.24), AISI 316 (see Figure 6.13), and carbon steel [15, 23] (see Figure 2.3 (d) and Figure 2.8).

Figure 6.20 shows significant accumulations of pile-up materials on both the top and bottom edge of the impact scar under normal impact, trends which did not occur with AISI types 304 and 316. This could be connected to the low ductility of EN8 leading to more materials being deformed on both edges rather than being compressed as zero wear volume or removed as wear volume. These results support and confirm the previous results presented in Section 6.2.3 (Figure 6.6) and Section 6.3.1.1 (Figure 6.12) which revealed significant amount of plastic flow for EN8 with all impact angles.

The impact wear damage mechanisms with an impact angle of  $60^\circ$  are quite similar to those for both types of stainless steel, as shown in Figure 6.21.

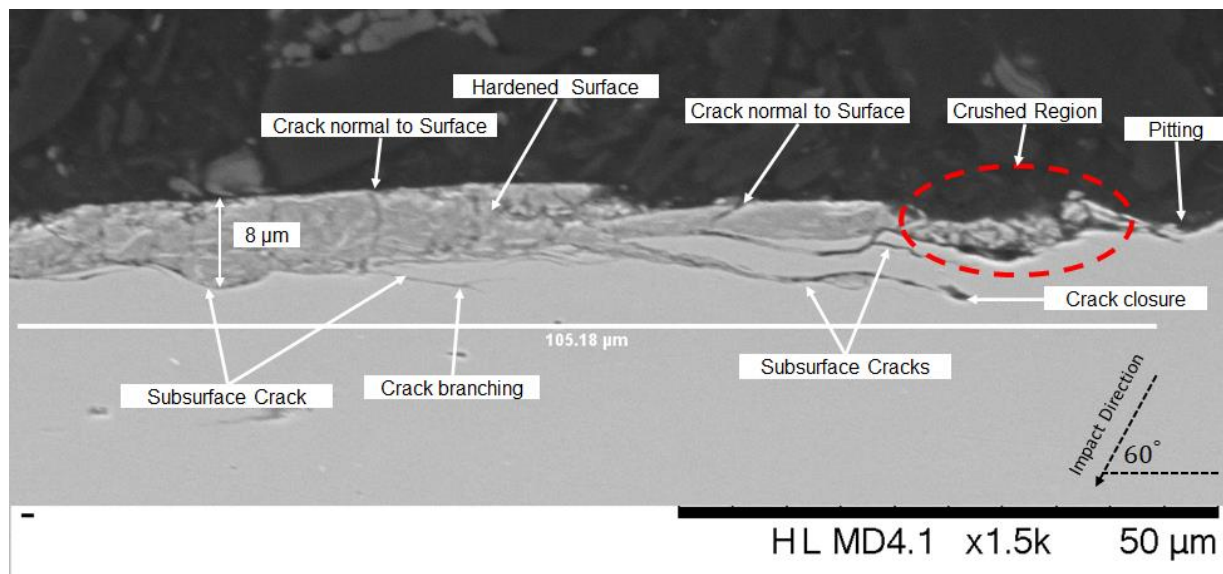


Figure 6.21 SEM image of subsurface damage for EN8 after 54,000 cycles under compound impact 60°

Figure 6.21 reveals a hardened layer with a depth of approximately 8  $\mu\text{m}$  and length of 105  $\mu\text{m}$  that will eventually leave the surface as a result of surface degradation. Both types of microcrack (surface and subsurface), lead to severe damage on the surface. The large parallel surface or subsurface crack cause delamination, while the small crack normal to the surface is connected with small parallel crack and cause crushed particles, as seen on the right side of Figure 6.21 (highlighted with a red colour), and lead to spalling.

It is most likely that the small pits resulted from the crushed particles leaving the surface and causing spalling to the surface, whereas the large pits most likely resulted from the delamination layer leaving the surface and creating wider pits, while the small ones will be deeper.

Similar to AISI 316, the EN8 surface shows multiple layers of delamination near the bottom edge with an impact angle of 60°, as shown in Figure 6.22 and Figure 6.23. Figure 6.24 shows the wear damage for the centre region of the impact scar with an impact angle of 45°.

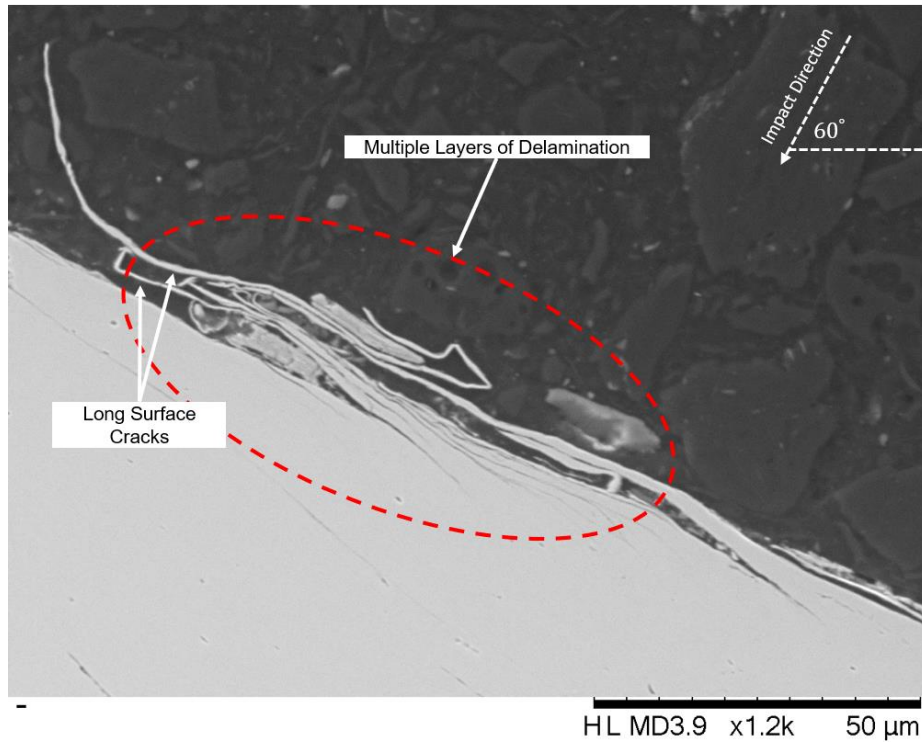


Figure 6.22 Multiple layers of delamination for EN8 near the bottom edge of the impact scar after 54,000 cycles under compound impact 60°

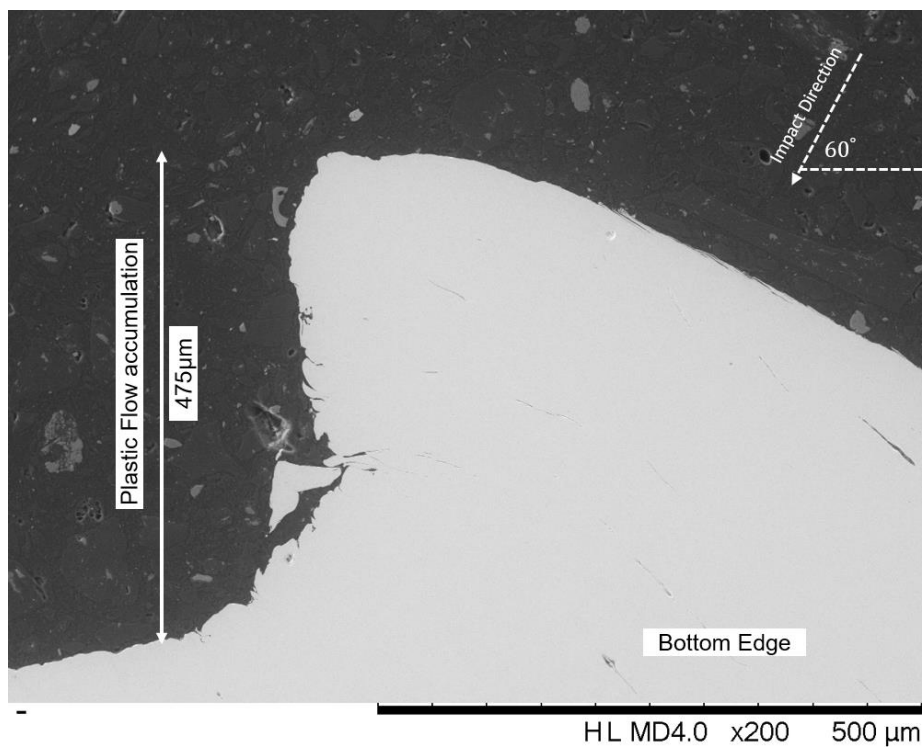
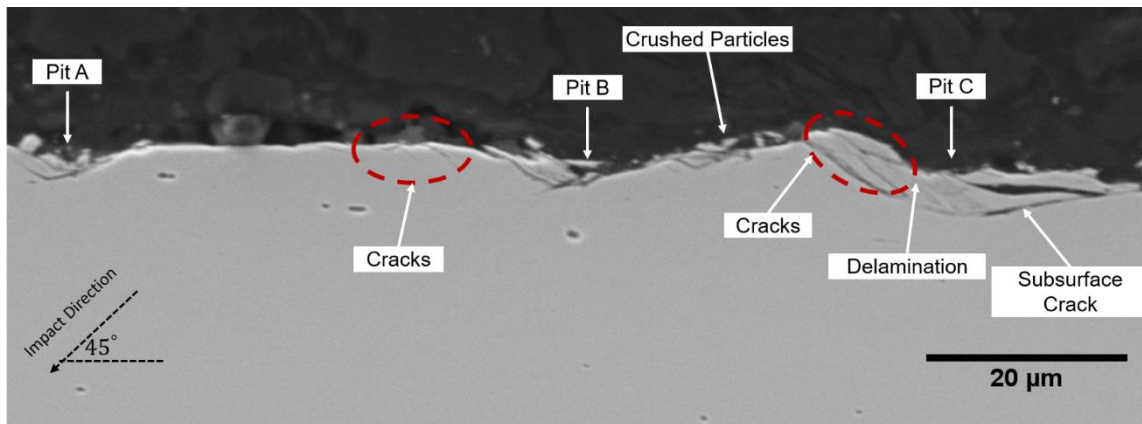
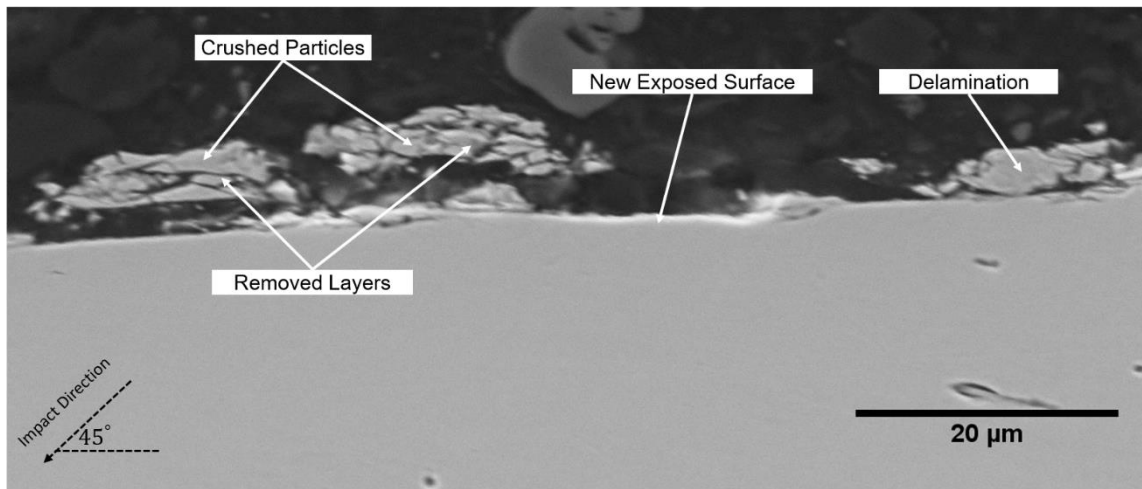


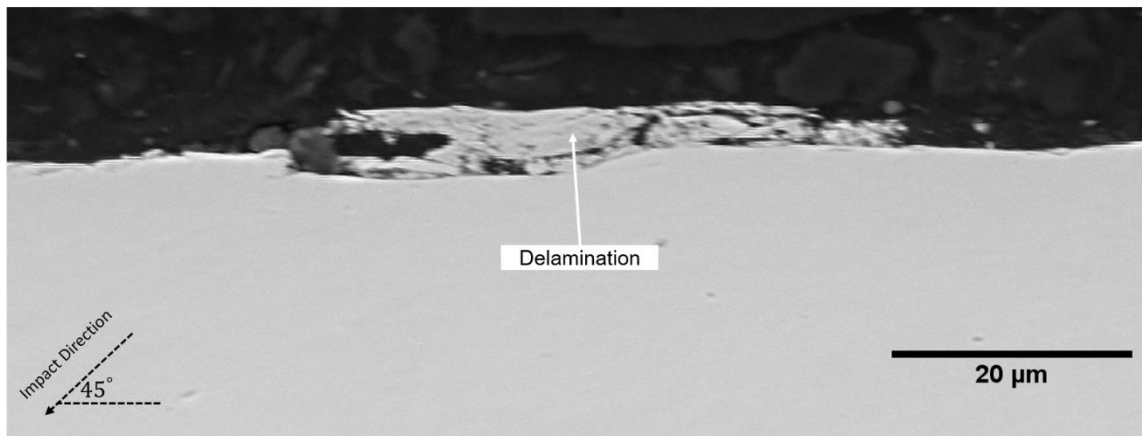
Figure 6.23 SEM image of pile up materials on the bottom edge of the impact wear scar for EN8 after 54,000 cycles under compound impact 60°



(a)



(b)



(c)

Figure 6.24 SEM image showing the wear damage mechanisms for EN8 after 54,000 cycles under compound impact 45°: (a) shows three pits, (b) shows obvious crushed particles, and (c) reveals the delamination layer

Figure 6.24 shows that the damage that occurred due to microcracks that initiated and propagated from both the surface and subsurface; these cracks are similar to those described in the literature for medium carbon steel with an impact angle of 45° (see Figure 2.7 (a)) [17].

Figure 6.24 (a) reveals three pits on the surface. Pit A, which seems smaller than the others, could have resulted from spalling, while pit B and pit C, which seem wider, most likely resulted from delamination. Significant amounts of crushed particles have been removed from the surface which has a network of internal multiple cracks, as is obvious in Figure 6.24 (b). Figure 6.24 (c) reveals a delaminated layer about to leave the surface. This layer exhibits internal multiple cracks with different directions which eventually lead to spalling within this layer; these results are quite similar to the previous ones for both types of stainless steel.

The extruded plastic flow extend outside the impact wear scar region and have undergone a series of microcracks on the bottom edge in addition to multiple layers of delamination near the bottom edge, as shown in Figure 6.25. The extruded materials, which are highly deformed, contain a network of surface and subsurface microcracks.

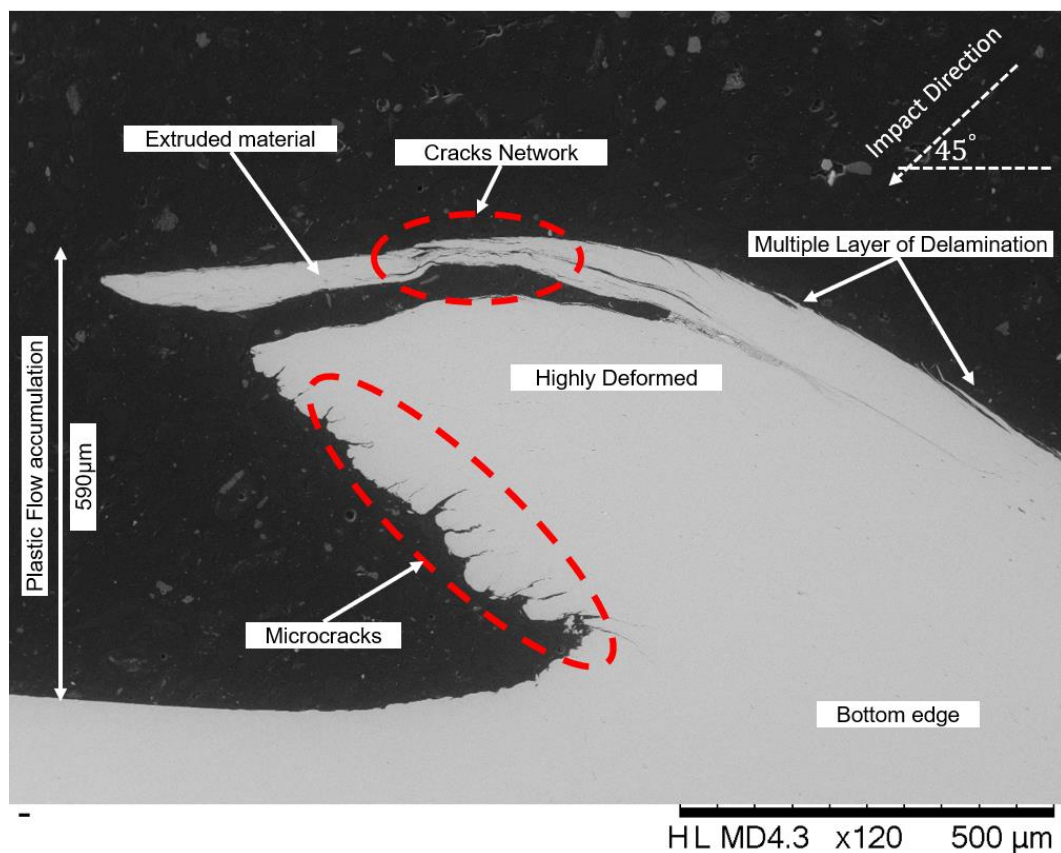


Figure 6.25 SEM image of pile up materials extruded outside the impact scar in EN8 after 54,000 cycles under compound impact  $45^\circ$

EN8 showed significant increase in wear volume loss with compound impact, especially with an impact angle of  $45^\circ$  (see Figure 6.1), similar to both AISI types 304 and 316. To confirm this result again for EN8 and support the surface examination results shown in Figure 6.10, further work was accomplished.

Perpendicular sectioning in the impact direction of three specimens after 54,000 cycles with three impact angles ( $90^\circ$ ,  $60^\circ$ ,  $45^\circ$ ) is shown in Figure 6.26.

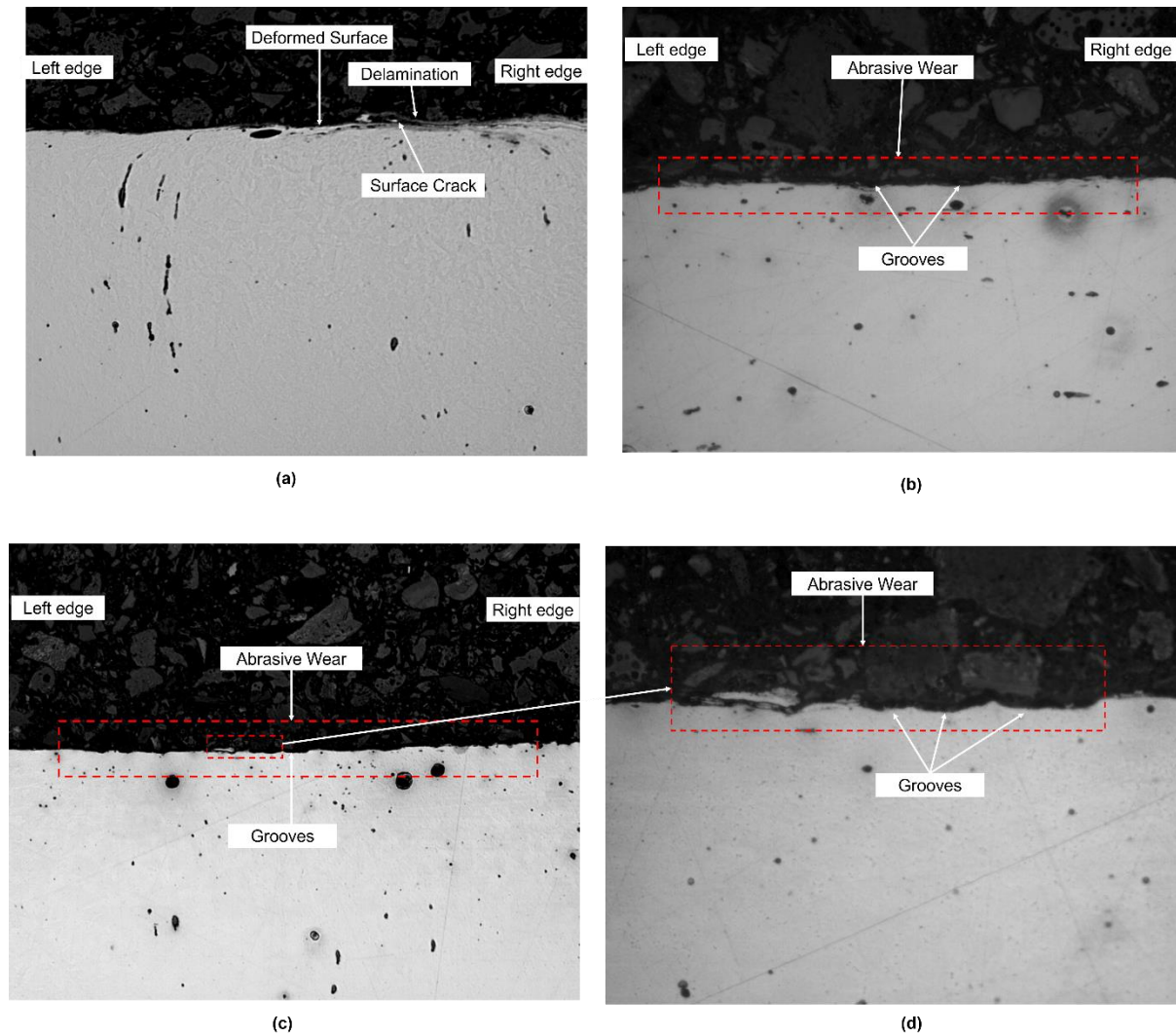


Figure 6.26 Optical images with perpendicular sectioning to the impact direction for the centre of the impact scar for EN8 showing the wear damage under: (a) normal impact  $90^\circ$ , (b) compound impact  $60^\circ$ , and (c) and (d) compound impact  $45^\circ$  after 54,000 cycles

The results of perpendicular sectioning of the impact wear scar revealed, as expected, that no abrasive wear occurred with normal impact since there was no tangential component during impact. Then, changing the impact angle from normal to compound impact led to abrasive wear and formation of grooves. With an impact angle of  $60^\circ$ , a series of grooves resulted from abrasive wear that tended to be small in general compared with an impact angle of  $45^\circ$ . These grooves look wider and deeper with an impact angle of  $45^\circ$  and these results agree with the previous finding for AISI 304 (see Figure 5.32). The current results explain the significant increase in wear volume with an impact angle of  $45^\circ$  and support the surface results in Section 6.3.1.1 (Figure 6.10 (b), (c)).

### 6.3.3 Electro Etching of AISI 316

In order to detect the size and the deformation of grains and the depth of the deformed region with different impact angles, electro etching of AISI 316 was achieved using the same methodology as for AISI 304, which was described in Section 3.7.4.1.

Figure 6.27 shows the image taken by a Nikon optical microscope for the impact scar after 54,000 cycles under normal impact and the centre region of the impact scar is marked with a blue dotted line where the highest values of impact force and stresses occurred and caused the maximum depth of impact scar.

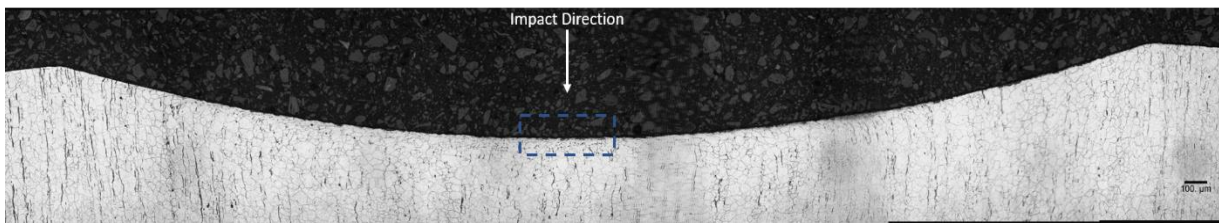


Figure 6.27 Optical microscope image for AISI 316 after 54,000 cycles under normal impact

Figure 6.28 shows the centre of the impact wear scar of AISI 316 after 54,000 cycles under normal impact. The microstructure was deformed by the effect of the impact wear process and the deformed grains reached a depth of approximately 45  $\mu\text{m}$ . Below this depth the effect of impact wear process decreased with increasing distance below the surface as marked by a black dotted line that separates the two regions (deformed and undeformed grains).

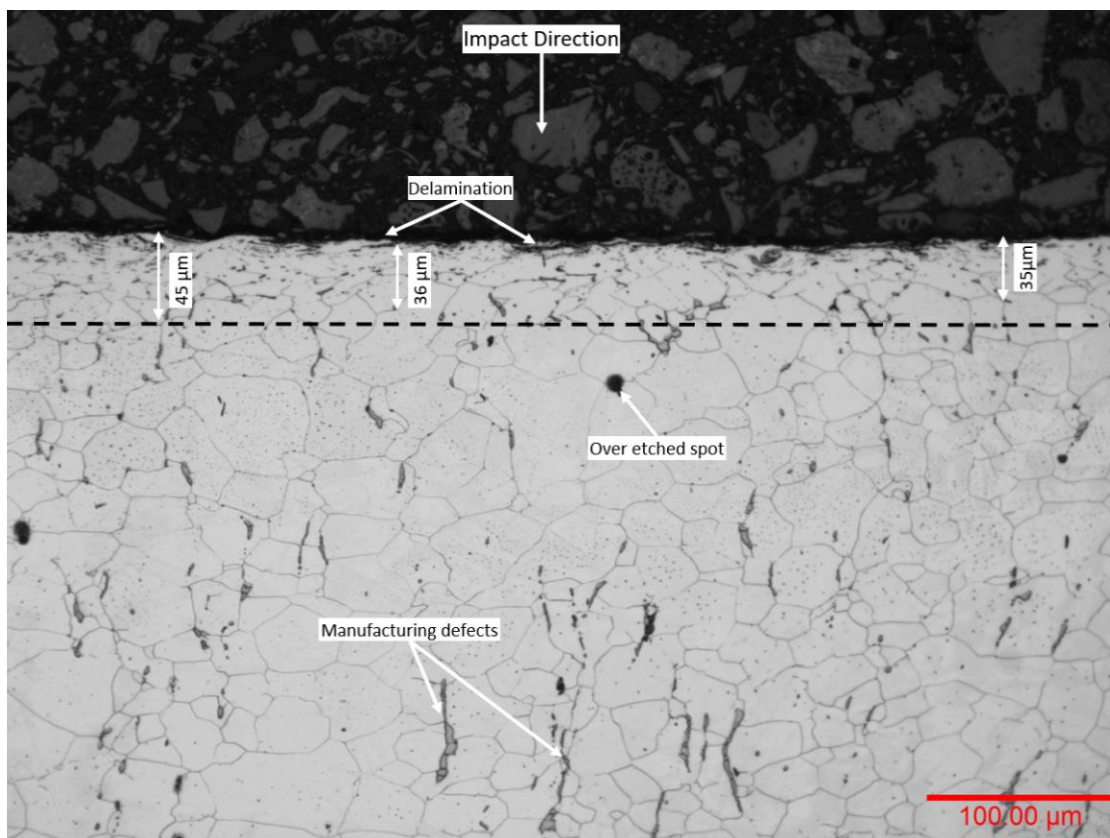


Figure 6.28 Optical microscope image of electro etching for AISI 316 under normal impact for the centre of the wear scar after 54,000 cycles showing the deformed and undeformed grains

Higher magnification for the centre region of the impact scar is shown in Figure 6.29 and revealed the deformed grains near the surface as a result of the repetitive impact. Also, while the delamination layers and cracks are still slightly obvious after etching, the cracks orientations inside the grains or within the grains' boundaries are unclear.

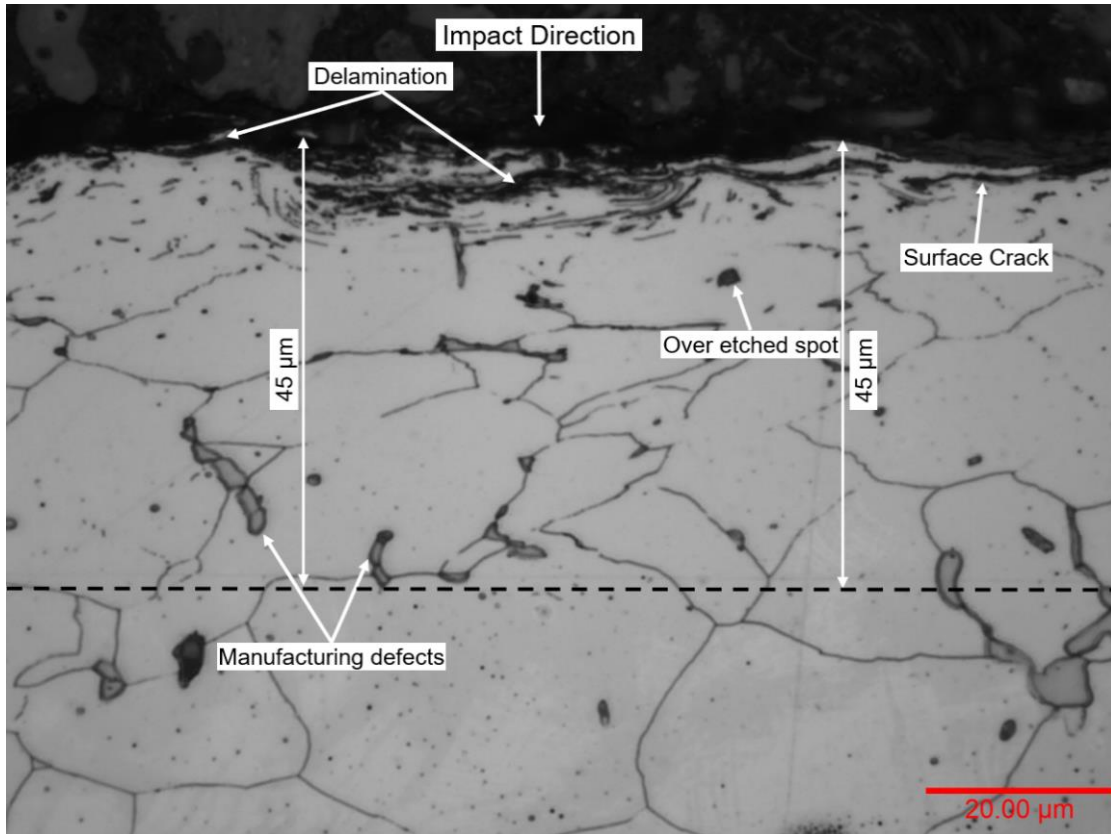


Figure 6.29 Higher magnification of optical microscope image of electro etching for AISI 316 under normal impact for the centre region of the wear scar after 54,000 cycles showing the deformed and undeformed grains

Figure 6.30 shows the impact wear scar of AISI 316 after 54,000 cycles with an impact angle of 60° and reveals two regions that were investigated (a and b) where (a) presents the centre region of the impact wear scar and (b) presents the deformed bottom edge of the impact wear scar. Figure 6.31 shows the centre region of the wear scar.

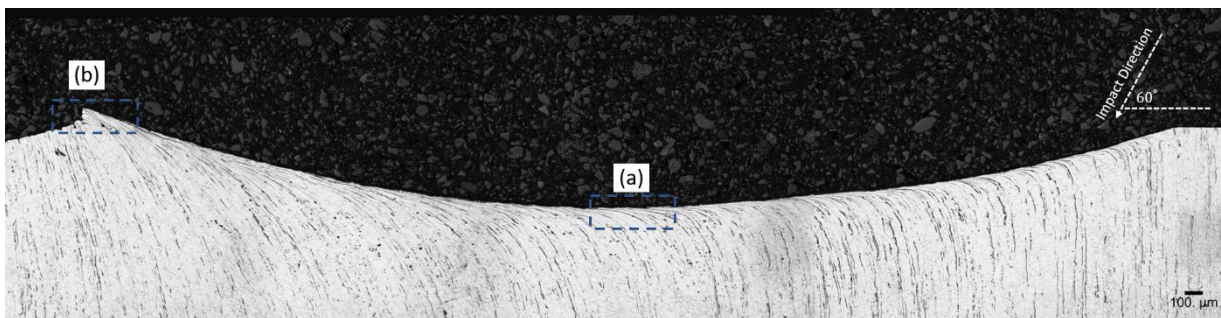


Figure 6.30 Optical microscope image for AISI 316 after 54,000 cycles under compound impact 60° where (a) is the centre of the wear scar and (b) is the bottom edge

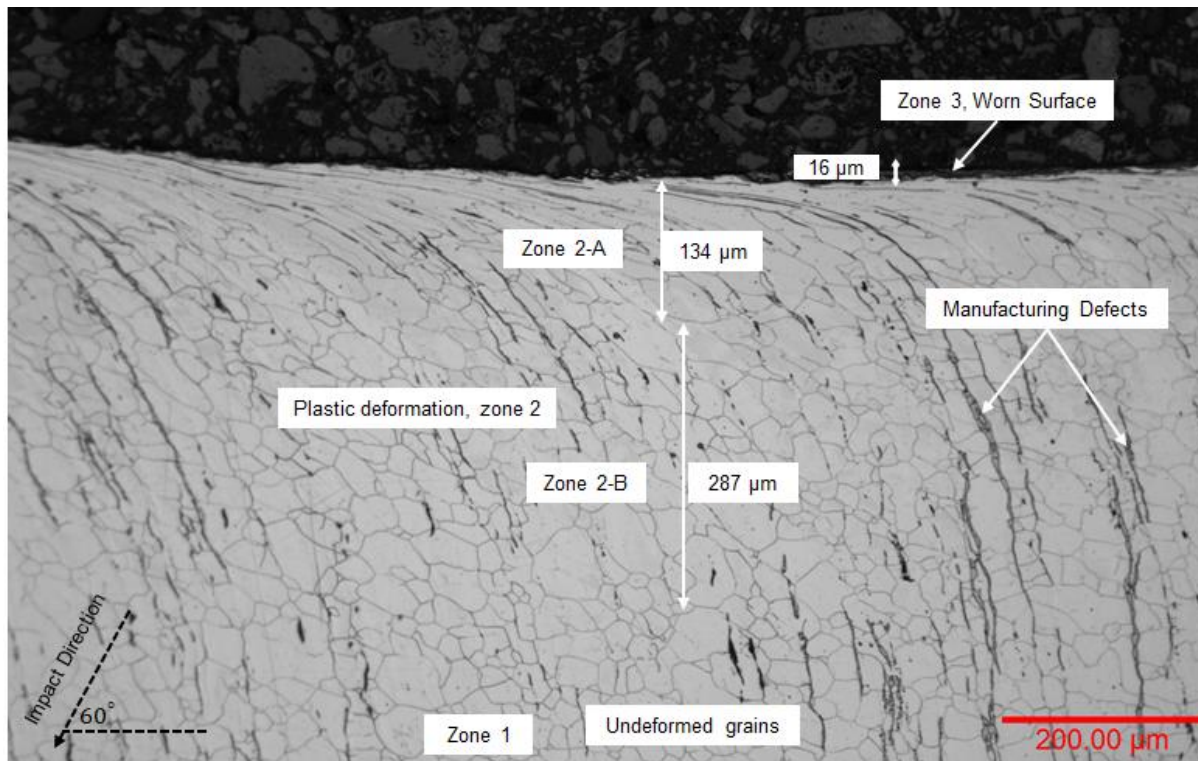


Figure 6.31 Optical microscope image of electro etching for AISI 316 steel under compound impact  $60^\circ$  for the centre of the wear scar after 54,000 cycles showing the deformed zones

Figure 6.31 reveals three regions of the centre of the impact wear scar, the deepest zone being the undeformed grains (zone 1). The second region is the plastic deformation region (zone 2) that reaches to approximately  $412 \mu\text{m}$  and has two sub-regions. Zone 2-B has less deformation, the grain boundaries can be revealed and it has a depth of  $287 \mu\text{m}$ . Above this region is a sub-region of highly deformed grains (zone 2-A) that has undergone an obvious change in grains orientation with sliding direction due to the effect of tangential force (shear force) during impact and reaches to approximately  $134 \mu\text{m}$ . The grains boundaries are unable to be detected by etching, especially near the surface, which reflects the deformation level in this zone.

Zone 3, which is the worn surface layer, has been severely deformed by the impact wear process. This layer has resulted from large parallel surface and subsurface cracks which eventually lead to formation of a large delamination layer. Figure 6.32 presents higher magnification for zone 3 and shows highly deformed grains, large parallel cracks and a crushed region highlighted with a red colour. Some of the grain boundaries of this layer disappeared as a result of repetitive impact which led to high deformation of these grains and their direction was changed by the effect of shear force with the direction of impact. Next, Figure 6.33 shows the plastic flow on the bottom edge of the wear scar.

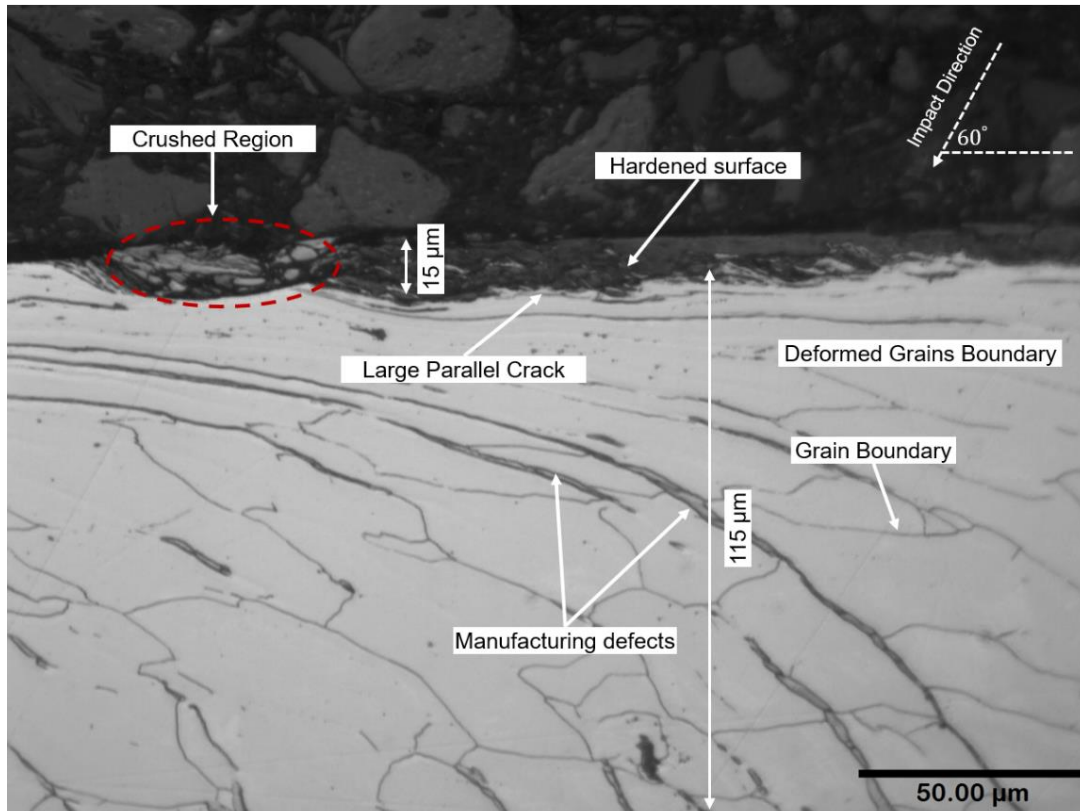


Figure 6.32 Higher magnification for the centre region of the impact wear scar for AISI 316 after 54,000 cycles with impact angle 60° showing the highly deformed grains beneath the worn surface (zone 3)

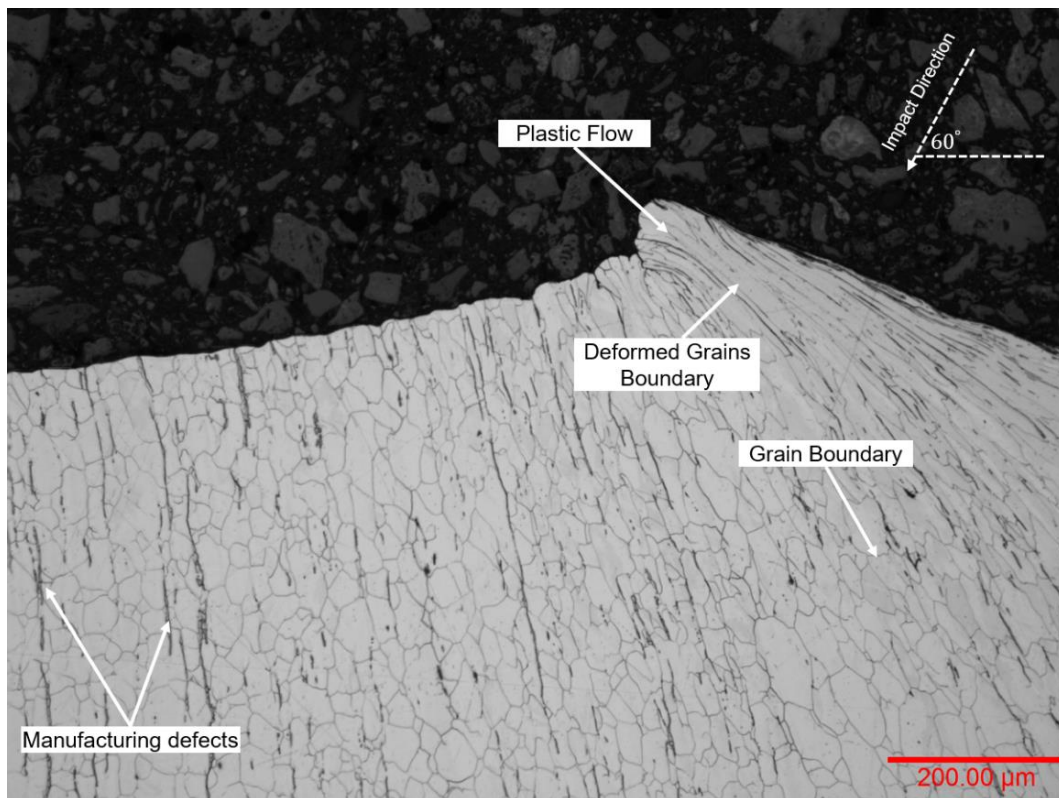


Figure 6.33 OM image of pile up materials for AISI 316 on the bottom edge after 54,000 cycles under compound impact 60° as revealed by electro etching

Figure 6.34 shows a typical impact wear scar with an impact angle of  $45^\circ$  after 54,000 cycles and three regions of interest for investigation, while Figure 6.35 shows the centre of the impact wear scar.

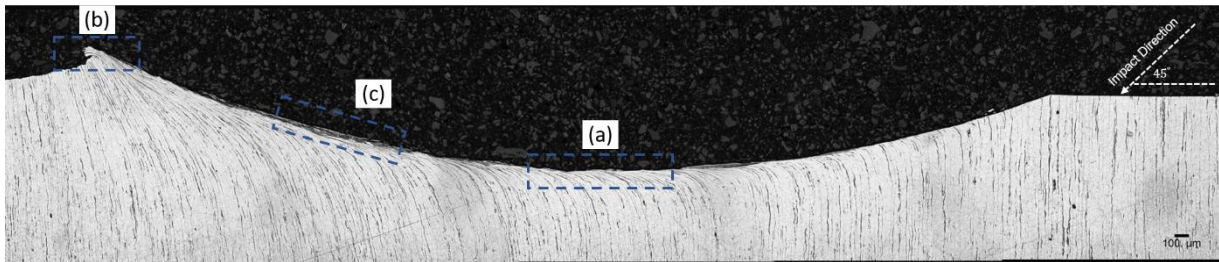


Figure 6.34 Optical microscope image for AISI 316 after 54,000 cycles under compound impact  $45^\circ$  where (a) is the centre region, (b) is a region of interest for investigation and (c) is the bottom edge

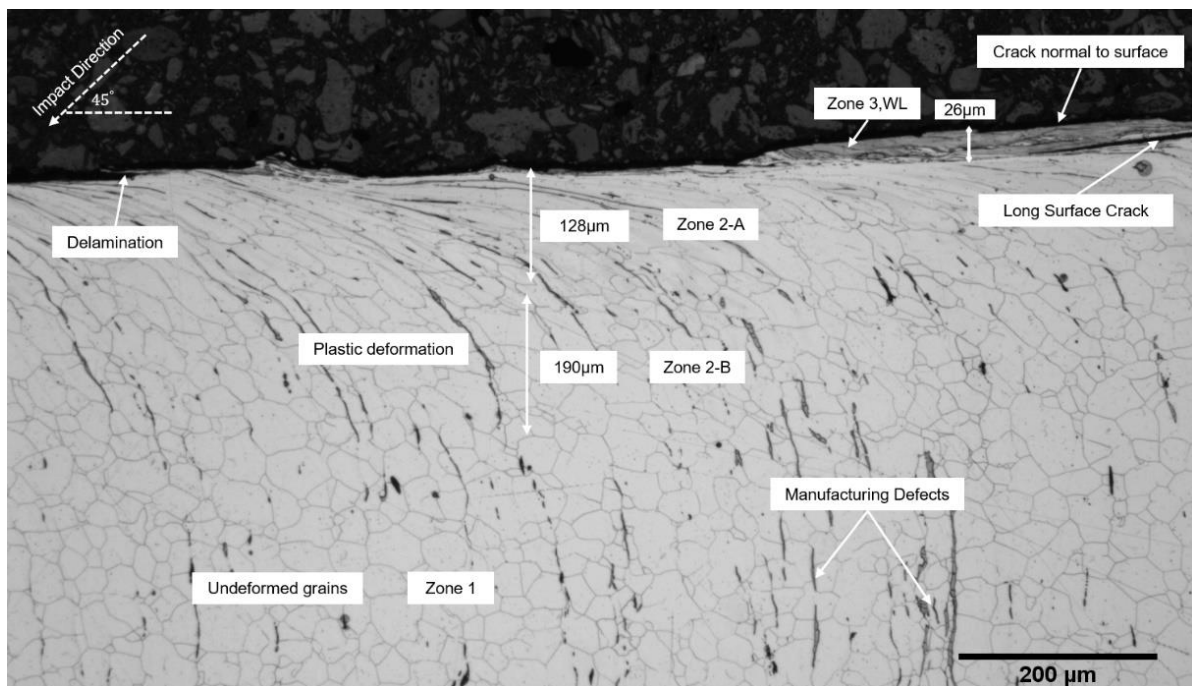


Figure 6.35 Optical microscope image of electro etching for AISI 316 under compound impact  $45^\circ$  for the centre of the wear scar after 54,000 cycles showing the deformed zones

Figure 6.35 shows that the deformed region (zone 2) reaches to approximately  $318 \mu\text{m}$ , which is less than with impact angle  $60^\circ$  ( $412 \mu\text{m}$ ). Zone 2-A reaches to approximately  $128 \mu\text{m}$ , slightly less than with an impact angle of  $60^\circ$  ( $134 \mu\text{m}$ ). These results support the previous findings on AISI 304 presented in Section 5.3.2.2 (see Figure 5.35 and Figure 5.39).

Figure 6.36 presents higher magnification for the centre region of the impact wear scar and shows the separation of materials from the hardened layer. It also reveals that extensive deformation has occurred to the grains in zone 2-A where the grains boundaries near the worn layer are unable to be detected by etching. Figure 6.37 shows the wear damage mechanisms that have occurred in the worn surface layer of the material at an impact angle of  $45^\circ$ .

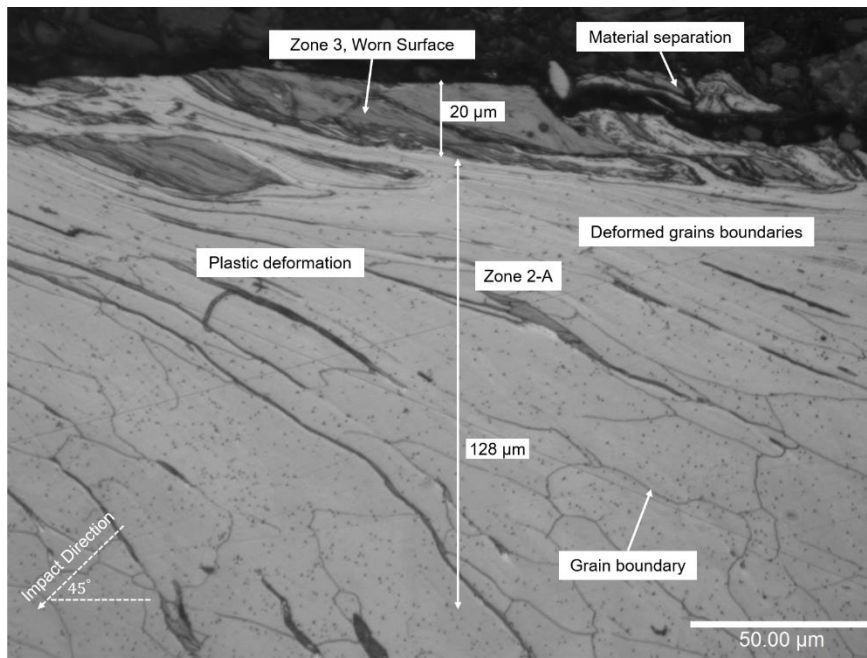


Figure 6.36 Higher magnification for the centre region of impact wear scar of AISI 316 after 54,000 cycles with impact angle 45° showing the highly deformed grains beneath the worn surface

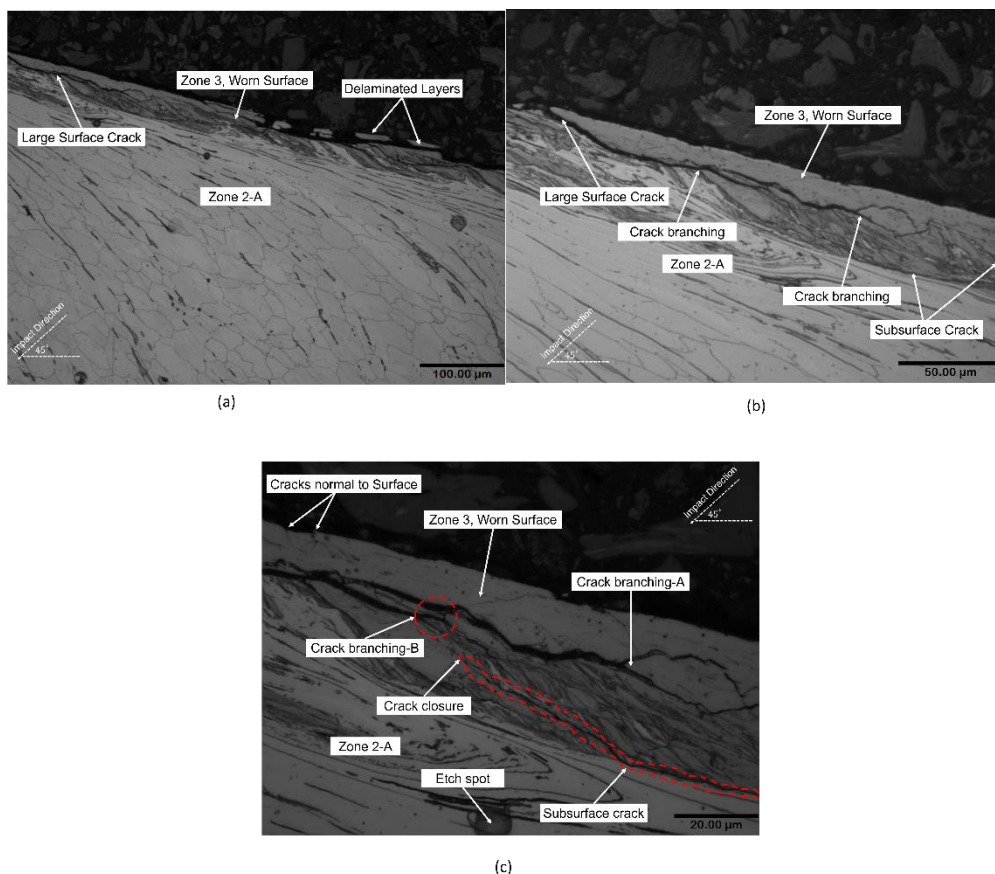


Figure 6.37 Optical microscope images revealing wear damage mechanisms that have occurred in the worn surface layer for AISI 316 after 54,000 cycles with impact angle 45°

Figure 6.37 (a) shows the separation of materials from the worn surface as delaminated layers resulting from surface crack that propagated parallel to the surface. Figure 6.37 (b) shows an obvious large crack

that initiated from the surface and propagated beneath the worn surface to eventually branch into two small cracks in two different locations. The large crack will eventually lead to formation of a large delamination layer, while the small cracks that resulted from the branching of the large surface crack will also propagate and cause further damage. Figure 6.37 (c) shows a subsurface crack that initiated below the worn surface and propagated to the surface to connect with the surface cracks and cause further damage to the surface.

The accumulation of plastic flow near the bottom edge of the wear scar (Figure 6.34 (b)) is shown in Figure 6.38.

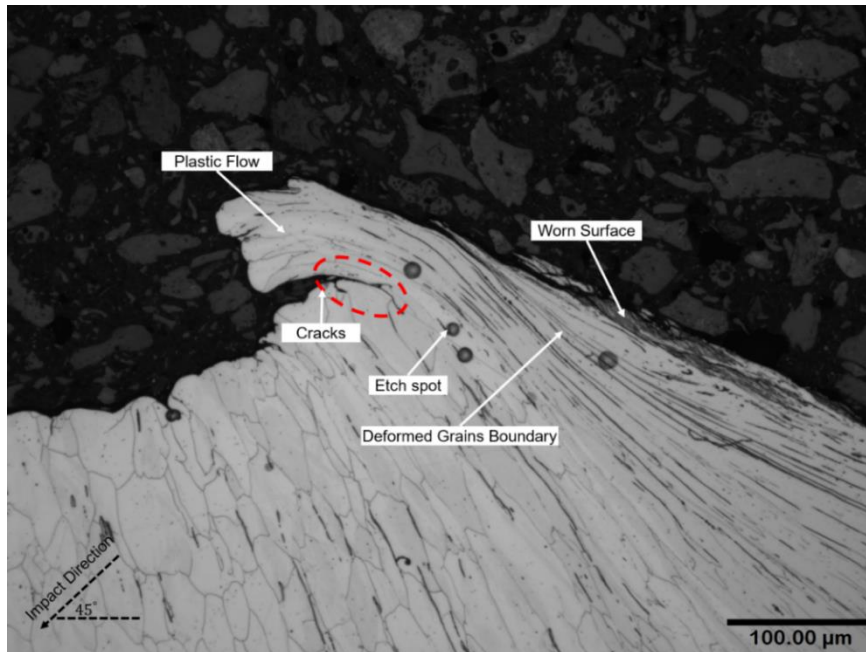


Figure 6.38 Optical microscope image of pile up materials for AISI 316 on the bottom edge after 54,000 cycles under compound impact  $45^\circ$

### 6.3.4 Chemical Etching of EN8

The deformed grains, grains orientation and depth of plastic deformation for EN8 with different impact angles were revealed using 2% nital etching which comprised 100 ml of industrial methylated spirits (IMS) with 2 ml nitric acid according to ASTM E407-15 [88] as described in Section 3.7.4.2.

Figure 6.39 shows the whole impact wear scar after 54,000 cycles under normal impact  $90^\circ$  and three regions that have been investigated (a, b and c). Here, (a) is the centre region of the impact wear scar and (b) and (c) are the deformed top and bottom edges of the impact wear scar, respectively. Figure 6.40 shows the wear damage mechanism that occurred at the centre of the impact wear scar under normal impact.

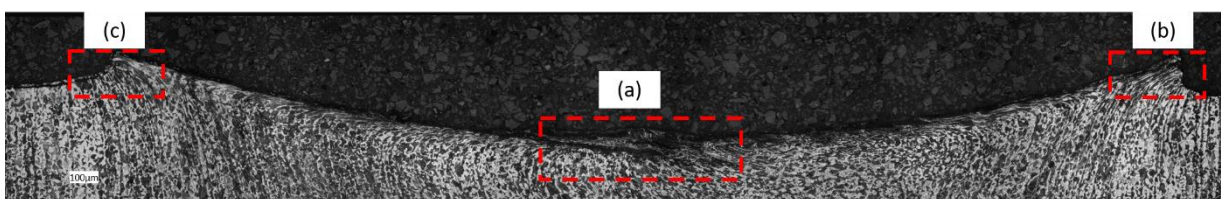


Figure 6.39 Optical microscope image for EN8 after 54,000 cycles under normal impact  $90^\circ$  where (a) is the centre region, (b) is the top edge, and (c) is the bottom edge

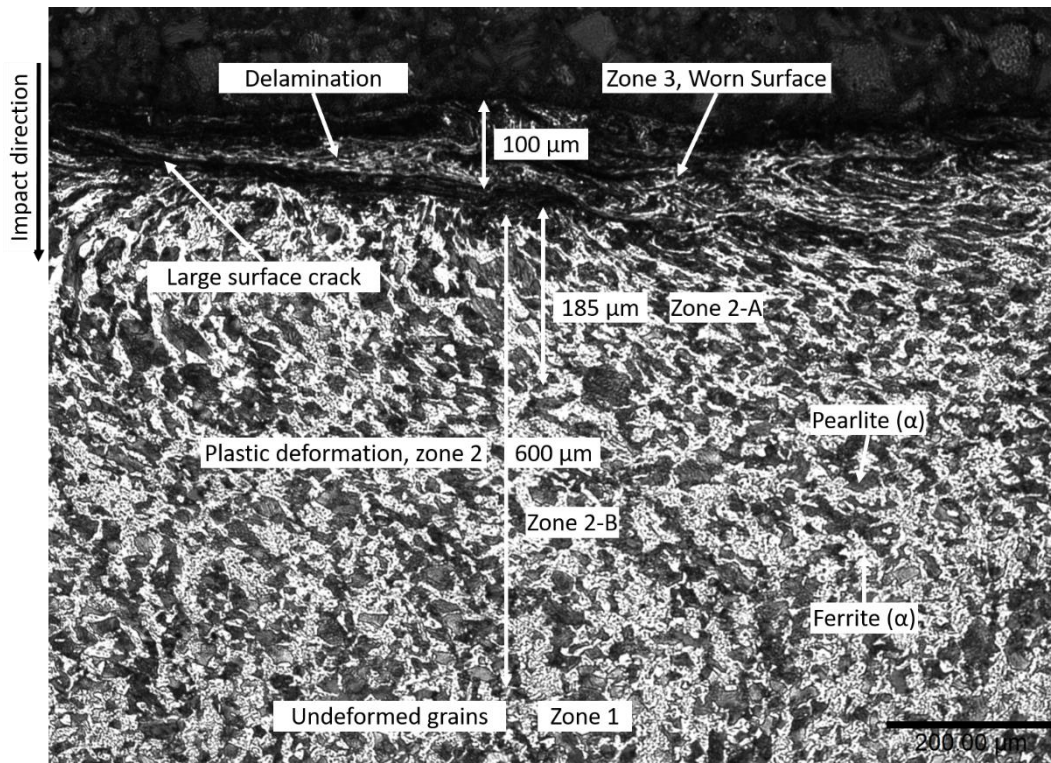


Figure 6.40 Optical microscope image of chemical etching for EN8 under normal impact for the centre of the wear scar after 54,000 cycles

Three zones are illustrated in Figure 6.40. The undeformed grains (zone 1) reveal no deformation or change in the grains' directions compared with other regions. Zone 2 is a plastic deformation region where the microstructure of both ferrite and pearlite was deformed by the impact wear process and reaches to a depth of 600 μm. Zone 2-A consists of highly deformed grains near the surface and extends to a depth of 185 μm below the hardened surface (zone 3) which cannot easily be distinguished from other regions and has a depth of 100 μm. Figure 6.41 shows the accumulated plastic flow on both the top and bottom edges of the impact wear scar after 54,000 cycles under repetitive normal impacts.

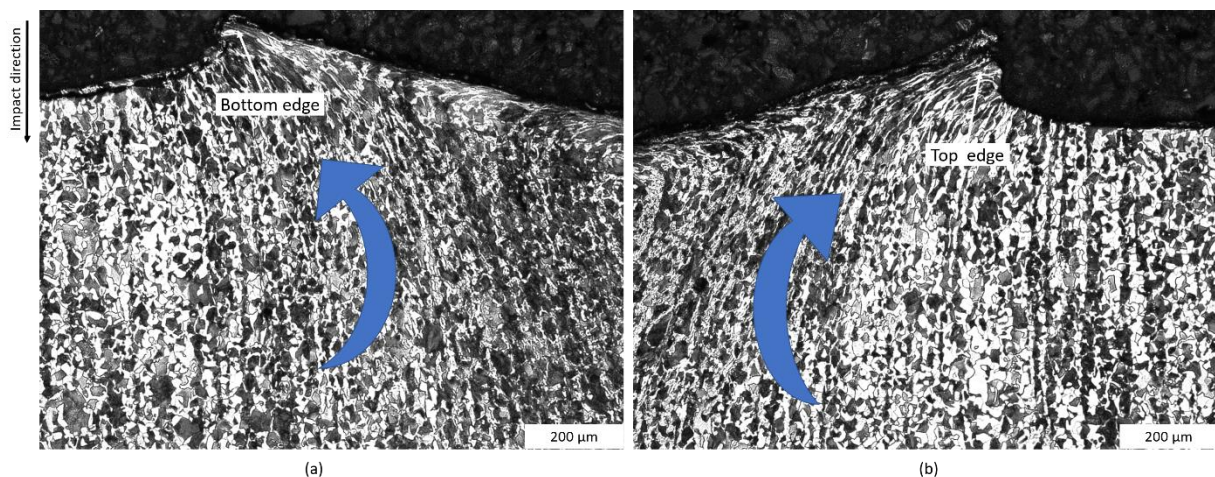


Figure 6.41 Optical microscope images of top (a) and bottom (b) edges for EN8 after 54,000 cycles under normal impact

Figure 6.42 shows the whole impact wear scar after 54,000 cycles with an impact angle of 60° and reveals two regions of interest: (a) the centre of the wear scar and (b) the bottom edge. Figure 6.43 shows

the wear damage that has occurred to the centre of the impact wear scar, while Figure 6.44 shows the accumulated plastic flow on the bottom edge.

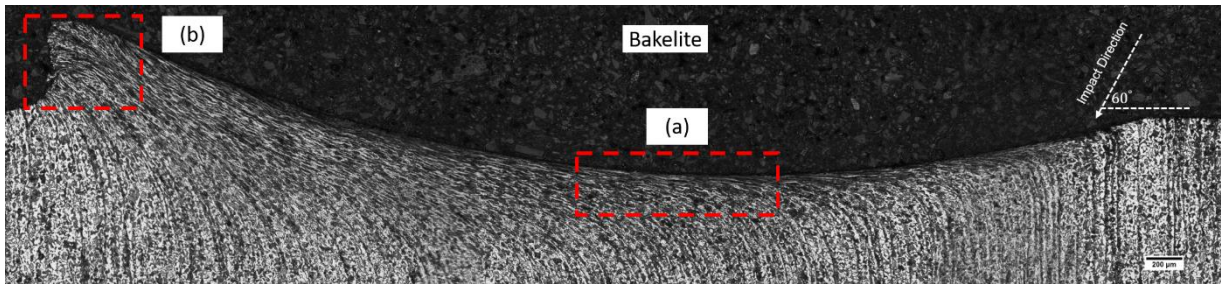


Figure 6.42 Optical microscope image for EN8 after 54,000 cycles under compound impact  $60^\circ$  where (a) is the centre region, and (b) is the bottom edge

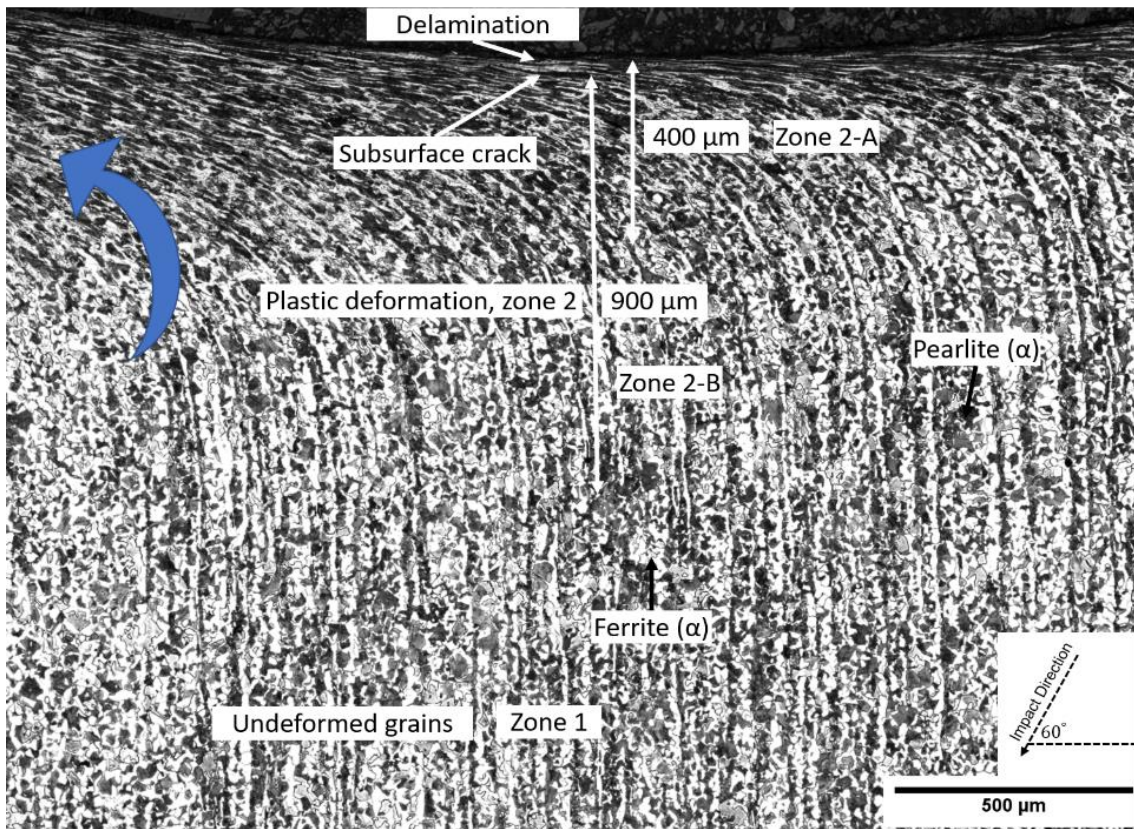


Figure 6.43 Optical microscope image of chemical etching for EN8 with impact angle  $60^\circ$  for the centre of the wear scar after 54,000 cycles showing the deformed zones

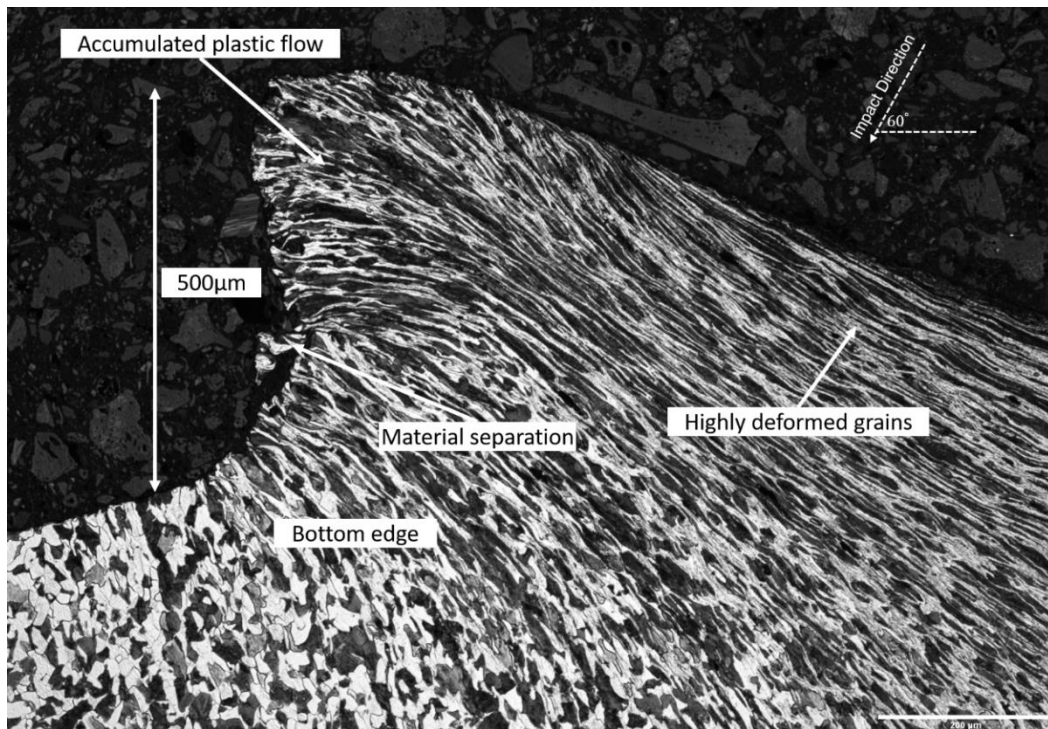


Figure 6.44 Optical microscope image of pile up materials on the bottom edge for EN8 after 54,000 cycles under compound impact  $60^\circ$  as revealed by chemical etching

Due to the chemical etching, zone 3, which is the worn surface or the hardened surface, was not obvious in Figure 6.43 as all the surface and subsurface cracks were filled with the nital solvent. Also, the deformed grains of the pearlite, which has a black colour similar to Bakelite, made it more difficult to distinguish this region or to recognise the surface and subsurface cracks. This illustrates the importance of detecting the surface and subsurface cracks without using etching.

The purpose of using chemical etching was to reveal the plastic deformation region (zone 2), which is obvious in Figure 6.43 and reaches to a depth of approximately  $900\ \mu\text{m}$ , while the highly deformed grains (zone 2-A) reach to a depth of  $400\ \mu\text{m}$ . Beneath the plastic deformation region there are undeformed grains and it is obvious that no change in the grains' orientation has occurred within this region. However, the grains' orientation in the plastic deformation region has changed with the direction of impact due to the effect of shear force (highlighted with a blue arrow).

Figure 6.45 shows the whole impact wear scar of the material after 54,000 cycles with an impact angle of  $45^\circ$  and reveals two regions of interest: (a) the centre of the wear scar and (b) the bottom edge. Figure 6.46 shows the wear damage that has occurred to the centre of the impact wear scar and the extruded plastic flow is shown in Figure 6.47.

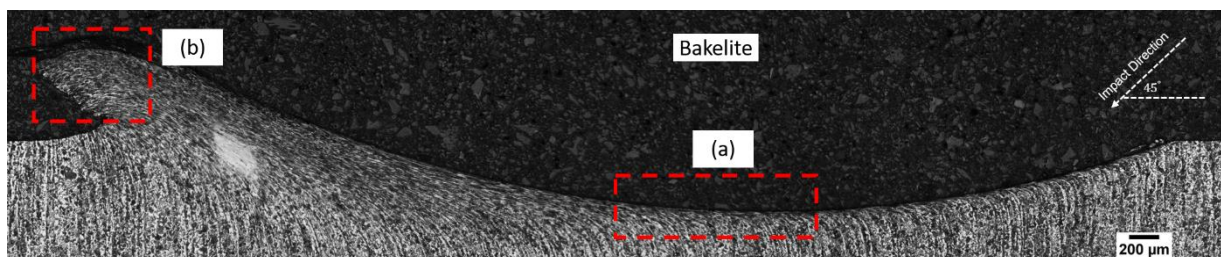


Figure 6.45 Optical microscope image for EN8 after 54,000 cycles under compound impact  $45^\circ$  where (a) is the centre region of the wear scar and (b) is the bottom edge

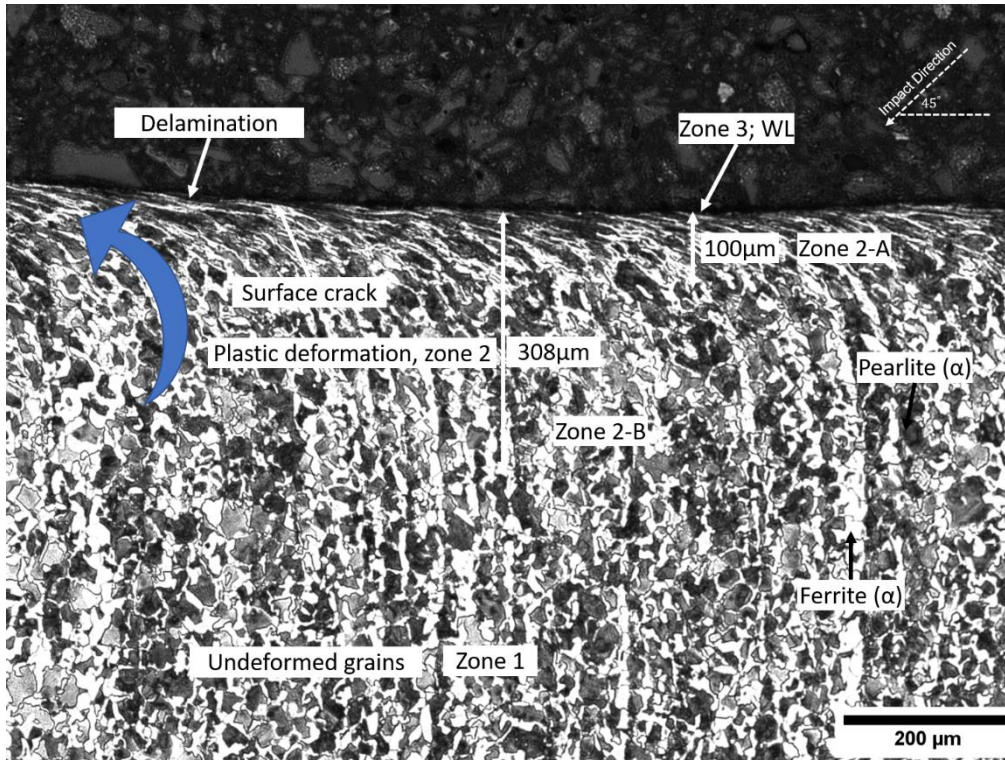


Figure 6.46 Optical microscope image of chemical etching for EN8 with impact angle 45° for the centre of the wear scar after 54,000 cycles showing the deformed zones

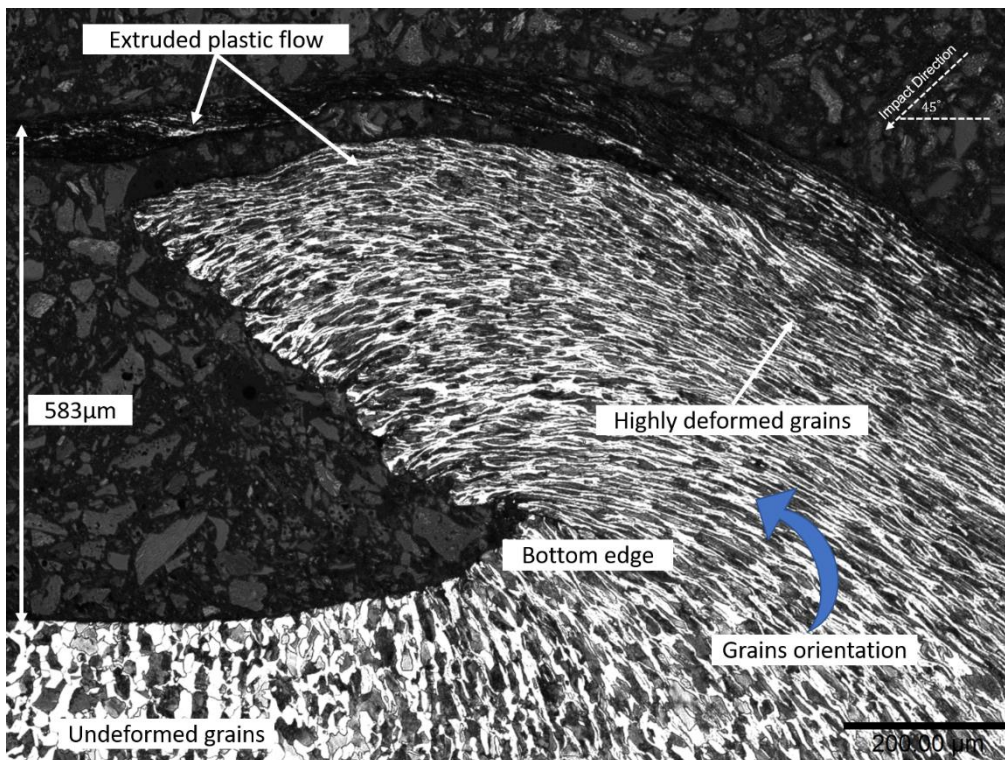


Figure 6.47 Optical microscope image of extruded materials near the bottom edge for EN8 after 54,000 cycles under compound impact 45° as revealed by chemical etching

Figure 6.46 reveals the plastic deformation region (zone 2) where the grains boundary direction has changed with the impact direction (highlighted with blue arrow) and which reaches to a depth of

approximately 308  $\mu\text{m}$ . Highly deformed grains (zone 2-A) reach to a depth of 100  $\mu\text{m}$ , while beneath the plastic deformation region there are undeformed grains.

Figure 6.47 shows the extruded plastic flow materials outside the bottom edge of the impact wear scar and highly deformed grains which reveal an obvious change in orientation toward the bottom edge (with the direction of impact) compared with the undeformed grains outside the wear scar region.

### 6.3.5 Microhardness Results

The microhardness measurement procedure for both materials is similar to that for AISI 304 as described in Section 5.3.3.

The microhardness measurements of impacted regions were taken away from the centre of the wear scar, below zone 3 and toward zone 1. For AISI 316 the microhardness measurements was about 80  $\mu\text{m}$  which represents about 2.5 times the diagonal size of the indents (30-33  $\mu\text{m}$ ) for the unimpacted region. For EN8 the microhardness measurements was about 70  $\mu\text{m}$  which also represents 2.5 times the diagonal size of the indents (28)  $\mu\text{m}$  based on ASTM E384 [60].

The variation in microhardness results for both materials with different impact angles below the maximum indentation depth of impact wear scar is shown in Figure 6.48 for AISI 316 and Figure 6.49 for EN8. Table 6.3 then summarises the results for the effect of impact force and angle correlated with surface hardening value and depth below the surface for both materials.

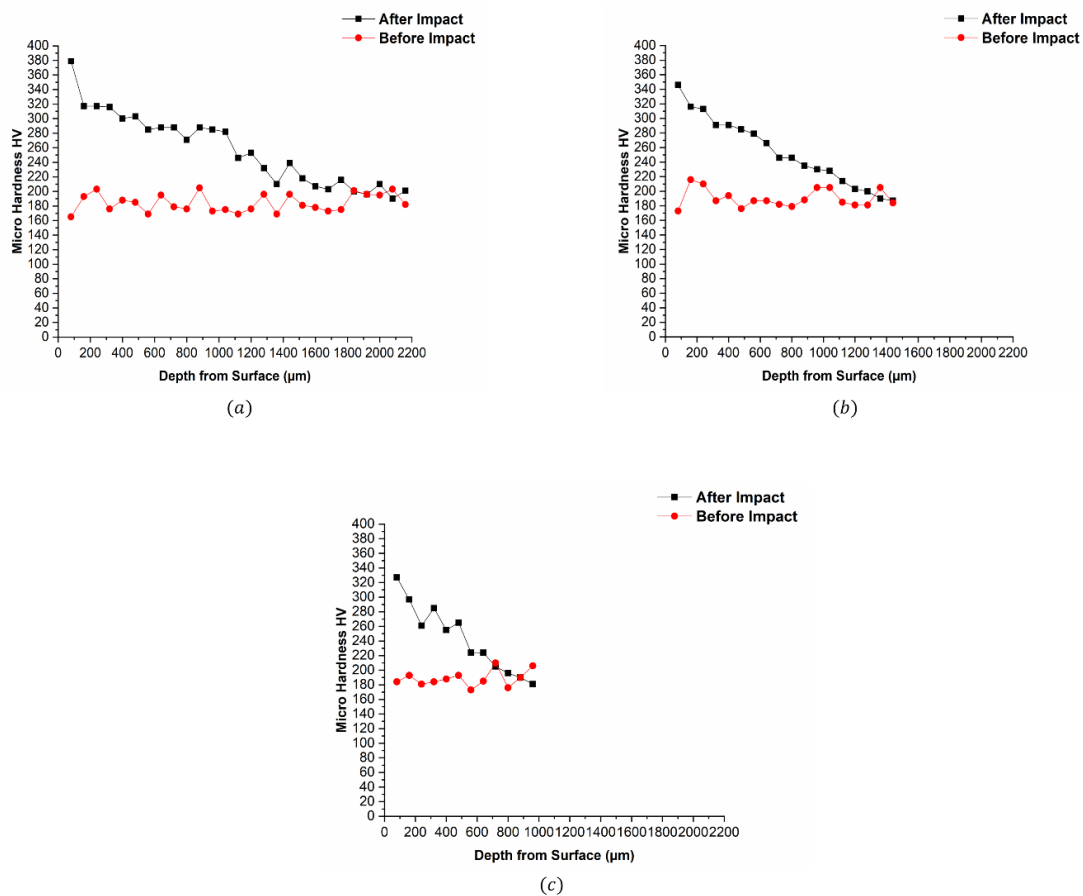


Figure 6.48 Microhardness profile of original and impacted regions of tested specimens for AISI 316 at impact force of 3476 N where (a) normal impact, (b) impact angle 60°, and (c) impact angle 45°

## Role of Impact Angle on Surface and Subsurface Deformation of Alloy Steels

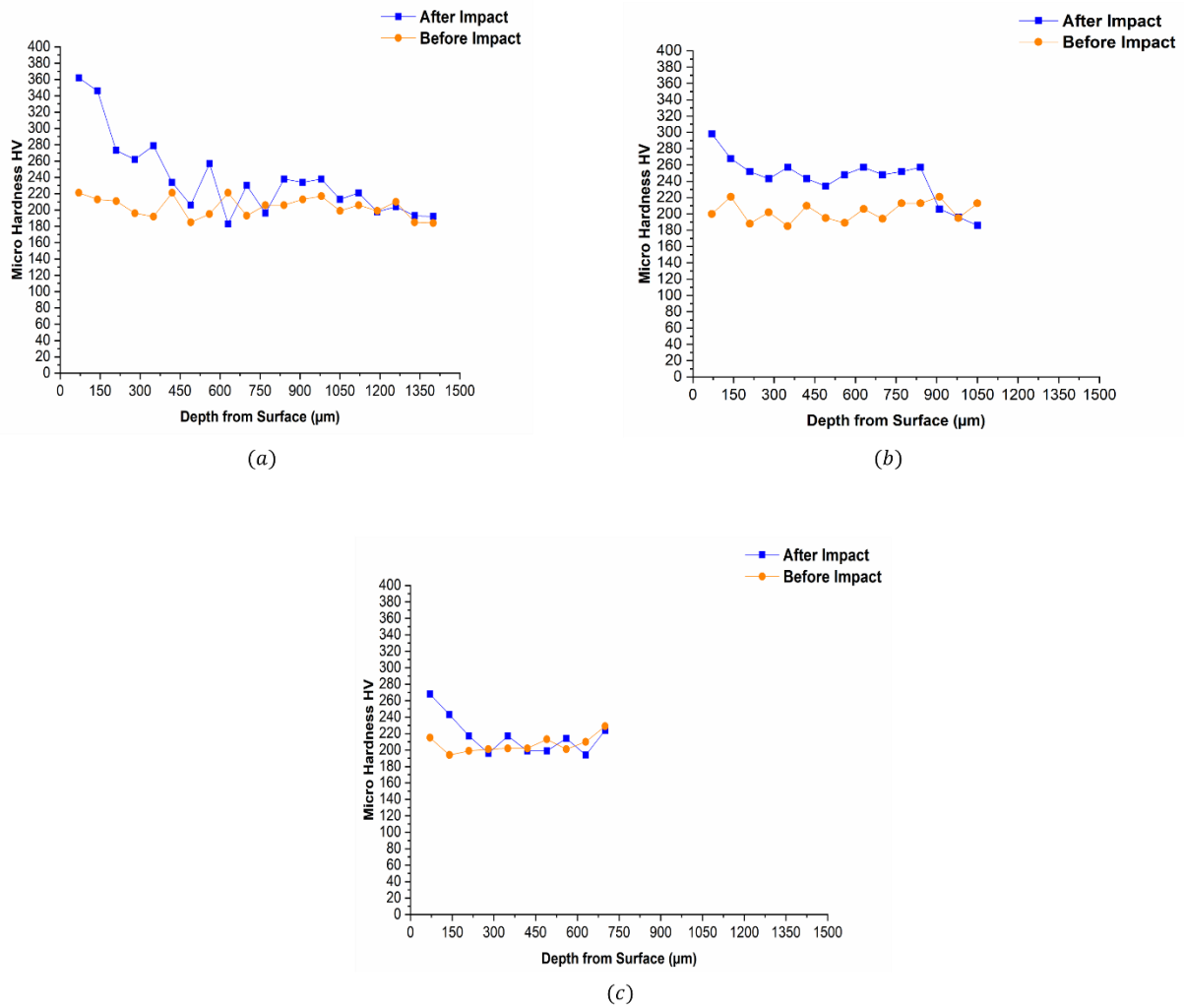


Figure 6.49 Microhardness profile of original and impacted regions of tested specimens for EN8 at impact force of 3476 N where (a) normal impact, (b) impact angle 60°, and (c) impact angle 45°

Table 6.3 Correlation between the impact force and surface hardening of the two materials

Material	Normal Impact Force (N)	Tangential Impact Force (N)	Impact angle ( $\theta$ )	Surface Hardening ( $\text{HV}_{0.1}$ )	Location of Hardening from surface ( $\mu\text{m}$ )	Hardening Depth (mm)
AISI 316	2457	2457	45°	327	80	0.7
	3010	1738	60°	346	80	1.4
	3476	0	90°	379	80	2
EN8	2457	2457	45°	268	70	0.3
	3010	1738	60°	298	70	1
	3476	0	90°	362	70	1.2

Figure 6.48-6.49 and Table 6.3 show the differences in work hardening ability between the two materials. Significant increases in the hardness values occurred with AISI 316 in a similar way to previous results for AISI 304 presented in Section 5.3.3 (see Figure 5.42). EN8 also shows an increase in hardness, but not to a great extent as compared with AISI 316. For both materials the maximum increases in hardness occurred with normal impact  $90^\circ$ , followed by an impact angle of  $60^\circ$ , and finally an impact angle of  $45^\circ$ .

This could be explained by the significant decrease in normal impact force from 3476 N to 3010 N at  $60^\circ$  to 2457 N at  $45^\circ$  and change in the wear mechanism from pure compression under normal impact to sliding wear with compound impact. These results support the previous findings and explanation presented in Section 6.3.3 (Figure 6.31, Figure 6.35) and Section 6.3.4 (Figure 6.43, Figure 6.46).

Also, for both materials significant decreases in hardening depth were identified for different impact angles, with the maximum depth measured under an impact angle of  $90^\circ$  and the least under an impact angle of  $45^\circ$ . This could be explained by the significant increases in shear force from 0 to 1738 N at  $60^\circ$  and to 2457 N at  $45^\circ$  and change in the wear mechanism from pure compression under normal impact to abrasive wear with compound impact. Thus, the shear force removed most of the hardened surface in the abrasive wear process. It is important to highlight that the papers discussed in the literature review have not reported the effects of impact angle on the hardness value and depth under both normal and tangential impact force for any materials.

Further investigations for readings very close to surface were carried out during this work, as well as about  $35\ \mu\text{m}$  from the surface for both materials. EN8 showed no noticeable differences in hardness from results described in Table 6.3, while for AISI 316 significant increases were observed, as summarised in Table 6.4. An example showing the microhardness indentation inside the deformed grains ( $35\ \mu\text{m}$  from surface) is presented in Figure 6.50 for AISI 316 under impact angles  $60^\circ$  and  $45^\circ$  after 54,000 cycles.

Table 6.4 Correlation between the impact force and surface hardening of AISI 316 at a distance of approximately  $35\ \mu\text{m}$  below the impact surface in the centre of the wear scar

Number of cycles (N)	Normal Impact Force (N)	Impact angle ( $\theta$ )	Surface Hardening (HV <sub>0.1</sub> )	Location of Hardening from surface ( $\mu\text{m}$ )
54,000	2457	$45^\circ$	393	35
54,000	3010	$60^\circ$	440	35
54,000	3476	$90^\circ$	482	35

Table 6.4 shows significant increases in hardness with all impact angles for AISI 316 compared with the results presented in Table 6.3 which are realistic since these results derive from indentations very close to the surface ( $35\ \mu\text{m}$ ). These results are in great agreement with the previous results for AISI 304 presented in Section 5.3.3.

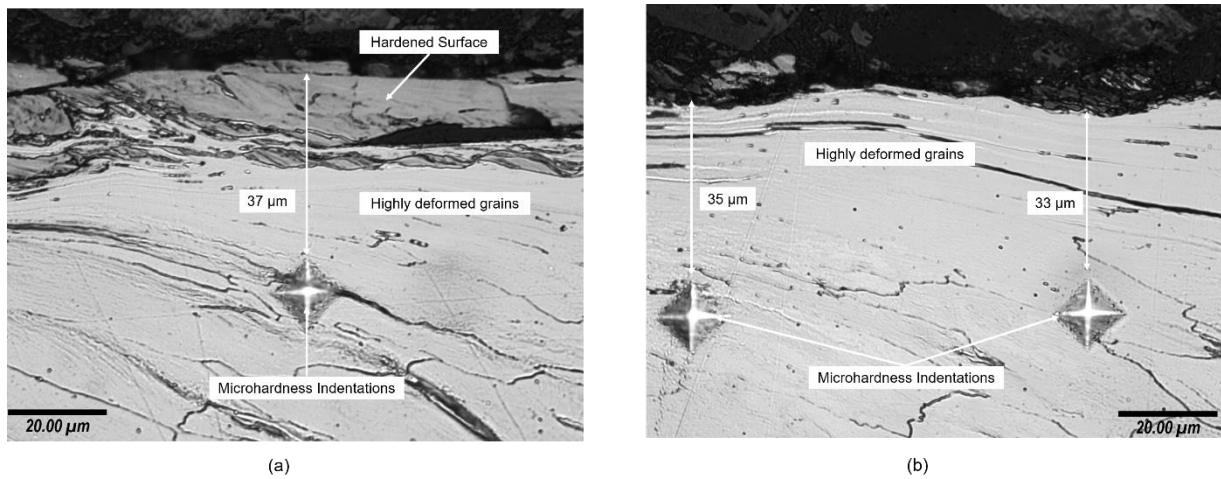
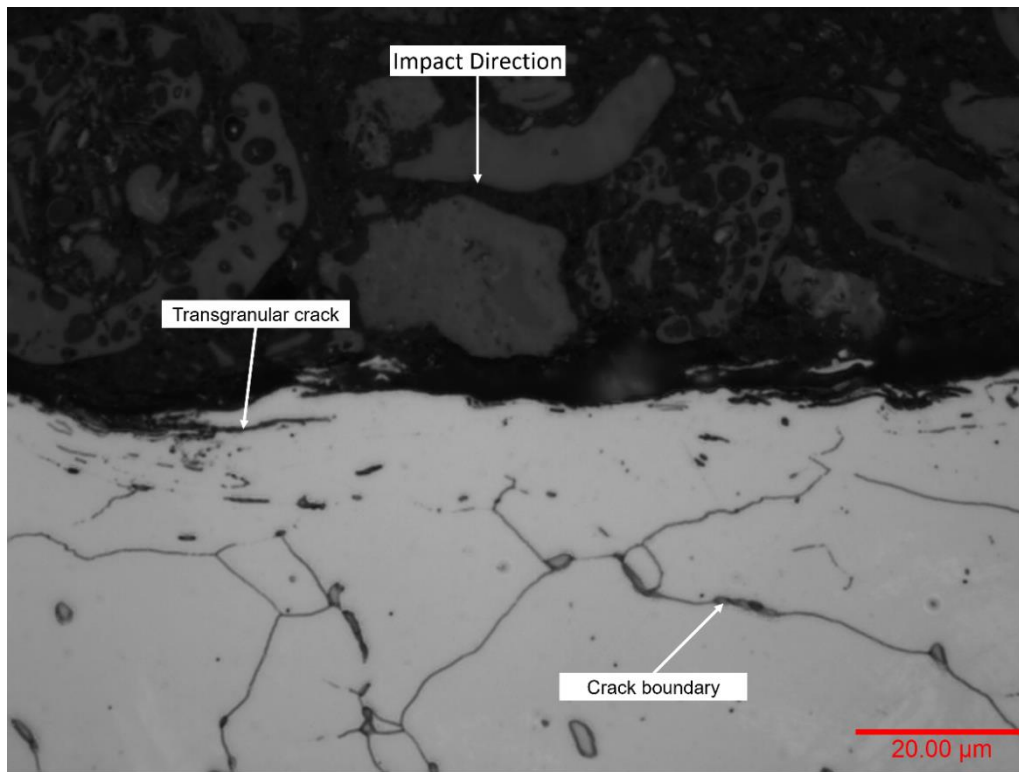


Figure 6.50 Optical microscope image for the microhardness indentation inside the deformed grains of AISI 316 for (a) compound impact  $60^\circ$  and (b) compound impact  $45^\circ$  after 54,000 cycles

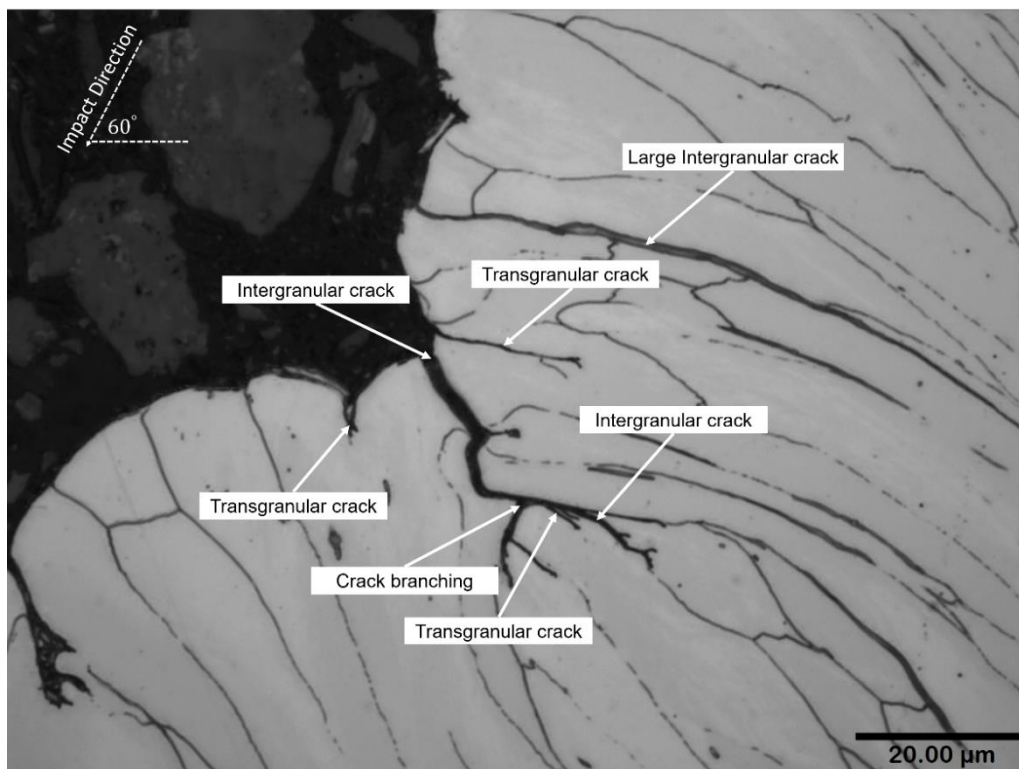
### 6.3.6 Crack Orientation

One of the objectives described in Section 2.2.2.1, is to identify the nature of crack during repetitive normal and compound impact (intergranular or transgranular). These topics have not been studied before for any material.

The previous investigation of AISI 304 (Section 5.3.4) revealed that both intergranular and transgranular crack occur during repetitive impact regardless of the impact angle. Therefore, further work was carried out with both materials to gain insight about the nature of these cracks and support the previous results. Figure 6.51 shows the crack orientation for AISI 316, Figure 6.52 shows the same features for EN8 under normal impacts, and Figure 6.53 shows the EN8 results for compound impact.



(a)



(b)

Figure 6.51 Optical microscope image showing both transgranular and intergranular cracks propagation inside and within the grains for AISI 316 after 54,000 cycles under: (a) normal impact  $90^\circ$  and (b) compound impact angle  $60^\circ$

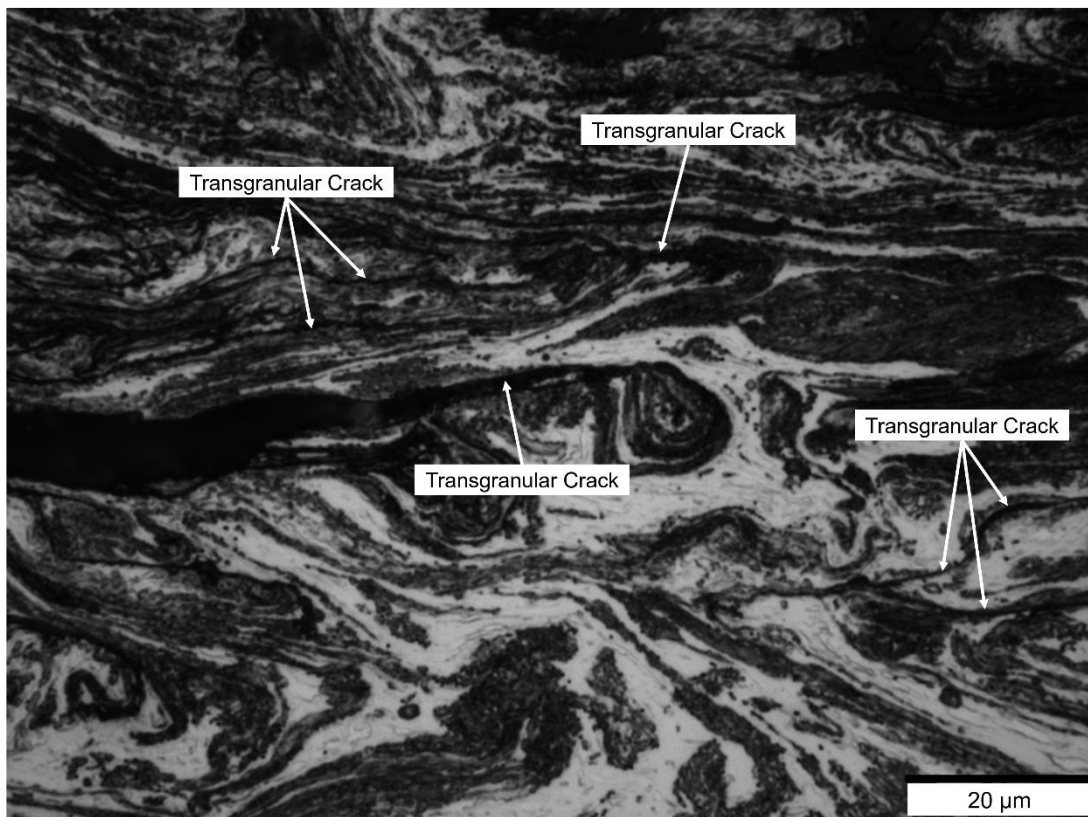
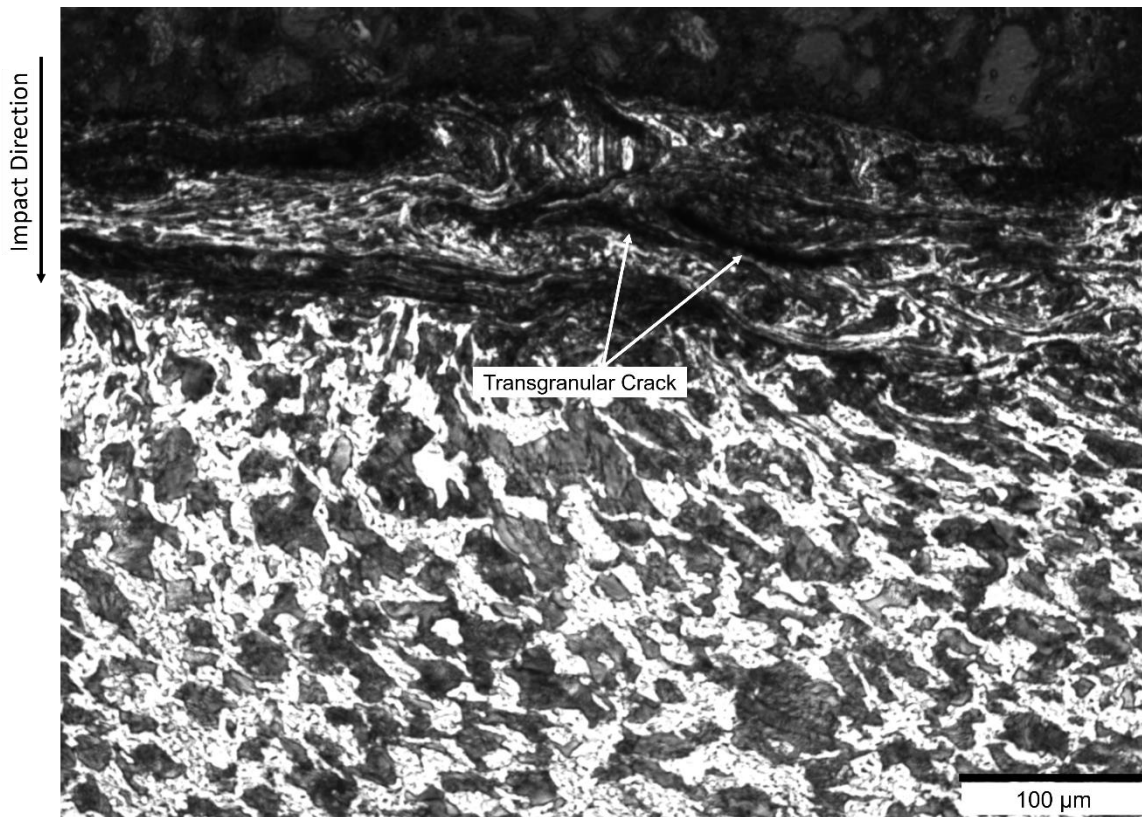


Figure 6.52 Optical microscope image showing both transgranular and intergranular cracks propagation inside and within the grains for EN8 after 54,000 cycles under normal impact angle  $90^\circ$

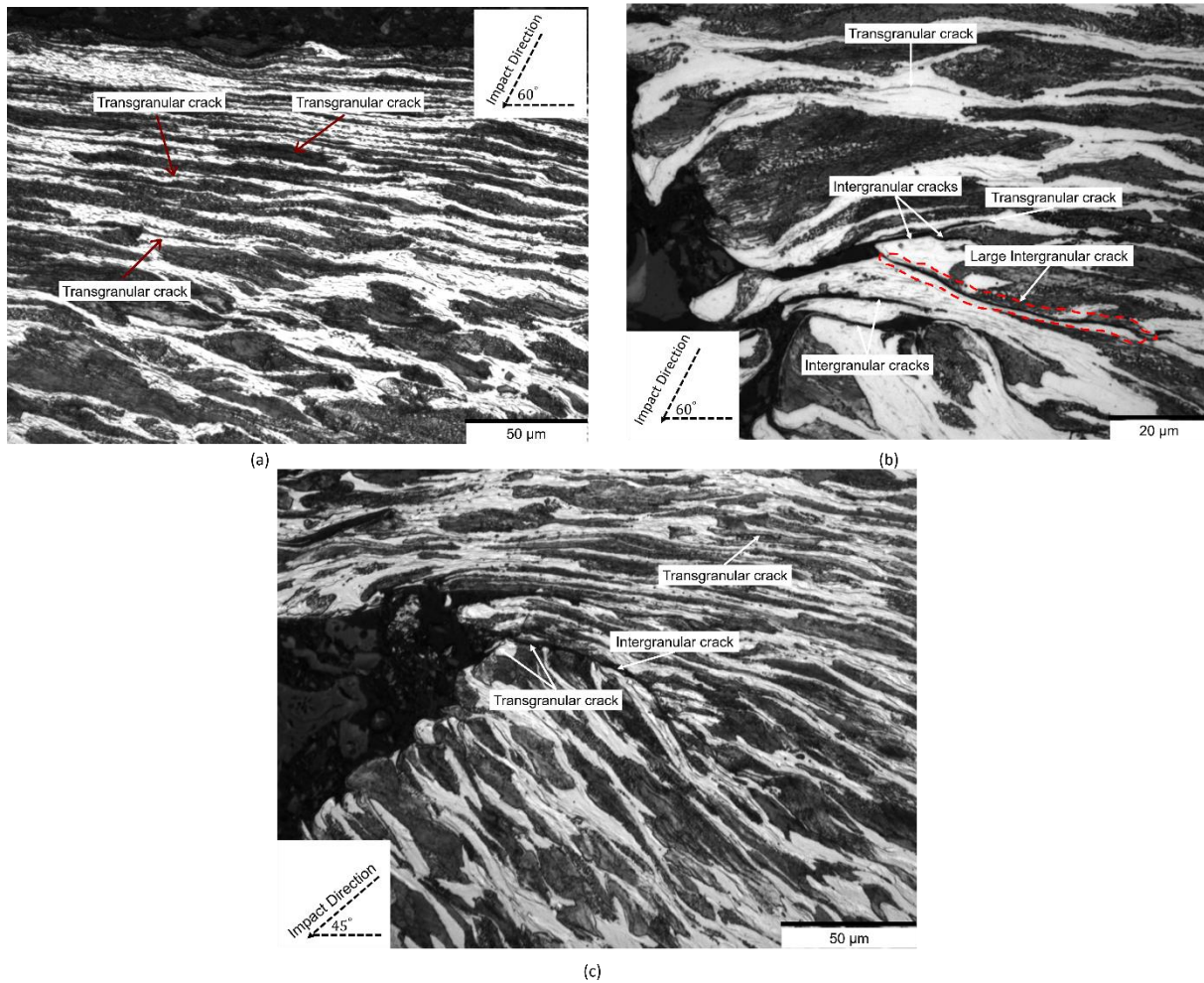


Figure 6.53 Optical microscope image showing both transgranular and intergranular cracks propagation inside and within the grains for EN8 after 54,000 cycles under: (a) and (b) compound impact  $60^\circ$ , and (c) impact angle  $45^\circ$

Figure 6.51 (a and b) shows similar results to those for AISI 304 (see Figure 5.45), with both intergranular and transgranular crack occurring during impact regardless of the impact angle.

Figure 6.52 shows that the majority of cracks under normal impacts were transgranular and happened in the pearlite rather than the ferrite phase and since the pearlite phase is harder than the ferrite, a series of cracks occurred within it. For compound impacts (Figure 6.53), both intergranular and transgranular crack occurred during impact and the transgranular crack occurred within both the ferrite and pearlite phase, but in general the majority of cracks occurring in EN8 were transgranular.

## 6.4 Discussion

### 6.4.1 Wear Volume and Wear Measurements

The results for both materials indicate that the mass loss and wear volume are inversely proportional to impact angle, with significant increases in materials loss occurring with compound impact due to the effect of shear force. The results are consistent with previous results for AISI 304 presented in Section 5.2.1 (see Figure 5.1).

The wear volume under normal impacts was small compared with compound impacts for both materials due to the role of work hardening, since the nature of contact was purely dynamic compression under normal impact and thus involved the role of zero wear volume during normal impacts [71].

Figure 6.1 also indicates that changing the impact angle resulted in a progressive increase in material loss, suggesting that the wear conditions became more severe, similar to AISI 304 (see Figure 5.1). This means that more sliding led to more mass loss due to the role of the tangential component of impact force during compound impact, the highest material loss occurring at impact angle  $45^\circ$  with both materials similar to AISI 304.

Similar to results obtained by mass scale measurement, the impact scar depth, diameter and volume, as described in Section 6.2.2 and measured by 3D non-contact profilometer, increased with decreasing impact angle, with noticeable increases at the lowest impact angle of  $45^\circ$  (see Figure 6.3).

The results for 2D profile, see (Figure 6.6), revealed a significant amount of pile up could be seen with EN8 with all impact angles due to the low ability of work hardening for EN8 and therefore, it is plastically flow on the shoulders (pile-up) with all impact angles [87].

The wear volume, as measured by scale, and total volume loss, as measured by 3D non-contact profilometer, always increased with decrease in the impact angle. These results support the previous results for AISI 304 described in Section 5.2.1 and Section 5.2.2 and the findings of Rigaud & Le Bot [29], Tyfour [30], Zanoria [54] and others [77-79].

The current results for zero wear volume support those obtained previously for AISI 304, as described in Section 5.2.2 (Figure 5.4). Figure 6.4 shows the importance of zero wear volume in AISI 316 under normal impacts, while it decreases with compound impacts to a potentially negligible level, especially with an impact angle of  $45^\circ$ .

Section 6.2.2 revealed that both 3D non-contact profilometer (see Figure 6.3) and spherical cap method (see Figure 6.5) should be used to measure the total volume loss, whereas the wear volume should be measured by mass scale and the results obtained from these two methods should then be compared.

### 6.4.2 Wear Scar Analysis

#### 6.4.2.1 Wear Damage and Crack Propagation

The SEM examination after 54,000 cycles showed similarity in terms of the wear damage mechanisms that depended on the impact angle. For normal impact, plastic deformation and surface fatigue occurred as a result of delamination and spalling resulted from microcracks and micro pitting on the surface (see Figure 6.7 and Figure 6.10). These results agree with those found previously for AISI 304 and explained in Section 5.5.2.1.

Both materials show that the hardened surface layer which resulted from excessive compressive impact force suffered from reduction in ductility near the edges of the newly exposed surface (see Figure 6.7 and Figure 6.10). These regions exhibited multiple cracks that eventually leave the surface as small crushed particles.

In the cases of compound impact angles  $60^\circ$  and  $45^\circ$ , the morphological characteristics and surface degradation were found to be different from those for normal impact. The wear mechanisms, besides plastic deformation, included surface fatigue (delamination and spalling) and abrasive wear (see Figure 6.7 and Figure 6.10) as two and three body (defined earlier in Section 5.5.2.1), Figure 6.54 shows an example of hard particles transferred from the AISI 316 specimen surface and attached to the striker ball which also indicates the adhesive wear occurs to the specimens (in small scale).

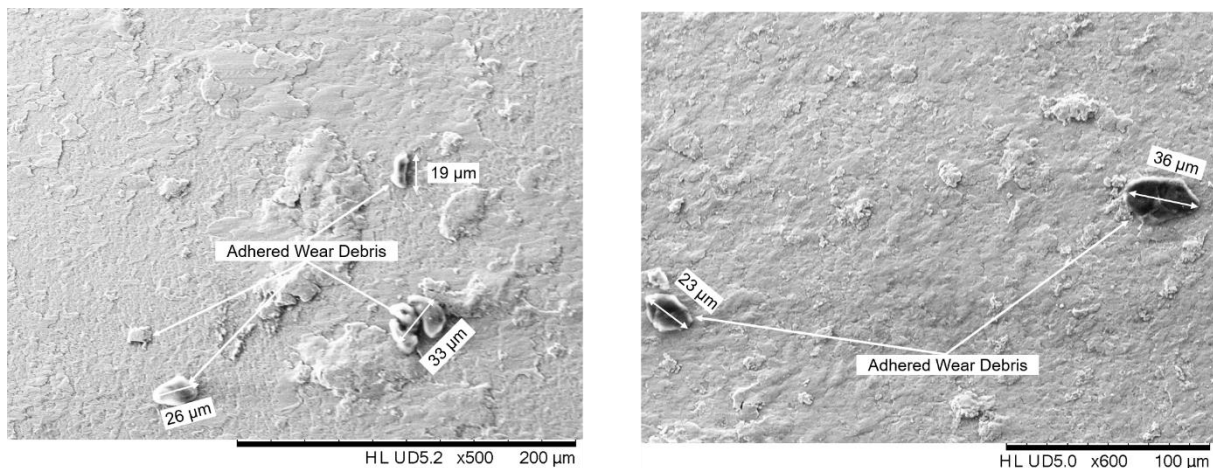


Figure 6.54 SEM image shows the adhered wear particles transferred from the AISI 316 worn surface to the striker surface with impact angle  $60^\circ$

With compound impacts, multiple layers of delamination were revealed for both materials (see Figure 6.8 and Figure 6.11) near the bottom edge, with a tendency for more delamination to occur at impact angles  $60^\circ$  and  $45^\circ$ . The current results agree with the previous finding for AISI 304 (see Figure 5.18).

Crushed particles were found with all impact angles for both materials, with an obvious increase in the amount of these particles with compound impact which could be explained as the additional role of shear force in accelerating the formation of these particles. Therefore, the wear damage for compound impact developed more quickly than for normal impact.

Both materials exhibited extensive accumulation of plastic flow near the bottom edge with compound impact (see Figure 6.9 and Figure 6.12), which is similar to the results previously obtained by Lindroos [20, 82] and explained in Section 5.5.2.1.

The only difference between the two materials is that EN8 exhibited plastic flow under normal impact. The plastic flow that occurred with all impact angles for EN8 can be explained as the low propensity of work hardening (generally hard) for EN8 and therefore, it is plastically flow on the shoulders (pile-up) rather than being compressed as was the case with both types of austenitic stainless steel (generally soft and have high propensity for work hardening) [87].

Subsurface examination of AISI 304, as described in Section 6.3.2.1 (see Figure 6.13), and EN8, as described in Section 6.3.2.2 (see Figure 6.14), showed that under normal impact the majority of cracks

were initiated from the surface and propagated beneath the surface in a parallel plane to cause delamination. With similar patterns of cracking found for AISI 304 and explained in Section 5.5.2.1.

Multiple layers of delamination resulting from parallel microcracks were the main wear features contributing to surface fatigue in addition to spalling and small crushed particles found on the surface, which supported the results obtained in Figure 6.7. The higher value of impact force occurring under normal impact led to more material being compressed and the majority of cracks were parallel to the impacted surface.

No evidence of crack initiation from the subsurface was found with normal impact; however, this is more likely to occur with compound impact due to the effect of the tangential component (shear force) during impact. The small sized crack that led to small layers of delamination reflect the small amount of wear volume under normal impact.

Specimens under compound impact revealed different impact wear damage mechanisms, surface fatigue as a result of both large surface and subsurface microcracks that led to larger delamination was obvious with both impact angles ( $60^\circ$  and  $45^\circ$ ).

These larger cracks and delamination layers were caused by the effect of shear force during impact, with shear force also causing an increase in amounts of crushed particles under both angles as shown in Section 6.3.2.1 (Figure 6.17). Contrary to normal impact, significant amounts of subsurface cracks initiation and propagation were found beneath the surface under compound impact ( $60^\circ$  and  $45^\circ$ ) (see Figure 6.14, Figure 6.16 and Figure 6.21 ). These results agree with AISI 304, Yang [17] and Zhang [23] and are explained in Section 5.3.2.1.

The abrasive wear was more obvious in surface examination, as shown in Figure 6.10 (b) and (c), for both angles and was confirmed by subsurface examination of EN8, as shown in Figure 6.26. This explained the further material loss that occurred with both angles, AISI 316 being very similar to AISI 304; therefore, no further perpendicular sectioning was done to demonstrate the abrasive wear during compound impact.

For AISI 316, the amount of plastic flow that accumulated near the bottom edge was dependent on the material's work hardening [87] and the shear force which depended on the impact angle. The high ability for work hardening of AISI 316 led to more materials being compressed under normal impact, rather than formation of plastic flow on the edges. While larger amount of materials extrusion with impact angle  $45^\circ$  reflects the application of the highest shear force value.

In the case of EN8, which has much lower ductility than AISI 316, more materials were plastically deformed uniformly on both the top and bottom edges under normal impact. Additionally, more plastic flow was found on the bottom edge under compound impact than with AISI 316, which supports the 2D profile results in Section 6.2.2 (Figure 6.6).

The electro etching of AISI 316 described in Section 6.3.3 revealed three morphological zones within the impact wear scar. The surface layer is zone 3, which suffered severe degradation, deformation and shearing off in the impact wear process (see Figure 6.31 and Figure 6.32). This layer will eventually be detached from the surface by the effect of large cracks that propagate parallel to the surface, leading to separation. Zone-2, which is the plastic deformation region, can also be divided into a highly deformed region (zone 2-A) and less deformed region (zone 2-B), while beneath this region are the undeformed grains of zone 1.

The chemical etching of EN8 described in Section 6.3.4 also revealed three morphological zones, but it was difficult to recognise the hardened layer (zone 3). Normal impact conditions revealed obvious deformation to zone 2 that reaches to a depth of 600  $\mu\text{m}$  beneath the worn surface (see Figure 6.40) compared with 45  $\mu\text{m}$  for AISI 316 (see Figure 6.28).

The surface crack of EN8 that initiated from the surface and propagated beneath the surface parallel to the surface will eventually cause delamination (see Figure 6.40) reaching to a depth of 100  $\mu\text{m}$  below the worn surface, while with both AISI types, 304 and 316, the surface crack remained very close to the surface (see Figure 6.28).

The grain orientation, as marked with blue arrows in Figure 6.41, changed with the direction of the plastic flow. This did not occur with either type of austenitic stainless steel (see Figure 5.33 and Figure 6.27) since no significant amount of plastic flow accumulated under normal impact after 54,000 cycles.

Investigation of the crack orientation during impacts revealed that the current results supported the previous results of AISI 304 in Section 5.3.4, showing that the cracks were intergranular and transgranular for both types of material. Examination of EN8 under normal impact did not reveal any intergranular cracks, but that does not mean none existed, only that due to the high deformation level on the surface, it was not possible to detect these cracks as with compound impact.

The majority of transgranular crack occurred in the harder phase (pearlite) rather than the ferrite under normal impact, thus indicating that harder materials under normal impact may suffer more damage than softer materials. With compound impact it is obvious that the cracks were intergranular and transgranular for both types of materials. Both intergranular and trans granular cracks were defined earlier in Section 5.5.2.1.

#### **6.4.2.2 Microhardness Examination**

The current results revealed the greater work hardening ability of AISI 316 in comparison with EN8. These results, described in Section 6.3.5, revealed an increase in surface hardness for AISI 316 that varied from (74-102) % in comparison with the bulk hardness (188 HV). For EN8 the variation was from (25-69) % in comparison with the bulk hardness (205 HV), see Table 6.3.

This result could be explained as the role of high ductility of AISI 316 as compared with EN6. Additionally, the considerable difference between the tensile strength and the yield strength for the two materials: 298 MPa for AISI 316 compared with 111 MPa for EN8, is another possible reason for these differences in hardening ability. These results confirm and support the previous ones presented in Chapter 4 and Chapter 5 and also results obtained by Fricke [22].

Similar to AISI 304, when the depth of plastic deformation or amounts of deformed grains for the etched samples of AISI 316 were compared with the hardening depth by measuring the microhardness, the differences were considerable. For example, Figure 6.28 showed that the deformed grains reached to a depth of 45  $\mu\text{m}$ , while the microhardness measurement showed that the hardness had increased to reach a depth of 2 mm (see Figure 6.48). The same result was found with both impact angle 60° (see Figure 6.31) (1.4 mm) and impact angle 45° (see Figure 6.35) (0.7 mm). The differences in results between the depth of plastic deformation revealed by SEM or OM and the hardening depth measured by the microhardness were explained earlier in Section 5.5.2.2, as the role of residual stresses induced and remaining in the contact region area (in the crystal lattice of grains).

For EN8, the chemical etching and the hardening depth as measured by microhardness revealed great compatibility with the plastic deformation to the grains, except for some deviation that occurred with

normal impact. Figure 6.40 shows that the plastic deformation reached to a depth of 700  $\mu\text{m}$  including the worn layer, whereas hardening reached 1.2 mm in depth as measured by microhardness. Meanwhile, Figure 6.43 showed that the plastic deformation reached a depth of 900  $\mu\text{m}$ , which is the same result as obtained by microhardness measurement, a similarity also shown in Figure 6.46, with both reaching a depth of 300  $\mu\text{m}$ .

## 6.5 AISI 316 and EN8 Summary

A summary of the findings derived from the experimental work on both materials discussed in this chapter is presented below:

- The wear volume is inversely proportional to the impact angle (for those tested), with highest materials loss occurring at impact angle  $45^\circ$ , similar to AISI 304.
- For both materials, impact wear scar volume, depth and diameter, as measured by 3D profilometer, were inversely proportional to the impact angle.
- The wear damage mechanism for both materials is highly dependent on the impact angle.
  1. For normal impact conditions, the main wear damage mechanisms are plastic deformation and surface fatigue due mainly to surface delamination and spalling, similar to AISI 304.
  2. For compound impact, in addition to plastic deformation and surface fatigue, adhesive and abrasive wear are responsible for the extra increase in material loss, which reflects the severe damage that occurs to the worn surface.
- The amount of plastic flow that accumulates on the bottom edge is governed by the impact angle and material ductility.
- Multiple layers of delamination near the bottom edge occurred for both materials with compound impact, while normal impact did not produce these layers since the nature of contact is frictionless.
- Perpendicular sectioning of EN8 revealed that abrasive wear is the main wear damage that occurs to the material under compound impact, especially with impact angle  $45^\circ$ .
- Both intergranular and transgranular cracks occur during normal and compound impact wear for AISI 316 and EN8 regardless of the impact angle.
- AISI 316 shows great work hardening ability in comparison with EN8, due to its high ductility, similar to AISI 304.
- Shear force, as represented by the tangential component of impact force, plays an important role not only in the amount of mass loss but also in the type of wear damage mechanisms and the amount of materials plastically deformed near the bottom edge.
- The hardening value and depth are inversely proportional to the impact angle and are reduced significantly with compound impact angles  $60^\circ$  and  $45^\circ$  compared to normal impact angle  $90^\circ$ .

## Chapter 7 New Proposed Impact Wear Model

### 7.1 Introduction

The work presented in this chapter is following one of the objectives highlighted in Chapter 1 and outlined in Chapter 2 that there are no models considering the role of shear force during compound impact.

This chapter presents the new proposed impact wear model extracted from the experimental work of three metal alloys, AISI types (304 and 316) and EN8 using the impact wear rig. Then the new model is compared with other data from published papers and discussed in detail including its limitations. The summary of the main discoveries and the key findings are listed at the end of this chapter.

### 7.2 Limitation of Extant Wear Models

The major drawbacks of the extant impact wear models were discussed in detail in Chapter 2 Section 2.4.2. A number of developed impact wear models described in Sections 2.4.2.1-2.4.2.6 have a similar form to those defined earlier to predict erosive wear. These erosion models are typically presented either as a function of impact velocity [44, 89] or as function of impact energy [90].

The impact wear modes illustrated in Figure 1.1 show that both (b) and (c) involve a small amount of interfacial sliding (small arrow) that the existing models (Section 2.4.2) do not directly account for and this are unable to include in their predictions. However, it should be noted that using any of the previously developed impact wear models described in Section 2.4.2 will clearly produce a 'result' but the accuracy of that will vary depending on the basis of the model and, for the majority, will be increasingly inaccurate the further from normal the impact is.

Therefore, this chapter proposes a simple, easily applied, wear model that is able to predict the wear volume due to surface impingement at different impact angles and then validated through comparison with experimental data of three metal alloys widely use in engineering applications.

### 7.3 Development of the New Model

The need for a model that can predict impact wear loss with any impact angle to simulate the excessive wear that occurs at smaller impact angles, and thus leads to under prediction of existing models, was the motivation for developing the new impact wear model that is described here.

The results described in Section 2.5.1 show that the impact angle strongly influence on wear volume. It means that this new model cannot be defined solely in terms of the applied impact force, since neglecting the shear force would lead to inaccurate results.

The two components of the new model were derived from experimental work, initially AISI 304 with different angles of impact ( $90^\circ$ ,  $60^\circ$  and  $45^\circ$ ) and specific numbers of cycles (54,000) using impact wear rig described in Section 3.1.1. Analysis of the experimental results of AISI 304 revealed that the highest wear volume always occurs when the impact angle is  $45^\circ$  as shown in Figure 5.1. This was found to be true for all of number of cycles studied and that the wear volume under normal impact is very small compared with at  $60^\circ$  and  $45^\circ$  due to the role of zero wear volume during normal impact [71].

The significant increase in wear volume that occurred with compound impact is considered due to the role of tangential component of impact force during impact. Despite the normal component of impact force decreasing with decreasing the impact angle from 3476N at an impact angle of  $90^\circ$  to 2457 N at

an impact angle of 45°, the wear volume increased significantly since the tangential components increased from 0 at an impact angle of 90° to 2457 N at an impact angle of 45°.

The sliding distance ( $x$ ) that the striker slides against the inclined specimen surface of AISI 304 during impact was measured experimentally by using a high-speed camera. Due to the sliding distance being very small it was only realistic to obtain values due to the first impacts due to the decay of the motion. The sliding distance stays constant with number of impacts and six impacts taken were measured for each angle and the mean values were 0.35 mm for 60° and 0.6 mm for 45° with standard deviation of 0.05 and 0.03 respectively.

Further investigation using specimens manufactured from EN8 and AISI 316 with the same methodology and number of cycles (54,000), also revealed a similar trend to that exhibited by AISI 304. More wear volume loss occurring at 60° and the largest volume at 45° as described in Chapter 6 (see Figure 6.1).

Based on data from experiments with the AISI 304, a correlation between wear volume and number of cycles was determined (see Figure 5.1). This is inversely proportional with hardness of impacted materials, since EN8 has relatively the highest hardness among the tested materials and showed lower wear volume compared with both types of austenitic stainless steel (see Figure 6.1). Despite the fact that the three metal alloys have relatively similar hardness, the EN8 has the highest value and shows the least wear volume with compound impact. Additionally the tangential component of the new model has a similar form to the Archard equation [67] where the hardness of softer materials (especially applicable for steel) is inversely proportional to the wear volume.

The repetitive normal impact of AISI 304 revealed that increasing the impact force will always lead to an increase in wear volume. Similar results were found with both AISI 316 and EN8, leading to a correlation between impact force and wear volume for different materials as outlined in Section 7.3.1 (Figure 7.1).

The new proposed impact wear model can be sensibly divided into two components, as proposed previously by Lewis [46] (see Section 2.4.2.4).

Firstly, a component accounting for the normal impact, in a similar fashion to the models described by Wellinger [44] (see Section 2.4.2.1) or Fricke [22] (see Section 2.4.2.3), but in terms of normal force rather than impact velocity or energy. Secondly, a component accounting for the non-normal (i.e., sliding) impact, in a similar fashion to the Archard equation [67], but in terms of tangential force rather than applied force.

Both components then contribute to the total wear volume predicted for a compound impact. This approach also allows the model to be used to represent either solely under normal impacts only (by setting the tangential component to zero) or compound impact and also be validated either separately or in combination.

Therefore, the general form of the new model proposed here, and subsequently referred to as the Zalzal-Lewis-Slater (ZLS) model, is as follows:

$$W = \left( KNF_n^{n_{ZLS}} + \frac{kNxF_t^{m_{ZLS}}}{H_s} \right) \quad 7.1$$

where:

$W$  is the wear loss (mm<sup>3</sup>)

$K$  is the normal impact wear coefficient

$N$  is the number of impact cycles

$F_n$  is the normal component of impact force (N)

$k$  is the dimensionless sliding impact wear coefficient

$x$  is the sliding distance during compound impact (mm)

$F_t$  is the tangential component of impact force (N)

$H_s$  is the hardness of the softer material (specimen) (MPa)

$n_{ZLS}$  and  $m_{ZLS}$  are normal and sliding impact wear exponents in Zalzal-Lewis-Slater Model

The results of Fricke [22] under normal impact conditions shows that AISI 440C with a hardness of 710 HV has more mass loss than AISI 304 (164 HV), 1210 (242 HV), and 817M40 (554 HV). Also, the current results presented in Chapter 4 (see Figure 4.5) revealed that ductile cast iron (238 HV) has more mass loss than both AISI 304 (190 HV) and EN8 (213 HV). Therefore, hardness has not been considered as a primary parameter controlling the wear volume of different materials under normal impact, such an approach is similar to the models described by Wellinger [44] (see Section 2.4.2.1) or Fricke [22] (see Section 2.4.2.3).

This equation predicts wear volume and can be used with different impact angles or solely for normal impact only. The model has considered the impact force, rather than impact energy, in order to be able to use measured peak impact forces for each impact, rather than impact energy calculated theoretically or derived from high-speed video camera data and to highlight the role of shear force during compound impact.

### 7.3.1 Derivation of Model Parameters

#### 7.3.1.1 Normal Impact Component

The normal impact wear coefficient  $K$  and impact force exponent  $n_{ZLS}$  were calculated from the experimentally derived relationship between the measured experimental impact force (1982 N, 2783 N, and 3476 N) and wear volume by specific number of cycles (54,000) as shown in Table 7.1 for the tested alloys.

Figure 7.1 shows the derivation of the normal component of tested alloys with impact angle  $90^\circ$  using a line fitting method similar to the work of Wellinger [44] and Fricke [22], the error bar represents the standard deviation of four repetitions of the data.

Table 7.1 Normal impact wear coefficient  $K$  and exponent  $n$  for tested materials

Material	$K$	$n_{zls}$
AISI 304	$1.85 \times 10^{-9}$	0.816
AISI 316	$5.64 \times 10^{-9}$	0.816
EN8	$2.04 \times 10^{-8}$	0.655

## New Proposed Impact Wear Model

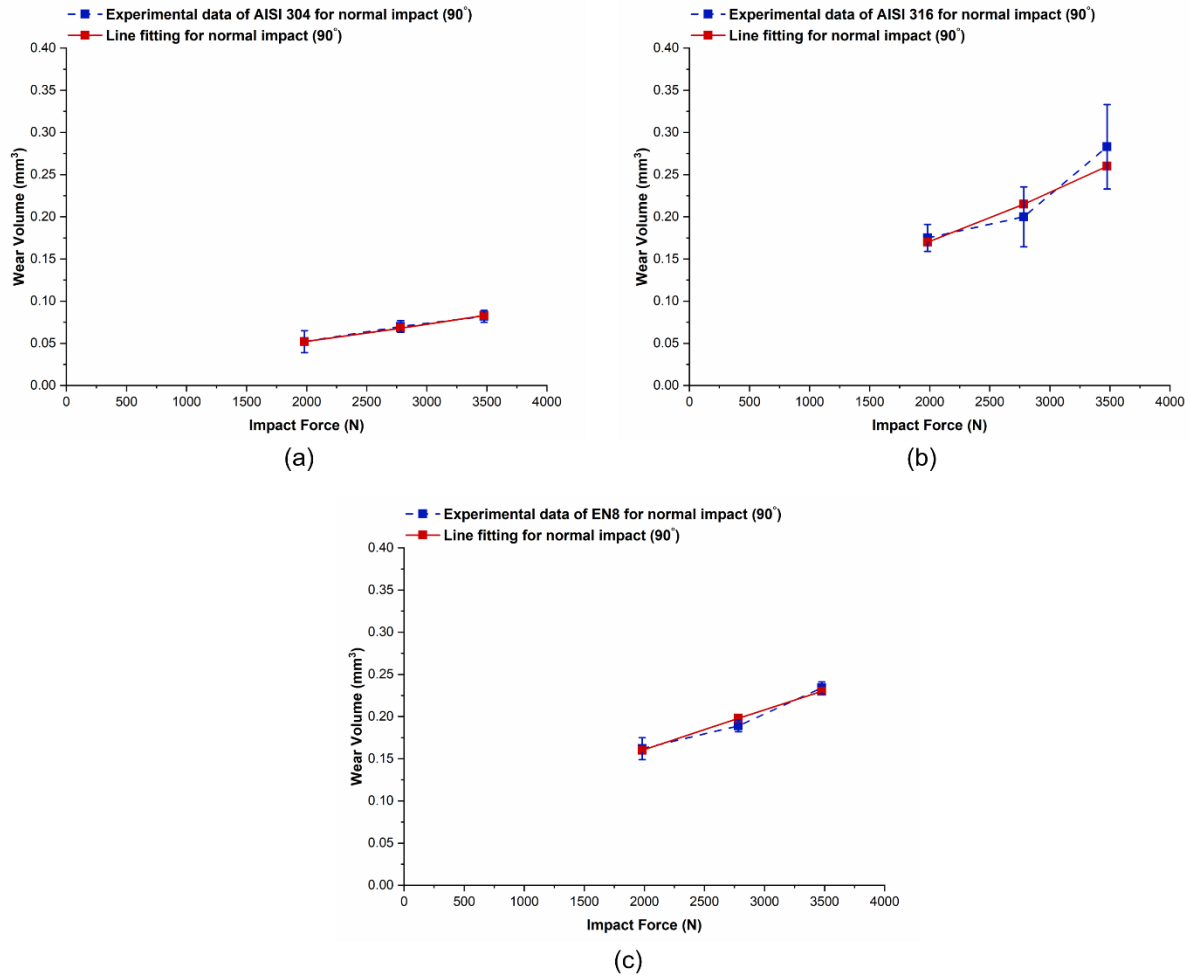


Figure 7.1 Line fitting from the experimental data of (a) AISI 304, (b) AISI 316 and (c) EN8 under normal impact after 54,000 cycles

This number of cycles (54,000) was selected to obtain measurable wear volume as explained earlier in Section 6.2. The normal component of materials in Table 7.1 have been tested with the work of other papers with different number of cycles and shows good agreement (Section 7.4).

### 7.3.1.2 Sliding due to Impact Component

Due to lack of data in the literature describing wear as a function of tangential force for tested alloys, experiments to derive the sliding impact wear coefficient  $k$  and exponent  $m_{ZLS}$  to be used in the new model, were conducted only using AISI 304 specimens. Therefore, data from experiments using other materials would not be able to be then validated against the work of others. That said, in order to give confidence in the data from these experiments conducted for this work the results were compared with the experimental work of Rigaud & Le Bot [29] using the same material and at impact angles of 60°, 45° and 30°.

The tangential component of impact force was calculated from the experimentally derived relationship between the tangential impact force (1738 N for 60° impacts and 2457 N for 45° impacts) and wear volume by specific number of cycles (54,000). Using a similar line-fitting approach as for the normal component of Figure 7.1 to gives value for  $k$  of  $1.45 \times 10^{-7}$  and for  $m_{ZLS}$  of 1.85 that can be then used as the basis for the new model. It should be noted that because the load cell described in Chapter 3-Section 3.3.2 used throughout this work was a uniaxial, the tangential forces (1738 N for 60° impacts

and 2457 N for 45° impacts) were calculated theoretically from the normal forces recorded experimentally.

## 7.4 Validation of the New Proposed Model

The new model has been validated with four published papers that present three different materials either solely under normal impact and using the normal component set of the model (applied for three papers) or under compound impact using the two sets of the model (applied for one paper). Such validation has not been reported for any of the models described in Section 2.4.2.

### 7.4.1 Austenitic Stainless Steel (AISI 304)

The new model proposed here was validated with experimental results from literature by Rigaud & Le Bot [29] under different impact angles using the same exponent  $n_{ZLS}$  (0.816) and wear coefficient  $1.85 \times 10^{-9}$ , since the same material was being used. A comparison is provided in Figure 7.2 and shows some deviation between the experimental data and the new model with different impact angles and specific number of cycles (560,000).

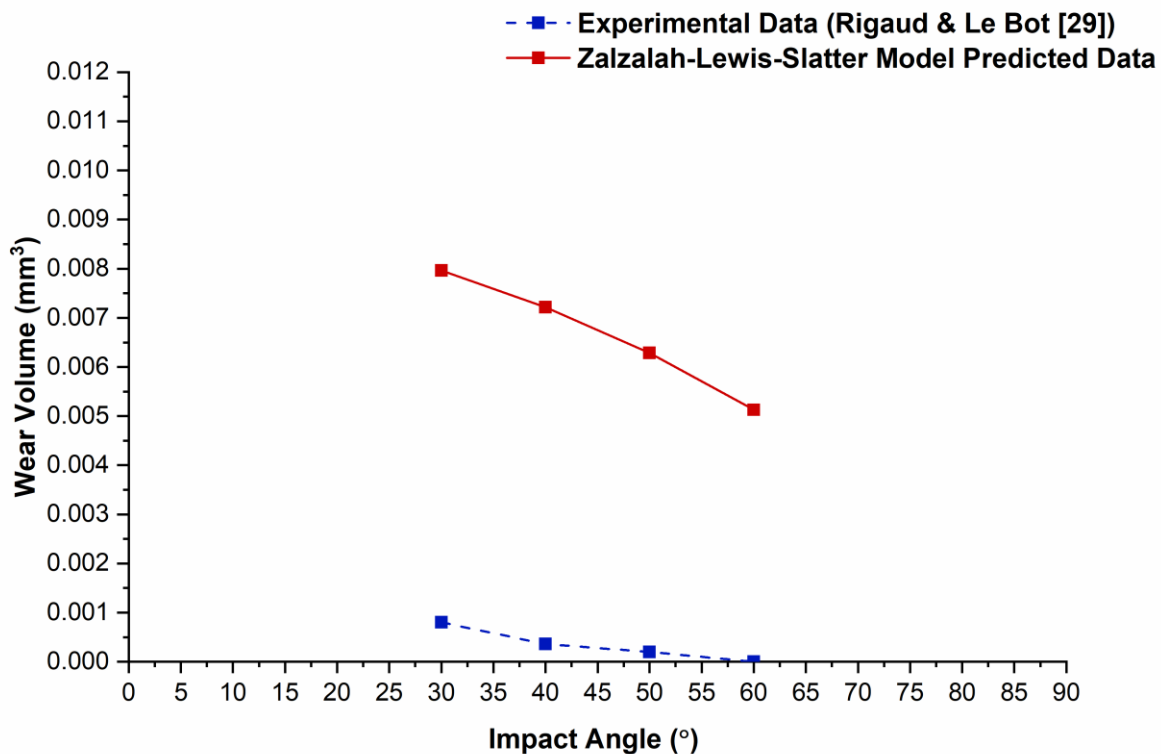


Figure 7.2 Experimental data of Rigaud & Le Bot [29] compared with the Zalzal-Lewis-Slater model data.

The deviation between the experimental data of Rigaud & Le Bot and model data is likely to be as a result of large differences between the number of cycles reported in literature and the actual number of cycles (e.g., mismatch between excitation frequency and impact frequency).

This indicates that the dynamic system is strongly nonlinear and the rig is unstable during tests caused by vibration during impact and induced dispersion in impact location (see Figure 2.15) which may reduce the wear volume significantly since the impact is not occurs in the same contact region.

It is also possible that variation in surface roughness could influence sliding impacts, even if that effect in a very small scale. Liang [91], for example, found that the wear volume of materials increased from

1 mm<sup>3</sup> with a surface roughness of  $R_a=0.1\mu\text{m}$  to 3 mm<sup>3</sup> with surface roughness  $R_a=0.5$  (within the range of the work presented here).

Lastly, the experimental data of Rigaud & Le Bot has not been repeated which reduce the confidence of the results. This deviation between the experimental data and the model data should be considered against very small predicted values for both approaches (less than 0.008 mm<sup>3</sup>).

#### 7.4.2 Austenitic Stainless Steel (AISI 316)

Validations using data from work using AISI 316 were limited to using the normal component of the new model because of a lack of information about the tangential impact force in those studies. Experimental data from testing of unburnished specimens (310 HV) and burnished specimens (405 HV) from a study by Yilmaz & Sadeler [28] was compared with the new model.

In that work, the specimens were subjected to normal impact (impact force 560 N for 1000, 10,000, and 100,000 impacts) and the wear volumes were directly measured by 3D non-contact profilometry, Figure 7.3 shows result for both specimens.

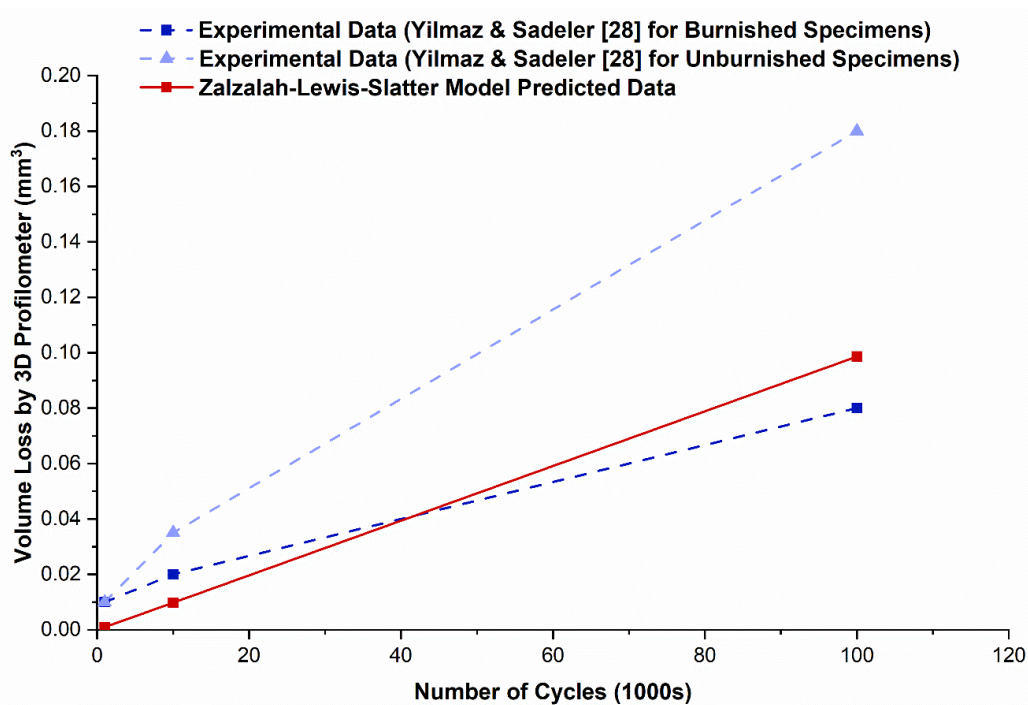


Figure 7.3 Experimental data of Yilmaz & Sadeler [28] under normal impact compared with Zalzalal-Lewis-Slater model data.

Very good correlation was found with the data reported for the burnished specimens but much weaker for the unburnished. This can be attributed to the fact that the new model, in common with the other extant models described in Section 2.4.2, is based on wear volumes derived from measured mass loss (Figure 5.1) rather than the 3D non-contact profilometry used by Yilmaz & Sadeler. It means that the latter method will detect the extra volume loss resulting from zero wear [71]. Having been subjected to mechanical working, the burnished specimens will likely not experience significant zero wear phenomenon, thus the wear reported by 3D non-contact profilometry will be the same as that detected by the measured mass loss method.

### 7.4.3 Medium Carbon Steel (EN8)

Two validations were possible with carbon steel as the material of interest, and with normal impact conditions using the normal impact wear coefficient  $K$  and impact force exponent  $n_{ZLS}$  ( $2.04 \times 10^{-8}$  and 0.655, respectively) derived experimentally in this work (Section 7.3.1). Figure 7.4 shows good correlation between the predictions of the new model and the experimental data from the work of Jiang et al. [15] where rail steel and a welded rail steel joint (Figure 7.4) were subjected to normal impact.

The experimental results here were based on impact force of 200 N and different number of impact cycles (5,000-100,000) compare favourably the predictions of the new model, particularly for data points representing wear occurring after large numbers of cycles.

The variation between the experimental data and the predictions at lower numbers of cycles is again due to the role of zero wear, in this case because of the use of the spherical cap method which leads to results similar to the 3D non-contact profilometer, but with greater potential error. However, the better correlation of the model with higher number of cycles (end of life) is more desirable in an industrial context where total wear life is often of more immediate interest than the evolution of the early stages of wear, especially in contacts where that stage is effectively used as a running in period.

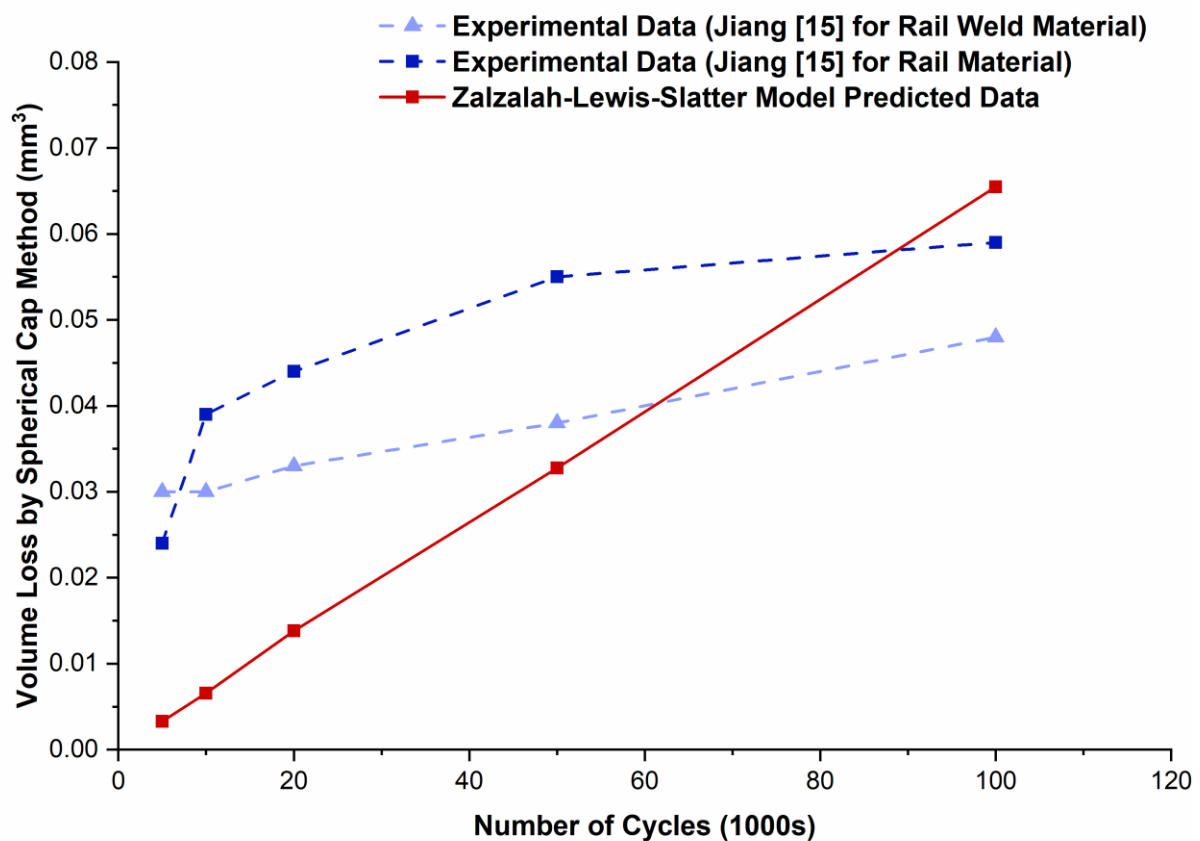


Figure 7.4 Comparison between the experimental data of Jiang et al. [15] for steel of rail material and rail weld joint material and data from Zalzalal-Lewis-Slatter model data.

A second validation was carried out between the new model's predictions and the experimental data obtained by Wang et al. [39] for 40Cr steel impacted normally (impact force of 80.9 N, and up to 100,000 cycles), this comparison is shown in Figure 7.5.

Similar to the comparison with the unburnished AISI 316 results shown in Figure 7.3, the new model under-predicts compared to the experimental data. In this case, the volume loss was also measured by 3D non-contact profilometer and neglecting the role of zero wear volume during normal impact, as in the present work.

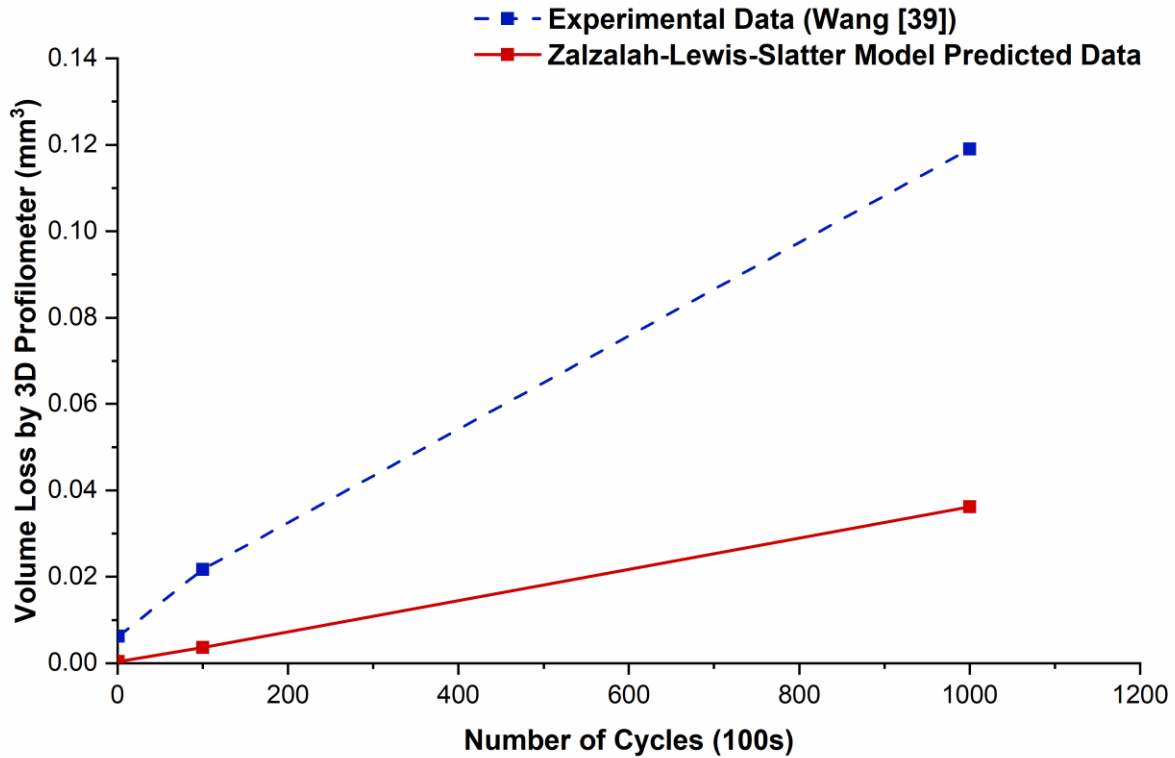


Figure 7.5 Experimental data of 40Cr steel from Wang [39] compared with the Zalzalalah-Lewis-Slatter model data.

## 7.5 Discussion

The new Zalzalalah-Lewis-Slatter model proposed here was developed based on specific parameters (number of cycles, normal and tangential impact force, sliding distance and hardness of softer material) to reflect information readily known about contacts in many real mechanical systems. This means that it can be easily used for predicting both normal and compound impact wear, including angle as a function, without requiring large number of experimentally derived parameters that often need apparatus not always found outside dedicated research facilities.

The model can be used under both normal and compound impact and the results easily compared with other data to obtain accurate values for the wear volume. Existing experimental data representing the behaviour of three widely used metal alloys has been used to validate its predictions for normal and compound impact. It is important to note that none of the experimental work from literature used for validation described any data robustness information (as discussed elsewhere [68]) could have affected the accuracy of the wear volume results. However, to some extent, good correlation was generally found with the model.

All the results were obtained with dry contacts since most impact wear applications fall within this field, hence the role of lubricant has not been taken into consideration during this work. Further work is required to understand the role of a lubricant, or other third body in transmitting the force applied in the

## New Proposed Impact Wear Model

impact. The model could also be developed to include the role of work hardening directly during impact and then compared with other experimental data. However, additional experimental parameters will be required, such as work hardening exponents for each material, as such trends are not easy to compare and validate.

The model was compared with volume loss results measured by 3D non-contact profilometer from the validated papers under normal impacts, it shows that the model underpredicted the results due to the role of zero wear volume which has not been considered during impact and highlighted by the Author of this thesis [71].

The model is expected to lead to better correlation with the wear volume results obtained by the standard method of mass loss (converted to wear volume by considering the material's measured density) than with data obtained via direct volume measurement methods especially under normal impact as explained earlier (see Figure 5.4 and Figure 6.4). Table 7.2 shows the differences in volume losses data produced under normal impact ( $90^\circ$ ) on the AISI 304 specimens (see Sections 5.2.1 and 5.2.2) and measured by mass loss (wear volume) and 3D non-contact profilometer (total volume loss) with different number of cycles. While Figure 7.6 shows the differences in results between the model and these experimental data which is mainly contributed to the role of zero wear volume during normal impacts [71].

Table 7.2 Mean wear volume and total volume loss of AISI 304 under normal impact with different number of cycles

Conditions	Mean Wear Volume $V_w$ ( $mm^3$ )	Standard Deviation $\sigma$ (STD)	Mean Total Volume Loss $V_t$ ( $mm^3$ )	Standard Deviation $\sigma$ (STD)
36000, $90^\circ$	0.042	0.0066	2.08	0.16
54000, $90^\circ$	0.082	0.012	2.1	0.18
72000, $90^\circ$	0.111	0.02	2.18	0.2

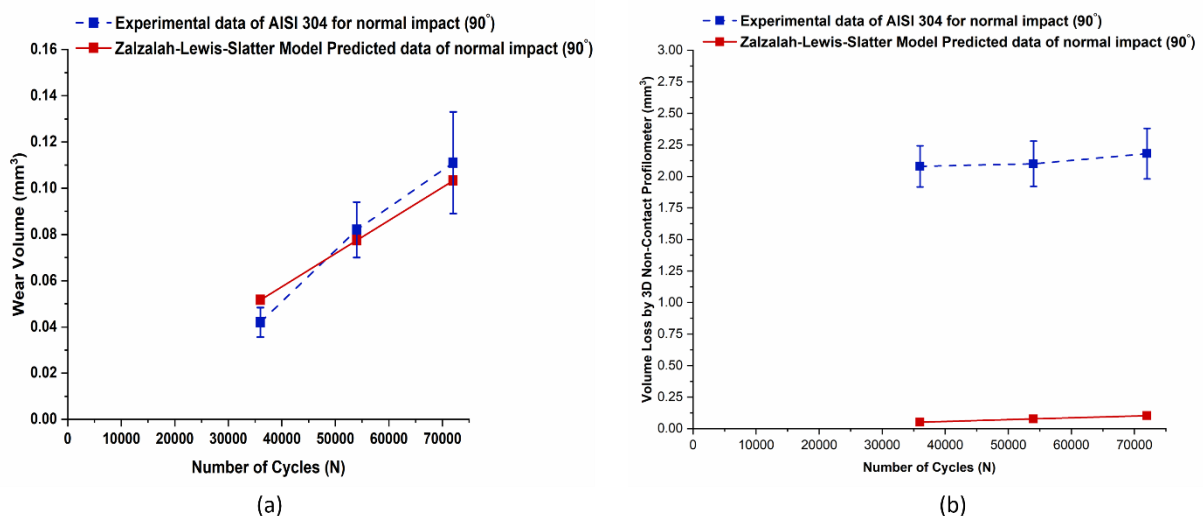


Figure 7.6 Comparison between the model and the experimental results of AISI 304 under normal impacts and impact force 3476 N where; (a) wear volume measured by mass scale and (b) volume loss measured by 3D non-contact profilometer

## New Proposed Impact Wear Model

Figure 7.6 (b) shows large deviation between the experimental data of AISI 304 measured directly by 3D non-contact profilometer and the model (based on wear volume). While this deviation is contributed to the role of zero wear volume, it reduced significantly with compound impact ( $60^\circ$  and  $45^\circ$ ) as shown for example in Figure 7.7 with an impact angle of  $60^\circ$ .

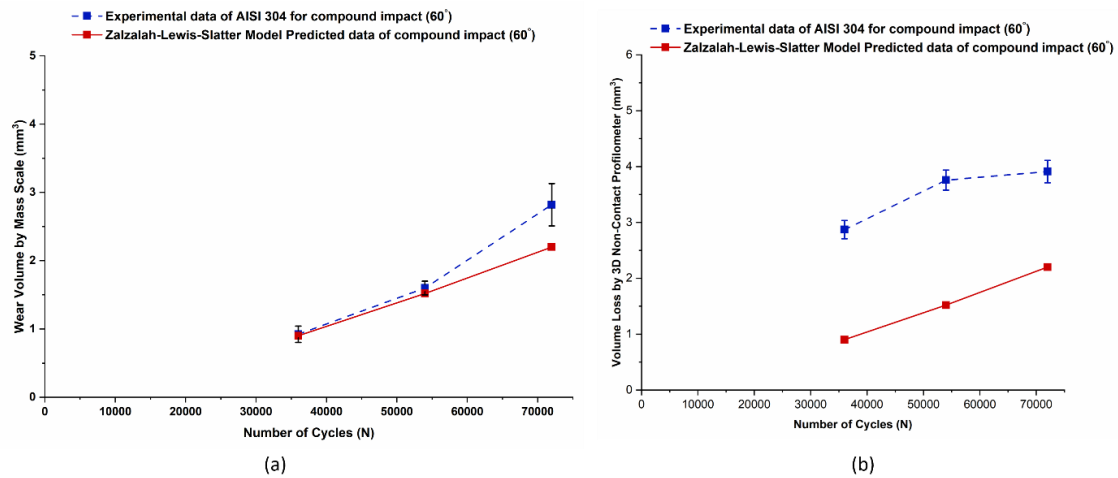


Figure 7.7 Comparison between the model and the experimental results of AISI 304 under compound impacts where; (a) wear volume measured by mass scale and (b) volume loss measured by 3D non-contact profilometer

The majority of deviation in Figure 7.7 (b), is contributed to the plastic flow volume that removed from the centre of wear scar and accumulated near the bottom edge (see Figure 5.7 (b), Figure 5.8 (b)) and minimising the effect of zero wear volume during compound impact as described in Section 5.2.2 (see Figure 5.4).

Figure 7.6 (a) and Figure 7.7 (a) show an excellent correlation between the experimental data of AISI 304 and the model under both normal and compound impacts with different number of cycles (36,000;72,000) to that the model was derived (54,000). This comparison and deviation is similar to that achieved by Fricke between the experimental data of AISI 431 and the model (Section 2.4.2.3) with different number of cycles [22].

The new model is based on wear volume measured by mass loss rather than total volume loss measured by 3D non-contact profilometer. This is the typical method for measuring the wear volume and calculate the impact wear coefficient and compare it with other value from the extant wear models. Also, this method is similar to all the extant wear models described in Section 2.4.2 (based on mass loss). While the 3D non-contact profilometer measure the total volume loss not the wear volume and this does not reflect the actual material loss as wear volume and eventually cannot identify the wear resistance of materials.

It is important to mention that the new model is only modelling the first impact, whereas the experiment will have all the subsequent impacts that contribute to the wear results.

Lastly, the current results showed that the impact wear coefficient  $K$  and sliding wear coefficient  $k$  of the tested materials both achieved values to an exponent in the range  $10^{-7}$ - $10^{-9}$ , potentially indicating the severity of wear during impact. Where a value of  $10^{-2}$  indicates very severe wear conditions and a value of  $10^{-9}$  indicates that the wear conditions are far less aggressive [92-94]. This means that the three tested alloys (AISI types (304 and 316) and EN8 ) could be considered as materials with good impact wear resistance within the impact conditions explored, and a value of  $10^{-5}$  and  $10^{-6}$  could indicate moderate wear conditions [22, 45, 95].

## 7.6 Impact Wear Model Summary

The summary of the findings derived from the new proposed impact wear model in this chapter are shown below:

- A new model for predicting both normal and compound impact wear taking into consideration the role of shear force (tangential force) is achieved in this work.
- The model is valid for ductile materials (mainly steels) since hardness is a parameter included in the model and therefore, it is not applicable for non-metallic materials such as ceramic (brittle).
- The model has with good agreement using data obtained from literature describing studies that considered normal and compound impacts on similar engineering alloys (with deviation up to three times the experimental data).
- The model correlates better wear volume data measured indirectly by mass scale (the de facto standard) than direct methods due to the role of zero wear.
- Further experimental to fully validate the experimental data under compound impact and subsequent model parameters for materials other than AISI 304 is required.

## Chapter 8 Conclusions and Future Work

### 8.1 Introduction

The final chapter of this thesis first summarises the research contributions of this study, then presents the main conclusions and findings extracted from this work and the related contributions to the field of impact wear. Finally, it provides recommendations for future work based on the outcomes of the work presented in this research.

### 8.2 Summary

The effect of impact wear parameters including the number of cycles and impact angle for a variety of engineering metallic alloys was analysed.

The selected materials, which had different mechanical properties and are used in many applications, included an austenitic stainless steels type (AISI 304 and 316); a medium carbon steel (EN8); a ductile cast iron (EN-GJS-600-3); an aluminium alloy (AlSi9Cu3) and a phosphor bronze (PB102).

The mechanical performance change and wear resistance of tested alloys were assessed using Vickers hardness and microhardness tests, and tests on an impact wear rig; while the wear scar features were analysed using microstructural characterisation.

### 8.3 Conclusions

The aim and objectives outlined in the first chapter of this research have led to the following main conclusions and suggestions:

#### 8.3.1 The Nature of Impact Wear Mechanisms

- AISI 304 shows the best impact wear resistance among the tested materials under normal impact despite its relatively low hardness compared with both EN8 and ductile cast iron.
- The experimental results revealed zero wear volume as the predominant volume loss occurring among all the tested materials under normal impacts and this shows the importance of using the mass scale together with the 3D non-contact profilometer.
- The impact wear volume of steels is inversely proportional to the impact angle and the wear damage mechanism changes from surface fatigue under normal impact ( $90^\circ$ ) to abrasive wear as the main form of wear damage with compound impact, especially with an impact angle of  $45^\circ$ .
- Two and three body abrasive wear occur during repetitive compound impact ( $60^\circ$  and  $45^\circ$ ) for the tested alloys (AISI types 304 and 316, and EN8).
- For the tested alloys (AISI types 304 and 316, and EN8), the cracks initiated from the surface and propagated beneath the surface with normal impact, while with compound impact, both surface and subsurface cracks initiation and propagation occurred, thus contributing to the overall wear damage of the steels.
- For the tested alloys (AISI types 304 and 316, and EN8), both intergranular and transgranular cracks were found during impacts, regardless of the impact angle.
- All metal alloys used in this work showed an increase in hardness for the centre of the wear scar and the maximum increases in hardness value and depth always occurs with normal impact.
- The new predictive impact wear model differs from other extant models in highlighting the contributions of both normal and tangential impact force on the accumulative wear volume and it shows good agreement with four papers presents three metal alloys.

### 8.3.2 Suggestions on Measurement Methods

The work presented in this thesis also suggests the following:

- Mass scale and direct volume measurements by 3D non-contact profilometer should both be used to detect the possible zero wear volume, as it would otherwise be neglected.
- A 3D non-contact profilometer is an important tool to detect the wear scar features such as depth, diameter, area and volume.
- Total volume loss of metallic materials under repetitive normal and compound impacts can be measured by using either 3D non-contact profilometer or spherical cap method for point contact geometry.
- Perpendicular sectioning is very important for demonstrating the abrasive wear during compound impacts where otherwise neglected under normal impact.

### 8.4 Novelty of Work

The novelty of this research, as described in Chapter 1, is its highlighting of the importance of calculating the zero wear volume in the field of impact wear under normal impact. Otherwise, it can be neglected with compound impact due to the role of plastic flow volume and wear volume during repetitive compound impact. The work reported in this thesis expands the understanding at the fundamental level of the role of impact angle in the surface and subsurface damage of metal alloys where no data about AISI types (304 and 316) are involved.

The new model could contribute to better understanding of the wear damage of any equipment under either normal or compound impact but this would require measurement of the impact force theoretically or experimentally.

### 8.5 Reflection and Future Work

The last section of this thesis focuses on the potential future work that can be completed to gain further understanding regarding the contribution of impact wear damage based on the work achieved in this research and the main conclusions.

#### 8.5.1 Impact Wear Rig

The impact wear rig used in this work was modified compared to the original one designed by Slatter [40] to measure the impact force during normal impact and heat test specimens for elevated temperature testing.

It is important to report certain limitations relating to this rig, the most commonly used and reliable type of rig for investigating the wear damage mechanisms of different materials. With the current rig, the work was limited to the range of  $90^\circ$  to  $45^\circ$  and it is recommended that the range of angles is widened to between  $90^\circ$  and  $30^\circ$  to cover a wide range of impacts that reflects different impact angles for engineering components.

Also, it is recommended to use a 3-axis load cell to measure the impact force with both normal and compound impact rather than a uniaxial load cell such as in this work, such a modification need a specific new designed load cell for this rig and it is more expensive.

### **8.5.2 Zero Wear Volume and Tested Alloys**

The zero wear volume has been tested on five metals alloys possessing different mechanical properties. Due to lack of information about the zero wear volume in the literature and in order to establish a database for zero wear volume, it is recommended that an investigation is carried out on further materials, such as low and high carbon steel, hardened steel, martensitic stainless steel and others under normal impact conditions. This would help to gain insights about whether these materials tend to have more plastic flow volume or zero wear volume and provided further support to the current results regarding the role of materials work hardening during normal impact.

### **8.5.3 Role of High Temperature during Repetitive Normal and Compound Impacts**

Due to lack of information in the literature about the role of high temperature during impact, further investigation is recommended, using continuous temperatures reaching up to 600°C for testing a variety of materials.

Due to the global pandemic crisis (Coronavirus) the planned high temperature work has not been done because the lockdown in March 2020 forced the closure of the labs. The AISI 304 and EN8 samples were ready to be tested under both normal and compound impacts; the connections of heater cartridges, block and controller box were completed and we were in the process of undertaking a new risk assessment of the rig to enable working with high temperatures.

It is highly recommended that besides AISI 304 and EN8, specimens from high carbon steel be prepared in the future for this work for testing at 200°C and 400°C in order to compare these results with the only available paper in this field by Ootani [33]. This would help to know if similar trends will be obtained.

### **8.5.4 Austenitic Stainless Steels**

The AISI types 304 and 316 results showed differences between the hardening depth measured by microhardness and the deformed grains revealed by electro etching, this attributed to the role of residual stresses during impact that remains inside the specimens. Therefore, it is recommended that a stress relieving treatment after impact is recommended to relieve stresses that absorbed by the specimens during impact process.

The following activities were planned to be achieved at the Materials Department of Leicester University:

- 1- Using higher magnification of SEM to obtain images that would show the cracks orientation and the deformed grains for AISI types 304 and 316.
- 2- AISI 304 samples to be prepared by means of a special polishing process, with use of silica suspension (0.06µm) to carry out the Electronic Back Scatter Diffraction (EBSD). This analysis technique uses to detect the microstructural characterisation regarding such as grains size and orientation, surface texture and any possible phase transformation from austenite to martensite in the region with crushed particles.

Due to Coronavirus, the above work has not been done.

### **8.5.5 Statistical Analysis**

For better statistics calculations and to reduce the standard deviation and standard error in wear volume, it is recommended that 5 repetitions should be performed. Due to the large number of tests being performed during this work and the limitation of the number of specimens, it was not possible to do further tests for the work presented in this thesis.

Also, specimens blinding was not considered in this work and therefore, it is recommended that blinding should be considered as a part of any future work to achieve the four set of criteria in the field of tribology (randomisation, blinding, use of control and repetitions).

### **8.5.6 Impact Wear Model**

The model has been validated under compound impact for only one material (AISI 304) due to lack of data from other materials in the literature and further experimental work for materials other than AISI 304 is required to fully validate the model and its parameters.

Further investigation could be carried out of the role of work hardening during impact as an independent parameter (not hidden within the wear coefficient). This could be included in a new model to highlight its role during impact. However, achieving such work would require more complicated parameters such as the work hardening coefficient and exponent for each tested material and it also means that no validation can be achieved with the current published papers.

## References

- [1] P. Engel, "Percussive impact wear: A study of repetitively impacting solid components in engineering," *TRIBOLOGY international*, vol. 11, pp. 169-176, 1978.
- [2] R. Lewis and R. Dwyer-Joyce, "Impact Wear Failures," Materials Park, OH: ASM International, 2002., pp. 965-974, 2002.
- [3] R. Lewis, C. Tsoraki, J. Broughton, J. Cripps, S. Afodun, T. Slatter, et al., "Abrasive and impact wear of stone used to manufacture axes in Neolithic Greece," *Wear*, vol. 271, pp. 2549-2560, 2011.
- [4] K. Swick, G. Stachowiak, and A. Batchelor, "Mechanism of wear of rotary-percussive drilling bits and the effect of rock type on wear," *Tribology international*, vol. 25, pp. 83-88, 1992.
- [5] S. Ge, Q. Wang, and J. Wang, "The impact wear-resistance enhancement mechanism of medium manganese steel and its applications in mining machines," *Wear*, vol. 376, pp. 1097-1104, 2017.
- [6] R. Lewis and R. Dwyer-Joyce, "Wear of diesel engine inlet valves and seat inserts," *Proceedings of the institution of mechanical engineers, part D: journal of automobile engineering*, vol. 216, pp. 205-216, 2002.
- [7] T. Slatter, H. Taylor, R. Lewis, and P. King, "The influence of laser hardening on wear in the valve and valve seat contact," *Wear*, vol. 267, pp. 797-806, 2009.
- [8] T. Slatter, R. Lewis, and A. Jones, "The influence of induction hardening on the impact wear resistance of compacted graphite iron (CGI)," *Wear*, vol. 270, pp. 302-311, 2011.
- [9] T. Slatter, R. Lewis, and A. H. Jones, "The influence of cryogenic processing on wear on the impact wear resistance of low carbon steel and lamellar graphite cast iron," *Wear*, vol. 271, pp. 1481-1489, 2011.
- [10] F. Lai, S. Qu, Y. Duan, R. Lewis, T. Slatter, L. Yin, et al., "The wear and fatigue behaviours of hollow head & sodium filled engine valve," *Tribology International*, vol. 128, pp. 75-88, 2018.
- [11] T. Bruce, H. Long, T. Slatter, and R. Dwyer-Joyce, "Formation of white etching cracks at manganese sulfide (MnS) inclusions in bearing steel due to hammering impact loading," *Wind Energy*, vol. 19, pp. 1903-1915, 2016.
- [12] S. Tianmin, H. Meng, and T. H. Yuen, "Impact wear behavior of laser hardened hypoeutectoid 2Cr13 martensite stainless steel," *Wear*, vol. 255, pp. 444-455, 2003.
- [13] N. Mahoney, R. Grieve, and T. Ellis, "A simple experimental method for studying the impact wear of materials," *Wear*, vol. 98, pp. 79-87, 1984.
- [14] C. Studman and J. Field, "A repeated impact testing machine," *Wear*, vol. 41, pp. 373-381, 1977.
- [15] W. Jiang, C. Liu, C. He, J. Guo, W. Wang, and Q. Liu, "Investigation on impact wear and damage mechanism of railway rail weld joint and rail materials," *Wear*, vol. 376, pp. 1938-1946, 2017.
- [16] K. G. Budinski, *Guide to friction, wear and erosion testing*: ASTM International West Conshohocken, PA, 2007.

## References

- [17] Y.-Y. Yang, H.-S. Fang, Y.-K. Zheng, Z.-G. Yang, and Z.-L. Jiang, "The failure models induced by white layers during impact wear," *Wear*, vol. 185, pp. 17-22, 1995.
- [18] N. P. Suh, "The delamination theory of wear," *Wear*, vol. 25, pp. 111-124, 1973.
- [19] R. Bulpett, T. Eyre, and B. Ralph, "The characterization of white layers formed on digger teeth," *Wear*, vol. 162, pp. 1059-1065, 1993.
- [20] M. Lindroos, V. Ratia, M. Apostol, K. Valtonen, A. Laukkanen, W. Molnar, et al., "The effect of impact conditions on the wear and deformation behavior of wear resistant steels," *Wear*, vol. 328, pp. 197-205, 2015.
- [21] V. Rastegar and A. Karimi, "Surface and subsurface deformation of wear-resistant steels exposed to impact wear," *Journal of materials engineering and performance*, vol. 23, pp. 927-936, 2014.
- [22] R. Fricke and C. Allen, "Repetitive impact wear of steels," *Wear*, vol. 162, pp. 837-847, 1993.
- [23] C. Zhang, P. Li, H. Dong, D. Jin, J. Huang, F. Mao, et al., "Repetitive Impact Wear Behaviors of the Tempered 25Cr3Mo2NiWV Fe-Based Steel," *Coatings*, vol. 10, p. 107, 2020.
- [24] Y. N. Petrov, V. G. Gavriljuk, H. Berns, and F. Schmalt, "Surface structure of stainless and Hadfield steel after impact wear," *Wear*, vol. 260, pp. 687-691, 2006.
- [25] S. L. Rice, "The role of microstructure in the impact wear of two aluminum alloys," *Wear*, vol. 54, pp. 291-301, 1979.
- [26] S. L. Rice and S. F. Wayne, "Wear of two titanium alloys under repetitive compound impact," *Wear*, vol. 61, pp. 69-76, 1980.
- [27] J. H. Groeger, S. F. Wayne, H. Nowotny, and S. L. Rice, "Wear of copper and copper alloys under repetitive impact sliding," *Materials Science and Engineering*, vol. 49, pp. 249-255, 1981.
- [28] H. Yilmaz and R. Sadeler, "Impact wear behavior of ball burnished 316L stainless steel," *Surface and Coatings Technology*, vol. 363, pp. 369-378, 2019.
- [29] E. Rigaud and A. Le Bot, "Influence of incidence angle on wear induced by sliding impacts," *Wear*, vol. 307, pp. 68-74, 2013.
- [30] W. R. Tyfour, M. T. Hayajneh, and R. Hendawi, "Role of impact angle reversal on impact wear of mild steel," *Proceedings of the Institution of Mechanical Engineers, Part J: Journal of Engineering Tribology*, vol. 232, pp. 97-105, 2018.
- [31] L. M. Roncery, L. A. Jácome, A. Aghajani, W. Theisen, and S. Weber, "Subsurface characterization of high-strength high-interstitial austenitic steels after impact wear," *Wear*, vol. 402, pp. 137-147, 2018.
- [32] M. Akhondizadeh, M. F. Mahani, M. Rezaeizadeh, and S. Mansouri, "Experimental investigation of the impact wear," *Mechanics & Industry*, vol. 15, pp. 39-44, 2014.
- [33] T. Ootani, N. Yahata, A. Fujiki, and A. Ehira, "Impact wear characteristics of engine valve and valve seat insert materials at high temperature (impact wear tests of austenitic heat-resistant steel SUH36 against Fe-base sintered alloy using plane specimens)," *Wear*, vol. 188, pp. 175-184, 1995.

## References

- [34] H. Nowotny, S. Rice, and S. Wayne, "Impact wear of a tool steel," *Wear*, vol. 81, pp. 175-181, 1982.
- [35] M. Akhondizadeh, M. F. Mahani, M. Rezaeizadeh, and S. Mansouri, "Propose a New Model for Prediction of the Impact Wear Using an Experimental Method," *Journal of Solid Mechanics* Vol, vol. 5, pp. 245-252, 2013.
- [36] S. L. Rice, "Variations in wear resistance due to microstructural condition in high strength steel under repetitive impact," *TRIBOLOGY international*, vol. 12, pp. 25-29, 1979.
- [37] Z. Wang, Z.-b. Cai, Z.-q. Chen, Y. Sun, and M.-h. Zhu, "Low-velocity impact wear behavior of ball-to-flat contact under constant kinetic energy," *Journal of Materials Engineering and Performance*, vol. 26, pp. 5669-5679, 2017.
- [38] K. Valtonen, V. Ratia, K. R. Ramakrishnan, M. Apostol, J. Terva, and V.-T. Kuokkala, "Impact wear and mechanical behavior of steels at subzero temperatures," *Tribology International*, vol. 129, pp. 476-493, 2019.
- [39] J. Wang, L. Lu, and Z. Ji, "A Study on the Impact Wear Behaviors of 40Cr Steel," *Tribology Online*, vol. 10, pp. 273-281, 2015.
- [40] T. J. Slatter, "Reducing Automotive Valve Recession with Surface Treatment," University of Sheffield, Department of Mechanical Engineering, 2011.
- [41] P. A. Engel, *Impact wear of materials vol. 2*: Elsevier, 1978.
- [42] P. Engel, "Analysis aid Design for Zero Impact Wear," *Journal of Lubrication Technology* JULY, p. 455, 1974.
- [43] P. Engel, T. Lyons, and J. Sirico, "Impact wear model for steel specimens," *Wear*, vol. 23, pp. 185-201, 1973.
- [44] K. Wellinger and H. Breckel, "Kenngrößen und verschleiss beim stoss metallischer werkstoffe," *Wear*, vol. 13, pp. 257-281, 1969.
- [45] E. Rabinowicz, "Friction and Wear of Materials," 1995.
- [46] R. Lewis, "A modelling technique for predicting compound impact wear," *Wear*, vol. 262, pp. 1516-1521, 2007.
- [47] J. Archard, "Contact and rubbing of flat surfaces," *Journal of applied physics*, vol. 24, pp. 981-988, 1953.
- [48] P. Engel and J. Sirico, "Impact wear study of lubricated contacts," *ASLE TRANSACTIONS*, vol. 18, pp. 279-289, 1975.
- [49] E. Rabinowicz, "The Wear Coefficient—Magnitude, Scatter, Uses," *Journal of Lubrication Technology*, vol. 103, pp. 188-193, 1981.
- [50] K. Guo, C. Tian, Y. Wang, Y. Wang, and W. Tan, "An energy-based model for impact-sliding fretting wear between tubes and anti-vibration bars in steam generators," *Tribology International*, p. 106305, 2020.
- [51] M. Apostol, V. Kuokkala, A. Laukkanen, K. Holmberg, R. Waudby, and M. Lindroos, "High velocity particle impactor—modeling and experimental verification of impact wear test," in *World Tribology Congress WTC*, 2013, pp. 8-13.

## References

- [52] W. Molnar, S. Nugent, M. Lindroos, M. Apostol, and M. Varga, "Ballistic and numerical simulation of impacting goods on conveyor belt rubber," *Polymer Testing*, vol. 42, pp. 1-7, 2015.
- [53] J. Williams, *Engineering tribology*: Cambridge University Press, 2005.
- [54] E. S. Zanoria and P. J. Blau, "Effect of Incidence Angle on the Impact-Wear Behavior of Silicon Nitride," *Journal of the American Ceramic Society*, vol. 81, pp. 901-909, 1998.
- [55] M. Harmon and R. Lewis, "Review of top of rail friction modifier tribology," *Tribology-Materials, Surfaces & Interfaces*, vol. 10, pp. 150-162, 2016.
- [56] D. Preece, R. Lewis, and M. Carré, "A critical review of the assessment of medical gloves," *Tribology-Materials, Surfaces & Interfaces*, pp. 1-10, 2020.
- [57] K. Ishizaka, S. R. Lewis, and R. Lewis, "The low adhesion problem due to leaf contamination in the wheel/rail contact: Bonding and low adhesion mechanisms," *Wear*, vol. 378, pp. 183-197, 2017.
- [58] T. Bruce, "Analysis of the premature failure of wind turbine gearbox bearings," University of Sheffield, 2016.
- [59] W. J. Stronge, *Impact mechanics*: Cambridge university press, 2018.
- [60] ASTM, "E384-11E1," Standard Test Method for Knoop and Vickers Hardness of Materials, 2007.
- [61] K. L. Johnson and K. L. Johnson, *Contact mechanics*: Cambridge university press, 1987.
- [62] R. Dwyer-Joyce, "Tribological design data part 3: Contact mechanics," University of Sheffield, 1997.
- [63] X.-f. Qin, F. Li, and X. Zhao, "An Approach for Subsurface Rolling Contact Fatigue Damage Assessment of Backup Roll Material," *Journal of Failure Analysis and Prevention*, vol. 17, pp. 942-947, 2017.
- [64] F. C. Bell and D. E. Sonon, "Improved metallographic etching techniques for stainless steel and for stainless steel to carbon steel weldments," *Metallography*, vol. 9, pp. 91-107, 1976.
- [65] ASTM, "E112, 2010, standard test methods for determining average grain size astm international," West Conshohocken, 2010.
- [66] ASTM, "E407-07, Standard practice for microetching metals and alloys," ed: ASTM International West Conshohocken, PA, 2015.
- [67] J. Archard, "Contact and rubbing of flat surfaces', *Journal of Applied Physics*," 1953.
- [68] M. Watson, P. Christoforou, P. Herrera, D. Preece, J. Carrell, M. Harmon, et al., "An analysis of the quality of experimental design and reliability of results in tribology research," *Wear*, vol. 426, pp. 1712-1718, 2019.
- [69] D. C. Montgomery, *Design and analysis of experiments*: John wiley & sons, 2017.
- [70] D. W. Hetzner, "Microindentation hardness testing of materials using ASTM e384," *Microscopy and Microanalysis*, vol. 9, pp. 708-709, 2003.

## References

- [71] M. Zalzal, R. Lewis, and T. Slatter, "Defining the role of "zero wear volume" in percussive impact," *Wear*, p. 203535, 2020.
- [72] P. Shipway and N. Ngao, "Microscale abrasive wear of polymeric materials," *Wear*, vol. 255, pp. 742-750, 2003.
- [73] C. Yuan, Z. Peng, X. Zhou, and X. Yan, "The characterization of wear transitions in sliding wear process contaminated with silica and iron powder," *Tribology international*, vol. 38, pp. 129-143, 2005.
- [74] R. Juránek, S. Machalík, and P. Zemčík, "Analysis of wear debris through classification," in *International Conference on Advanced Concepts for Intelligent Vision Systems*, 2011, pp. 273-283.
- [75] R. M. Dan, "Multi-view and Three-dimensional (3D) Images in Wear Debris Analysis (WDA)," University of Manchester, 2013.
- [76] C. Yunxia, G. Wenjun, and K. Rui, "Review and propositions for the sliding/impact wear behavior in a contact interface," *Chinese Journal of Aeronautics*, vol. 33, pp. 391-406, 2020.
- [77] P. A. Engel and F. F. Ling, "Impact wear of materials," ed: American Society of Mechanical Engineers Digital Collection, 1978.
- [78] S. L. Rice, "Reciprocating impact wear testing apparatus," *Wear*, vol. 45, pp. 85-95, 1977.
- [79] F. C. White, S. T. Noah, C. F. Kettleborough, and R. B. Griffin, "An apparatus for the study of wear under dynamic loading conditions," *Wear*, vol. 97, pp. 179-197, 1984.
- [80] Z. Wang, Z.-b. Cai, Y. Sun, J.-f. Peng, and M.-h. Zhu, "Low velocity impact wear behavior of MoS<sub>2</sub>/Pb nanocomposite coating under controlled kinetic energy," *Surface and Coatings Technology*, vol. 326, pp. 53-62, 2017.
- [81] N. P. Suh, "An overview of the delamination theory of wear," *Wear*, vol. 44, pp. 1-16, 1977.
- [82] M. Lindroos, M. Apostol, V.-T. Kuokkala, A. Laukkanen, K. Valtonen, K. Holmberg, et al., "Experimental study on the behavior of wear resistant steels under high velocity single particle impacts," *International Journal of Impact Engineering*, vol. 78, pp. 114-127, 2015.
- [83] N. E. Dowling, *Mechanical Behavior of Materials: International Edition: Pearson Higher Ed*, 2013.
- [84] A. P. Mouritz, *Introduction to aerospace materials: Elsevier*, 2012.
- [85] W. T. Becker and R. J. Shipley, *Failure analysis and prevention vol. 11: ASM International*, 2002.
- [86] G. Cassar, S. Banfield, J. A.-B. Wilson, J. Housden, A. Matthews, and A. Leyland, "Impact wear resistance of plasma diffusion treated and duplex treated/PVD-coated Ti-6Al-4V alloy," *Surface and Coatings Technology*, vol. 206, pp. 2645-2654, 2012.
- [87] D. Tabor, *The hardness of metals: Oxford university press*, 2000.
- [88] A. E407-07, "Standard practice for microetching metals and alloys," ed: ASTM International West Conshohocken, PA, 2015.

## References

- [89] I. Hutchings, R. Winter, and J. E. Field, "Solid particle erosion of metals: the removal of surface material by spherical projectiles," *Proceedings of the Royal Society of London. A. Mathematical and Physical Sciences*, vol. 348, pp. 379-392, 1976.
- [90] I. Finnie, "Some observations on the erosion of ductile metals," *wear*, vol. 19, pp. 81-90, 1972.
- [91] G. Liang, S. Schmauder, M. Lyu, Y. Schneider, C. Zhang, and Y. Han, "An investigation of the influence of initial roughness on the friction and wear behavior of ground surfaces," *Materials*, vol. 11, p. 237, 2018.
- [92] J. A. Williams, "Wear and wear particles—some fundamentals," *Tribology International*, vol. 38, pp. 863-870, 2005.
- [93] J. Challen, P. Oxley, and B. Hockenhull, "Prediction of Archard's wear coefficient for metallic sliding friction assuming a low cycle fatigue wear mechanism," *Wear*, vol. 111, pp. 275-288, 1986.
- [94] E. Rabinowicz, "The wear coefficient—magnitude, scatter, uses," 1981.
- [95] L. Yang, "A test methodology for the determination of wear coefficient," *Wear*, vol. 259, pp. 1453-1461, 2005.

## Appendix A

### Map Grading Criteria

Reference Number	Primary Category	Secondary Category	Criteria					Total score
			1	2	3	4	5	
2	Impact Wear Testing	Impact Wear Rigs	Y	Y	N	N	N	2
5	Impact Wear Testing	Impact Wear Rigs	Y	Y	N	N	N	2
7	Impact Wear Testing	Wear Measurements	Y	Y	N	N	N	2
8	Impact Wear Testing	Wear Measurements	Y	Y	N	N	N	2
9	Impact Wear Testing	Wear Measurements	Y	Y	N	N	N	2
11	Impact Wear Models	Impact Wear Simulation	Y	Y	N	Y	N	3
12	Impact Wear Parameters	Hardness	Y	Y	N	N	N	2
13	Impact Wear of Metals	Ferrous Materials	Y	Y	N	N	N	2
14	Impact Wear of Metals	Ferrous Materials	Y	Y	N	N	N	2
15	Impact Wear of Metals	Ferrous Materials	Y	Y	N	N	N	2
16	Impact Wear of Metals	Ferrous Materials	Y	Y	N	N	N	2
17	Impact Wear of Metals	Ferrous Materials	Y	Y	N	N	N	2
18	Impact Wear of Metals	Ferrous Materials	Y	Y	N	N	N	2

## Appendix A

19	Impact Wear of Metals	Ferrous Materials	Y	Y	N	N	N	2
20	Impact Wear of Metals	Ferrous Materials	Y	Y	N	N	N	2
21	Impact Wear of Metals	Ferrous Materials	Y	Y	N	N	N	2
22	Impact Wear of Metals	Ferrous Materials	Y	Y	N	Y	N	3
23	Impact Wear of Metals	Ferrous Materials	Y	Y	N	N	N	2
24	Impact Wear of Metals	Ferrous Materials	Y	Y	N	N	N	2
25	Impact Wear of Metals	Non-Ferrous Materials	Y	Y	N	N	N	2
26	Impact Wear of Metals	Non-Ferrous Materials	Y	Y	N	N	N	2
27	Impact Wear of Metals	Non-Ferrous Materials	Y	Y	N	N	N	2
28	Impact Wear Parameters	Hardness	Y	Y	N	N	N	2
29	Impact Wear Parameters	Roughness	Y	Y	N	N	N	2
30	Impact Wear Parameters	Impact Angle	Y	Y	N	N	N	2
31	Impact Wear Testing	Wear Measurements	Y	Y	N	N	N	2
32	Impact Wear Testing	Wear Measurements	Y	Y	N	N	N	2
33	Impact Wear Testing	Wear Measurements	Y	Y	N	N	N	2
34	Impact Wear Testing	Wear Measurements	Y	Y	N	N	N	2

## Appendix A

35	Impact Wear Testing	Wear Measurements	Y	Y	N	Y	N	3
36	Impact Wear Testing	Wear Measurements	Y	Y	N	N	N	2
37	Impact Wear Testing	Wear Measurements	Y	Y	N	N	N	2
38	Impact Wear Testing	Wear Measurements	Y	Y	N	N	N	2
39	Impact Wear Testing	Wear Measurements	Y	Y	N	N	N	2
41	Impact Wear Model	Zero Wear Model	Y	Y	N	Y	N	3
44	Impact Wear Model	Extant Wear Models	Y	Y	N	Y	N	3
45	Impact Wear Model	Extant Wear Models	Y	Y	N	Y	N	3
46	Impact Wear Model	Extant Wear Models	Y	Y	N	Y	N	3
50	Impact Wear Model	Extant Wear Models	Y	Y	N	Y	N	3
51	Impact Wear Model	Impact Wear Simulation	Y	Y	N	Y	N	3
52	Impact Wear Model	Impact Wear Simulation	Y	Y	N	Y	N	3
53	Impact Wear Parameters	Impact Angle	Y	Y	N	N	N	2
54	Impact Wear Parameters	Impact Angle	Y	Y	N	N	N	2

## Appendix B

### MATLAB Coding for Tested Materials

% Example of stress distribution for PB102

#### Surface stresses calculation

```

Fn= 3476;           % F is the impact force
E1= 1.21e11;       % E is the young Modulus of PB102 material
E2= 2.1e11;       % E is the young Modulus of Ball Bearing materials
R=0.0075;         % R is the radius of the ball
mu1=0.34;         % poisson Ratio of PB102 material
mu2=0.29;         % poisson Ratio of Ball bearing material
RR=(1/R1);
R=(1/RR);
EE=((1-mu1^2)/(E1)) +((1-mu2^2)/(E2));
E=1/EE;
a=((3*Fn*R)/(4*E)).^(1/3); % Where a is the radius of contact area
Po=(3*Fn)/(2*pi*a.^2); % Where Po is the Maximum contact Pressure on surface
Pavg=(Fn)/(pi*a.^2); % Where Pavg is the average contact Pressure on surface
r = -a:a/150:a; % Where r is the is ratio of a
Pr=-Po.*(1-(r.^2/a.^2)).^0.5; % pressure distribution on the surface
Sr=Po.*((((1-(2*mu2))/3).*((a.^2)/(r.^2)).*(1-(1-((r.^2)/(a.^2))).^(3/2)))-(1-((r.^2)/(a.^2))).^(0.5));
Stheta=Po.*((((-1*(1-(2*mu2))/3).*((a.^2)/(r.^2)).*(1-(1-((r.^2)/(a.^2))).^(3/2)))-(2*mu2)*(1-((r.^2)/(a.^2))).^(0.5));
Sz = -Po.*(1-(r.^2/a.^2)).^0.5;
xlim([-0.6 0.6]);
ylim([-6000 6000]);
set(gca, 'XTick', [-0.6 -0.55 -0.5 -0.45 -0.4 -0.35 -0.3 -0.25 -0.2 -0.15 -0.1 0 0.1 0.15 0.2 0.25 0.3 0.35 0.4 0.45 0.5 0.55 0.6 ],'fontsize',10,'FontName','Times New Roman');
set(gca, 'YTick', [-6000 -5500 -5000 -4500 -4000 -3500 -3000 -2500 -2000 -1500 -1000 -500 0 500 1000 1500 2000 2500 3000 3500 4000 4500 5000 5500 6000 ],'fontsize',10,'FontName','Times New Roman');
set(gca,'FontName','Times New Roman','fontsize',12);
plot(r*1000,Sr/1000000,'r') % where r in mm and stress in MPa
hold on
plot(r*1000,Stheta/1000000,'g') % where r in mm and stress in MPa
hold on
plot(r*1000,Sz/1000000,'k') % where r in mm and stress in MPa
hold on
plot(r*1000,Pr/1000000) % where r in mm and stress in MPa
legend('Sr','Stheta','Sz','Pr')
xlabel('Contact Radius(a) in mm')
ylabel('Surface stress distribution (MPa)')

```

## Appendix B

min(Sr) % mean the maximum value of the radial stress in the subsurface  
 min(Stheta) % mean the maximum value of the radial stress in the subsurface  
 min(Sz) % mean the maximum value of the stress in the z direction for the subsurface  
 max(Pr)

**Subsurface stresses calculations**

```

Fn= 3476; % F is the impact force
E1= 1.21e11; % E is the young Modulus of PB102 material
E2= 2.1e11; % E is the young Modulus of Ball Bearing materials
R1=0.0075; % R1 is the radius of the ball
mu1=0.34; % possion Ratio of PB102 material
mu2=0.29; % possion Ratio of Ball bearing material
RR=((1/R1));
R=(1/RR);
EE=((((1-mu1^(2))/(E1))+((1-mu2^(2))/(E2))));
E=1/EE;
a=((3*Fn*R)/(4*E)).^(1/3); % Where a is the radius of contact area
Po=(3*Fn)/(2*pi*a.^2); % Where Po is the Maximum contact Pressure on surface
Pavg=(Fn)/(pi*a.^2); % Where Pavg is the average contact Pressure on surface
dd=-1500e-6; % value used by the software
z = 0:dd/150:dd; % Where r is the is ratio of a
Sz=-Po.*((1+((z.^2)/(a.^2))).^-1);
Sr=Po.*(((-1).*(1+mu2).*(1-(z./a).*atan(a./z)))+0.5.*((1+((z.^2)/(a.^2))).^-1));
Stheta=Po.*(((-1).*(1+mu2).*(1-(z./a).*atan(a./z)))+0.5.*((1+((z.^2)/(a.^2))).^-1));
Trz=0.5*(Sz-Sr);
Vm=-((0.5*((Sr - Stheta).^2 + (Sr - Sz).^2 + (Sz - Sr).^2)).^0.5;
Tmax=-0.31*Po;
xlim([-2000 500]);
ylim([-0.5 0]);
set(gca, 'XTick', [-0.6 -0.55 -0.5 -0.45 -0.4 -0.35 -0.3 -0.25 -0.2 -0.15 -0.1 0 0.1 0.15 0.2 0.25 0.3 0.35
0.4 0.45 0.5 0.55 0.6 ],'fontsize',10,'FontName','Times New Roman');
set(gca, 'YTick', [-6000 -5500 -5000 -4500 -4000 -3500 -3000 -2500 -2000 -1500 -1000 -500 0 500
1000 1500 2000 2500 3000 3500 4000 4500 5000 5500 6000 ],'fontsize',10,'FontName','Times New
Roman');
set(gca,'FontName','Times New Roman','fontsize',12);
set(gca,'FontName','Times New Roman','fontsize',14);
plot(Sr/1000000,z*1000,'b') % where Z is the depth in Z direction in mm and stress in MPa
hold on
plot(Sz/1000000,z*1000,'k') % where Z is the depth in Z direction in mm and stress in MPa
hold on
plot(Trz/1000000,z*1000,'g') % where Z is the depth in Z direction in mm and stress in MPa
hold on
plot(Vm/1000000,z*1000,'r') % where Z is the depth in Z direction in mm and stress in MPa
legend('Sr','Sz','Trz','Vm')
xlabel('Stress distribution in (MPa)')

```

```
ylabel('Depth in z direction')
min(Trz)    % mean the maximum value of the Shear stress in the subsurface
min(Sr)    % mean the maximum value of the radial and theta stresses in the subsurface
min(Sz)    % mean the maximum value of the stress in the z direction for the subsurface
min(Vm)    % mean the maximum value of the von mises stress in the z direction for the subsurface
[M1, I1]=min(Trz); % to identify the loaction of the line where max subsurafce shear stress occur
z1_value=z(I1);  % to identify the value of the Z where max subsurafce shear stress occur at line I
[M, I]=min(Vm); % to identify the loaction of the line where max subsurafce Von mises stress occur
z_value=z(I);  % to identify the value of the Z where max subsurafce Von mises stress occur at line I
```